University of Kentucky
UKnowledge

Theses and Dissertations--Earth and Environmental Sciences

Earth and Environmental Sciences

2012

INTEGRATED GEOPHYSICAL INVESTIGATION OF KARST FEATURES – INNER BLUEGRASS REGION OF KENTUCKY

Jamin C. Frommel
University of Kentucky, jfr228@uky.edu

Right click to open a feedback form in a new tab to let us know how this document benefits you.

Recommended Citation
Frommel, Jamin C., "INTEGRATED GEOPHYSICAL INVESTIGATION OF KARST FEATURES – INNER BLUEGRASS REGION OF KENTUCKY" (2012). *Theses and Dissertations--Earth and Environmental Sciences*. 5.
https://uknowledge.uky.edu/ees_etds/5

This Master's Thesis is brought to you for free and open access by the Earth and Environmental Sciences at UKnowledge. It has been accepted for inclusion in Theses and Dissertations--Earth and Environmental Sciences by an authorized administrator of UKnowledge. For more information, please contact UKnowledge@lsv.uky.edu.

STUDENT AGREEMENT:

I represent that my thesis or dissertation and abstract are my original work. Proper attribution has been given to all outside sources. I understand that I am solely responsible for obtaining any needed copyright permissions. I have obtained and attached hereto needed written permission statements(s) from the owner(s) of each third-party copyrighted matter to be included in my work, allowing electronic distribution (if such use is not permitted by the fair use doctrine).

I hereby grant to The University of Kentucky and its agents the non-exclusive license to archive and make accessible my work in whole or in part in all forms of media, now or hereafter known. I agree that the document mentioned above may be made available immediately for worldwide access unless a preapproved embargo applies.

I retain all other ownership rights to the copyright of my work. I also retain the right to use in future works (such as articles or books) all or part of my work. I understand that I am free to register the copyright to my work.

REVIEW, APPROVAL AND ACCEPTANCE

The document mentioned above has been reviewed and accepted by the student's advisor, on behalf of the advisory committee, and by the Director of Graduate Studies (DGS), on behalf of the program; we verify that this is the final, approved version of the student's dissertation including all changes required by the advisory committee. The undersigned agree to abide by the statements above.

Jamin C. Frommel, Student

Dr. Edward W. Woolery, Major Professor

Dr. Alan E. Fryar, Director of Graduate Studies

INTEGRATED GEOPHYSICAL INVESTIGATION OF KARST FEATURES – INNER BLUEGRASS REGION OF KENTUCKY

THESIS

A thesis submitted in partial fulfillment of the
requirements for the degree of Master of Science in the
College of Arts and Sciences
at the University of Kentucky

By

Jamin C. Frommel

Lexington, Kentucky

Director: Dr. Edward W. Woolery, Professor of Geological Sciences

Lexington, Kentucky

2012

Copyright© Jamin C. Frommel

ABSTRACT OF THESIS

Integrated Geophysical Investigation of Karst Features—Inner Bluegrass Region of Kentucky

High-resolution electrical-resistivity, seismic-refraction, and seismic-reflection surveys were performed at three locations in the Inner Bluegrass Region of Kentucky along coincident survey lines in order to correlate results and determine which method is most effective at locating karst features in this area. The first two survey locations at Slack's Cave and the Kentucky Horse Park were chosen in order to investigate known karst features. High and low electrical-resistivity anomalies were correlated to air- and water-filled karst voids, respectively. Seismic velocity anomalies, including parabolic time suppressions, amplitude terminations, and surface-wave backscatters, were also observed and correlated to these karst voids. These findings were applied to a third location along Berea Road in order to investigate undiscovered karst voids. Three seismic targets were selected based on backscatter anomaly locations and were aligned in a northwest trend following the general bedrock dip, joint orientations, and suspected conduit orientation. Overall, the seismic-reflection method provided the highest resolution and least ambiguous results; however, integration of multiple methods was determined to help decrease ambiguities in interpretation created by the inherent non-uniqueness found in the results of each method.

KEYWORDS: karst, geophysics, electrical resistivity tomography, seismic refraction tomography, seismic reflection profiling

Jamin C. Frommel

May 2012

INTEGRATED GEOPHYSICAL INVESTIGATION OF KARST FEATURES—INNER BLUEGRASS REGION OF KENTUCKY

By

Jamin C. Frommel

Edward W. Woolery
Director of Thesis

Alan E. Fryar
Director of Graduate Studies

May 2011

Table of Contents

Table of Contents iv
List of Tables vi
List of Figures vii
CHAPTER ONE 1
1.1 Problem Being Addressed 1
1.2 Study Objectives 2
1.3 Study Locations 3
1.4 Regional Geology 4
1.5 Related Studies 5
1.5.1 Related Studies—Methodology 5
1.5.1.1 Karst Investigations Using Electrical Methods 6
1.5.1.2 Karst Investigations Using Seismic Methods 7
1.5.1.3 Karst Investigations Integrating Electrical and Seismic Methods 8
1.5.2 Inner Bluegrass Karst Geophysical Investigations 9
CHAPTER TWO 21
2.1 Integrated Multimethod Geophysical Studies 21
2.2 Electrical-Resistivity Tomography 21
2.2.1 Method Justification 21
2.2.2 Data Acquisition 22
2.2.3 Data Processing 24
2.2.4 Resolution 25
2.3 Near-Surface Seismic Methods 25
2.3.1 Method Justification 25
2.3.2 Data Acquisition 26
2.3.3 Data Processing 28
2.3.3.1 Seismic-Refraction Tomography 28
2.3.3.2 Seismic-Reflection Profiling 28
2.3.4 Resolution 30
CHAPTER THREE 41
3.1 Electrical-Resistivity Data Interpretation 41

3.1.1 ER Survey 1, Slack's Cave 41
3.1.2 ER Survey 2, Kentucky Horse Park 43
3.1.3 ER Survey 3, Berea Road 44
3.2 Seismic Refraction Data Interpretation 45
3.2.1 Refraction Survey 1, Slack's Cave 46
3.2.2 Refraction Survey 2, Kentucky Horse Park 47
3.2.3 Refraction Survey 3, Berea Road 48
3.3 Seismic-Reflection Data Interpretation 49
3.3.1 Reflection Survey 1, Kentucky Horse Park 49
3.3.2 Reflection Survey 2, Berea Road 51
CHAPTER FOUR 84
4.1 Comparison of Method Results 84
4.1.1 Slack's Cave Study Area 84
4.1.2 Kentucky Horse Park Study Area 84
4.1.3 Berea Road Study Area 85
CHAPTER FIVE 91
APPENDIX A 93
Appendix A 94
Section 1 94
Appendix A 111
Section 2 111
Appendix A 127
Section 3 127
APPENDIX B 142
Appendix B 143
BIBLIOGRAPHY 188
VITA 193

List of Tables

Table 2.1. Common resistivity ranges for various earth materials 33
Table 2.2. Data acquisition parameters for electrical-resistivity surveys 34
Table 2.3. Inversion settings applied to ER data..... 35
Table 2.4. Data-acquisition parameters for seismic-reflection surveys 36
Table 2.5. Generalized processing steps for seismic-reflection data 37

List of Figures

Figure 1.1. Physiographic diagram of Kentucky 11
Figure 1.2. Generalized block diagram of Inner Bluegrass karst 12
Figure 1.3. Location map of study areas in the Inner Bluegrass Region of Kentucky 13
Figure 1.4. Overlay map of Slack's Cave. 14
Figure 1.5. Photo of Slack's Cave karst window. 15
Figure 1.6. Diagram of regional structural features of Kentucky 16
Figure 1.7. Diagrammatic cross section of Inner Bluegrass Region 17
Figure 1.8. Stratigraphic section measured at the Vulcan Quarry. 18
Figure 1.9. Twelve-fold CDP stack depicting seismic responses to coal-mine voids. 19
Figure 1.10. Diagrammatic models of earth structure distorted by variation in velocity. 20
Figure 1.11. Synthetic model depicting seismic backscatters. 20
Figure 2.1. Combined parallel ER survey lines used to create a 2.5D tomographic profile. 37
Figure 2.2. Generalized diagrams of ER survey arrays. 38
Figure 2.3. Example of a 52-electrode dipole-dipole command file configuration. 39
Figure 2.4. Simplified model depicting a subsurface void. 40
Figure 3.1. Example of a measured apparent resistivity pseudosection 53
Figure 3.2. Slack's Cave electrical-resistivity survey line locations. 54
Figure 3.3. Slack's Cave ERT profiles from survey line 1. 55
Figure 3.4. Slack's Cave ERT profiles from survey lines 3 to 5 56
Figure 3.5. 2.5D image from Slack's Cave study area. 57
Figure 3.6. Kentucky Horse Park electrical-resistivity survey line locations. 58
Figure 3.7. Inverted section from Kentucky Horse Park ER survey line 1 59
Figure 3.8. Kentucky Horse Park ERT profiles from lines 1−5 60
Figure 3.9. Right: 2.5D ERT image from Kentucky Horse Park survey 61
Figure 3.10. Berea Road electrical-resistivity survey line location. 62
Figure 3.11. Berea Road ERT profile from survey line 1 63
Figure 3.12. Slack's Cave refraction survey line locations. 64
Figure 3.13. Raw data file from Slack's Cave refraction line 1 65
Figure 3.14. Slack's Cave SRT profile from survey line 1 66
Figure 3.15. Slack's Cave SRT profile from survey line 2 67
Figure 3.16. Kentucky Horse Park refraction survey line location. 68
Figure 3.17. Kentucky Horse Park SRT profile from survey line 1 69
Figure 3.18. Berea Road refraction survey line locations. 70
Figure 3.19. Berea Road reflection survey line locations. 71
Figure 3.20. Berea Road SRT profile from survey line 1. 72
Figure 3.21. Uninterpreted and interpreted CDP stack reflection profiles from Berea Road survey line 3. 73
Figure 3.22. Uninterpreted and interpreted common offset reflection profiles from Berea Road survey line 3 74
Figure 3.23. Interpreted CDP profile and SRT profile from Berea Road. 75

Figure 3.24. Berea Road SRT profile from survey line 2 76
Figure 3.25. Kentucky Horse Park reflection survey line locations. 77
Figure 3.26. Interpreted CDP stack reflection profiles from Kentucky Horse Park survey line 1. 78
Figure 3.27. Uninterpreted and interpreted CDP stack reflection profiles from Kentucky Horse Park survey line 3 79
Figure 3.28. Uninterpreted and interpreted CDP stack reflection profiles from Berea Road survey line 1 80
Figure 3.29. Uninterpreted and interpreted common offset reflection profiles from Berea Road survey line 1..... 81
Figure 3.30. Uninterpreted and interpreted CDP stack reflection profiles from Berea Road survey line 2 82
Figure 3.31. Uninterpreted and interpreted common offset reflection profiles from Berea Road survey line 2..... 83
Figure 4.1. Slack's Cave ERT profile and SRT profile from survey line 1..... 87
Figure 4.2. Kentucky Horse Park ERT profile, SRT profile, and CDP stack reflection profile from survey line 1..... 88
Figure 4.3. Berea Road ERT profile, SRT profile, and common offset reflection profile..... 89
Figure 4.4 Berea Road reflection survey map..... 90

CHAPTER ONE
INTRODUCTION

1.1 Problem Being Addressed

Detecting shallow subsurface voids has been a challenge for geologists and engineers for decades. Both natural (karst) and manmade (tunnels, abandoned mines, catacombs) subsurface voids can pose public safety hazards through subsidence, sinkhole formation, and by undermining building foundations. In the eastern United States alone, karst sinkholes are responsible for millions of dollars of damage to land and infrastructure (Dinger et al, 2007). In addition to engineering hazards, groundwater contamination is of particular concern in karst areas for two primary reasons: 1) water and chemicals can move directly from the surface into the groundwater and 2) water and associated chemicals flow very rapidly with little filtration (Felton and Currens, 1994). Therefore, in order to determine pollution sources and outlets, their subsurface locations must be located. However, karst system geometries and structures are typically complex and unpredictable, thereby complicating the detection and delineation processes. Traditional subsurface karst exploration methods involved "blind" drilling in simple geometric patterns, which is neither cost nor time effective. Geophysical exploration techniques provide methods of detecting karst in a non-invasive manner with much higher resolution than simple geometric drilling patterns can produce. In addition, technological and procedural advances in near-surface geophysical methods have led to increases in data quality and survey efficiency coupled with decreases in survey costs, thereby further establishing these as viable options for subsurface void detection. The

success of each method depends on its ability to resolve the specified target at depth, however.

The Inner Bluegrass Region of Kentucky (Fig. 1.1) has a high concentration of karst features including caves, sinkholes, and solution conduits (Fig. 1.2). Of particular interest to this study is a mature karst system that facilitates the transport of pollutants in the Royal Spring Basin. Paylor and Currens (2004) performed dye-tracing tests in this basin, and based on the results hypothesized that it was a major conduit in the main karst aquifer that supplies water northwest into Royal Spring in Georgetown, Kentucky, the primary water source for the city's 7,000 residents (Fig. 1.3). In order to evaluate the concentration of pollutants at various locations, and thus determine the upstream sources of the contamination, spatial delineation of the system is necessary. Consequently, integrated geophysical surveys were performed to address this problem.

1.2 Study Objectives

An integrated, high-resolution geophysical investigation of karst features in the Inner Bluegrass Region was performed in order to correlate geophysical signal anomalies with subsurface karst features. Specifically, the study utilized seismic refraction and reflection, as well as 2 and 2.5D electrical resistivity tomography profiling to identify acoustic and electrical property variations within the near-surface bedrock that could indicate karst-associated voids. Two sites having accurate subsurface locations of known karst voids were chosen as reference sites for calibrating the associated geophysical signals. The characteristic or anomalous electrical and seismic responses from the reference sites were used for delineating spatial locations of the solution voids at a third

location, the Berea Road site. Furthermore, the characteristic geophysical signals found in this study can be applied to future studies in this region or other areas with similar geologic conditions.

1.3 Study Locations

One of the reference sites was Slack's Cave (Fig. 1.3), which is located in Scott County near Georgetown, Kentucky. It has been surveyed and mapped by the Kentucky Geological Survey (Fig. 1.4). This cave was chosen as a calibration site because of the access to a priori information regarding the cave's spatial characteristics and ease of access. The cave dimensions at the point of the geophysical measurements are approximately 10 m wide by 6 m tall with approximately 3 to 5 m of residual soil overburden, the thickness of which gradually increases inboard from the karst window (Fig. 1.5). The other reference site is at the Kentucky Horse Park in Lexington, Kentucky (Fig. 1.3), where the karst solution tributary conduit was located by drilling. The dimensions of the conduit are approximately 5 m wide by 2 m tall, and it is located at a depth of approximately 18 m below ground surface. There is approximately 0.5 m of residual soil overburden. This particular conduit is speculated to extend southeast into the third study area, which is approximately 2 miles from the Horse Park study area and adjacent to Berea Road in Lexington, Kentucky (Fig. 1.3).

1.4 Regional Geology

The Inner Bluegrass Region of Kentucky is characterized by interbedded limestone and shale bedrock. The north–south-trending Cincinnati Arch (Fig. 1.6) is the main structural feature in this area and controls the overall gentle northwest dip of the bedrock strata (Cressman, 1967). The Jessamine and Nashville Domes are formed along its axis, separated by a saddle in Cumberland County, Kentucky (Nosow et al., 1960). Several small faults cross the area in a general northwest trend along with a set of joints that are oriented northwest and northeast (Taylor, 1992). Based on dye-trace results, the solution conduit discovered at the Kentucky Horse Park that feeds Royal Spring is thought to follow the general northwest trend of the resultant dipping bedrock strata and major fault and joint sets (Paylor and Currens, 2004; Zhu et al., 2011).

The primary stratigraphic sequence of the region consists of (in descending order) the Clays Ferry Formation, Lexington Limestone, High Bridge Group, Wells Creek Formation and St. Peter Sandstone, and the Knox Group (Fig. 1.7). The Clays Ferry Formation consists of calcareous shale and thin-bedded limestone, and contains enough insoluble shale to inhibit the formation of karst terrain in most areas of the Inner Bluegrass (Thrailkill, 1982). In areas of karst topography, only isolated inliers are typically found as either topographic highs or faulted structural lows (Graham, 1995). The Lexington Limestone is the primary karst-forming unit in this study and is subdivided into 11 members (Cressman, 1967). Exposed outcrops are generally absent in the area; however, a section of approximately 21 m has been measured at the Vulcan Quarry (Fig. 1.8), located approximately 5 to 10 mi from the study locations. The Grier, Brannon, Tanglewood, and Millersburg Members (in ascending order) are exposed at the

surface (Bonita, 1993). The Grier Member consists mainly of fossiliferous bioclastic limestone, generally occurring in lumpy-surfaced beds with thin, undulating shale nodules (Black et al., 1965). The Brannon Member is composed of very thin to thin, tabular beds of limestone interbedded with gray shale (Black et al., 1965). The Tanglewood Member is characterized by calcarenite consisting of bioclastic carbonate sand grains cemented with crystalline calcite and generally occurs in planar-surfaced beds (Black et al., 1965). The Millersburg Member is very similar to the Grier in character and type of limestone but contains much higher amounts of shale, and the beds are generally discontinuous with irregular surfaces (Black et al., 1965). The High Bridge Group is subdivided (in ascending order) into the Camp Nelson Limestone, Oregon Limestone, and Tyrone Limestone (Cressman, 1965). The primary members of the Knox Group in this area are (in ascending order) the Copper Ridge Dolomite and the Beekmantown Dolomite (Cressman, 1965).

1.5 Related Studies

1.5.1 Related Studies—Methodology

Numerous studies aimed at using surface geophysical methods to locate and delineate shallow subsurface voids have been undertaken since the 1950s, though few published studies were well documented prior to the early 1990s (Chalikakis et al., 2011). Gravity, electromagnetic, electrical (including self-potential and resistivity/conductivity), and seismic methods, along with ground penetrating radar (GPR) have all been used in a variety of settings in an attempt to locate various types of subsurface voids. Each method has its own advantages and challenges based on the geologic and void characteristics;

therefore, many studies integrate multiple methods in order to determine which is better suited to the site specific conditions.

GPR has been used in several karst investigation studies and is capable of higher resolution than most other methods, as it can operate at high frequencies ranging between 12 MHz and 500 MHz (Cook, 1975; Ballard, 1983; Daniels 1988; Elawadi et al., 2006); however, when used in areas overlain with conductive soils, such as the Inner Bluegrass Region, signal attenuation limits depth of investigation to a few meters at best, making GPR an ineffective method (Doolittle and Collins, 1998; Cardarelli et al., 2006). Electromagnetic and gravity methods have also been used in karst investigation studies, but they offer lower resolution than seismic and electrical methods (Burger et al., 2006); therefore, seismic and electrical methods were determined the best options for the study objectives.

1.5.1.1 Karst Investigations Using Electrical Methods

Air-filled cavities (located above or disconnected from the water table) typically display high electrical-resistivity anomalies relative to the surrounding rock, whereas water-filled cavities (below the water table) exhibit low electrical-resistivity anomalies relative to the surrounding rock, making the electrical-resistivity method suitable for both scenarios (Smith, 1986). The U.S. Geological Survey (USGS), in cooperation with the Ohio Department of Transportation, performed dipole-dipole and Wenner surveys to investigate abandoned mine voids using electrical resistivity tomography (ERT) (Sheets, 2002). The voids were located in coal seams at depths of 1.8 to 9.4 m with thicknesses ranging from 0.9 to 1.5 m. High electrical-resistivity anomalies were observed and

correlated to the location of the air-filled mine voids. Elawadi et al. (2006) explored subsurface karst features with 2D electrical-resistivity profiling using both a dipole-dipole and Schlumberger array, and were able to detect two high-resistivity anomalies at depths of 3.4 and 5 m that were interpreted to be cherty limestone blocks or air-filled cavities.

1.5.1.2 Karst Investigations Using Seismic Methods

Miller and Steeples (1991) applied high-resolution P-wave reflection seismology to detect air-filled abandoned coal-mine voids. They found that surgical muting of noise (including top muting of refraction energy) would have been disadvantageous to the reflection energy because it was concentrated within refraction, direct-, and air-wave energy. Refracted energy was stacked along with reflected signals to avoid adversely affecting the reflection arrivals. Voids were manifested on 1D seismic profiles as either increases in the dominant frequency or losses of reflector coherency, resulting in a "chaotic zone" (Fig. 1.9). Anomalies occur when subsurface sample points are closer together than the diameter of the first Fresnel zone, creating discontinuities within continuous reflectors. Anderson (1998) also used reflection seismology to map abandoned air-filled coal-mine voids, which were anomalously manifested on 1D seismic profile lines as time-structurally low. They interpreted that this time-structure relief could not be attributed to actual structure but rather was a "pushdown" velocity effect (Fig. 1.10) caused by several factors including relief at the bedrock level, the presence of void space, caving, stress fracturing of the post-mine strata, and buckling of the mine floor. Sloan et al. (2010) observed a relationship between subsurface voids and three different

types of seismic attributes: diffracted body waves, backscattered surface waves (Fig. 1.11), and shear-wave velocity variations. They found that diffraction imaging was useful for detecting relatively small subsurface anomalies that are typically difficult to detect with traditional reflection imaging. Surface-wave backscatter analysis was determined to be a suitable technique for detecting anomalies such as air-filled cavities or voids due to the abrupt change in material properties between the geologic medium and the air. Grandjean and Leparoux (2004) observed P-wave attenuation, P-wave diffraction, Rayleigh-wave phase shifts, and Rayleigh-wave diffraction and attenuation relating to a cellular polystyrene cylinder buried at a controlled test site. Sheehan (2005) applied seismic-refraction tomography to investigate air-, water-, and mud-filled karst cavities in Tennessee. At one site, they observed a prominent low-resistivity anomaly in three parallel survey profiles at a depth of approximately 20 m with approximate dimensions of 10 m wide and 5 m tall. They interpreted these low-velocity anomalies, along with their linear orientation, to represent a long water- or mud-filled conduit in carbonate bedrock. The approximate depth and width of this conduit are similar to those of the conduit found at the Kentucky Horse Park study area, though taller (5 m compared to 2 m) than the latter.

1.5.1.3 Karst Investigations Integrating Electrical and Seismic Methods

Studies integrating electrical resistivity tomography with seismic reflection and/or refraction tomography to locate subsurface voids have also been performed. Sumanovac and Weisser (2001) used all three methods to investigate water-filled karst fracture zones in Croatia. They determined that electrical-resistivity surveys efficiently located shallow

karst water targets, but that seismic methods were better suited for deeper targets because of the poor depth resolution of the electrical-resistivity methods. Electrical-resistivity tomography (using both dipole-dipole and Wenner arrays) and seismic-refraction tomography were used to investigate manmade air-filled subsurface cavities in Rome, Italy (Cardarelli et al., 2006). These cavities were built into a layer of pyroclastic formations (primarily pozzolana and tuff) at a depth of approximately 9 m with interior dimensions of 2 to 5 m wide and tall. High apparent resistivity anomalies on 2D ERT profiles were observed in the same location as low-velocity anomalies on seismic refraction tomography (SRT) profiles, and these anomalies were correlated to the locations of the air-filled cavities.

1.5.2 Inner Bluegrass Karst Geophysical Investigations

Several studies utilizing self-potential (SP) and ERT have also been performed in the Inner Bluegrass Region to locate and image karst features (Graham, 1995; Tripathi, 2009; Zhu et al.. 2011). At the Kentucky Horse Park survey location in this study, SP and ERT were used to investigate and image the subsurface water-filled karst conduit that feeds Royal Spring. Tripathi (2009) found that low-resistivity anomalies were reflected as negative SP anomalies in most cases, and these were interpreted to correlate to the water-filled conduit. Drilling produced mixed results, however, as some drillholes encountered water-bearing conduits whereas others did not. Zhu et al. (2011) used 2D, 2.5D, and time-lapse electrical-resistivity surveys to explore the same conduit. Low-resistivity anomalies were interpreted to correlate to moisture zones in the subsurface but were indistinguishable from water-filled conduits and other water-filled zones. Drilling

produced mixed results similar to those found by Tripathi (2009), suggesting that an integrated geophysical investigation in this area might reduce ambiguities seen in the electrical methods.

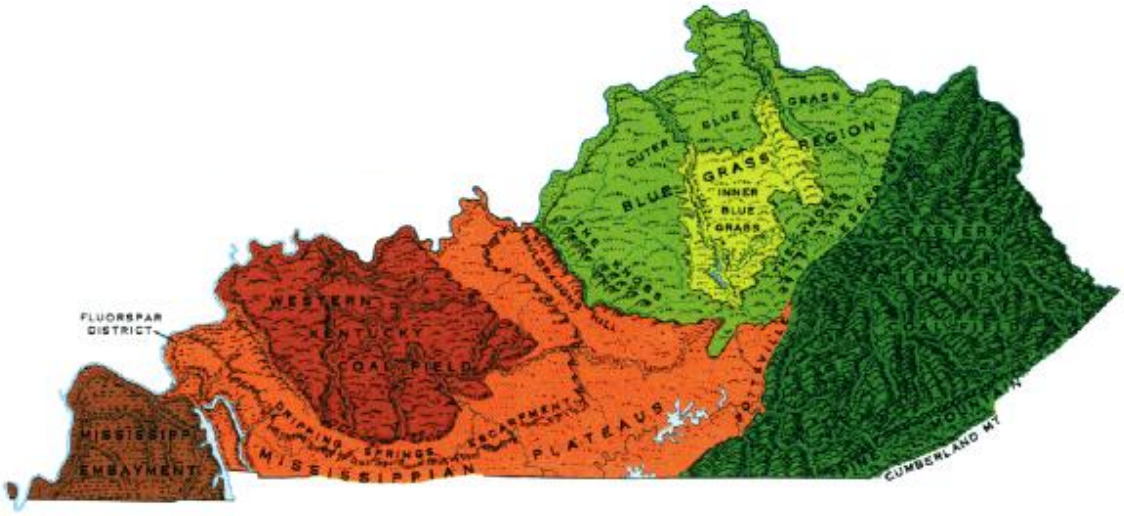

Figure 1.1. Physiographic diagram of Kentucky. The Inner Bluegrass Region is highlighted in yellow. From http://www.uky.edu/KentuckyAtlas/kentucky-atlasp.html

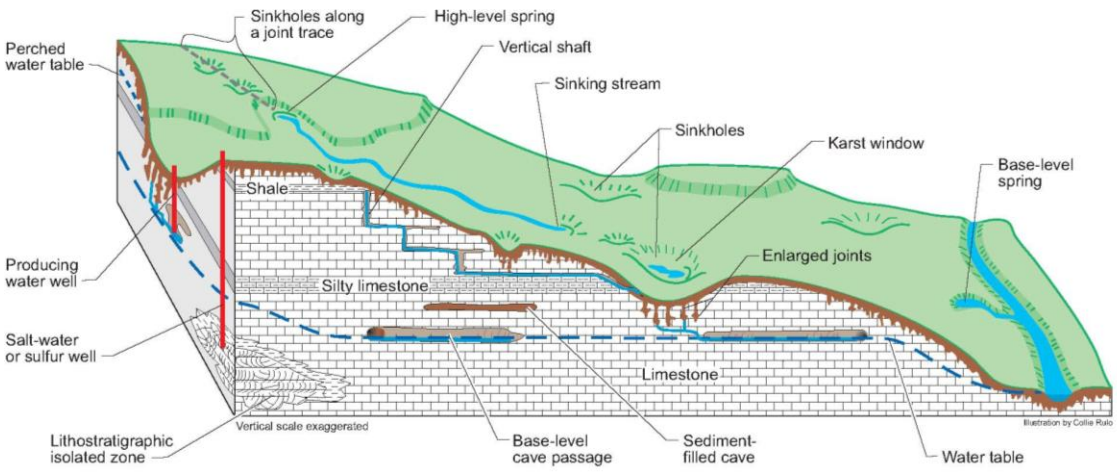

Figure 1.2. Generalized block diagram of Inner Bluegrass karst (modified from Currens, 2001). From http://kgs.uky.edu/kgsweb/olops/pub/kgs/mc15_12.pdf

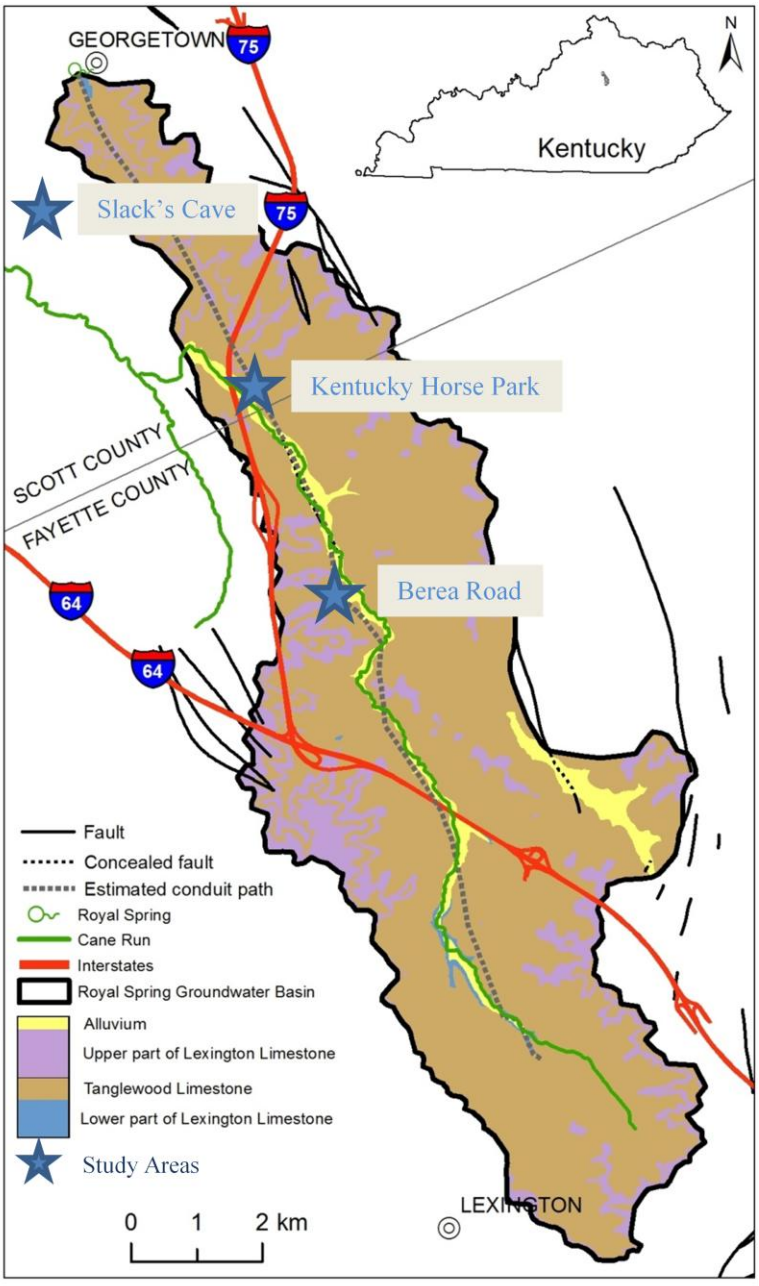

Figure 1.3. Location map of study areas in the Inner Bluegrass Region of Kentucky. Modified from Zhu et al. (2011).

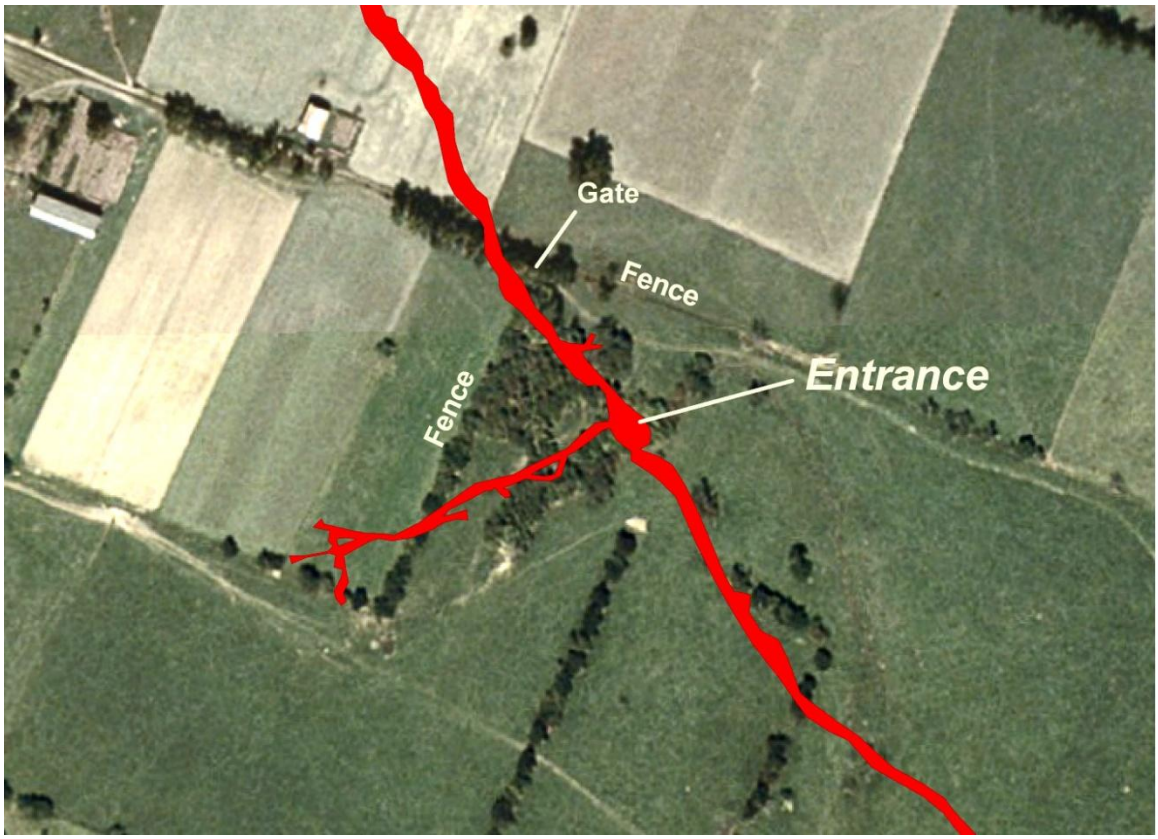

Figure 1.4. Overlay map of Slack's Cave. From James Currens (personal communication).

Figure 1.5. Photo of Slack's Cave karst window.

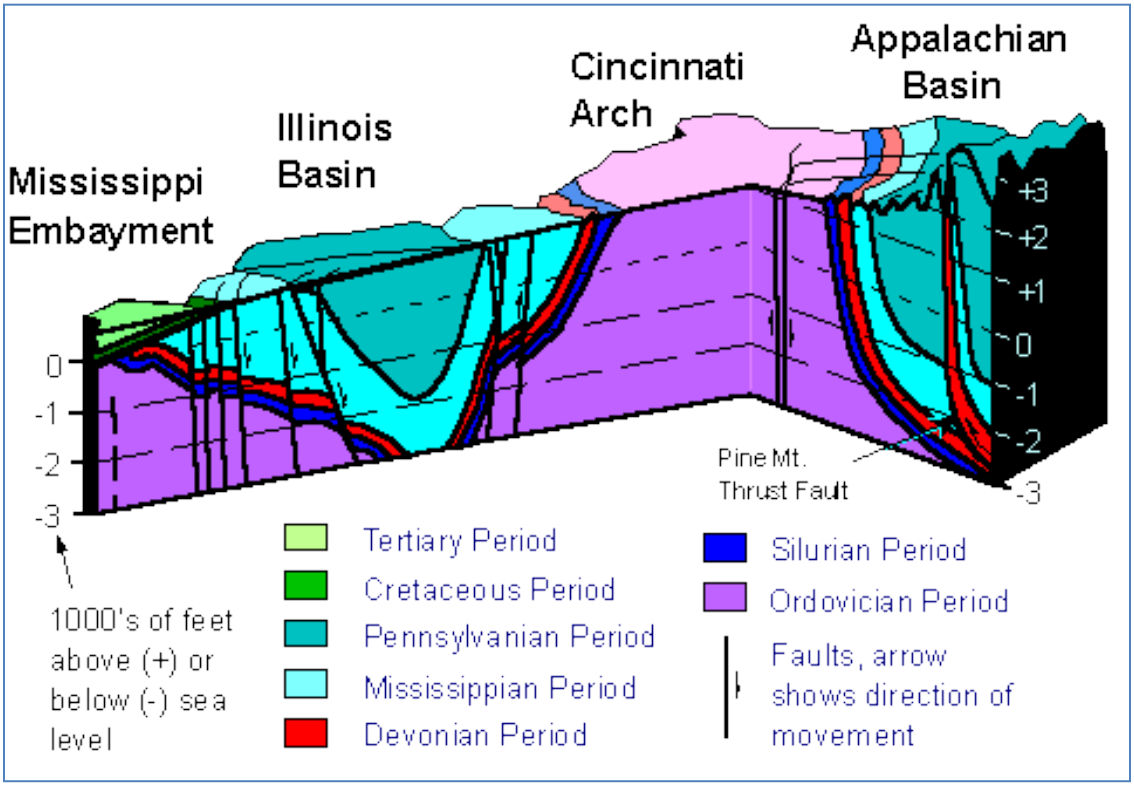

Figure 1.6. Diagram of regional structural features of Kentucky. From http://www.uky.edu/KGS/geoky/beneath.htm

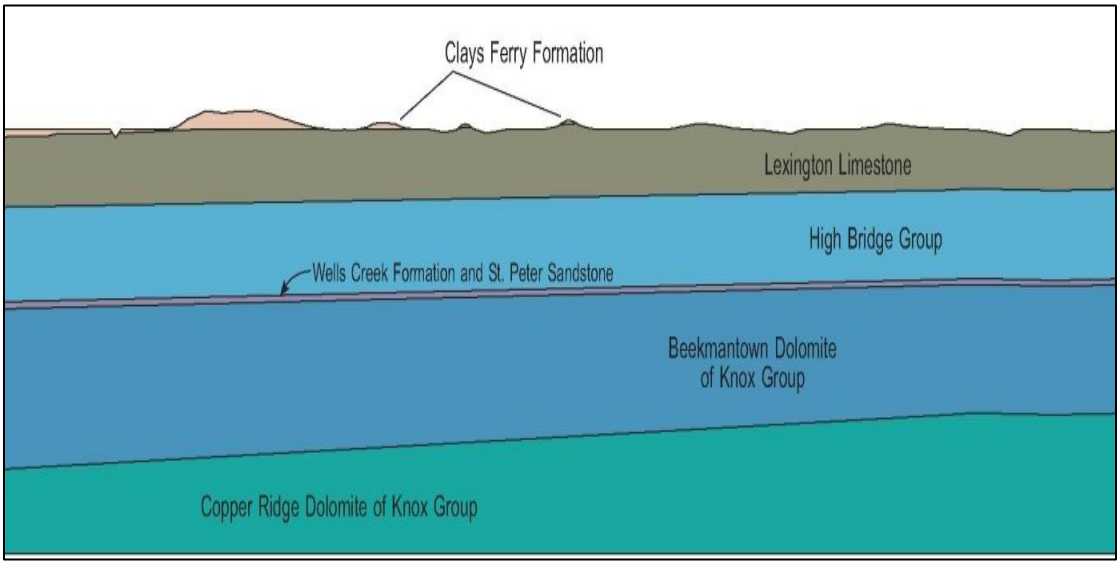

Figure 1.7. Diagrammatic cross section of Inner Bluegrass Region (modified from Sparks et al. 2002). From http://kgs.uky.edu/kgsweb/olops/pub/kgs/ GMS_002_ 12.djvu ?djvuopts&thumbnails=yes&menu=yes&zoom=page

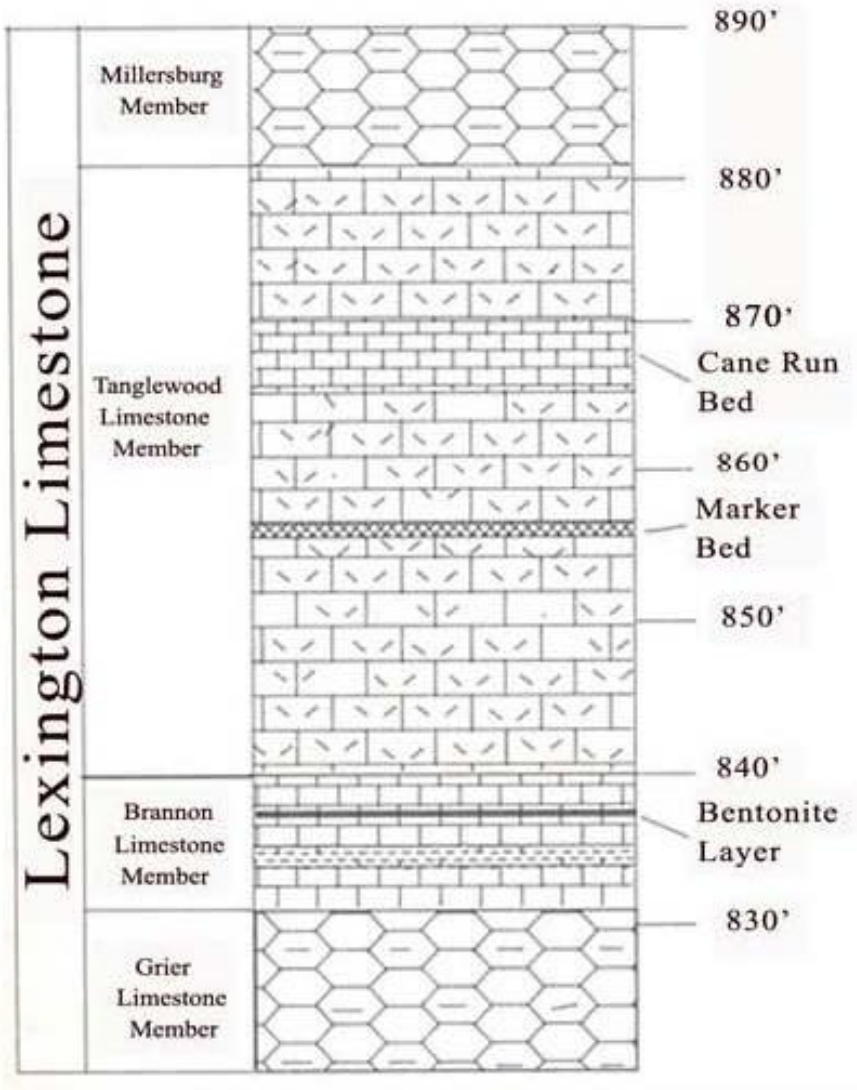

Figure 1.8. Stratigraphic section measured at the Vulcan Quarry. From Bonita (1993).

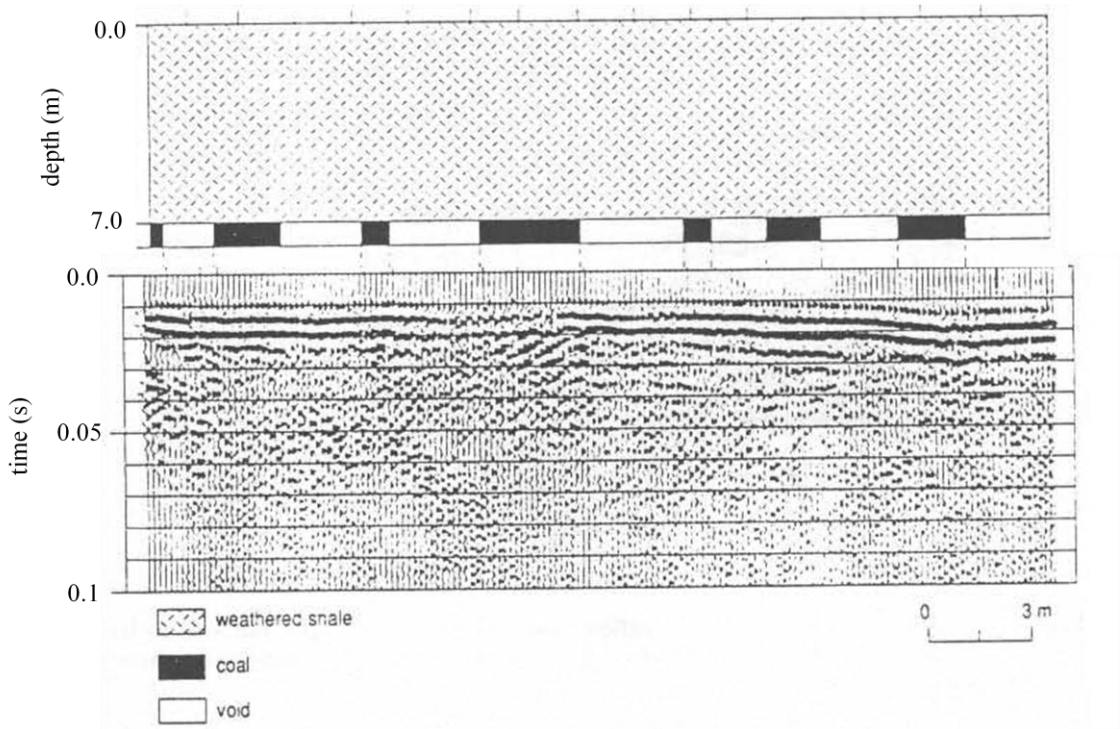

Figure 1.9. Twelve-fold CDP stack depicting seismic responses to coal-mine voids. Voids are displayed as interruptions in the coherent reflector at a time depth of approximately 0.21 to 0.3 s. Modified from Miller and Steeples (1991).

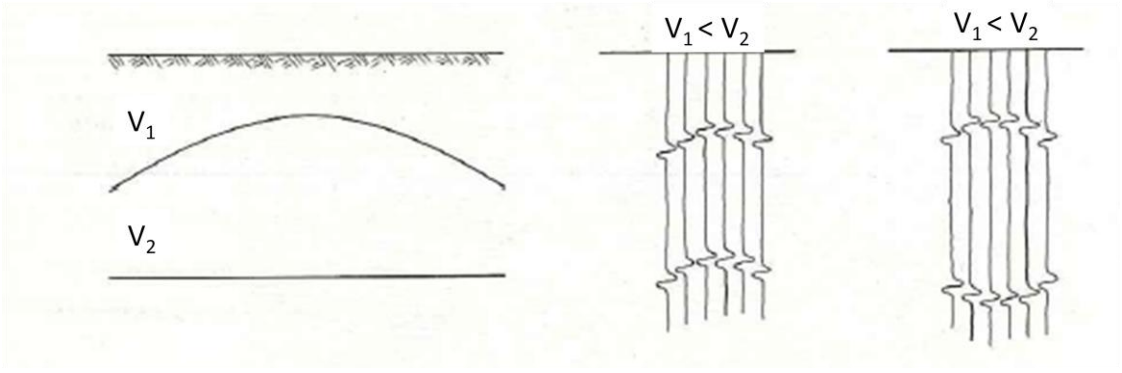

Figure 1.10. Diagrammatic models of earth structure distorted by variation in velocity. A curved "push up, pull down" velocity anomaly (right) can be created by lateral velocity variations. Modified from Robinson and Coruh (1988).

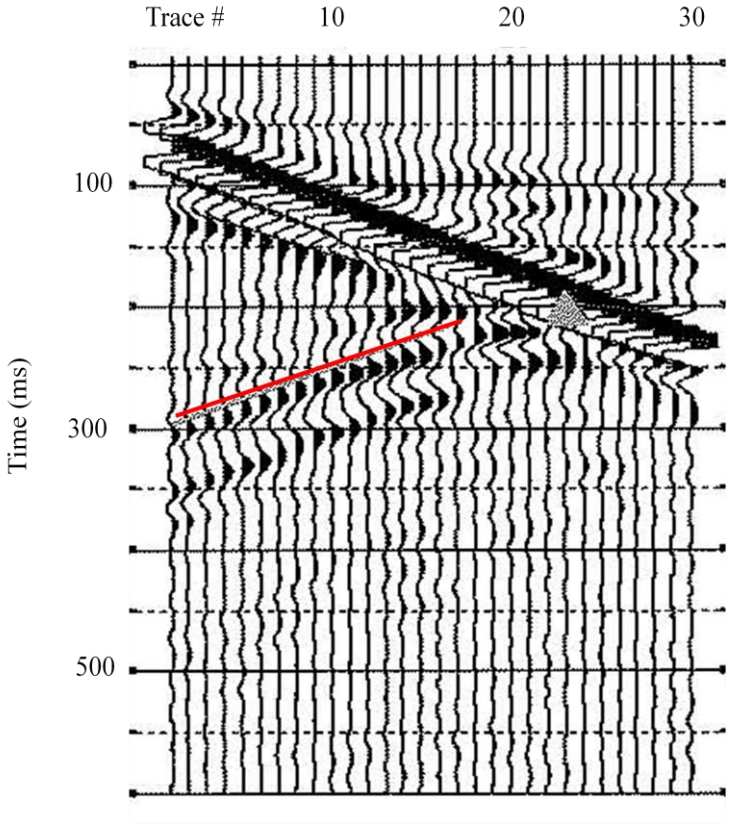

Figure 1.11. Synthetic model depicting seismic backscatters (below red line) created by a void (gray triangle). Modified from Sloan (2011).

CHAPTER TWO
METHODOLOGY

2.1 Integrated Multimethod Geophysical Studies

Decreases in data acquisition and processing times have made it economical to integrate multiple geophysical methods. Chalikakis et al. (2011) compiled an overview of studies related to karst exploration using geophysical methods and determined that no one geophysical method is superior to another in terms of cavity detection due to factors such as heterogeneities in geologic composition, structural and stratigraphic character, target depth and size, and saturation levels. Each method has its own advantages and disadvantages, and improved clarity can be achieved by applying several methods to the given problem (McCann et al., 1987).

2.2 Electrical-Resistivity Tomography

2.2.1 Method Justification

Electrical-resistivity methods utilize an array of electrodes placed on the ground surface, with any two electrodes used to induce current into the ground and another set of two electrodes used to measure the voltage potential between the two points. Variations in potential difference measurements recorded at the surface are created by variations in resistance to current flow in the subsurface, which can be used to interpret subsurface materials and structure (Burger et al., 2006). The basic concepts from Ohm's Law apply here:

$$R = \frac{V}{I}$$

where *R* is resistance in ohms, *V* is potential difference in volts, and *I* is current in amperes. Resistance *R* is dependent on resistivity ρ, length *l*, and cross-sectional area *A* of the measured unit:

$$R = \rho \frac{l}{A}$$

Resistivity is an intrinsic property of earth materials and it is a measure of the material's ability to oppose electric current. Information is available regarding typical resistivity ranges for common earth materials (Table 2.1); however, resistivity measurements can be affected by site-specific conditions such as moisture content, dissolved electrolytes, porosity, temperature of pore fluids (resistivity decreasing with increasing temperature), and resistivity of minerals (AGI, 2007). Electrical-resistivity field measurements provide information regarding horizontal and vertical variations in resistivity that can be used to create a vertical cross section through inversion (Griffiths and Barker, 1993). Voids in the shallow subsurface can create either high- or low-resistivity anomalies relative to the surrounding geologic materials depending on whether they are air- or water-filled, respectively. Two-dimensional tomographic profiles can be created using a single inverted resistivity section, and 2.5D ("pseudo" 3D) tomographic profiles can also be created by combining several parallel sections (Fig 2.1).

2.2.2 Data Acquisition

Various electrode array configurations can be utilized based on the purpose of the resistivity survey. Three different electrode array configurations were utilized at the

Slack's Cave study area: Wenner, Schlumberger, and dipole-dipole (Fig. 2.2). The Wenner array has the highest signal-to-noise ratio, with excellent vertical resolution but poor lateral resolution, as it is more sensitive to local, near-surface lateral variations (Burger et al., 2006; AGI, 2007). The Schlumberger array has similar advantages and disadvantages as the Wenner array, and neither method is capable of utilizing multiple channels (AGI, 2007). The dipole-dipole array offers the best resolution and also has the advantage of utilizing multiple channels, thereby greatly reducing data collection times (AGI, 2007). Upon reviewing the ERT profiles from the Slack's Cave survey, where all three above-mentioned array configurations were used, it was determined that apparent resistivity ranges were better correlated and void dimensions were better constrained by the dipole-dipole survey; therefore, this array was selected for the Kentucky Horse Park and Berea Road study areas.

All electrical-resistivity surveys were performed using an AGI SuperSting^{TM} with Swift^{TM} automatic resistivity and IP system, which is capable of utilizing up to eight channels. This instrument consists of 12-volt DC batteries, a switch box, 84 stainless-steel electrode stakes, and 12 passive-electrode cables with seven electrodes in each cable. Acquisition parameters are listed in Table 2.2. Maximum injection current was set at 2,000 milliamps (mA), with a maximum error of 2 percent between any two selected readings. Electrode spacing for all surveys was 3.048 m (10 ft), and depth of investigation was assumed to be from 15 to 25 percent of the line length, depending on the array and site conditions. Command files for electrode configuration settings were created and loaded into the SuperSting^{TM} system based on array type and optimum data-acquisition parameters (Fig. 2.3).

2.2.3 Data Processing

Data processing and inversion from each electrical-resistivity survey were performed using EarthImager 2D version 2.3.0 and/or EarthImager 3D version 1.5.3 (AGI, 2006) to create 2D and 2.5D "pseudo" 3D profiles, respectively. The purpose of the inversion is to create a model that most accurately fits the measured data, with quality of fit measured by the root mean square (RMS) error. Three inversion options are available with EarthImager 2D: damped least squares, smooth model inversion, and robust least-squares inversion. The robust least-squares method was selected because it produces models by minimizing the absolute value of data misfit, making it more efficient in removing noise compared to the other methods (Dahlin and Zhou, 2004). A second method of removing noisy data is by manual interactive selection and deletion.

Initial, forward modeling, and resistivity inversion thresholds can also be adjusted to remove excess noise, and any data beyond these levels will automatically be removed through inversion (Table 2.3). A finite-element forward method was used to create models with the Dirichlet boundary condition and the models were solved using Cholesky decomposition. The number of mesh divisions between two electrodes was set at 2 with thickness incremental factors and depth factor set at 1.1, thereby assuming that layer thicknesses increase with depth (Tripathi, 2009). In the resistivity inversion settings, the stop criteria were set as follows: number of iterations set at 8, max RMS error set at 3 percent, and error reduction set at 5 percent. Smoothing and damping factors were set at 10, with robust data and modeling conditioners set at 1 to avoid oversmoothing the resultant model (Tripathi. 2009). The resolution factor was set at 0.2, minimum resistivity set at 1 ohm-m, and maximum resistivity set at 10,000 ohm-m. Model parameter width

and height were both set at 1 to maintain a 1-to-1 scale ratio. In order to enhance the effect of lateral variations along the profile, the horizontal/vertical roughness ratio was set at 1.5 (Tripathi, 2009).

2.2.4 Resolution

The resolution of an electrical-resistivity survey is mainly controlled by the geometry of the survey, but is also affected by subsurface resistivities. There is a trade-off between electrode spacing and resolution. Subsurface features could be resolved to as little as one-half of the electrode spacing, but caution is recommended in interpreting features less than one electrode spacing (AGI, 2007). However, although decreasing the electrode spacing can increase the resolution of small features, it also decreases the depth of penetration. In addition, resolution decreases with depth and therefore targets located at the maximum effective survey depth may not be resolved. An electrode spacing configuration of 3.048 m (10 ft) was selected based on known target size and depth at Slack's Cave and the Kentucky Horse Park study areas. Since target characteristics at the Berea Road study area were hypothesized to be analogous to those at the Kentucky Horse Park study area, a 3.048 m (10 ft) electrode spacing configuration was also selected for this location.

2.3 Near-Surface Seismic Methods

2.3.1 Method Justification

Near-surface seismic-refraction and -reflection surveys are performed by placing an inline array of geophones on the surface, which are connected via cables to a field

seismograph. Geophone design generally consists of a magnetized mass, which surrounds a fixed coil, both of which are isolated from the ground by suspension springs. Ground vibrations (seismic waves) move the coil in the magnet, thereby generating an electromagnetic current, the size of which is proportional to the magnitude of the vibration. Exploration geophones come in a range of natural frequencies from 4 to 100 Hz. Seismic cables, also referred to as takeout cables, carry the geophone current (or ground-motion signal) to the seismograph. Historically, analog seismographs were used to record continuous ground motion; now, digital systems more efficiently record geophone signals as discrete moments, which are generated by various seismic energy sources. Types of sources can be either impulsive or nonimpulsive (controlled). Impulsive sources include explosives and impacts (hammer or falling weight striking a plate, shotgun blast). Nonimpulsive sources include Vibroseis machines and pseudo random tampers. Walkaway tests are typically performed to determine the type of geophone, optimum array geometry, and source chosen.

2.3.2 Data Acquisition

Seismic surveys were collected with a 48-channel Geometrics StrataVisor® seismograph. The seismograph is a 24-bit system with an instantaneous dynamic range of 115 db that stores data on an internal hard drive. A low-cut filter of 15 Hz was used with no high-cut filter. A 60-Hz notch filter was applied at the Berea Road study area to account for cultural noise (power lines nearby), but was not needed at the other locations. Geophone arrays at each site utilized two inline spreads of 24 Mark Products 30-Hz S-wave geophones and/or 40-Hz P-wave geophones with 7.5-cm spikes. The seismic

energy source for all study areas was a steel plate struck vertically with 1.4-kg hammer for P-wave surveys and a section of steel H-pile struck horizontally with a 1.4-kg hammer for S-wave (horizontal shear-wave) surveys. The flanges of the H-pile were placed and struck perpendicular to the geophone spread for sh-mode generation. The H-pile was placed in prepared slit trenches to resist movement and improve the energy input into the ground. Polarity reversals and impacts of the sledgehammer on both sides of the energy source were recorded to ensure the correct identification of the S-wave energy.

For refraction surveys, a geophone array spacing of 1 m was used at all three sites, utilizing both 30-Hz S-wave and 40-Hz P-wave geophones. Shot offsets were 0, 12, 24, 36, and 48 m for each line surveyed, and three to five shots were stacked at each shot point to decrease noise and improve signal quality.

Seismic-reflection surveys were collected using the common midpoint (CMP), also known as common depth point (CDP), method. At the Kentucky Horse Park study area, two separate reflection surveys were performed (Table 2.4). The first survey was collected using 40-Hz P-wave geophones with shot and geophone spacings of 1 m and a near offset of 1 m. An additional survey was performed at the Kentucky Horse Park study area utilizing both 40-Hz and 100-Hz geophones with shot and geophone spacings of 6 inches and a near offset of 1.83 m (6 ft) (Table 2.4). Forty-Hz P-wave geophones were used at the Berea Road study area with shot and geophone spacings of 1 m and a near offset of 12 m (Table 2.4).

2.3.3 Data Processing

2.3.3.1 Seismic-Refraction Tomography

Seismic-refraction data processing was performed on a Pentium-based microcomputer using Geometrics' SeisImager 2D v. 3.3 software package. Picwin v. 4.2.0.0, a component of this package, was used to process raw data and pick first arrivals (refractions). Field files were transferred from the Geometrics StrataVisor® seismograph in .dat format, which is directly compatible with Picwin. A bandpass filter was applied to the data with a low-cut frequency between 15 and 20 Hz and a high-cut frequency between 150 and 160 Hz. Picks were applied to the trough of the first arrivals for the direct wave and refractions on each raw field file. Each file contained geophone input from 48 geophones, and each line of 48 geophones had five associated field files with source locations at 1, 12, 24, 36, and 48. Appropriate source locations and array geometries were applied to each field file to ensure that an accurate velocity model could be created. Another component of the SeisImager 2D software package, Plotrefa v. 2.9.1.9, was used to assign layer boundaries to the selected first-arrival picks, automatically correct reciprocal travel times, and create tomographic profiles via the time-term inversion option.

2.3.3.2 Seismic-Reflection Profiling

Seismic-reflection data were processed on a Pentium-based microcomputer using the Vista 7.0 software package. General processing procedures for all CDP-stacked seismic lines are listed in Table 2.5. Files were converted to the accepted SEG-Y format, and 24- and 12-channel files were extracted from the 48-channel field files, with roll-

along being performed as required. This provided 12- and six-fold stacked data sets, respectively. Mean gain and amplitude scaling were applied evenly to each. Bandpass filtering and automatic gain control (AGC) values were applied as needed, based on each raw data file. A geometry header was then created for each line and applied to the filtered files. In accordance with Miller and Steeples (1991), top muting of refraction energy was not applied. Data sets were then sorted and stacked by offset for semblance analysis, which was used to derive the velocity model. A normal moveout (NMO) correction was then applied, based on the velocity model. Finally, the data sets were CDP sorted and stacked, and a post-stack frequency-wave number (F-K) filter was applied to each CDP stack as needed, completing the process.

In addition to CDP stack processing, a common offset profile was created for each of the three seismic-reflection survey lines collected at the Berea Road study area. To create a common offset profile, the optimum window must first be determined from the raw data set, and then the optimum offset (optimum shot trace) must be chosen from within the optimum window. This single optimum trace is selected from each CDP data set and a profile is created that has continuous subsurface coverage without stacking or averaging any amplitude values. Therefore, NMO corrections are unnecessary since all source-receiver distances are the same (Burger et al., 2006). The benefits of this method include simpler and less time-consuming data processing while maintaining data integrity that could be lost or distorted through the stacking and averaging process. There are, however, two key factors to keep in mind when using the common offset method. First, the position of the reflector as displayed on the raw data file can be enhanced or depressed, depending on the velocity of the overlying material (Burger et al., 2006).

Second, a "stretching" distortion in the horizontal plane can be created depending on the orientation of the reflecting surface (Burger et al., 2006). In most cases, these factors are insignificant unless there are major relief variations (dips) in the subsurface or extreme variations in velocity values of overlying materials. Since subsurface strata at all survey locations are oriented horizontal and there are no major velocity variations in the overlying sediment, these factors do not produce any significant problems in this study area.

2.3.4 Resolution

Two types of resolution are associated with seismic profiling: vertical and horizontal. Vertical resolution describes the ability to distinguish the top and bottom of a formation or bed layer. Seismic vertical resolution follows the ¼-wavelength criteria:

$$R = \frac{1}{4}\lambda = \frac{V}{4f}$$

where R is vertical resolution, λ is wavelength, V is velocity, and f is frequency. A formation or bed layer can generally be detectable, meaning that it can be imaged without the ability to distinguish between the top and bottom, based on the 1/8-wavelength criteria:

$$D = \frac{1}{8}\lambda = \frac{V}{8f}$$

where D is detectable vertical resolution.

Horizontal resolution is defined by the radius of the first Fresnel zone in unmigrated data. Constructive interference of wave energy occurs within the first Fresnel

zone, with energy from successive zones effectively cancelling each other out. The radius of the first Fresnel zone is defined by:

$$R_1 = \frac{V}{2}\sqrt{\frac{t_0}{f}}$$

where V is velocity, t_0 is two-way travel time, and f is frequency.

Table 2.1. Common resistivity ranges for various earth materials (modified from AGI, 2007).

Rock Material/Type	Resistivity Range (Ωm)
Igneous	100–1,000,000
Limestone	100–10,000
Sandstone	100–10,000
Sand (both dry & wet sand)	1–10,000
Gravel	100–10,000
Clay (including wet clay)	1–100
Alluvium	1–1,000
Soil	1–10
Drill mud, hydraul-EZ	4.5
Fresh water	10–100
Salt water	0.1–1

Table 2.2. Data acquisition parameters for electrical-resistivity surveys.

Electrical-Resistivity Data Acquisition Parameters				
Site Name	Line Number(s)	Number of Electrodes	Electrode Spacing	Total Line Length
Slack's Cave	1	52	3.05 m	155.5 m
Slack's Cave	2	52	3.05 m	155.5 m
Slack's Cave	3-5	52	3.05 m	155.5 m
Kentucky Horse Park	1 - 5	61	3.05 m	182.9 m
Berea Road	1	65	3.05 m	195 m

Table 2.3. Inversion settings applied to ER data.

Initial Settings	
Minimum voltage (mV)	0.2
Minimum avs(V/I)-ohm	0.0005
Maximum repeat error (%)	3
Minimum apparent resistivity (ohm-m)	1
Maximum apparent resistivity (ohm-m)	10,000
Maximum reciprocal error	5
Inversion method	robust inversion
Forward Modeling Settings	
Forward modeling method	finite element
Forward equation solver	Cholesky decomposition
Type of boundary condition	Dirichlet
Number of mesh divisions	2
Thickness incremental factor	1.1
Depth factor	1.1
Resistivity Inversion Settings	
Number of iterations	8
Maximum RMS error (%)	2
Error reduction (%)	5
Smoothing factor/damping factor	10
Starting model	average apparent resistivity
Model parameter width	1
Model parameter height	1
Resolution	0.2
Horizontal/vertical roughness ratio	0.5-2.0

Table 2.4. Data-acquisition parameters for seismic-reflection surveys.

Seismic-Reflection Data-Acquisition Parameters						
Site Name	Line Number	Survey Type	Near Offset	Shot Interval	Geophone Spacing	Geophone (Hz)
Kentucky Horse Park	1	P-wave	1 m	1 m	1 m	40
Kentucky Horse Park*	2	P-wave	1.8 m	0.15 m	0.15 m	40
Kentucky Horse Park*	3	P-wave	1.8 m	0.15 m	0.15 m	100
Berea Road	1	P-wave	12 m	1 m	1 m	40
Berea Road	2	P-wave	12 m	1 m	1 m	40
Berea Road	3	P-wave	12 m	1 m	1 m	40

* SI units converted from English units

Table 2.5. Generalized processing steps for seismic-reflection data.

General Processing Steps for Seismic-Reflection Profiling	
Processing Step	Comment
Reformat data	Convert .DAT files to SEG-Y format
Combine files	Combine individual field files into one file
Exponential gain recovery	Apply spherical divergence gain
Apply mean gain	Weighted from mean of entire file
Bandpass filter	Attenuate noise outside of a selected range of frequencies
Automatic gain control	Weighted on average amplitude over a window of time
Geometry	Construct shot and receiver geometry for header information
Header	Apply header from geometry input
Trace kills	Remove noisy or "bad" traces
Sort by offset	Sort data into common-offset gathers
Stack by offset	Combine sorted files
Velocity analysis	Pick velocities using stacked field files
Normal moveout	Correct for source-receiver travel-time differences
Sort by CDP	Sort data by common depth point
Stack by CDP	Vertically sum NMO-corrected CDP gathers
F-K filter	Attenuate linear coherent noise

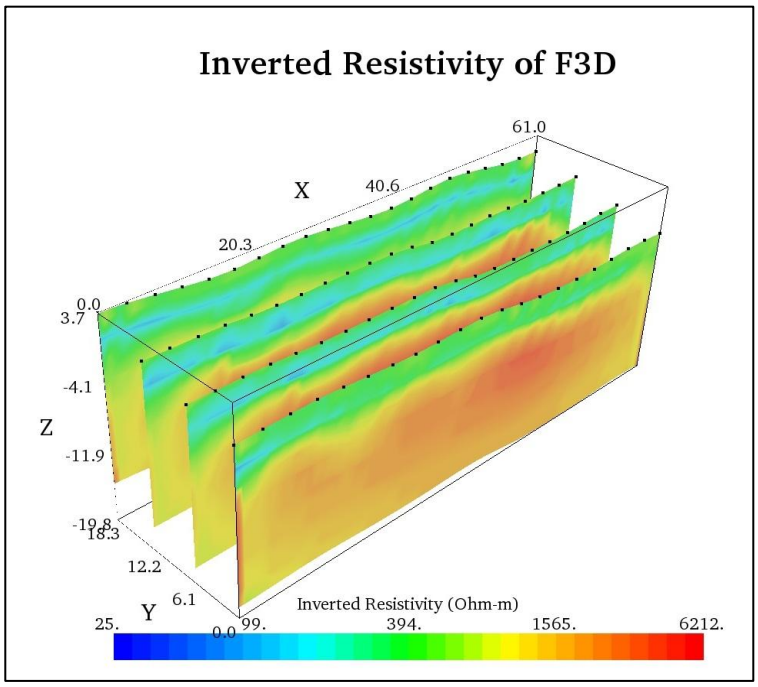

(a)

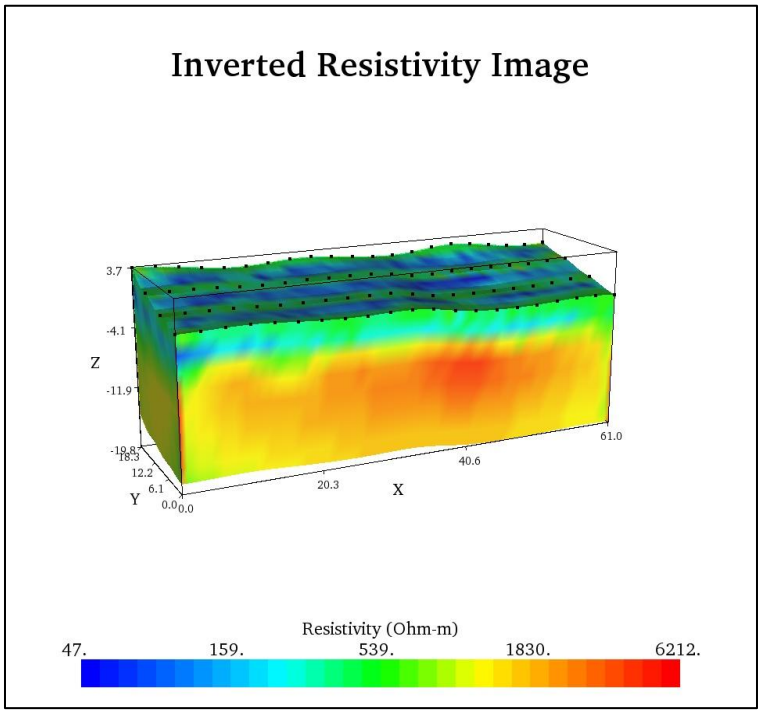

(b)

Figure 2.1. Example of (a) combined parallel ER survey lines used to create (b) a 2.5D tomographic profile. From Zhu et al. (2011).

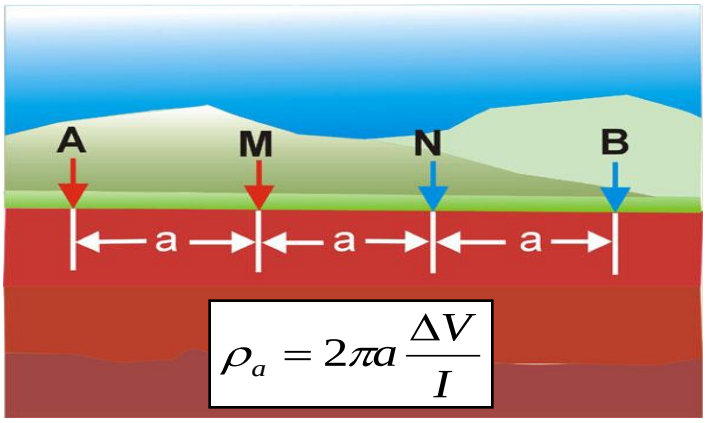

(a)

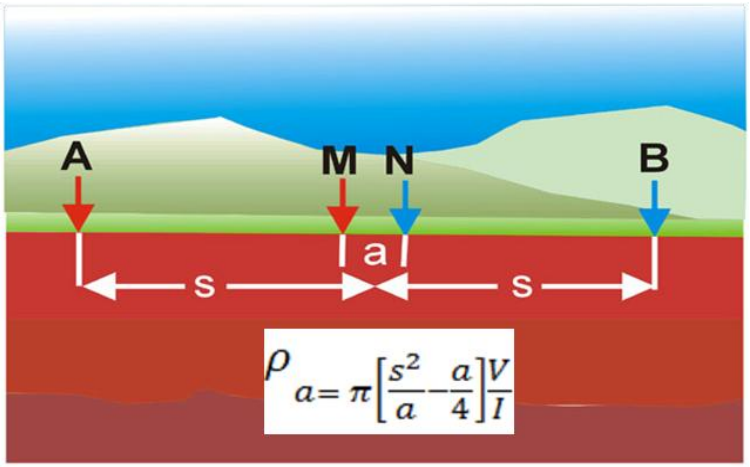

(b)

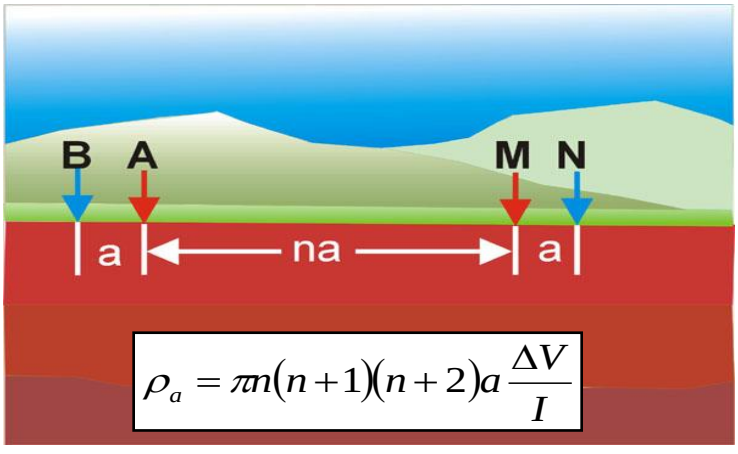

(c)

Figure 2.2. Generalized diagrams of ER survey arrays: (a) Wenner, (b) Schlumberger, (c) dipole-dipole. From AGI (2007).

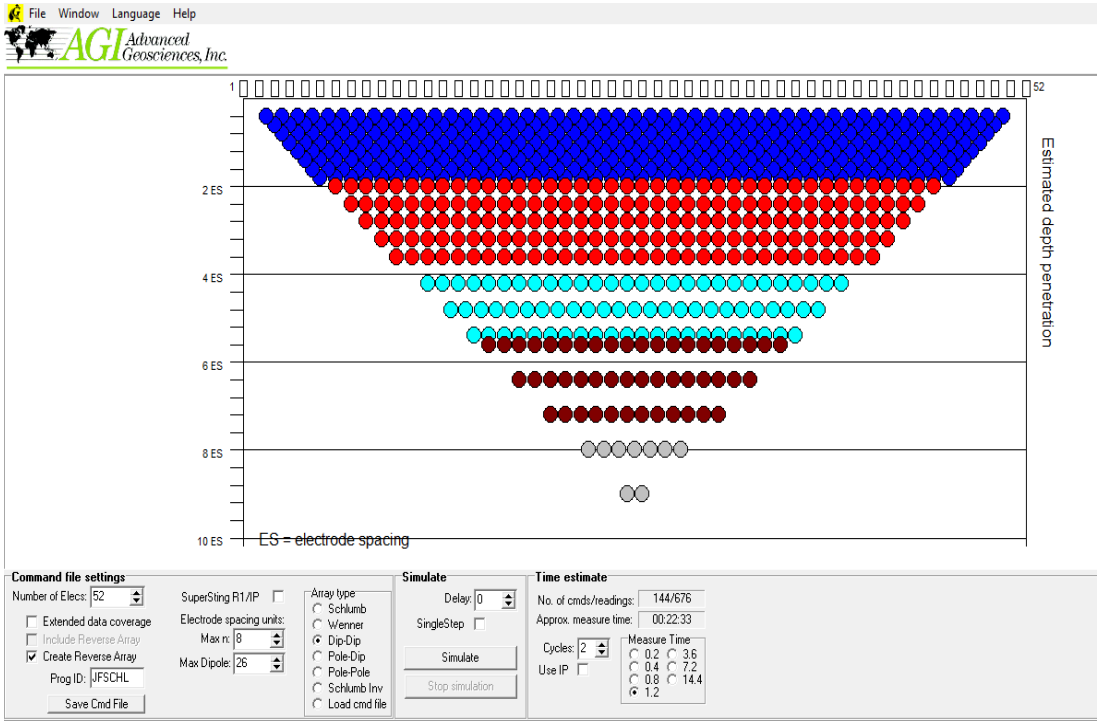

Figure 2.3. Example of a 52-electrode dipole-dipole command file configuration, taken from Slack's Cave survey line 1.

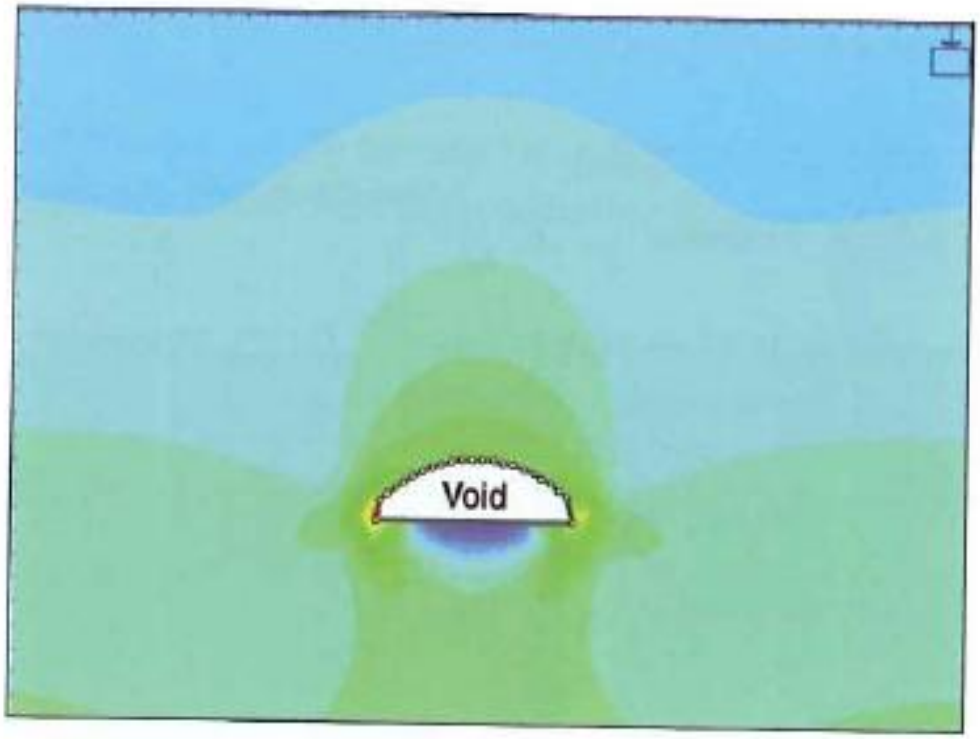

Figure 2.4. Simplified model depicting a subsurface void and corresponding increases in stress levels around the roof and walls (warm colors) and decreases in stress levels at the base (cool colors). From Sloan (2011).

CHAPTER THREE
INTERPRETATION

3.1 Electrical-Resistivity Data Interpretation

Inverted ERT profile sections (Fig. 3.1) were examined for vertical and lateral variations in resistivity values that could correspond to air- and/or water-filled void spaces, though caution was exercised in interpretation because of the inherent anisotropic and inhomogeneous nature of real earth materials. Access to a priori information at the Slack's Cave and Kentucky Horse Park study areas helped to constrain target size, depth, and geometry characteristics, which aided in the interpretation and delineation of subsurface void features. Similar constraints were applied to the Berea Road study area, based on the premise that the target subsurface void would have characteristics similar to those found at the Kentucky Horse Park study area.

3.1.1 ER Survey 1, Slack's Cave

Dipole-dipole, Schlumberger, and Wenner arrays were utilized for the 2D surveys on line 1 (Fig. 3.2), and three successive parallel dipole-dipole lines with similar geometries were spaced 6.096 m (20 ft) apart for the 2.5D survey. Poorly fit data above set thresholds (Table 2.5) were removed from each line prior to inversion.

The inverted dipole-dipole, Schlumberger, and Wenner 2D sections show a pronounced high-resistivity anomaly centered horizontally at 76 m (250 ft) at a depth of approximately 3 m (10 ft), extending to approximately 9 m (30 ft) (Fig 3.3). These values agree with measurements observed in the field. The location and geometry of the anomaly are best correlated to the cave by the dipole-dipole array, as the Wenner and

Schlumberger arrays exaggerate the cave dimensions, primarily height. The apparent resistivity of the anomaly has a maximum of 10,000 ohm-m on all profiles, which is the maximum preset value for the models. The cave is primarily air-filled, and typical resistivity values for air range from $1.3x10^{16}$ to $3.3x10^{16}$ ohm-m (Pawar et al., 2009). However, the values on the resistivity profiles represent a weighted average, which includes the surrounding soil and bedrock, which have resistivity values ranging from 1 to 10 ohm-m and 100 to 10,000 ohm-m (Table 2.1), respectively. A thin layer with resistivity values around 1,000 ohm-m is directly below the high-resistivity anomaly, which could correlate to the base of the cave, which has approximately 0.5 m of water flow. Fresh water has resistivity values ranging from 10 to 100 ohm-m (Table 2.1), depending on factors such as dissolved ion content and temperature, which would dramatically lower the weighted apparent resistivity average in this zone. Higher-resistivity zones below this low-resistivity zone are interpreted to correlate to the nonkarstic limestone bedrock. A similar anomaly was seen in the three parallel ER survey lines (Fig. 3.4), which was interpreted to be the cave location along those lines. A 2.5D profile was created (Fig. 3.5) by combining these three parallel lines; however, the resulting image was not representative of what was seen in the 2D profiles. The prominent high-resistivity zone that corresponded to the cave location in the 2D profiles is not displayed in the 2.5D profile. The 2D program assumes that resistivity variation only occurs within a vertical plane directly beneath the survey line, whereas the 3D program does not make such assumptions, and therefore does not always display similar results. In this case, the 2D profiles reveal more features than the 2.5D profile.

A second 2D line was acquired and is shown in Appendix A. The line ran parallel to and near a metal fence, creating anomalous artifacts that inhibited meaningful data interpretation.

3.1.2 ER Survey 2, Kentucky Horse Park

Previous drilling (well 25) located the conduit at a depth of approximately 18 m. The conduit is suspected to trend north-northwest, approximately orthogonal to the ER line (James Currens, personal communication). A dipole-dipole array was used for the 2D (line 1) and 2.5D surveys. For the 2.5D surveys, four additional ER lines (lines 2 through 5) were surveyed parallel to the original line, each 6.096 m (20 ft) apart. Poorly fit data above set thresholds (Table 2.5) were removed from each line prior to inversion.

A low-resistivity anomaly centered horizontally at 93 m (305 ft) at a depth of approximately 18 m (60 ft), extending to approximately 20 m (65 ft), was interpreted to correlate to the conduit, based on its known location under well 25 (Fig. 3.7). An overall low-resistivity zone appears at an angle from the surface to a depth past that of the conduit, which could be influenced by fractures or pores above and below the conduit. The actual conduit geometry is known to be approximately 5 m wide by 2 m high at this location, and is not well defined by the anomaly observed in the ER survey. The inability of the ER method to properly resolve this target could be attributed to target depth and size and the electrical properties of the surrounding materials that affect the weighted average of the section. However, the conduit should have a lower resistivity value than the surrounding bedrock, because it is primarily filled with fresh water. Average electrical resistivity values for the limestone bedrock range from 100 to 10,000 ohm-m,

whereas the electrical resistivity values for fresh water range from 10 to 100 ohm-m, depending on factors such as dissolved ion content and temperature (Table 2.5). A similar anomaly was seen in the four parallel ER survey lines (Fig. 3.8) that was interpreted to be the conduit location along those lines. This anomaly can be followed along the 2.5D profile (Fig. 3.9) to trend north-northwest.

A more prominent low-resistivity anomaly centered horizontally at 43 m (140 ft) at a similar depth of approximately 18 m (60 ft) is also observed on the profile from line 1 (Fig. 3.7), which may correlate to another fluid- or mud-filled karst anomaly. Drilling will be required to verify this interpretation.

3.1.3 ER Survey 3, Berea Road

This survey line consisted of 65 electrodes with spacings of 3.048 m (10 ft) trending northeast-southwest for a total line length of 195 m (640 ft) (Fig. 3.10). This profile was collected coincident to previous seismic-reflection and -refraction surveys to determine if an electrical-resistivity anomaly was present where seismic-velocity anomalies were observed. A low-resistivity anomaly centered horizontally at 58 m (190 ft) is observed at a depth of approximately 3 m (10 ft) (Fig. 3.11); it was interpreted to be a shallow conductive object such as a drain pipe and is not likely karst related. Seismic anomalies were observed centered horizontally near 110 m (360 ft), but no prominent electrical-resistivity anomalies were observed in this area on the resistivity-survey profile. This could be similar to what occurred at the Kentucky Horse Park, where the target may be too small and/or too deep to be resolved by the electrical-resistivity method. Another explanation could be that the surrounding materials have a strong

enough influence on the measured apparent resistivities to skew the weighted averages of the suspected karst zone, or there is simply not a karst void there. Drilling will be required to verify the seismic interpretation.

3.2 Seismic Refraction Data Interpretation

High-resolution near-surface P- and S-wave refraction seismic surveys were performed to determine which was better suited for the survey areas. P-wave data were collected using an array of 40-Hz P-wave geophones; S-wave data were collected coincident to the P-wave survey lines using 30-Hz S-wave geophones. The raw files showed that the P-wave refraction data provided better data quality with less noise; therefore, the S-wave survey data were not used for interpretation. P-wave refraction data were processed using Geometrics' SeisImager 2D software package. The Picwin module was used to process raw data and pick first arrivals (refractions). The Plotrefa module was then used to assign layer boundaries to the selected first-arrival picks, combine five different shotpoint files for each survey line, automatically correct reciprocal travel times, and create tomographic profiles via the time-term inversion option. One-layer models over a half space were yielded, which delineated the soil-bedrock interface. Total thickness of the Lexington Limestone bedrock in all survey areas ranges in excess of 30 m (100 ft); thus, the underlying High Bridge Group could not be sampled with the array geometry required for detecting small karst targets. The average P-wave velocity for limestone is approximately 2,750 m/s, whereas average P-wave velocities for fresh water and air are approximately 1,400 m/s and 331.5 m/s, respectively (Burger et al., 2006). Lateral variations in first-arrival travel times are attributed to velocity slow-downs related

to air- and/or water-filled void spaces. These lateral variations created parabolic time suppressions in the raw data files (Appendix B), in which sudden velocity decreases were observed coincident with known karst features. A normal velocity response was exhibited throughout the rest of the profile. Tomographic models display these anomalies as low-velocity intrusions between the soil/bedrock interface. This methodology was then applied to the Berea Road study area, with the assumption that subsurface characteristics were analogous to those at the Kentucky Horse Park.

3.2.1 Refraction Survey 1, Slack's Cave

P-wave seismic-refraction survey data were collected at the Slack's Cave area (Fig. 3.12) with an array of 40-Hz P-wave geophones spaced 1 m apart and oriented northwest-southeast, orthogonal to the trend of the cave. Line 1 was extended to a total length of 95 m by rolling along two successive geophone arrays along a line approximately coincident with ER line 1 (Fig. 3.2). Line 2 was collected as a single survey with a total line length of 48 m.

A low-velocity anomaly was observed on both the raw data files (Appendix B) and the tomographic profile (Figs. 3.13 and 3.14) from line 1. On the raw data files, the expected linear slope of the first seismic arrival (refraction) is interrupted between geophones 18 and 24, forming a parabolic time suppression before resuming the original slope for the rest of the survey. The location of this velocity anomaly correlates to the cave location observed in the field and is interpreted to be attributed to a slow-down in seismic velocity through the primarily air-filled cave, which was translated to the soil/bedrock interface.

A “double saddle” parabolic time-suppression anomaly was observed on both the raw data files (Appendix B) and the tomographic profile (Fig. 3.15) from line RSC2. Similar to line RSC1 field files, an interruption in the linear first arrival slope is observed between geophones 7 and 24, forming a “double saddle” time suppression. This anomaly correlates to a location in the subsurface where the cave splits (Fig. 1.5), continuing its north-south trend with an additional arm splitting off to the northwest. The “double saddle” shape of this velocity anomaly is interpreted to be created by the two primarily air-filled cave voids separated by a small section of limestone in between.

3.2.2 Refraction Survey 2, Kentucky Horse Park

P-wave seismic-refraction survey data were collected at the Kentucky Horse Park study area (Fig. 3.16) with an array of 40-Hz P-wave geophones spaced 1 m apart and oriented northeast-southwest, orthogonal to the trend of the suspected conduit. The line was extended to a total length of 72 m by performing two successive array roll-alongs approximately coincident with ER survey line 1 (Fig. 3.7). A low-velocity anomaly was observed on both the raw data files (Appendix B) and the tomographic profile (Fig. 3.17) from the refraction survey line. A saddle-shaped low-velocity anomaly similar to that seen at Slack’s Cave, though not as pronounced, is observed between geophones 32 and 42. The location of this velocity anomaly correlates to the conduit location beneath well 25 and is interpreted to be attributed to a slow-down in seismic velocity through the primarily water-filled conduit, which was translated to the soil/bedrock interface. Fluid-filled bedrock fractures near the surface or subsidence could also be contributing factors to such an anomaly, if either occurs at this location.

3.2.3 Refraction Survey 3, Berea Road

P-wave seismic-refraction survey data were collected at the Berea Road study area (Fig. 3.18) with an array of 40-Hz P-wave geophones spaced 1 m apart. Refraction line 1 was collected at a northeast-southwest trend with a total line length of 120 m, created by performing three successive surveys along a line coincident to seismic-reflection survey line 3 (Fig. 3.19) and ER survey line 1 (Fig. 3.10). Refraction line 2 was collected along a north-northeast—south-southwest trend parallel to a nearby fence.

A low-velocity anomaly was observed on both the raw data files (Appendix B) and the tomographic profile (Fig. 3.20) from refraction-survey line 1. A saddle-shaped low-velocity anomaly similar to that seen at Slack's Cave and the Kentucky Horse Park is observed between geophones 32 and 40. This anomaly correlates to a seismic backscatter anomaly (Figs. 3.30–3.23) observed on reflection survey line 3 and could correlate to an air- or water-filled karst conduit, a subsidence/collapse feature, a fluid-filled zone of fractured limestone, or a fault. Based on observations from previous surveys, this low-velocity feature was interpreted to correspond to a water-filled karst conduit similar to that found at the Kentucky Horse Park study area. Drilling will be required to verify the interpretation.

A less pronounced low-velocity anomaly was observed on both the raw data files (Appendix B) and the tomographic profile (Fig. 3.24) from refraction survey line 2. This anomaly forms a double-saddle feature similar to that seen on the tomographic profile from Slack's Cave refraction survey line 2 (Fig. 3.15). It could correlate to two subsurface voids separated by solid limestone. Drilling will be required to verify the interpretation.

3.3 Seismic-Reflection Data Interpretation

High-amplitude top-of-bedrock signals were seen in all profiles, caused by the high impedance contrast between the limestone bedrock and overlying unconsolidated sediments. Because of the shallow nature of known and suspected targets, only the first three or four dominant signals were examined. Interpretations focused on velocity anomalies such as loss of reflector coherency, diffractions, and backscatter, which could be related to karst void features. No seismic-reflection surveys were performed at the Slack's Cave study area.

3.3.1 Reflection Survey 1, Kentucky Horse Park

Three separate P-wave seismic-reflection surveys were performed at the Kentucky Horse Park study area, each centered over well 25, which marks the surface location of the subsurface conduit. The first survey (line 1) was collected using an array of 40-Hz P-wave geophones spaced 1 m apart with an initial shot offset of 1 m and shot spacings of 1 m (Fig. 3.25). The initial 48-geophone array was extended to a total length of 72 m by performing one end-on roll-along of the first 24 geophones. The second and third reflection surveys were collected on coincident lines using geophone and shot spacings of .15 m (6 inches) and an initial shot offset of 1.8 m (6 ft) (Fig. 3.25). The second survey (line 2) was collected with an array of 48 40-Hz P-wave geophones, with a line length extended to 11 m (36 ft) by performing two end-on roll-alongs of the first 24 geophones. The third survey (line 3) was collected with an array of 24 100-Hz P-wave geophones, with a line length extended to 7.3 m (24 ft) by performing three end-on roll-alongs of the first 12 geophones.

Three prominent velocity anomalies were observed on the reflection profile from survey line 1 (Fig. 3.26). Two "saddle shaped" low velocity time suppression anomalies are observed between CMP 44 and 56 and CMP 58 and 70 at a time depth of approximately 0.025 s. Two chaotic zones created by loss of reflector coherency, similar to that observed by Miller and Steeples (1991) (Fig. 1.10), were observed between CMP 27 and 36 at a time-depth range of 0.070 to 1.200 s and between CMP 47 and 58 at a time-depth range of 0.060 to 0.090 s. These were interpreted to be related to decreases in velocity in these zones created by either air-, mud-, or water-filled karst void features or fluid-filled zones of fractured limestone. A second anomalous feature is observed between CMP 61 and 74 at a time-depth range of 0.125 to 0.175 s (Fig. 3.26a), which is manifested as a backscatter anomaly that dips across the stacked time history. The angled nature of this feature is an artifact of surface-wave backscatter (Fig. 1.12), which occurs when part of the seismic-wave energy is diffracted back toward the source after encountering a discontinuity (Sloan, 2011). The discontinuity that created this backscatter anomaly was interpreted to correlate to the water-filled conduit based on its known subsurface location. This anomaly was not observed, however, when f-k filtering was applied to the profile (Fit. 3.26b); therefore caution was exercised when applying f-k filtering to other reflection profiles in this study.

Two prominent velocity anomalies were observed on the reflection profile from line 3 (Fig. 3.27). A chaotic zone created by loss of reflector coherency was observed between shotpoint 14 and 26 at a time-depth range of 0.020 to 0.050 s. Reflector pull-down can be seen on both sides of the anomaly, which is typically caused by lateral variations in velocity (Fig. 1.11). This was interpreted to be related to a decrease in

velocity in this zone created by either an air-, mud-, or water-filled karst void feature or a fluid-filled zone of fractured limestone. A backscatter anomaly is observed between shotpoint 40 and 52 at a time-depth range of 0.015 to 0.050 s, which was also interpreted to correlate to the water-filled conduit based on its known subsurface location.

3.3.2 Reflection Survey 2, Berea Road

Three velocity anomalies similar to those seen at the Kentucky Horse Park can be observed on both the CDP and common offset reflection profiles from line 1 (Figs. 3.28 and 3.29). Loss of reflector coherency coupled with reflector push-up/pull-down is observed in 2 locations, one centered around trace 120 on the CDP profile and trace 60 on the common offset profile and the other centered around trace 260 on the CDP profile and 130 on the common offset profile. These were both interpreted to be related to a decrease in velocity in these zone created by either an air-, mud-, or water-filled karst void feature or a fluid-filled zone of fractured limestone. A backscatter anomaly was also observed centered at trace 190 on the CDP profile and 95 on the common offset profile. The backscatter anomaly was the result of either an air-, mud-, or water-filled karst void feature or a zone of fractured limestone. Drilling this anomaly is planned.

Several velocity anomalies similar to those seen at the Kentucky Horse Park can be observed on both the CDP and common offset reflection profiles from line 2 (Figs. 3.30–3.31). These velocity anomalies were all similarly interpreted to be related to a decrease in velocity in this zone created by either an air-, mud-, or water-filled karst void feature or a fluid-filled zone of fractured limestone. Loss of reflector coherency coupled with reflector push-up/pull-down can be observed in four locations on the CDP profile,

centered around traces 60, 160, 290, and 360. A similar anomaly can be observed on the common offset profile centered around trace 80, but the anomaly centered around trace 60 on the CDP profile does not appear on the common offset profile. A backscatter anomaly can also be observed on the common offset profile that spanned from traces 150 to 180, cutting across the area that displays two separate anomalies on the CDP profile. Drilling is planned for this anomaly.

Two velocity anomalies similar to those seen at the Kentucky Horse Park can be observed on both the common offset and CDP reflection profiles from survey line 3 (Figs. 3.21−3.23). These anomalies are interpreted to be related to a decrease in velocity in this zone created by either an air-, mud-, or water-filled karst void feature or a fluid-filled zone of fractured limestone. A loss of reflector coherency coupled with reflector push-up/pull-down can be observed centered around trace 170 on the CDP profile and trace 15 on the common offset profile. A backscatter anomaly can also be observed centered around trace 100 on the CDP profile and trace 50 on the common offset profile. Drilling is planned for this anomaly.

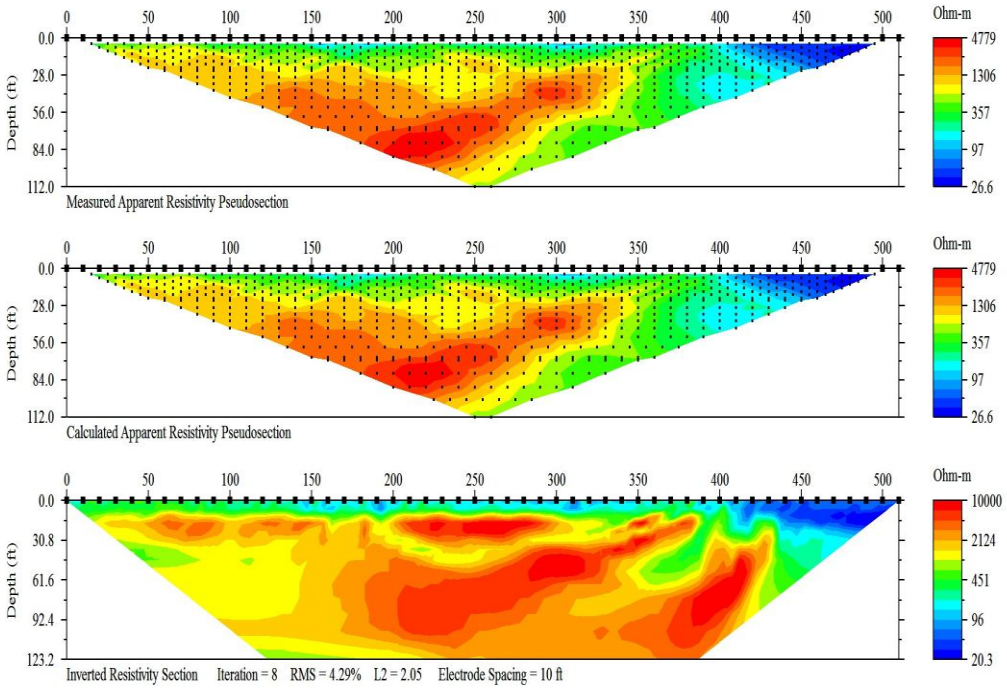

Figure 3.1. Example of a measured apparent resistivity pseudosection (top), a calculated resistivity pseudosection (middle), and an inverted resistivity section (bottom). From Slack's Cave survey line 1.

Figure 3.2. Slack's Cave electrical-resistivity survey line locations. Line 5 is at the top of the parallel survey section with (in order) lines 4, 3, and 1 below.

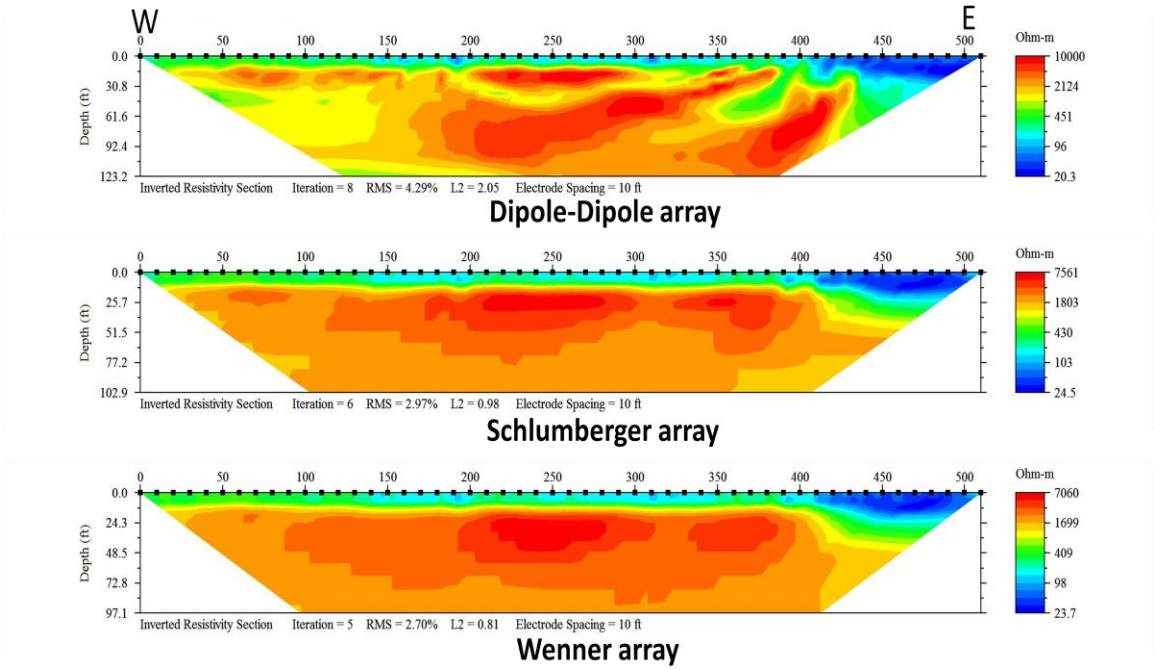

Figure 3.3. Slack's Cave ERT profiles from survey line 1. A pronounced high-resistivity anomaly can be observed centered horizontally at 76 m (250 ft) at a depth of approximately 3 m (10 ft), extending to approximately 9 m (30 ft), which correlates to the cave location.

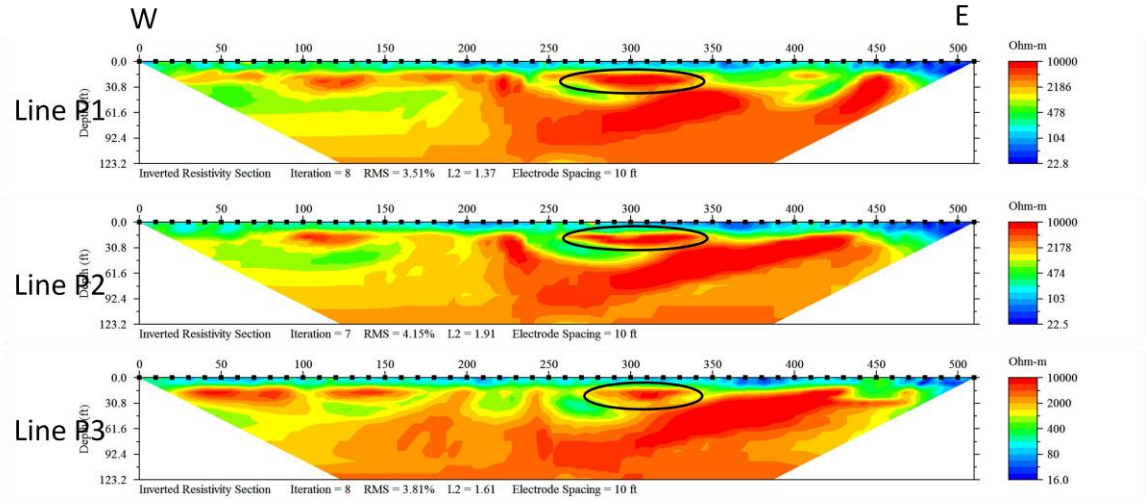

Figure 3.4. Slack's Cave ERT profiles from survey lines 3 to 5, which were spaced 6.096 m (20 ft) apart parallel and coincident to line 1. ⬭ represents the interpreted cave location, which is displayed as a pronounced high-resistivity anomaly centered horizontally at 91 m (300 ft) at a depth of approximately 3 m (10 ft), extending to approximately 9 m (30 ft), which correlates to the subsurface cave location and is similar to the anomaly seen on the profile from survey line 1.

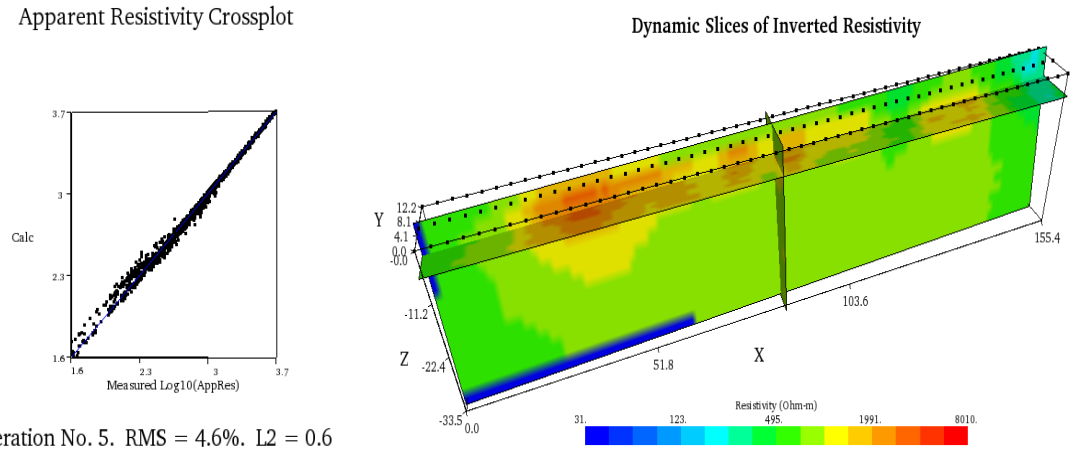

Figure 3.5. Right: 2.5D image from Slack's Cave study area created by combining parallel survey lines 3–5, which were spaced 6.096 m (20 ft) apart parallel and coincident to line 1. Left: The apparent resistivity cross plot displays the measured (log10) versus calculated data fit and RMS error percentage. The pronounced high-resistivity anomaly located near the center of the 2D profiles is distorted in the 2.5D image, which could be related to differences in the inversion algorithms used by the two different programs.

Figure 3.6. Kentucky Horse Park electrical-resistivity survey line locations.

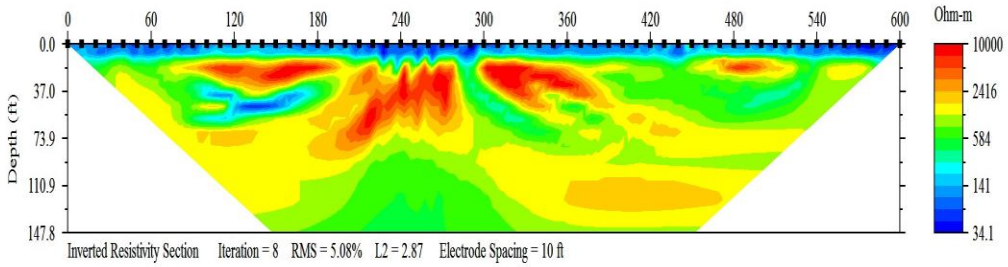

Figure 3.7. Inverted section from Kentucky Horse Park ER survey line 1. A low-resistivity anomaly centered horizontally at 93 m (305 ft) at a depth of approximately 18 m (60 ft) extending to approximately 20 m (65 ft) was interpreted to correlate to the conduit based on its known location under well 25.

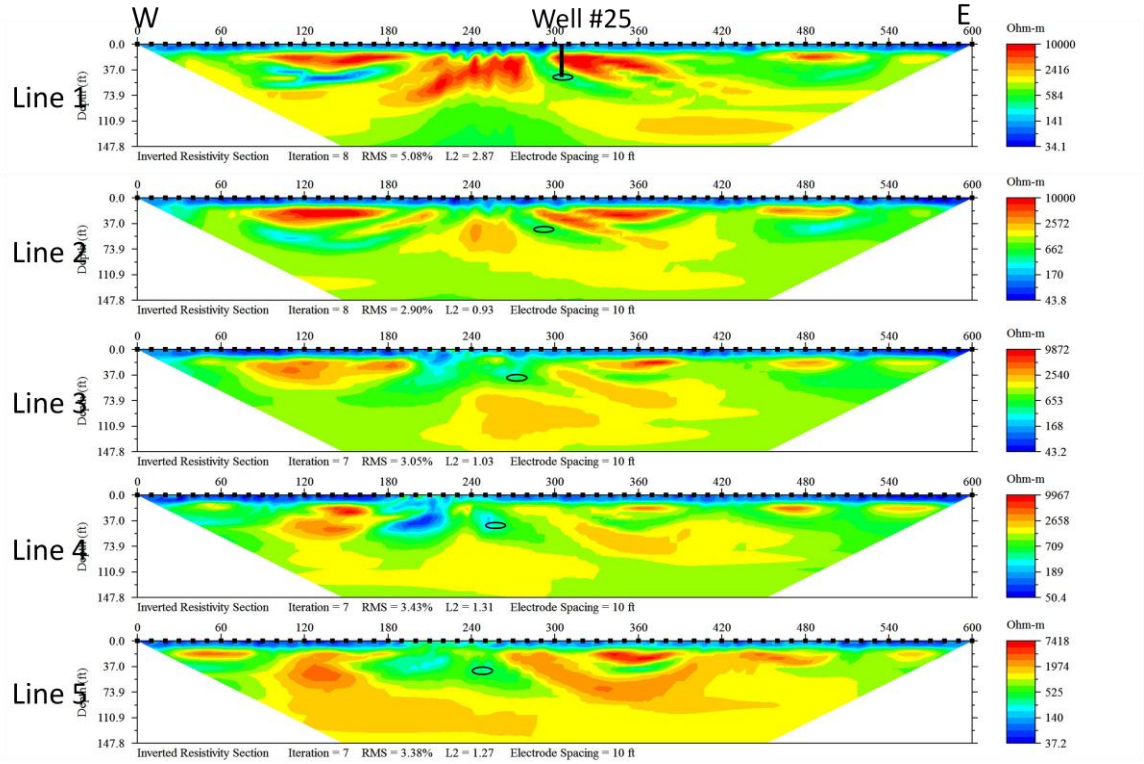

Figure 3.8. Kentucky Horse Park ERT profiles from lines 1−5. ⬭ represents the interpreted conduit locations.

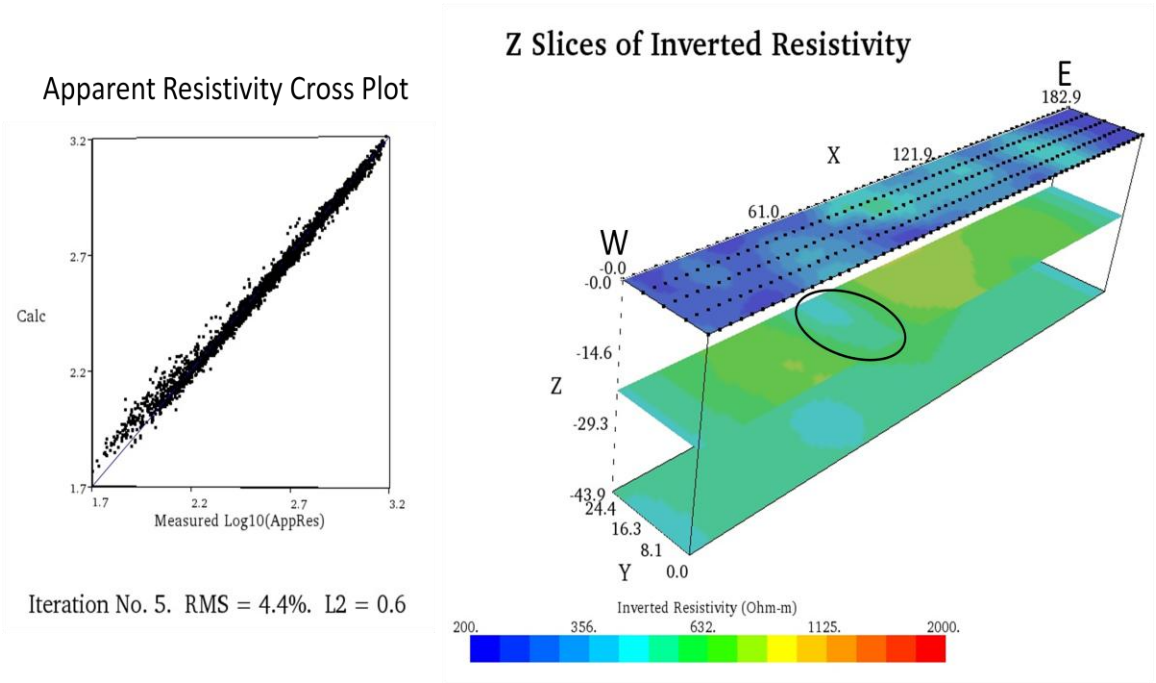

Figure 3.9. Right: 2.5D ERT image from Kentucky Horse Park survey. ⬭ represents the interpreted conduit location, which displays an overall northwest-southeast trend. Left: The apparent resistivity cross plot displays the measured (log10) versus calculated data fit and RMS error percentage.

Figure 3.10. Berea Road electrical-resistivity survey line location.

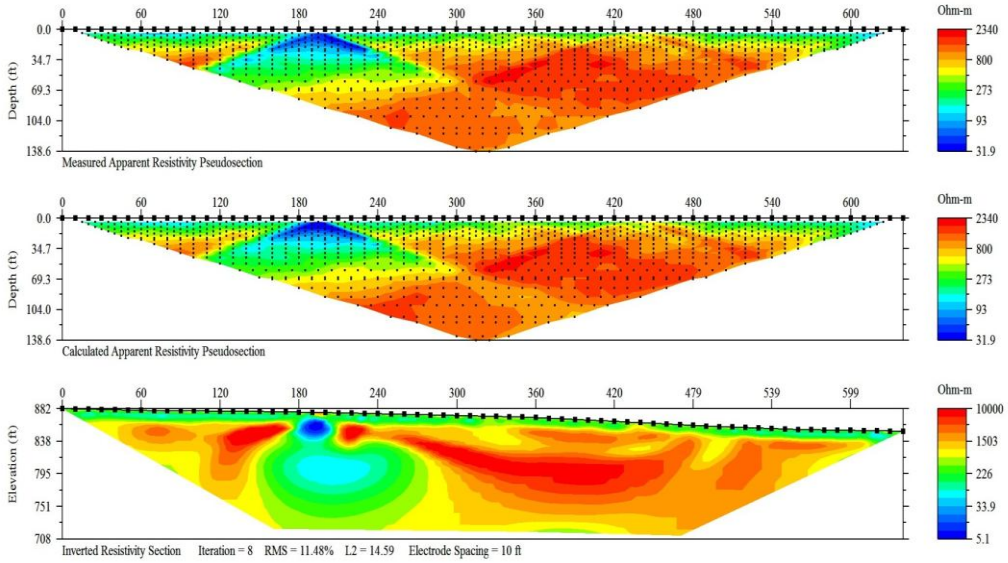

Figure 3.11. Berea Road ERT profile from survey line 1. A low-resistivity anomaly centered horizontally at 58 m (190 ft) can be observed at a depth of approximately 3 m (10 ft), which was interpreted to be a shallow conductive object such as a drain pipe and is not thought to be karst related.

Figure 3.12. Slack's Cave refraction survey line locations.

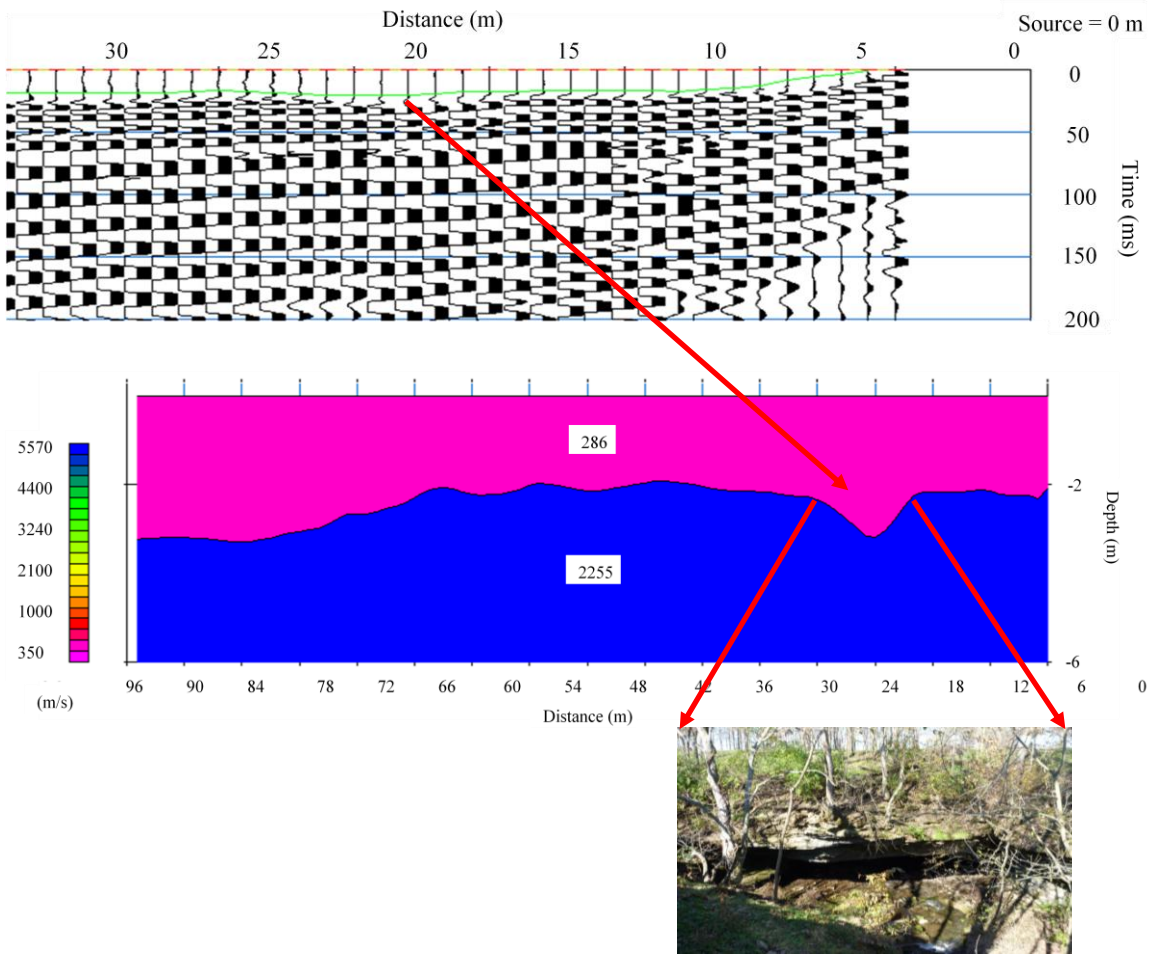

Figure 3.13. Raw data file from Slack's Cave refraction line 1 shot 1 (top), tomographic profile from Slack's Cave refraction survey line 1 (middle), and photo of Slack's Cave karst window (bottom).

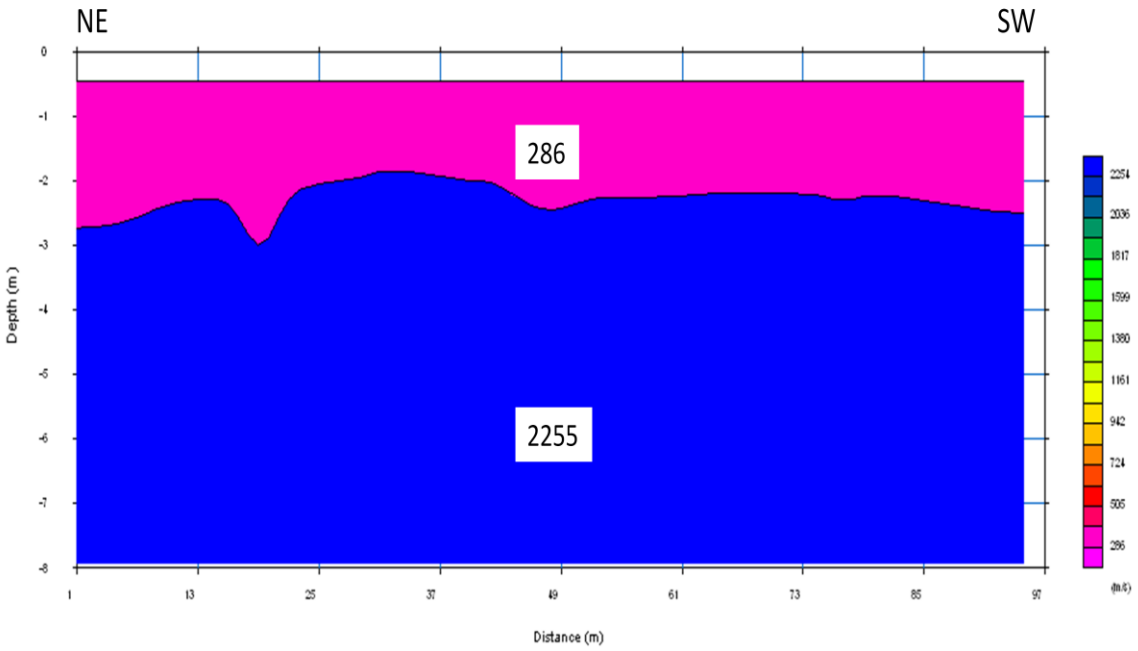

Figure 3.14. Slack's Cave SRT profile from survey line 1. Overburden velocity was calculated at 286 m/s and bedrock velocity was calculated at 2,255 m/s. A low-velocity anomaly can be observed at the soil-bedrock interface centered at approximately 19 m, forming a parabolic time suppression.

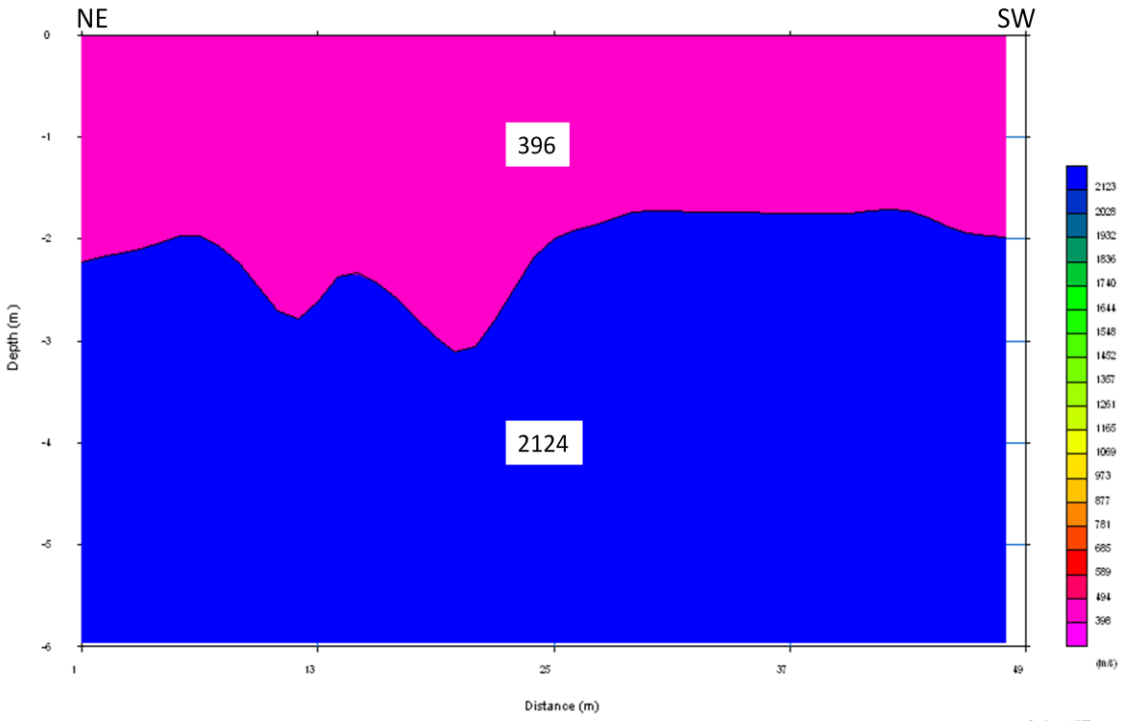

Figure 3.15. Slack's Cave SRT profile from survey line 2. Overburden velocity was calculated at 396 m/s and bedrock velocity was calculated at 2124 m/s. A double-saddle low-velocity anomaly can be observed at the soil-bedrock interface centered at approximately 15 m, which was interpreted to correlate to a location in the subsurface where the cave splits (Fig. 1.5), continuing its north-south trend with an additional arm splitting off to the northwest.

Figure 3.16. Kentucky Horse Park refraction survey line location.

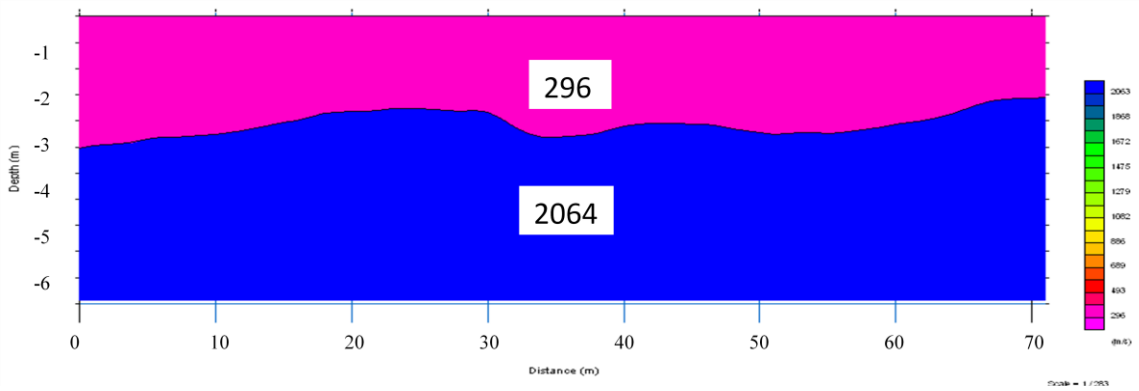

Figure 3.17. Kentucky Horse Park SRT profile from survey line 1. Overburden velocity was calculated at 296 m/s and bedrock velocity was calculated at 2,064 m/s. A saddle-shaped low-velocity anomaly similar to that seen at Slack's Cave, though not as pronounced can be observed between geophones 30 and 40. The location of this velocity anomaly correlates to the conduit location beneath well 25 and is interpreted to be attributed to a slow-down in seismic velocity through the primarily water-filled conduit, which was translated to the soil/bedrock interface.

Figure 3.18. Berea Road refraction survey line locations.

Figure 3.19. Berea Road reflection survey line locations.

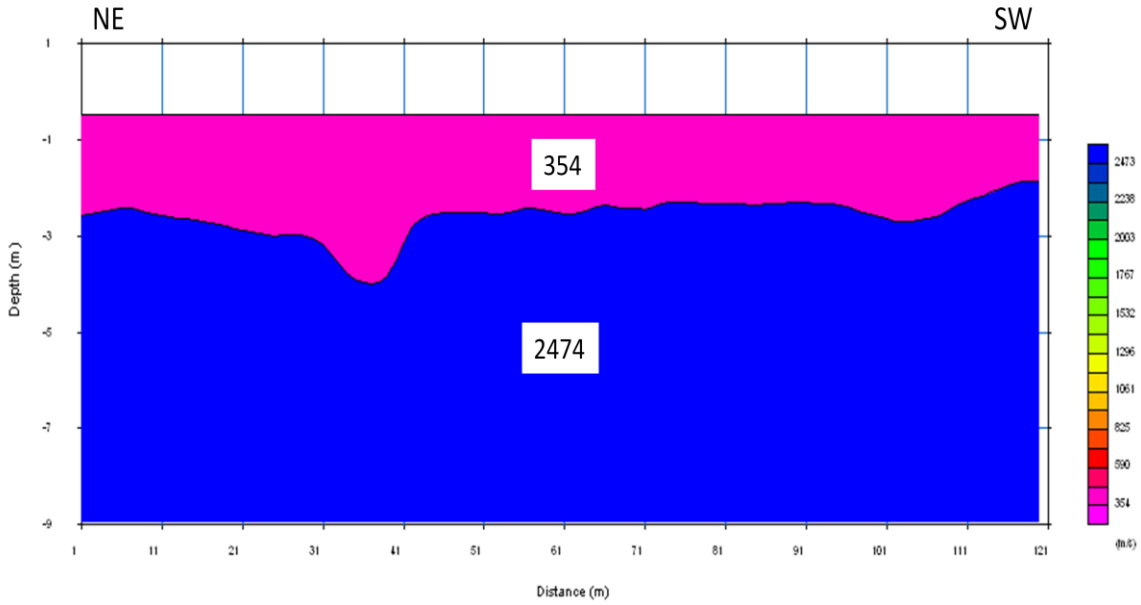

Figure 3.20. Berea Road SRT profile from survey line 1. Overburden velocity was calculated at 354 m/s and bedrock velocity was calculated at 2474 m/s. A saddle-shaped low-velocity anomaly similar to that seen at Slack's Cave and the Kentucky Horse Park can be observed between geophones 32 and 40. This anomaly correlates to a seismic backscatter anomaly (Figs. 3.30−3.23) observed on reflection survey profiles from line 3. This anomaly could correlate to an air- or water-filled karst conduit, a subsidence/collapse feature, a fluid-filled zone of fractured limestone, or a fault.

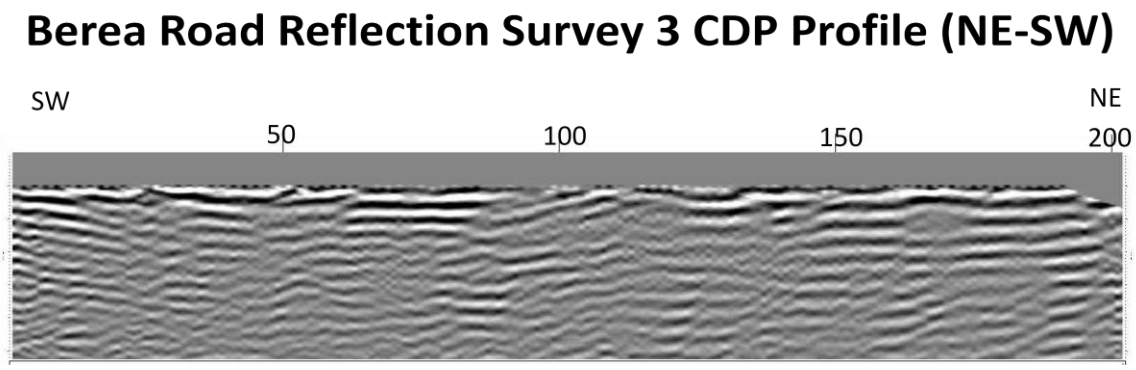

(a)

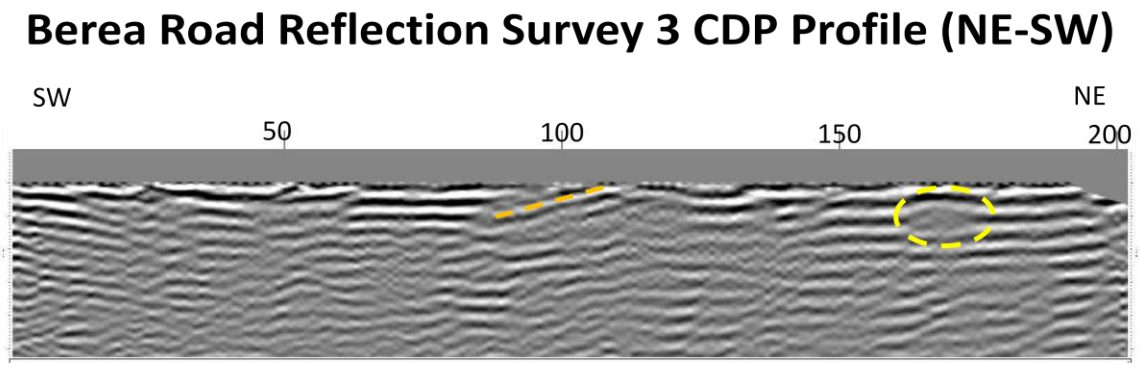

(b)

Figure 3.21. Uninterpreted (a) and interpreted (b) CDP stack reflection profiles from Berea Road survey line 3. The orange dashed line represents the interpreted backscatter anomaly, and the yellow dashed circle surrounds a chaotic zone in which reflector coherency is lost. Reflector pull-down/push-up can also be observed near these zones, caused by lateral seismic velocity variations. These anomalies could correlate to air-, mud-, or water-filled karst features.

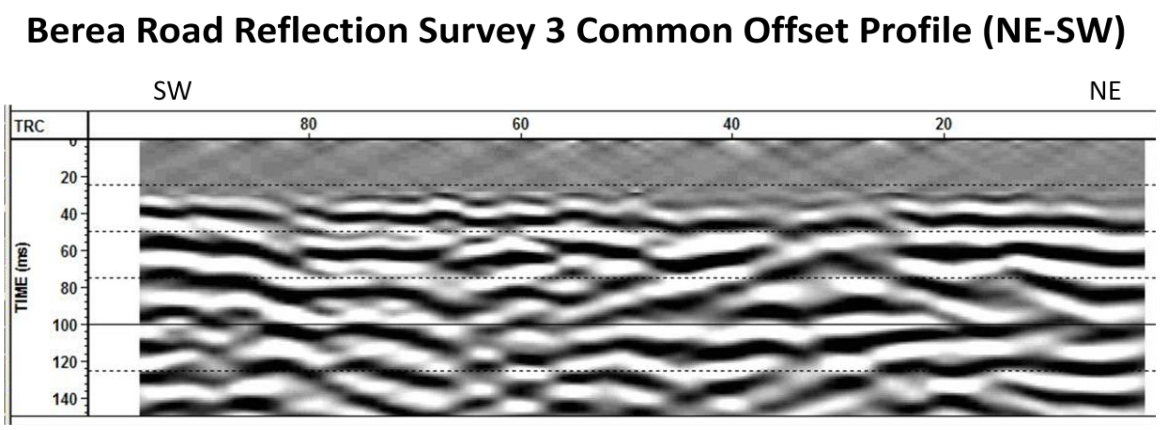

(a)

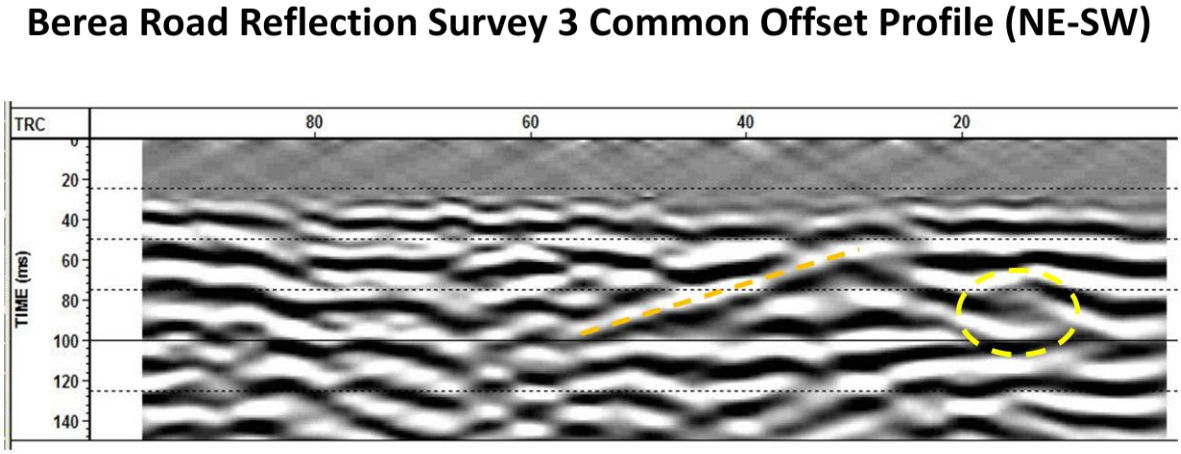

(b)

Figure 3.22. Uninterpreted (a) and interpreted (b) common offset reflection profiles from Berea Road survey line 3. The orange dashed line represents the interpreted backscatter anomaly, and the yellow dashed circle surrounds a chaotic zone in which reflector coherency is lost. Reflector pull-down/push-up can also be observed near these zones, caused by lateral seismic velocity variations. These anomalies could correlate to air-, mud-, or water-filled karst features.

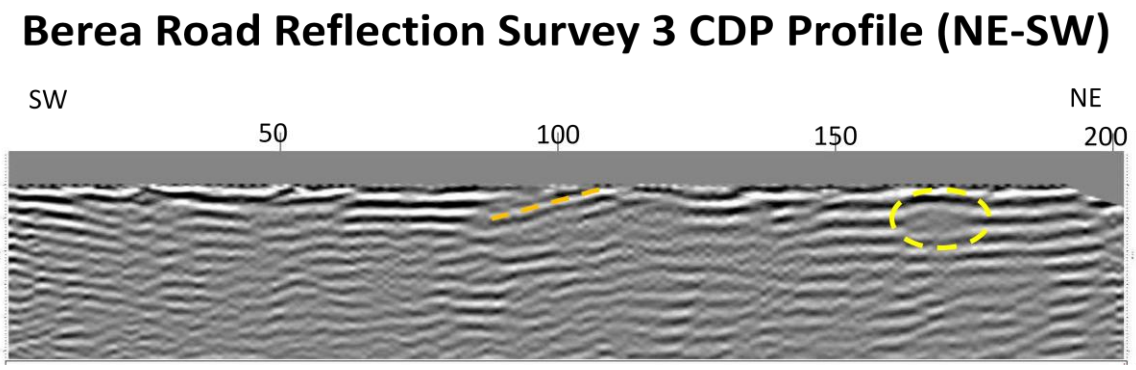

(a)

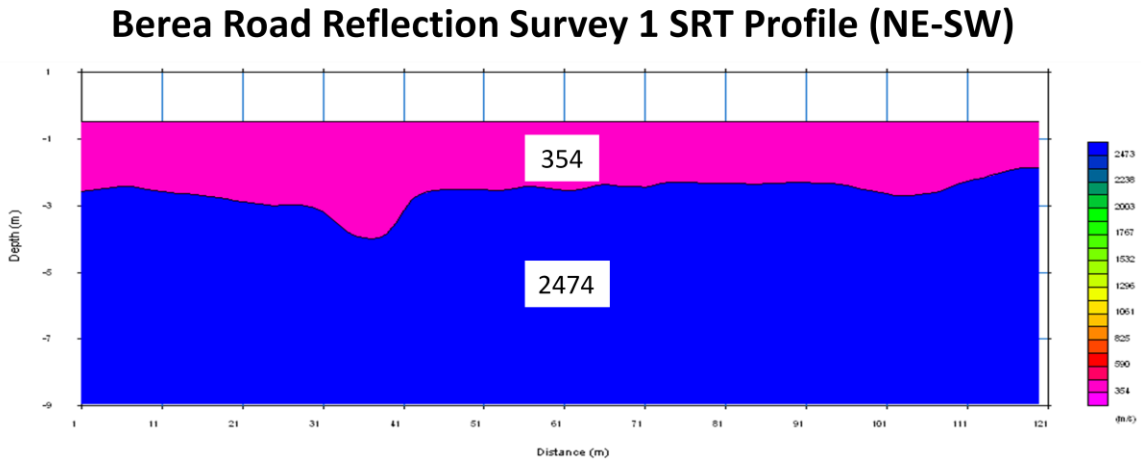

(b)

Figure 3.23. Interpreted CDP profile (a) and SRT profile (b) from Berea Road (reflection survey line 3, refraction survey line 1). The orange dashed line represents the interpreted backscatter anomaly, and this anomalous zone correlates to the low-velocity zone observed in the SRT profile centered at approximately 35 m. These anomalies were interpreted to correlate to a karst conduit similar to that found at the Kentucky Horse Park. A recommendation to drill was given to the Kentucky Geological Survey; results are pending.

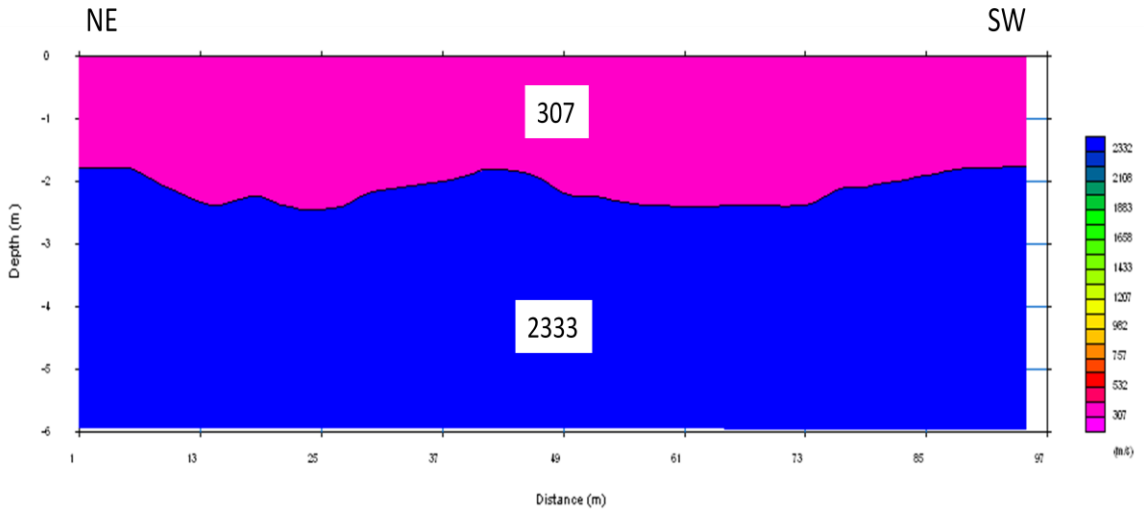

Figure 3.24. Berea Road SRT profile from survey line 2. Overburden velocity was calculated at 307 m/s and bedrock velocity was calculated at 2,333 m/s. This anomaly forms a double-saddle feature similar to that seen on the tomographic profile from Slack's Cave refraction survey line 2 (Fig. 3.12) and could possibly correlate to two subsurface voids separated by solid limestone. Drilling would be required to verify this interpretation.

Figure 3.25. Kentucky Horse Park reflection survey line locations.

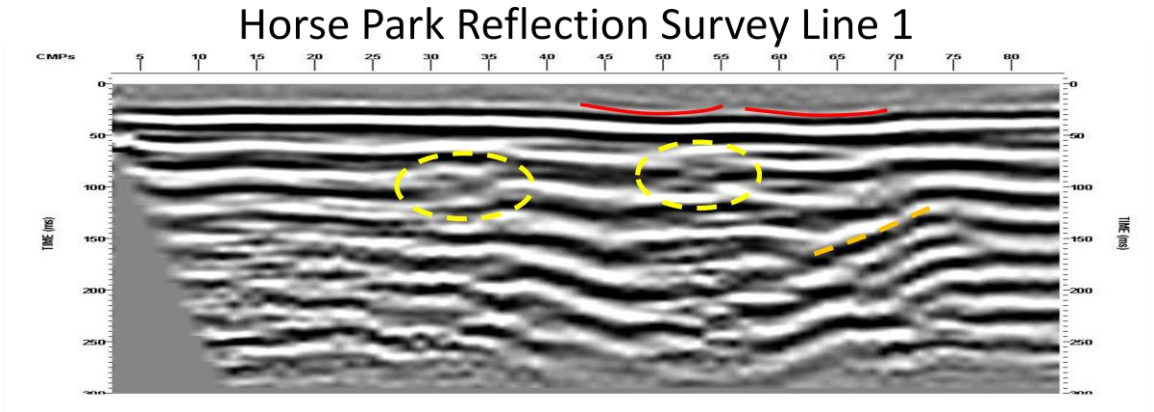

(a)

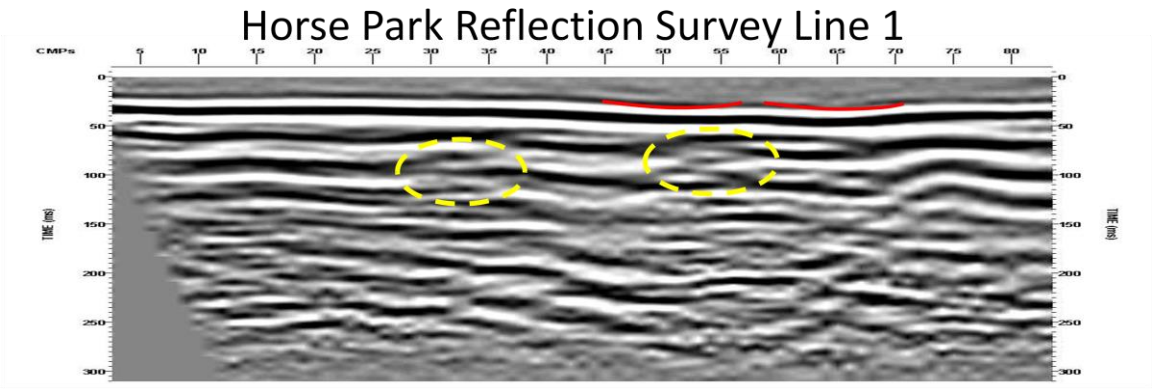

(b)

Figure 3.26. Interpreted CDP stack reflection profiles from Kentucky Horse Park survey line 1. F-k filtering was applied to profile b but not profile a. The red curved lines represent two "saddle shaped" low velocity anomalies observed in both profiles. The yellow dashed circles surround chaotic zones in which reflector coherency is lost. The orange dashed line observed in profile a represents the interpreted backscatter anomaly and correlates to the known location of the subsurface karst conduit. This feature is not observed in profile b due to excessive f-k filtering.

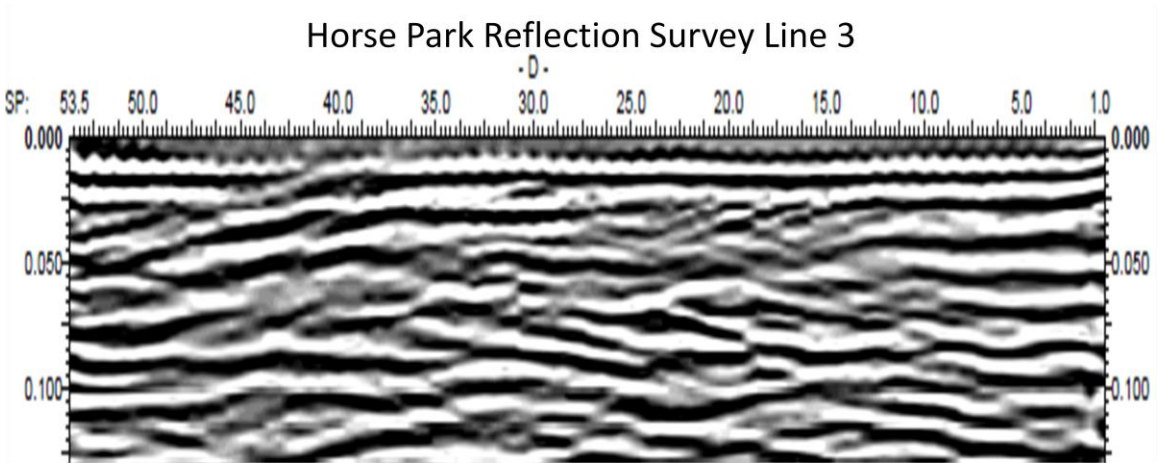

(a)

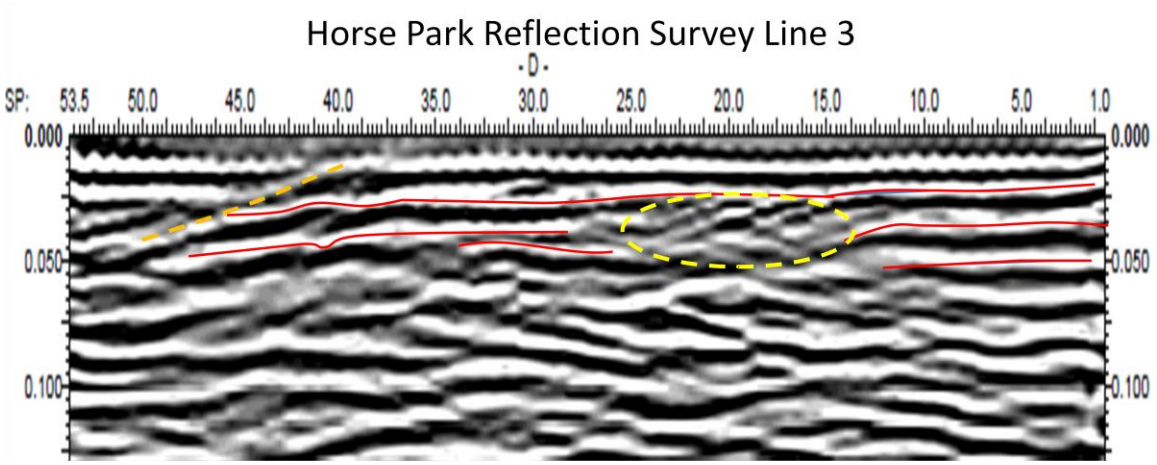

(b)

Figure 3.27. Uninterpreted (a) and interpreted (b) CDP stack reflection profiles from Kentucky Horse Park survey line 3. The orange dashed line represents the interpreted backscatter anomaly and correlates to the known location of the subsurface karst conduit. The yellow dashed circle surrounds a chaotic zone in which reflector coherency is lost. Reflector pull-down can also be observed near this zone, caused by lateral seismic velocity variations. This anomaly could correlate to another air-, mud-, or water-filled karst feature.

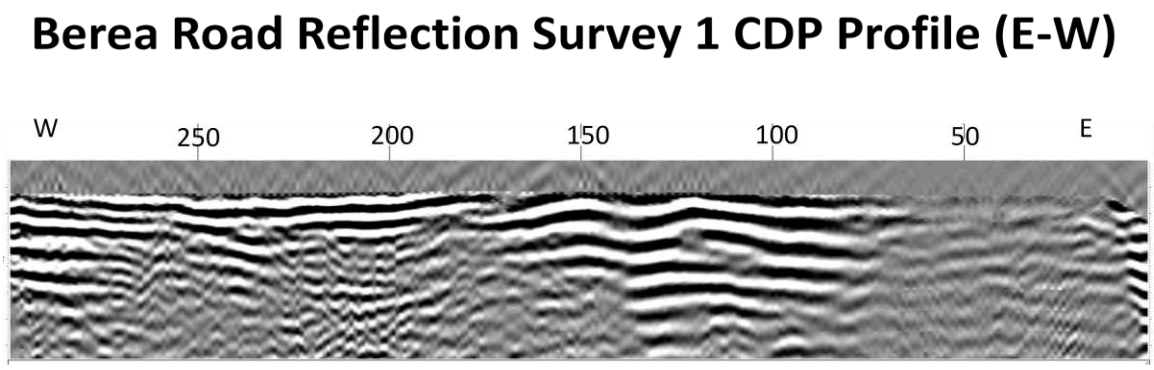

(a)

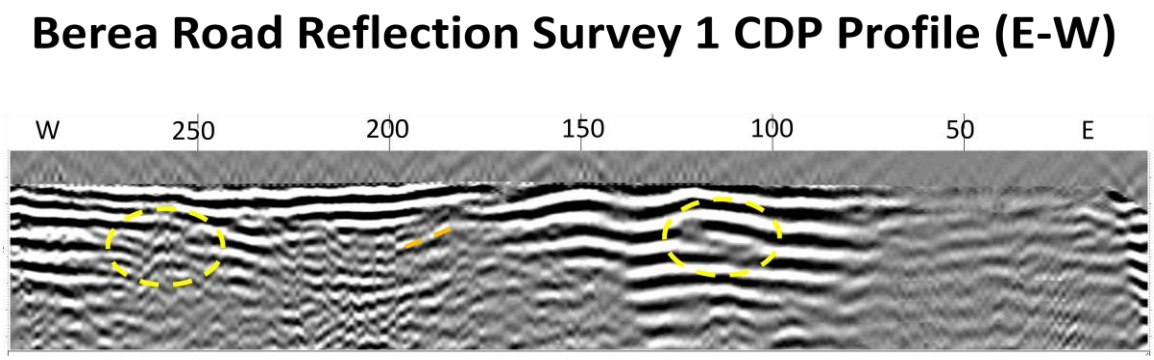

(b)

Figure 3.28. Uninterpreted (a) and interpreted (b) CDP stack reflection profiles from Berea Road survey line 1. The orange dashed line represents the interpreted backscatter anomaly, and the yellow dashed circles surround chaotic zones in which reflector coherency is lost. Reflector pull-down/push-up can also be observed near these zones, caused by lateral seismic velocity variations. These anomalies could correlate to air-, mud-, or water-filled karst features.

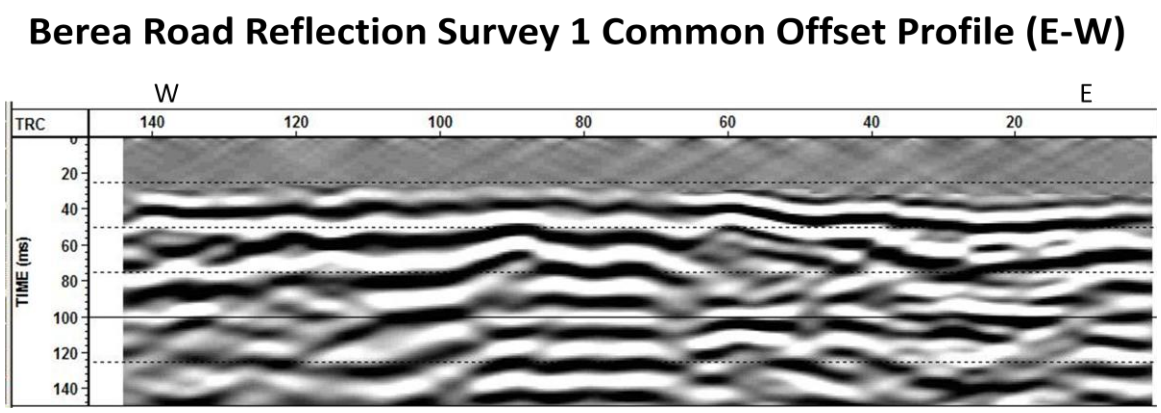

(a)

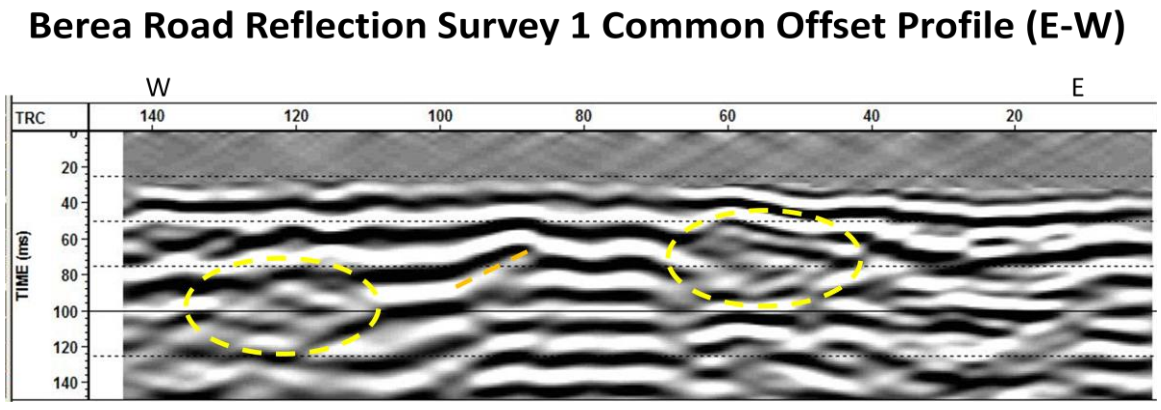

(b)

Figure 3.29. Uninterpreted (a) and interpreted (b) common offset reflection profiles from Berea Road survey line 1. The orange dashed line represents the interpreted backscatter anomaly, and the yellow dashed circles surround chaotic zones in which reflector coherency is lost. Reflector pull-down/push-up is also observed near this zone, caused by lateral seismic velocity variations. These anomalies could correlate to air-, mud-, or water-filled karst features.

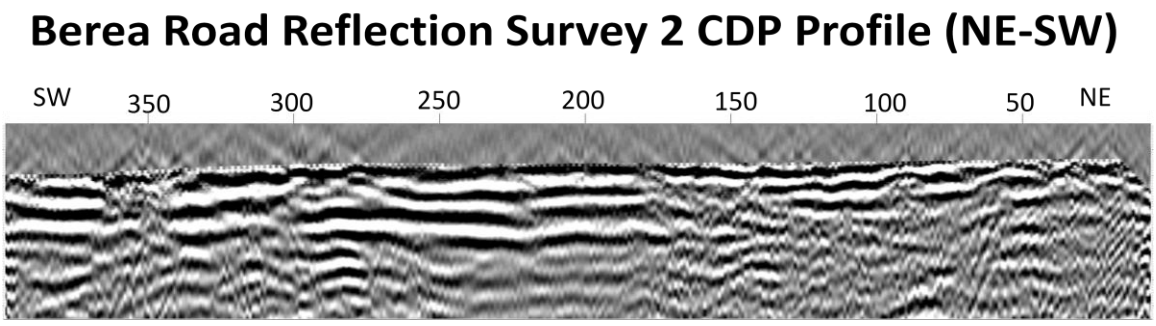

(a)

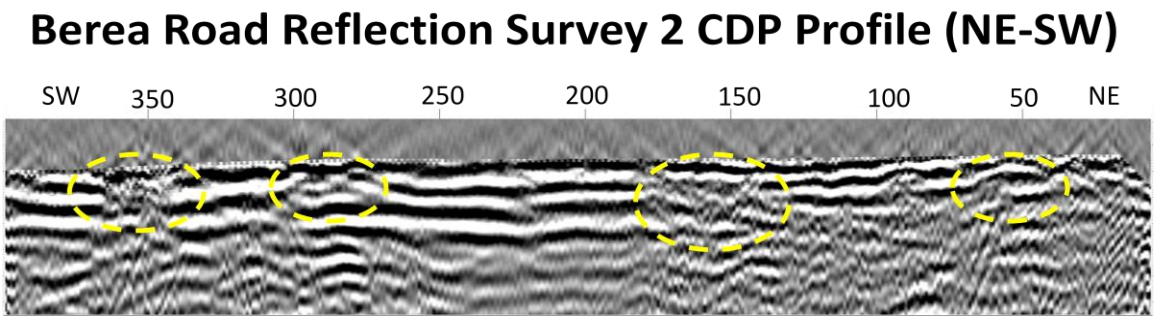

(b)

Figure 3.30. Uninterpreted (a) and interpreted (b) CDP stack reflection profiles from Berea Road survey line 2. The yellow dashed circles surround chaotic zones in which reflector coherency is lost. Reflector pull-down/push-up can also be observed near these zones, caused by lateral seismic velocity variations. These anomalies could correlate to air-, mud-, or water-filled karst features.

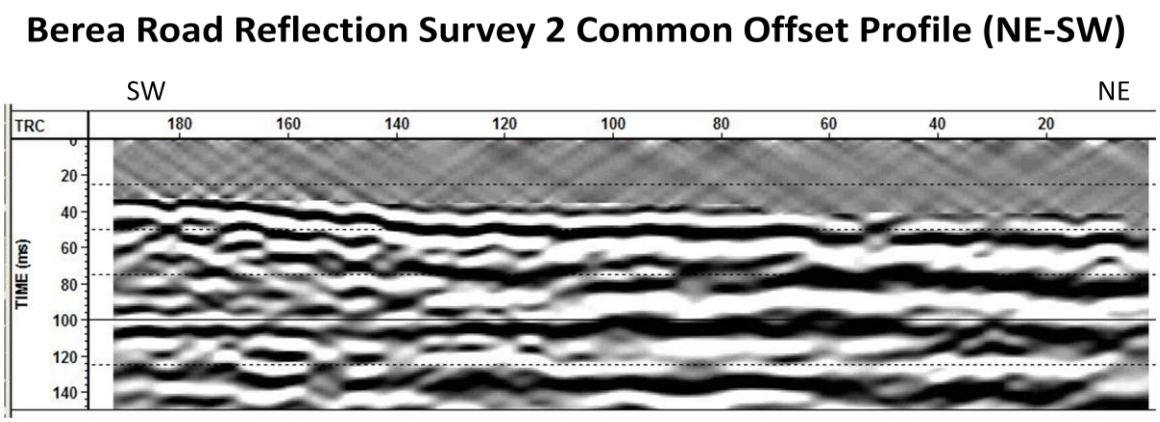

(a)

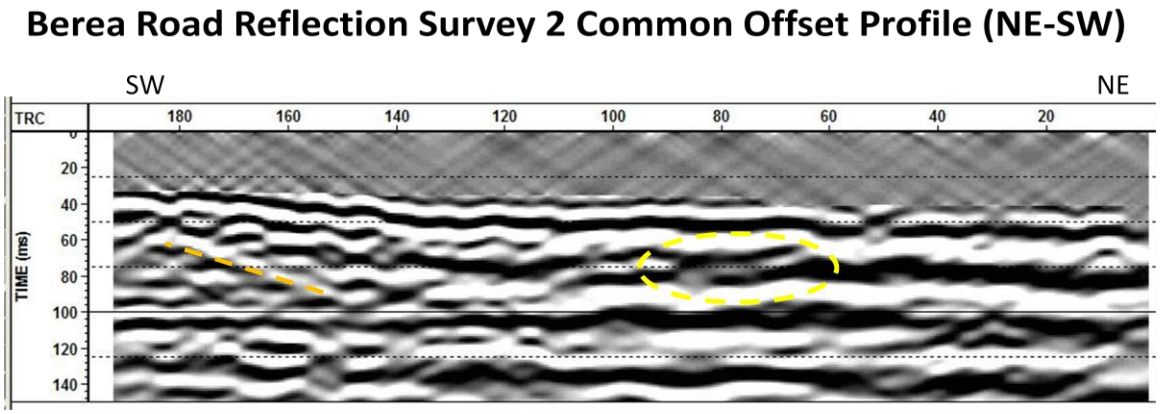

(b)

Figure 3.31. Uninterpreted (a) and interpreted (b) common offset reflection profiles from Berea Road survey line 2. The orange dashed line represents the interpreted backscatter anomaly, and the yellow dashed circle surrounds a chaotic zone in which reflector coherency is lost. Reflector pull-down can also be observed near this zone, caused by lateral seismic velocity variations. These anomalies could correlate to air-, mud-, or water-filled karst features.

CHAPTER FOUR
DISCUSSION

4.1 Comparison of Method Results

4.1.1 Slack's Cave Study Area

The inverted dipole-dipole resistivity section (Fig. 4.1) shows a pronounced high-resistivity anomaly at a depth of approximately 3 m (10 ft) that extends to approximately 9 m (30 ft). A pronounced low-velocity anomaly can be observed in the seismic-refraction tomographic profile (Fig. 4.1) at approximately the same depth. Both the high-resistivity ER anomaly and low-velocity seismic anomaly were correlated to the known cave location.

4.1.2 Kentucky Horse Park Study Area

The electrical resistivity anomaly observed on the inverted dipole-dipole resistivity section (Fig. 4.2) at the known location of the solution conduit was not very pronounced and would have been difficult to interpret without prior knowledge of the conduit location and dimensions. Other larger low-resistivity anomalies, such as the one seen between electrodes 110 and 180 at a depth of approximately 15 m (50 ft), could be mistaken for such a feature. This suggests that the electrical-resistivity method may not be very effective in resolving small water-filled targets at greater depths. Velocity anomalies can be observed in both the SRT profile (Fig. 4.2) and the seismic-reflection profile (Fig. 4.2). The low-velocity anomaly observed in the SRT profile was correlated to the known conduit location, but also may have been difficult to interpret without prior knowledge. A more pronounced backscatter anomaly seen on the seismic-reflection

profile was also correlated to the known conduit location. However, it was observed that excessive f-k filtering could remove this type of anomaly, so caution was exercised when applying f-k filtering to other reflection profiles in this study. Based on a comparison of these three methods, it appears that seismic-reflection profiling provides the highest resolution for detecting karst void features in this area with characteristics similar to the solution void found at the Kentucky Horse Park study area.

4.1.3 Berea Road Study Area

Velocity anomalies similar to those found at the Kentucky Horse Park can be observed in all CDP and common offset profiles from this study area (Fig. 4.3). A low-velocity anomaly can be observed on the SRT profile from refraction survey line 1 (Fig. 4.3), which correlates to a seismic backscatter anomaly that can be observed on the CDP and common offset profiles from line 3 (Fig. 4.3). The electrical-resistivity survey performed along this same line (Fig. 4.3), however, did not reveal any resistivity anomalies in the vicinity of the seismic velocity anomalies. Results from the ER survey at the Kentucky Horse Park previously showed that the electrical-resistivity method may not be the most effective method for resolving smaller, deeper targets; therefore, the fact that no anomalies were seen in the target zone at this location may be an issue of resolution. The seismic velocity anomalies observed in the refraction and reflection profiles could be created by features such as karst voids, collapse features, faults, or fluid-filled, fractured limestone. However, based on previous surveys, these velocity anomalies are interpreted to correspond to a water-filled solution conduit similar to that

found at the Kentucky Horse Park. Three drill targets were selected based on backscatter anomaly locations (Fig. 4.4).

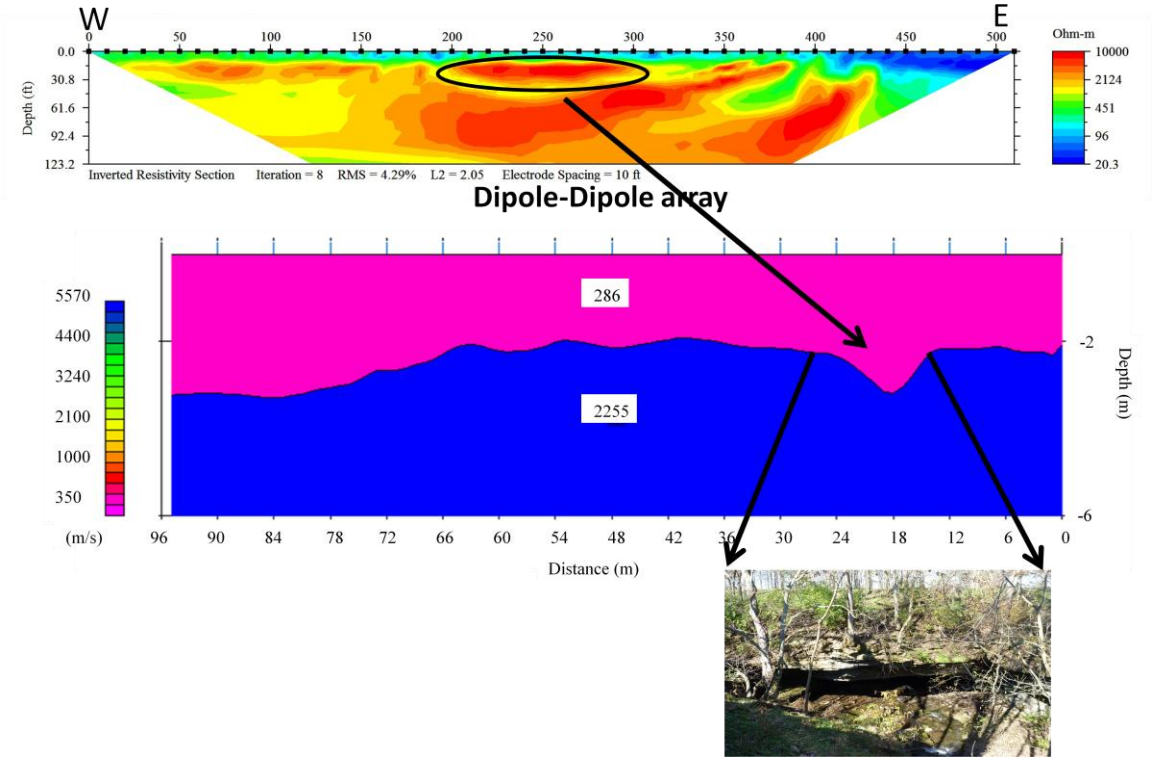

Figure 12. Slack's Cave ERT profile (top) and SRT profile (middle) from survey line 1. A pronounced high-resistivity anomaly can be observed on the ERT profile centered horizontally at 76 m (250 ft) at a depth of approximately 3 m (10 ft), extending to approximately 9 m (30 ft). A low-velocity anomaly can be observed on the SRT profile at the soil-bedrock interface centered at approximately 19 m, forming a parabolic time suppression. Both of these anomalies correlate to the cave location.

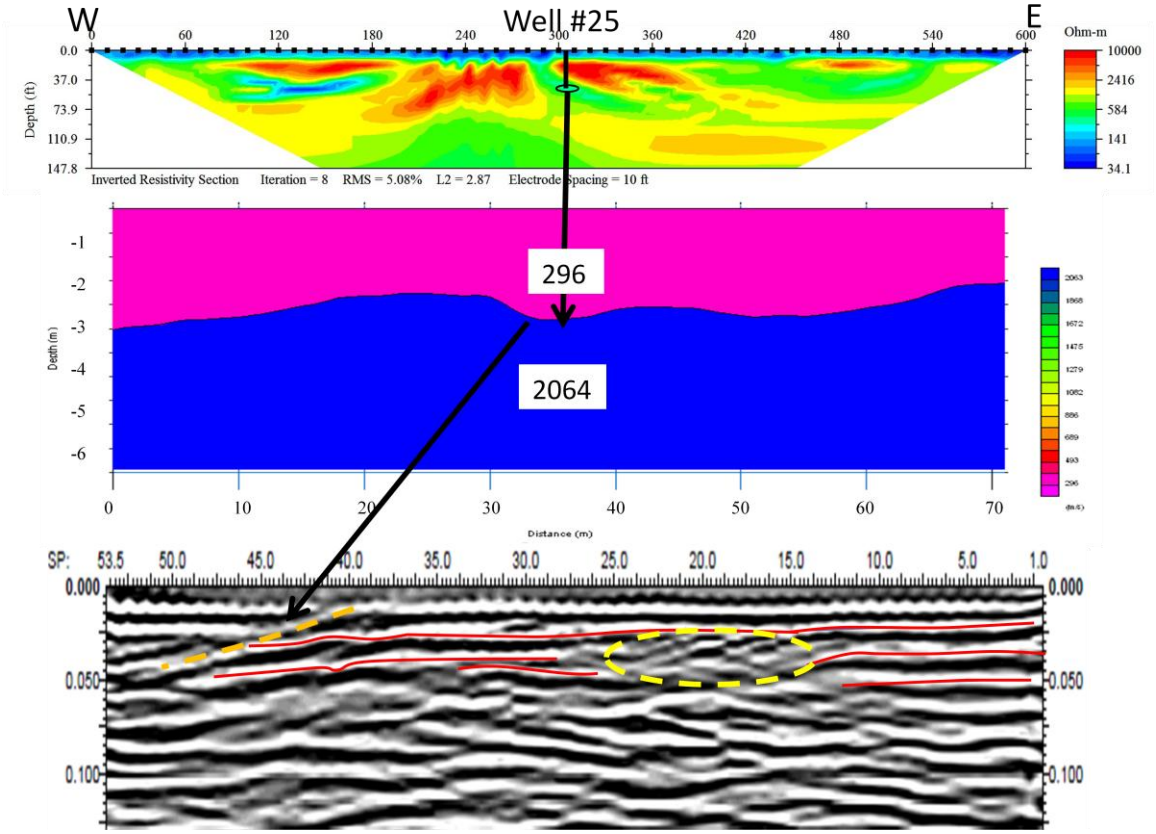

Figure 13. Kentucky Horse Park ERT profile (top), SRT profile (middle), and CDP stack reflection profile (bottom) from survey line 1. A low-resistivity anomaly can be observed on the ERT profile centered horizontally at 93 m (305 ft) at a depth of approximately 18 m (60 ft) extending to approximately 20 m (65 ft). A low-velocity anomaly can be observed on the SRT profile between geophones 30 and 40. The orange dashed line on the CDP stack profile represents the interpreted backscatter anomaly, and all three of these anomalies correlate to the location of the subsurface karst conduit.

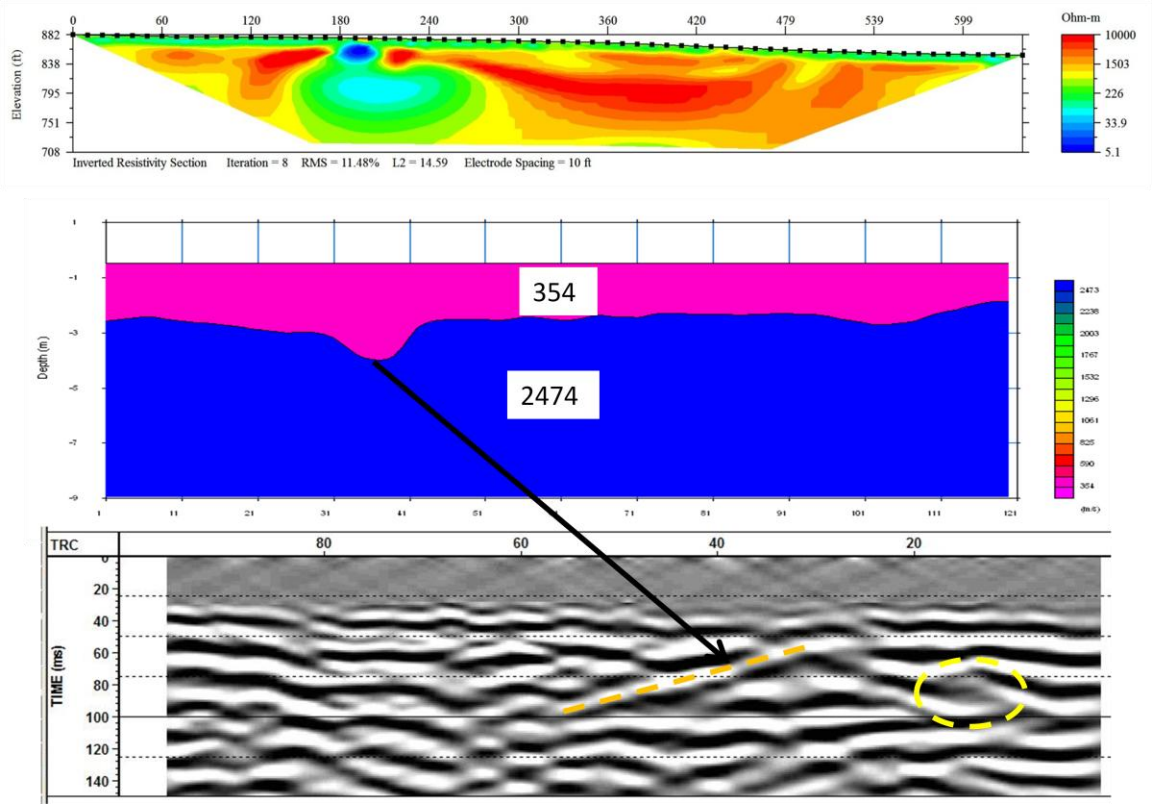

Figure 14. Berea Road ERT profile (top), SRT profile (middle), and common offset reflection profile (bottom). A low-resistivity anomaly can be observed on the ERT profile centered horizontally at 58 m (190 ft) at a depth of approximately 3 m (10 ft), which was interpreted to be a shallow conductive object such as a drain pipe and is not thought to be karst related. A low-velocity anomaly similar to that seen at Slack's Cave and the Kentucky Horse Park can be observed on the SRT profile between geophones 32 and 40. This anomaly correlates to a seismic backscatter anomaly observed on the common offset reflection profile. These seismic anomalies were interpreted to correlate to a karst conduit similar to that found at the Kentucky Horse Park.

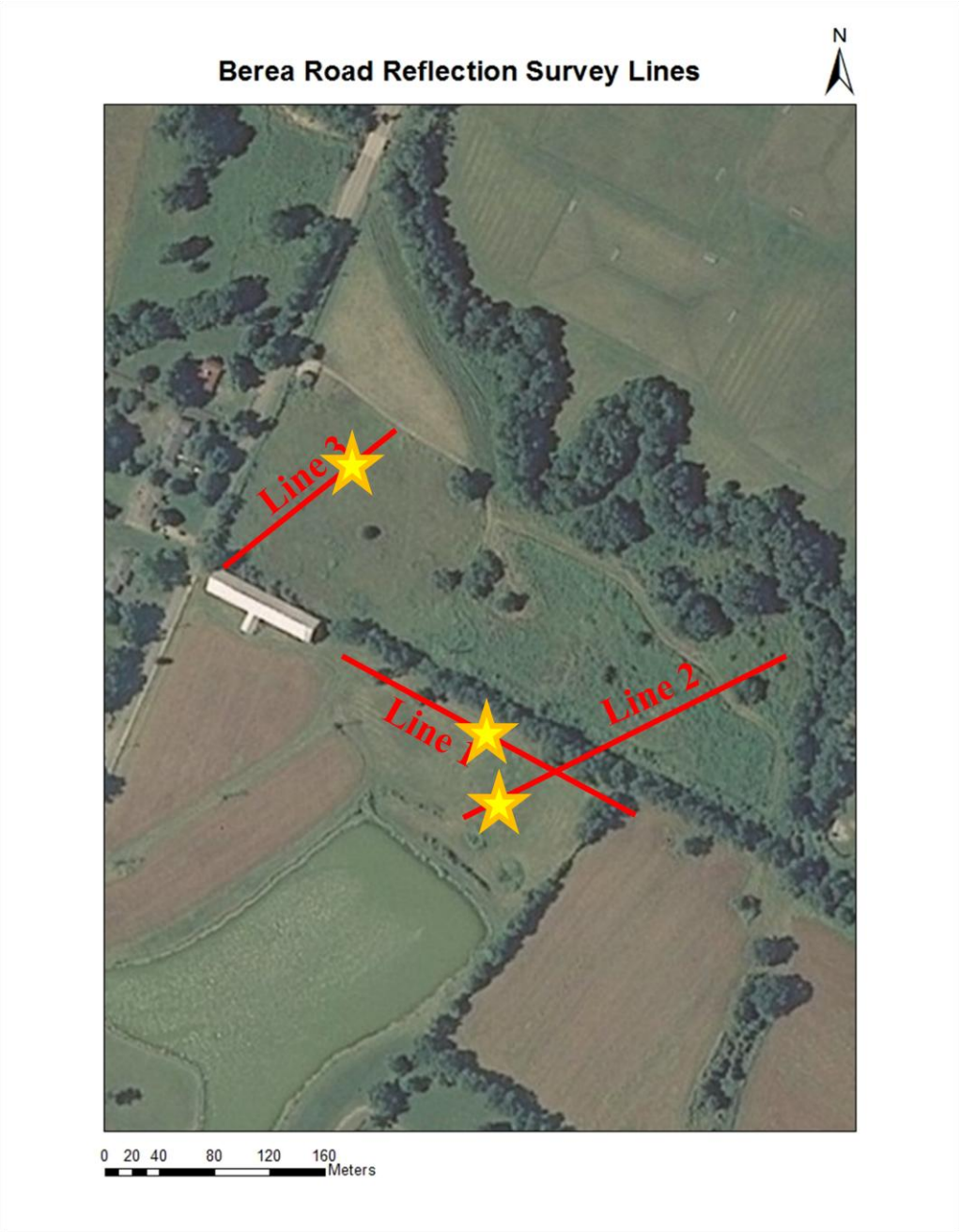

Figure 15 Berea Road reflection survey map. Drill targets based on backscatter anomaly locations are marked with a star.

CHAPTER FIVE
CONCLUSIONS

Electrical-resistivity, seismic-refraction, and seismic-reflection surveys were performed at three different locations in the Inner Bluegrass Region of Kentucky (except that a seismic-reflection survey was not performed at Slack's Cave). The three different geophysical techniques were applied along coincident survey lines in order to correlate the interpreted results and determine the effectiveness of each method in locating known and unknown karst void features in this region. Integration of multiple methods was determined to be useful in constraining the interpretation of geophysical data sets. Resultant interpretations of these surveys suggest:

- Seismic-refraction velocity-suppression zones and high electrical-resistivity anomalies were correlated to the location of the primarily air-filled Slack's Cave, suggesting that both methods are effective in locating this type of target in the Inner Bluegrass Region.

- Seismic-refraction velocity-suppression zones, seismic-wave backscatter, and low electrical-resistivity anomalies were correlated to the location of the primarily water-filled solution conduit at the Kentucky Horse Park. However, it was observed that excessive f-k filtering could remove backscatter anomalies from reflection profiles, so caution was exercised when applying f-k filtering to other reflection profiles in this study. The seismic-reflection method was determined to provide higher resolution

and produce less ambiguous results for this type of target in the Inner Bluegrass Region compared to the other two methods.

- Seismic-refraction velocity suppression zones and seismic-wave backscatter anomalies were observed in the same location at the Berea Road study area. They were interpreted to be a water-filled conduit similar to that found at the Kentucky Horse Park. Three seismic targets were selected based on backscatter anomaly locations (Fig. 4.4) and were aligned in a northwest trend following the general bedrock dip, joint orientations, and suspected conduit orientation. No electrical-resistivity anomalies were seen in the anomalous seismic zone, which could be a result of limitations of the electrical-resistivity method to resolve this type of smaller target at depth.

- Verification of the above-mentioned seismic interpretations at the Berea Road study area will require drilling. A recommendation to drill this target has been submitted to the Kentucky Geological Survey, and if drilling confirms this method is successful, it could be applied to other suspected karst-bearing sites in the Inner Bluegrass Region.

APPENDIX A

Appendix A

Section 1

Uninterpreted electrical resistivity tomography (ERT) profiles. The top profile represents the apparent resistivity pseudosection measured in the field, the middle profile represents the calculated apparent resistivity model, and the bottom profile is the inverted pseudosection that represents true earth resistivities based on the calculated model. All profiles were processed using the robust inversion option. Due to high quality of data, no misfit data was removed from any profile.

Slack's Cave line 1 dipole-dipole survey

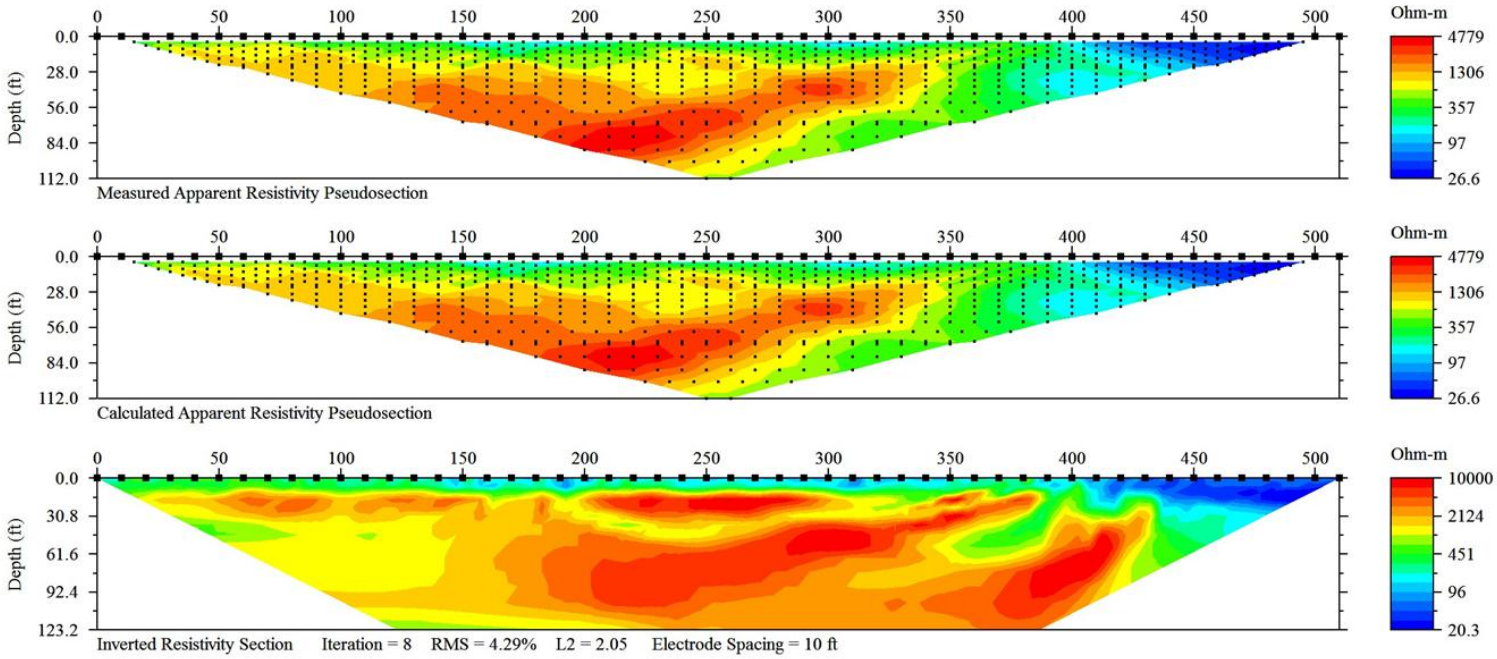

Slack's Cave line 1 Schlumberger survey

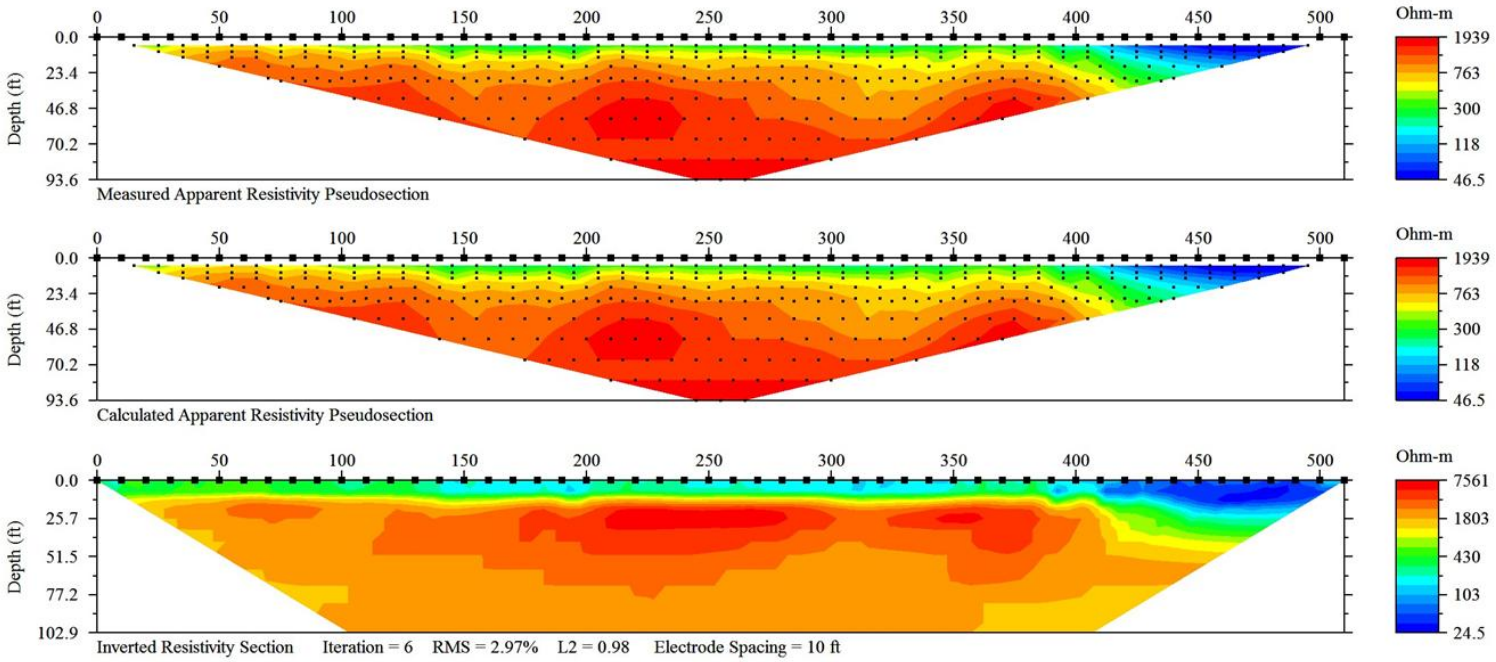

Slack's Cave line 1 Wenner survey

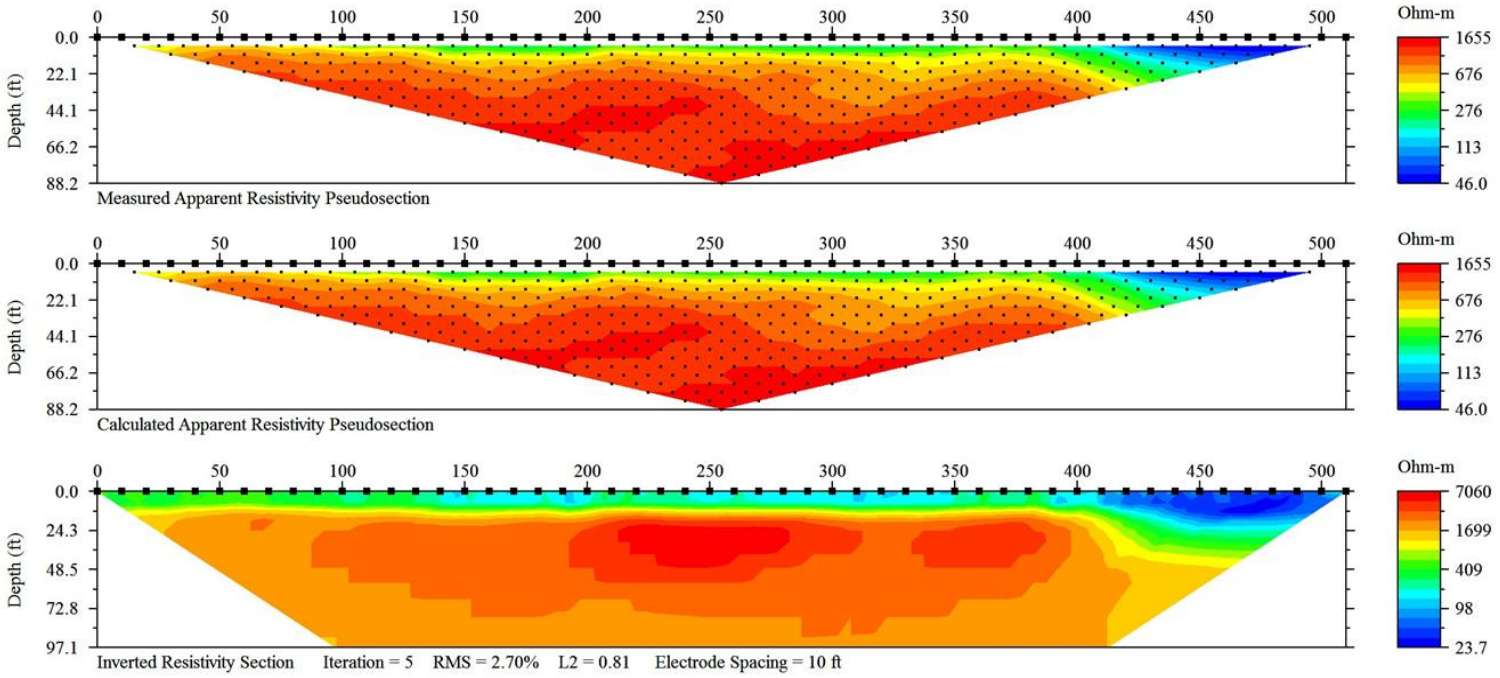

Slack's Cave line 2 dipole-dipole survey

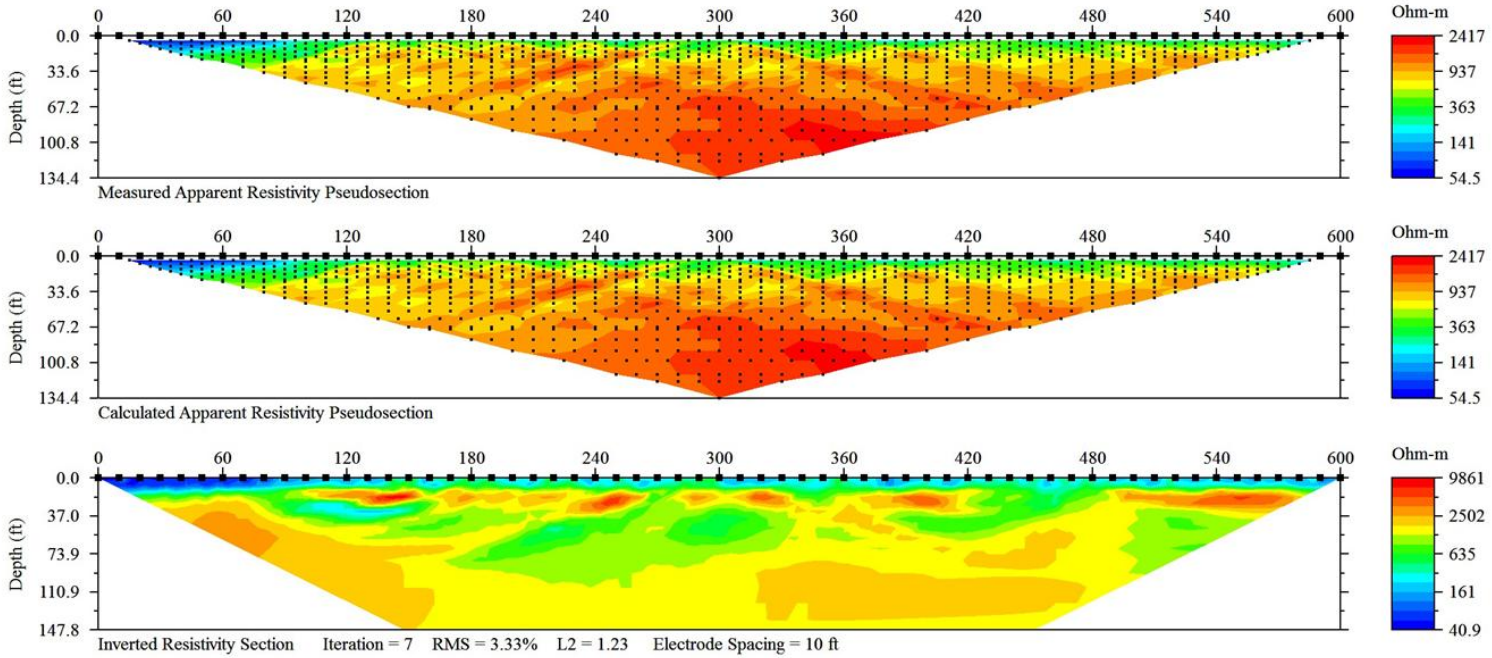

Slack's Cave line 3 dipole-dipole survey

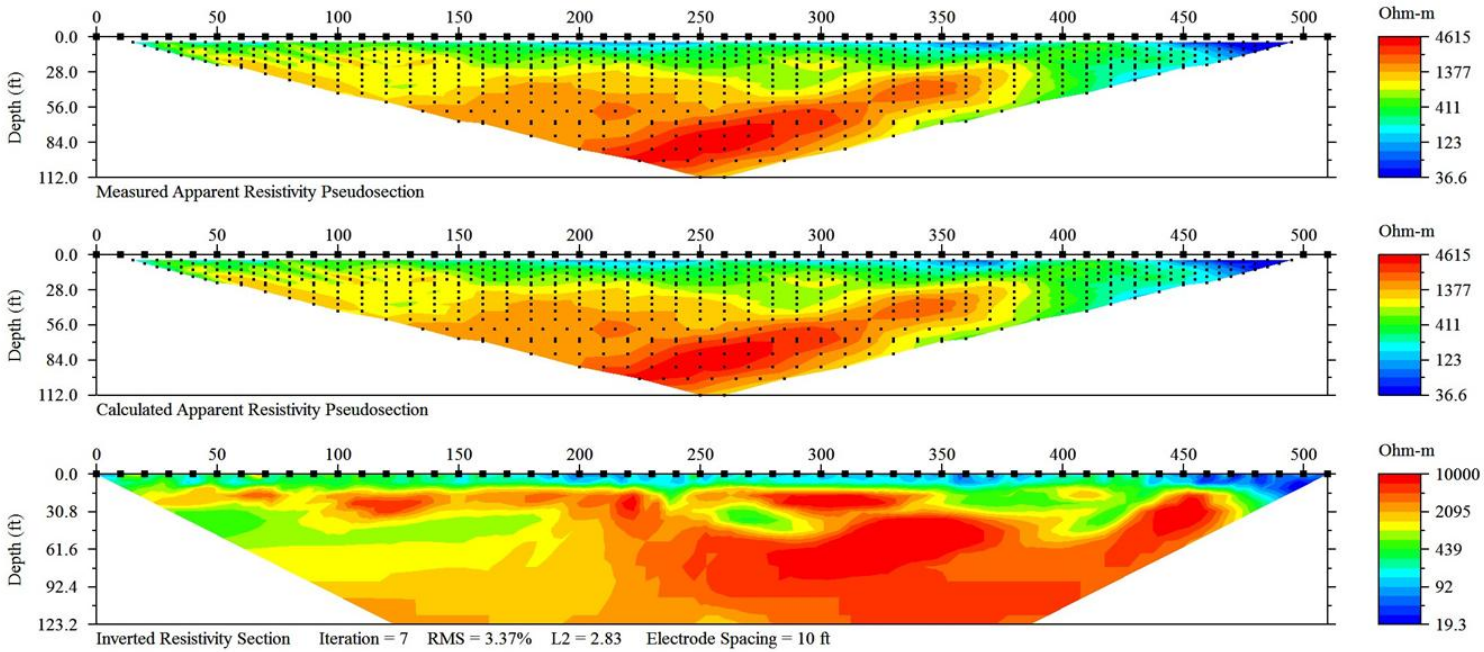

Slack's Cave line 4 dipole-dipole survey

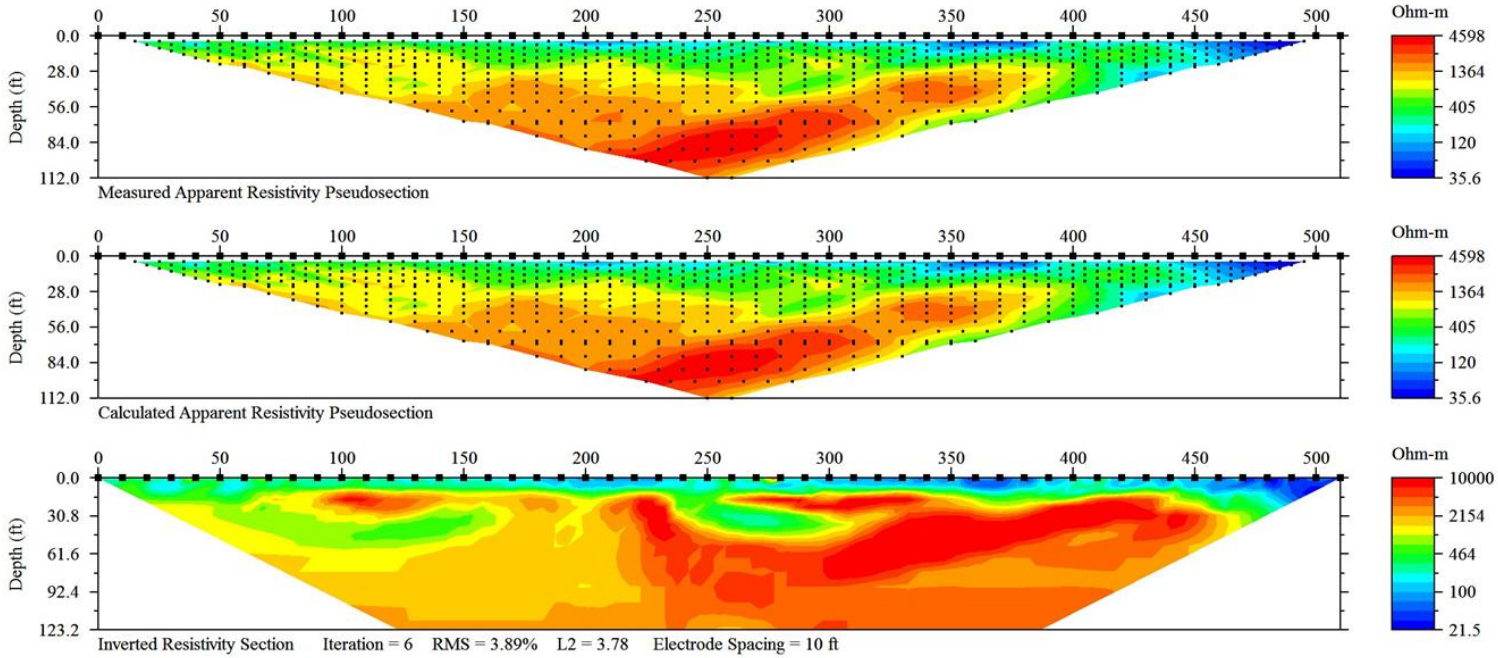

Slack's Cave line 5 dipole-dipole survey

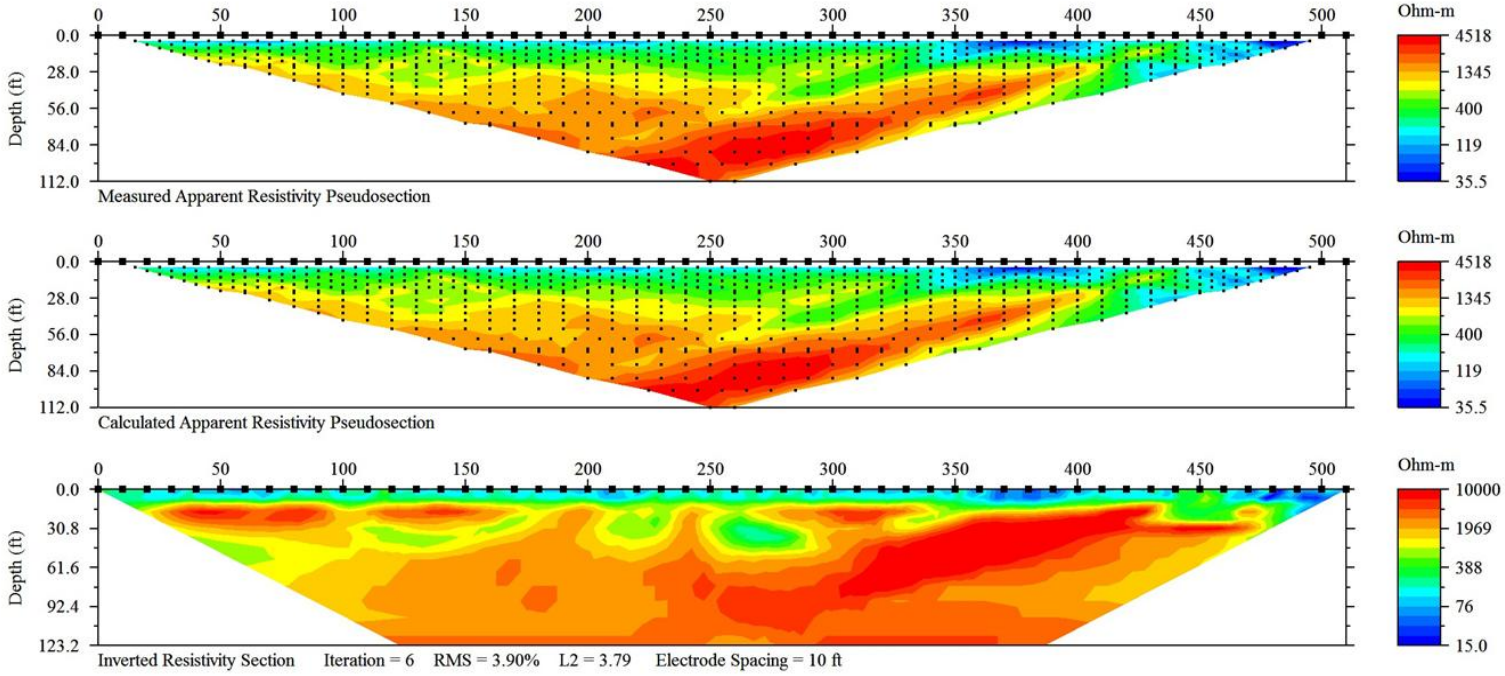

Slack's Cave line 5 Schlumberger survey

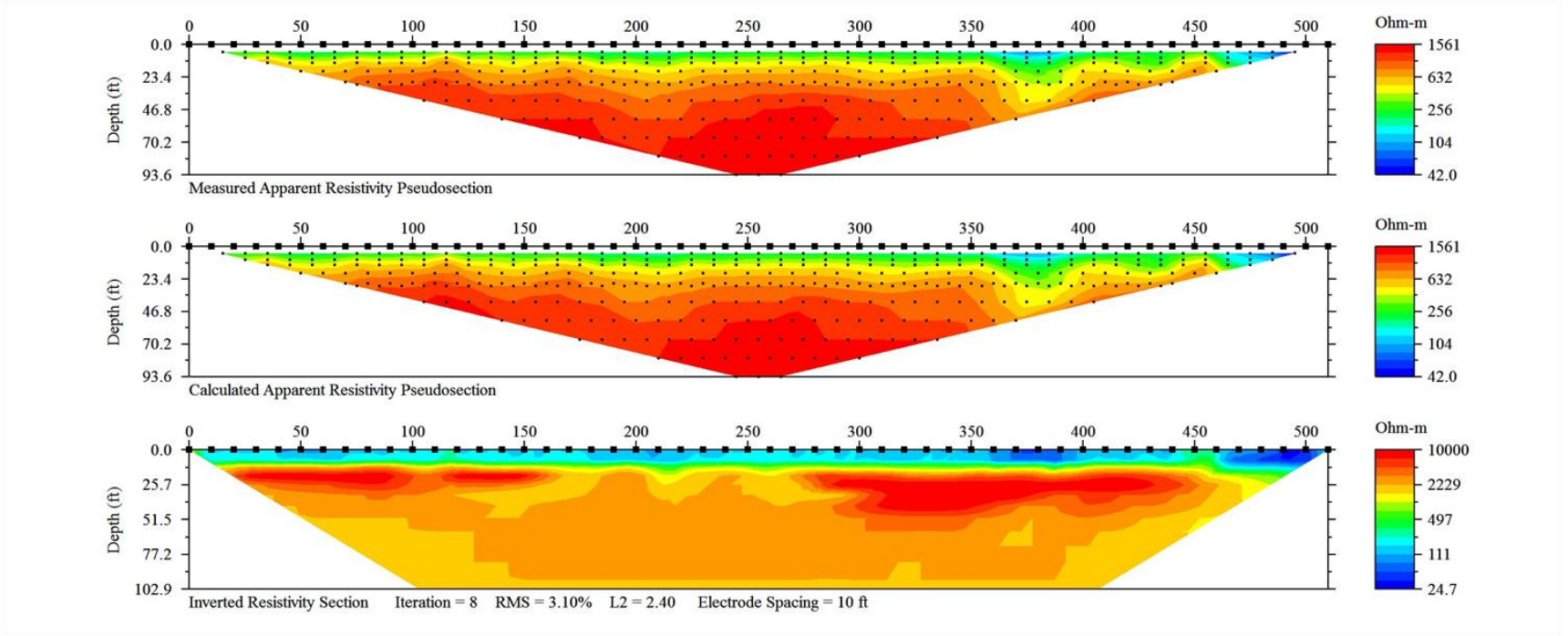

Slack's Cave line 5 Wenner survey

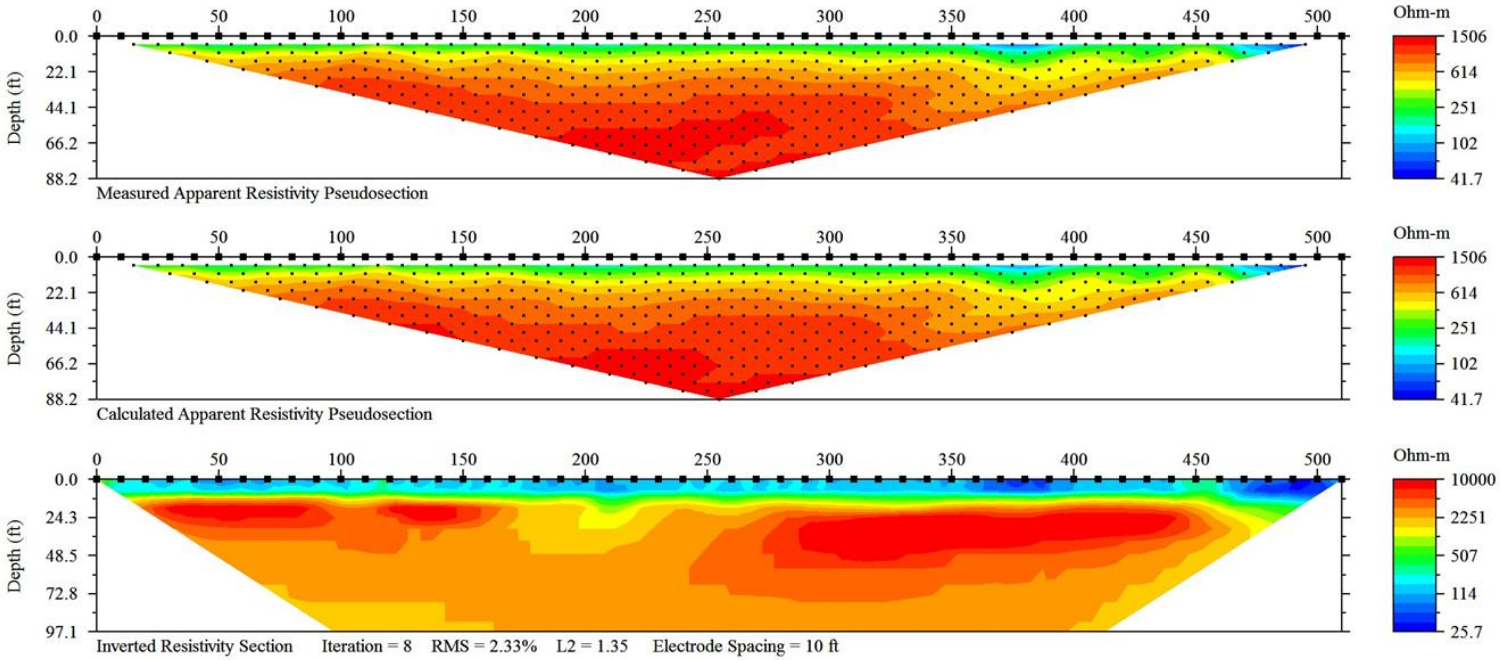

Kentucky Horse Park line 1 dipole-dipole survey

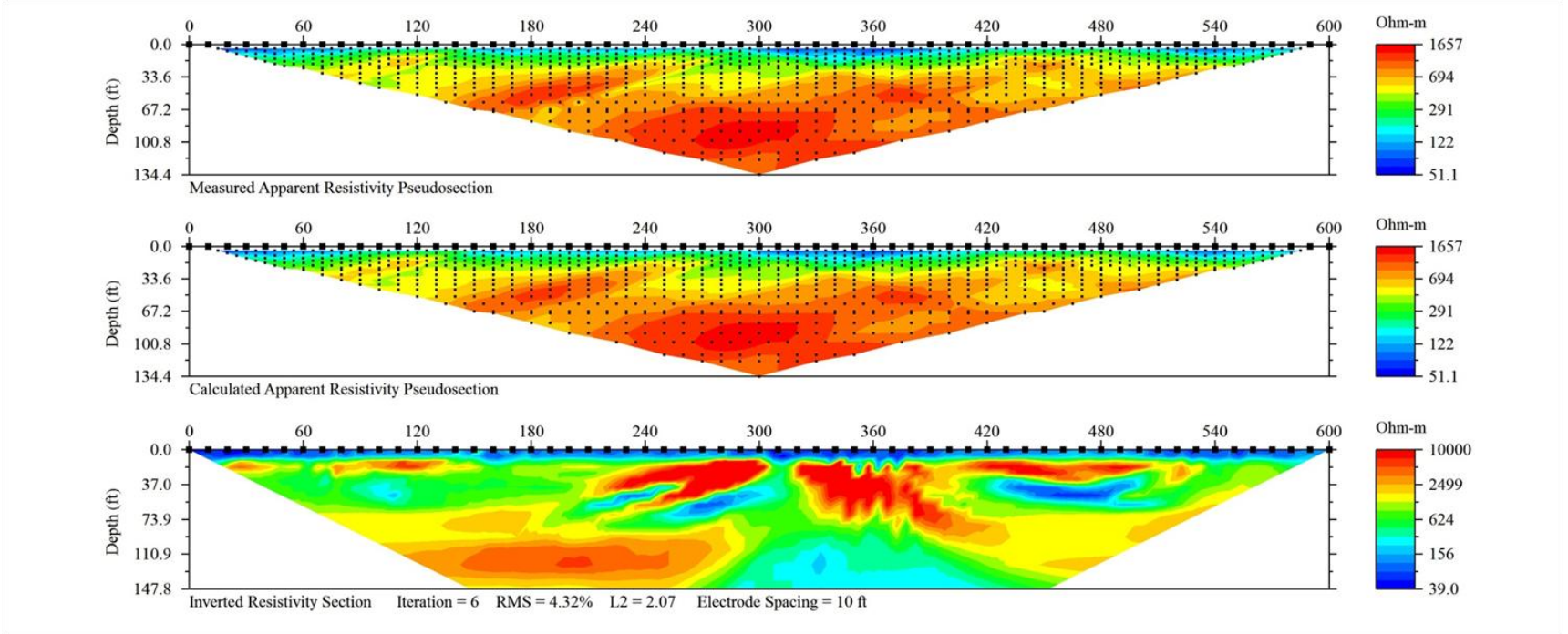

Kentucky Horse Park line 2 dipole-dipole survey

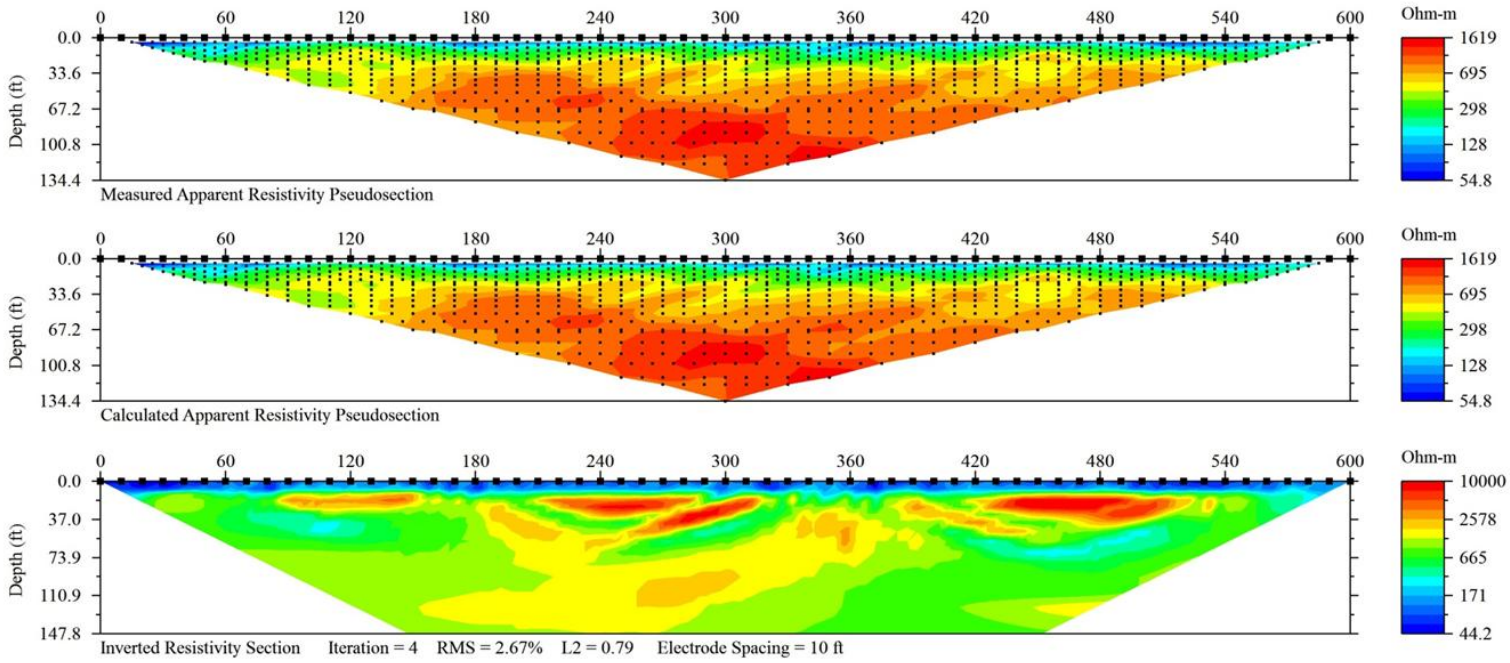

Kentucky Horse Park line 3 dipole-dipole survey

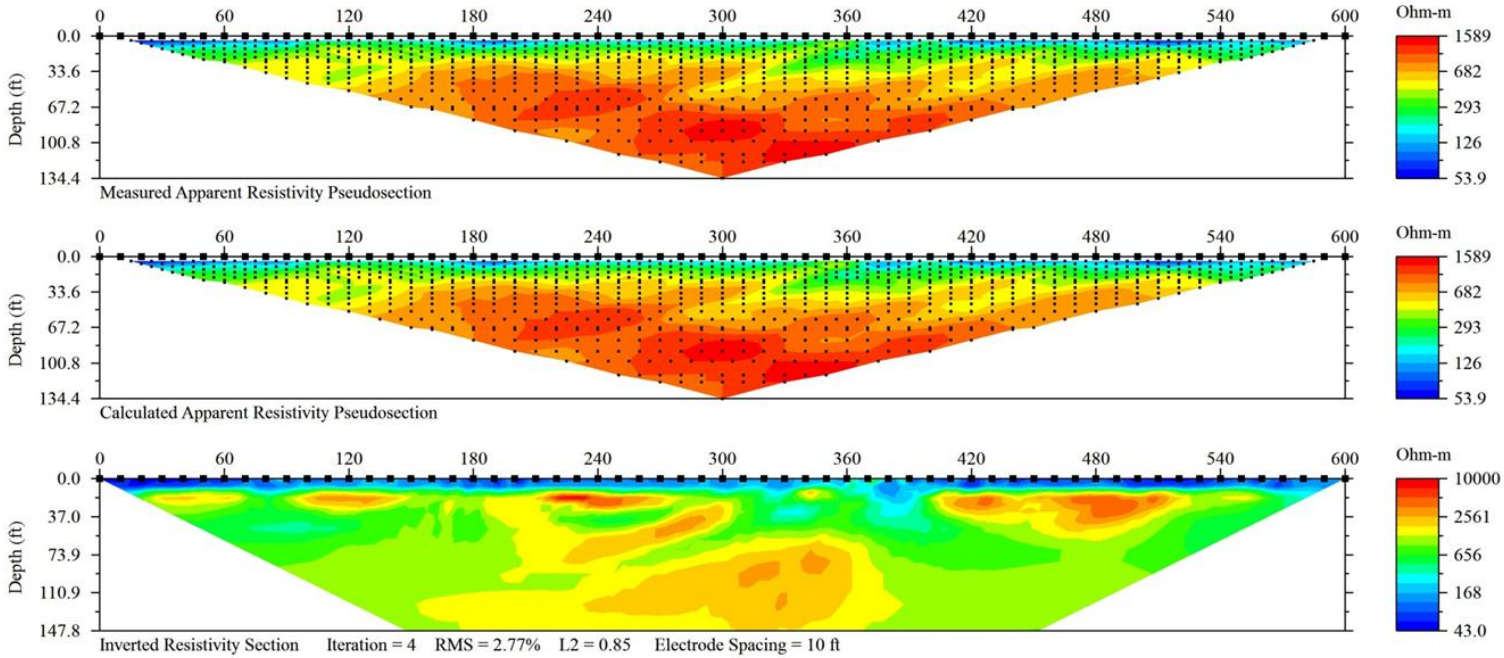

Kentucky Horse Park line 4 dipole-dipole survey

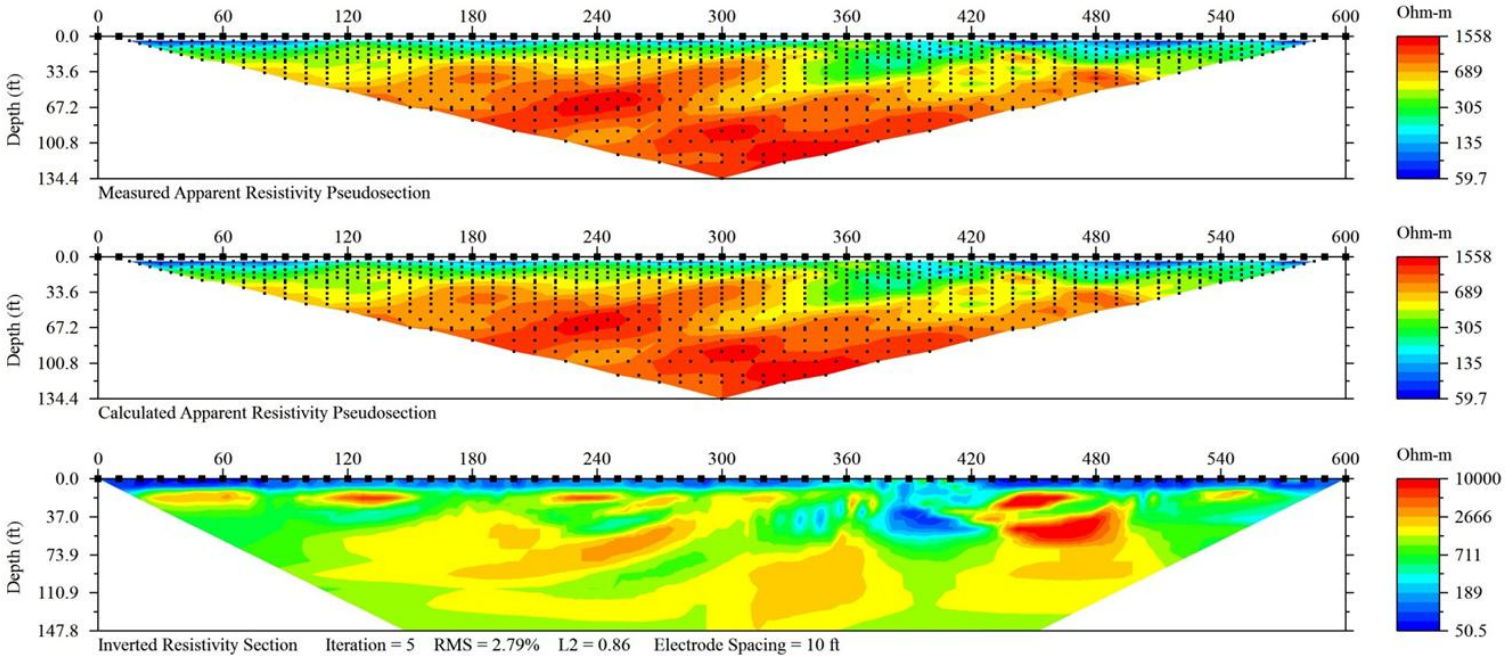

Kentucky Horse Park line 5 dipole-dipole survey

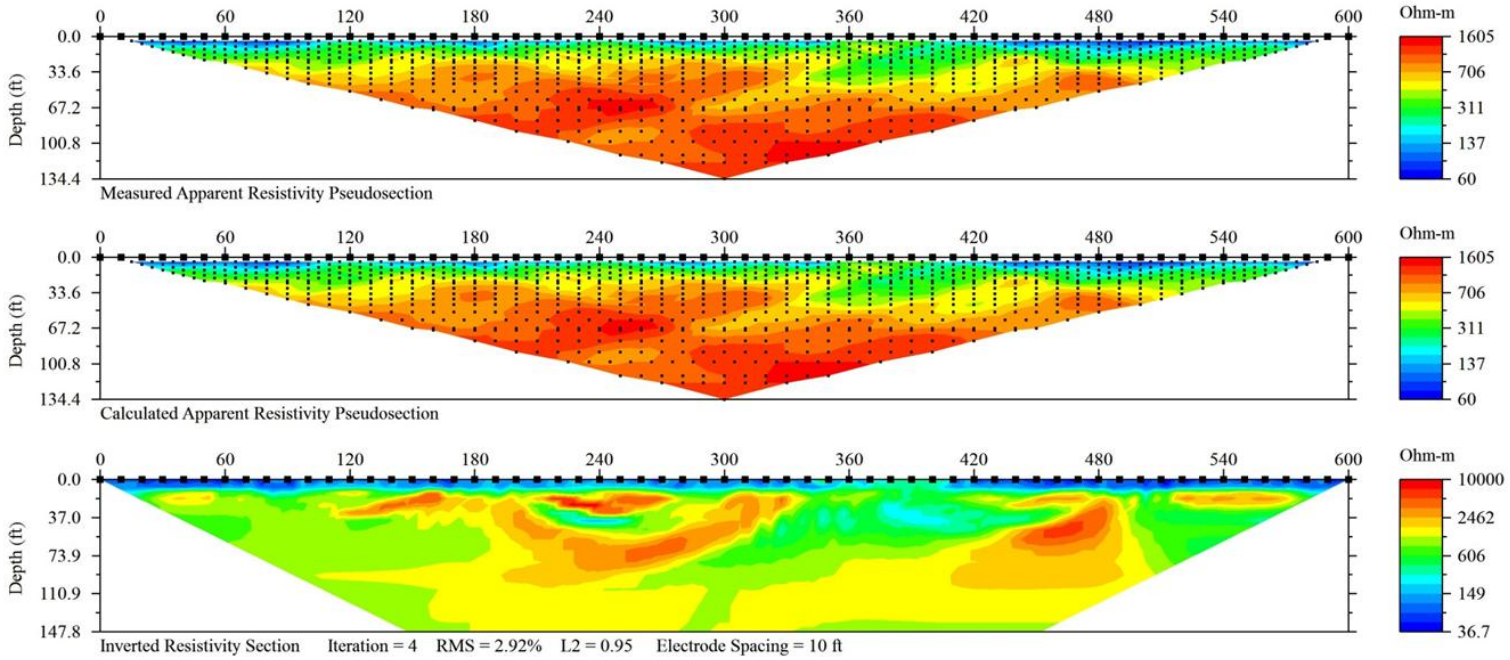

Berea Road line 1 dipole-dipole survey

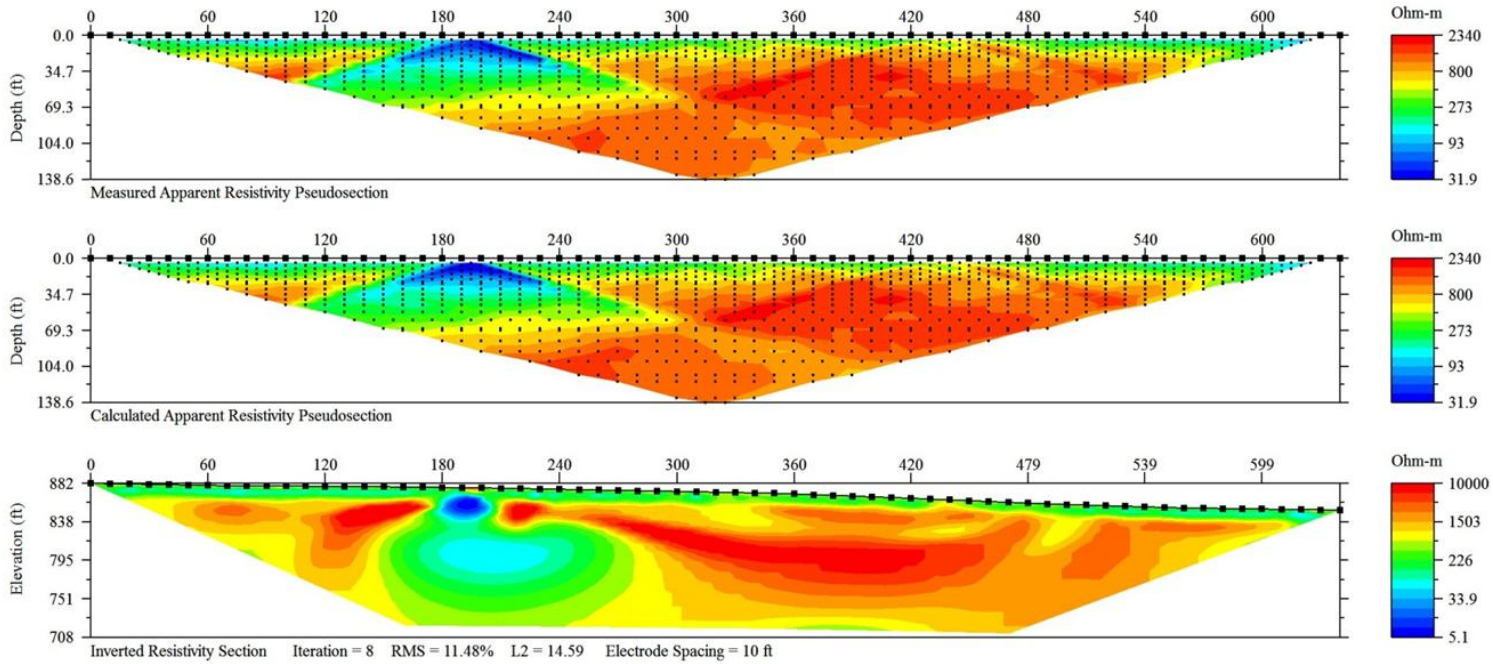

Berea Road line 1 dipole-dipole survey (first 22 electrodes removed)

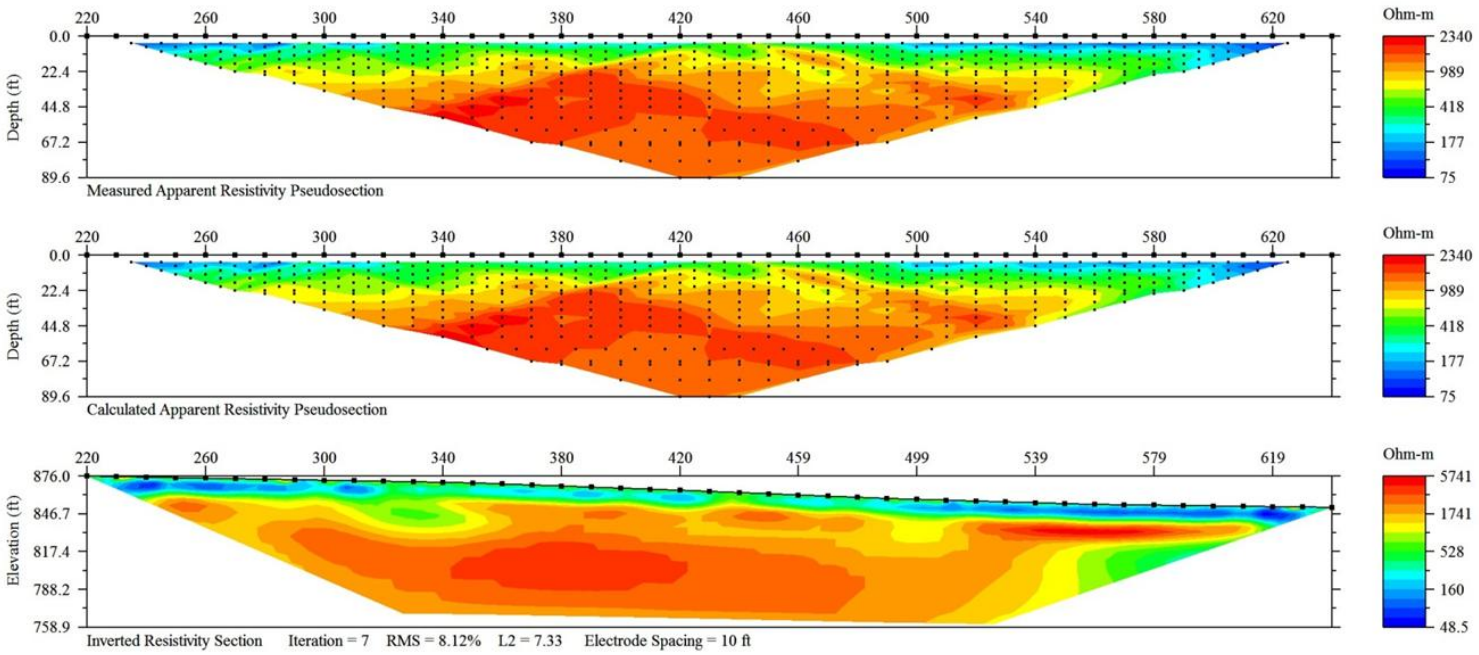

Appendix A

Section 2

Convergence curves of resistivity inversions which display the reduction in RMS error with successive iterations. No misfit data removed in any profile.

Slack's Cave line 1 dipole-dipole survey

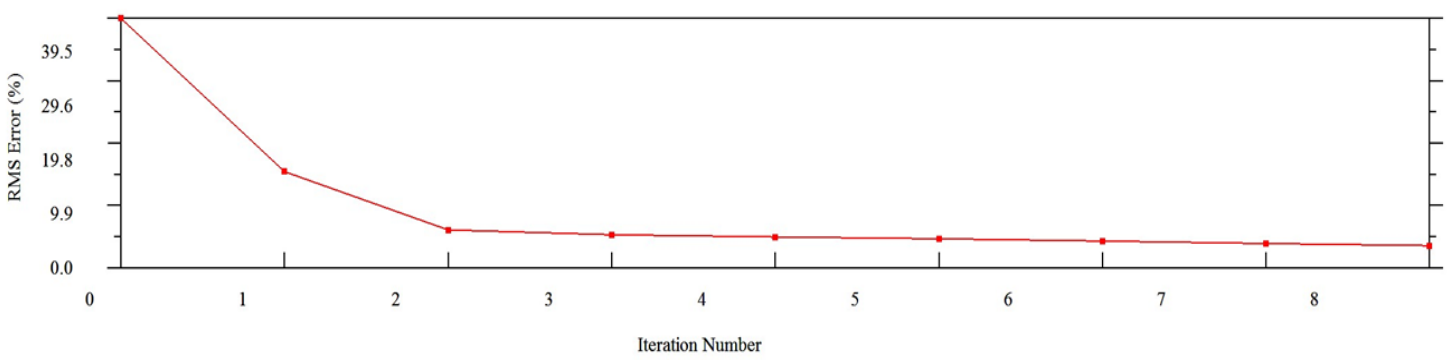

Slack's Cave line 1 Schlumberger survey

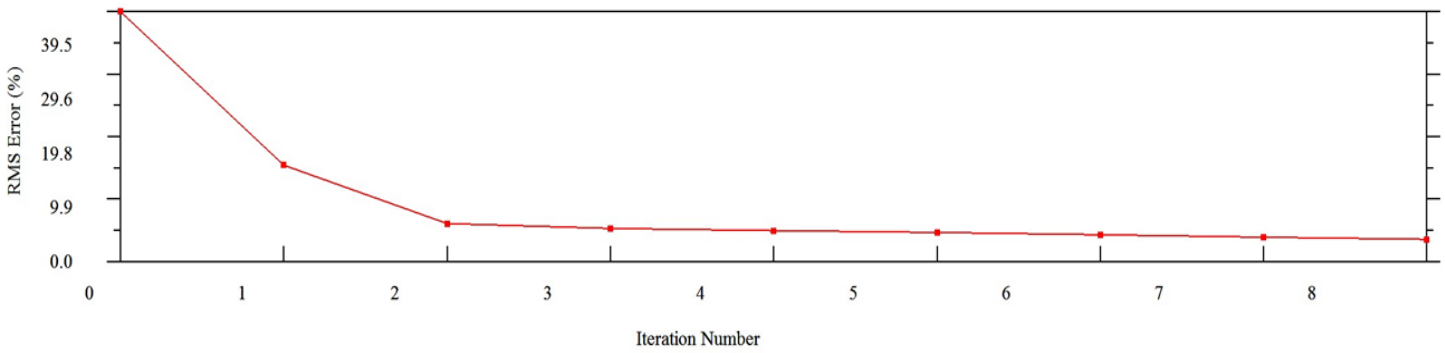

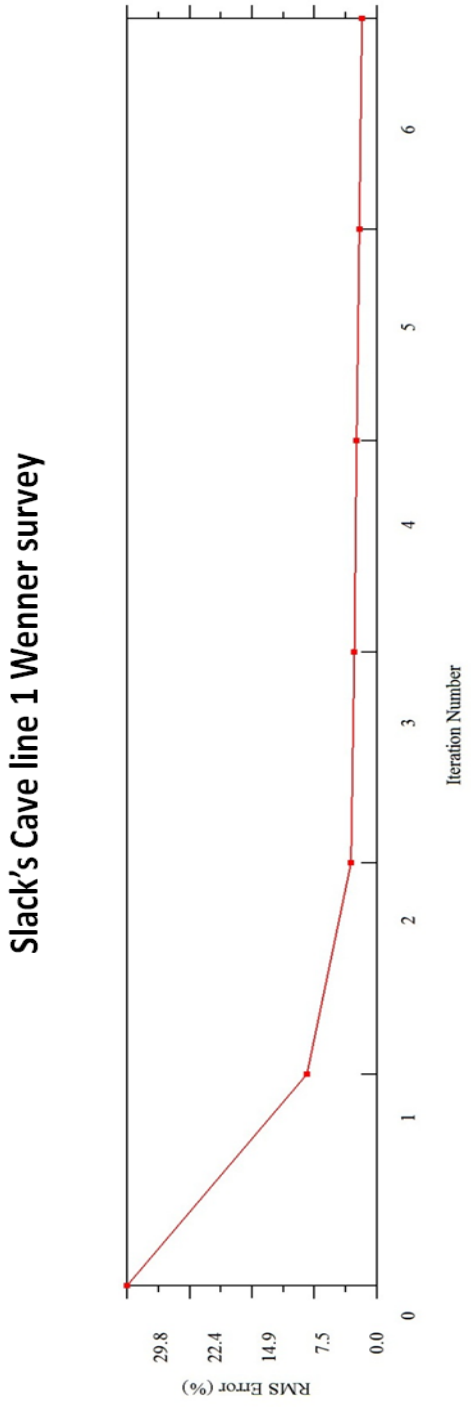
Slack's Cave line 1 Wenner survey
RMS Error (%)
29.8
22.4
14.9
7.5
0.0
0
1
2
3
4
5
6
Iteration Number

Slack's Cave line 2 dipole-dipole survey

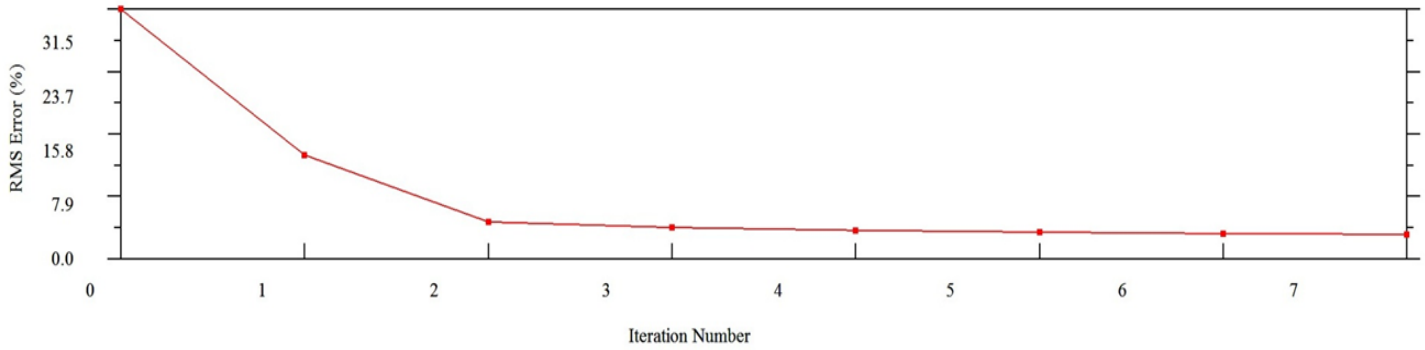

Slack's Cave line 3 dipole-dipole survey

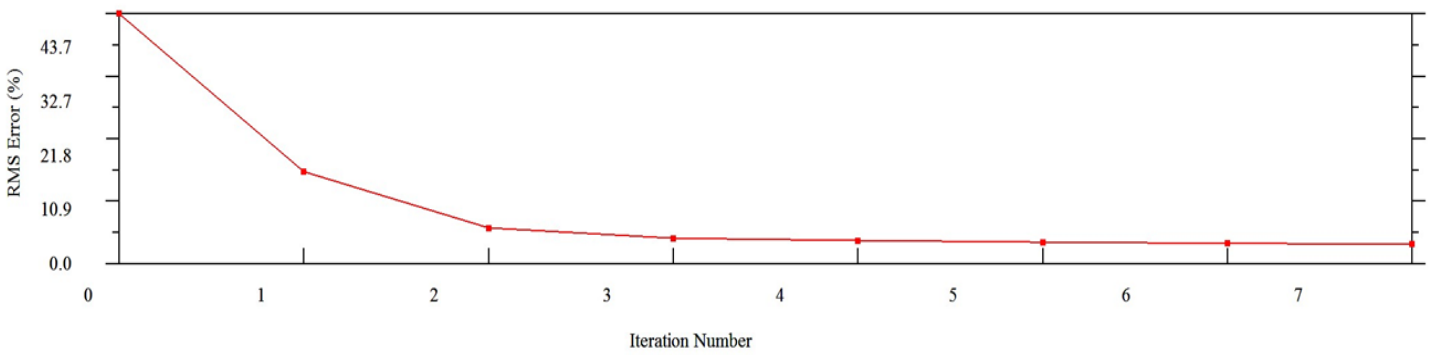

Slack's Cave line 4 dipole-dipole survey

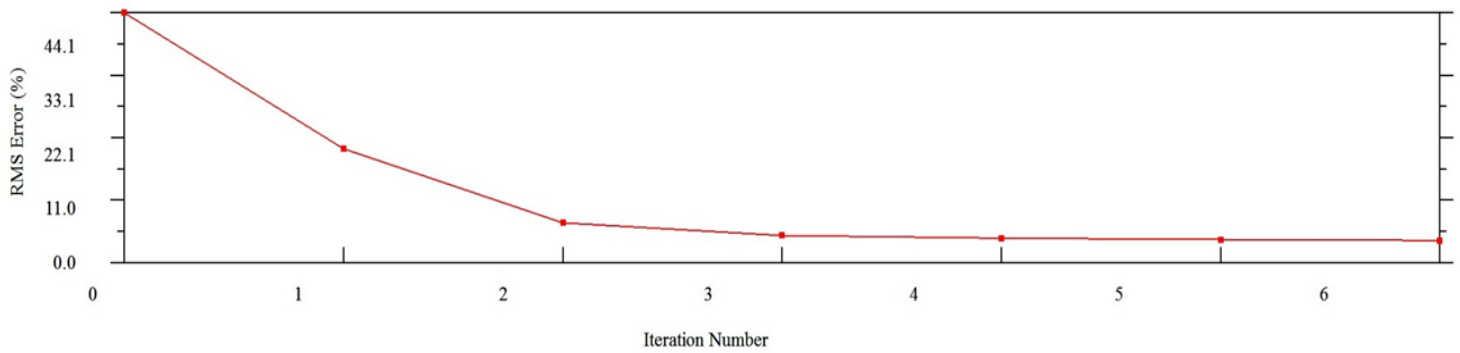

Slack's Cave line 5 dipole-dipole survey

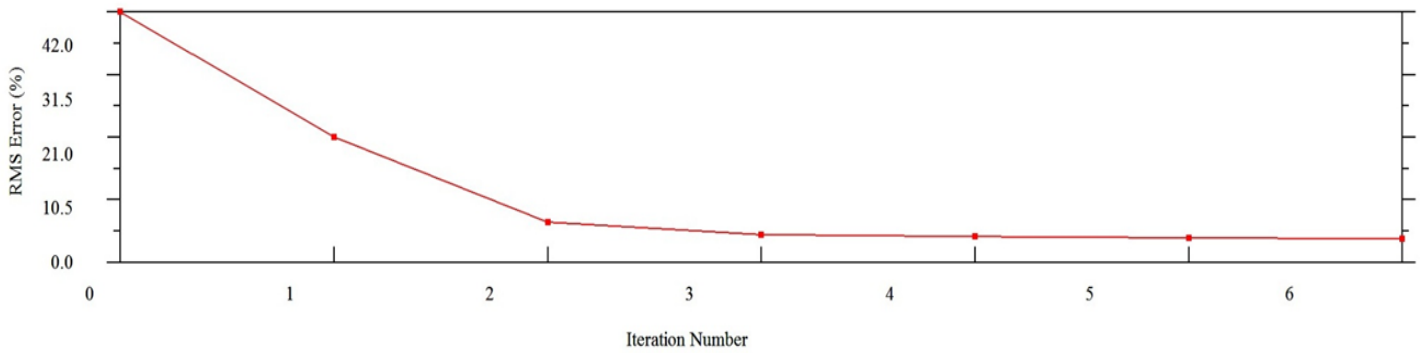

Slack's Cave line 5 Schlumberger survey

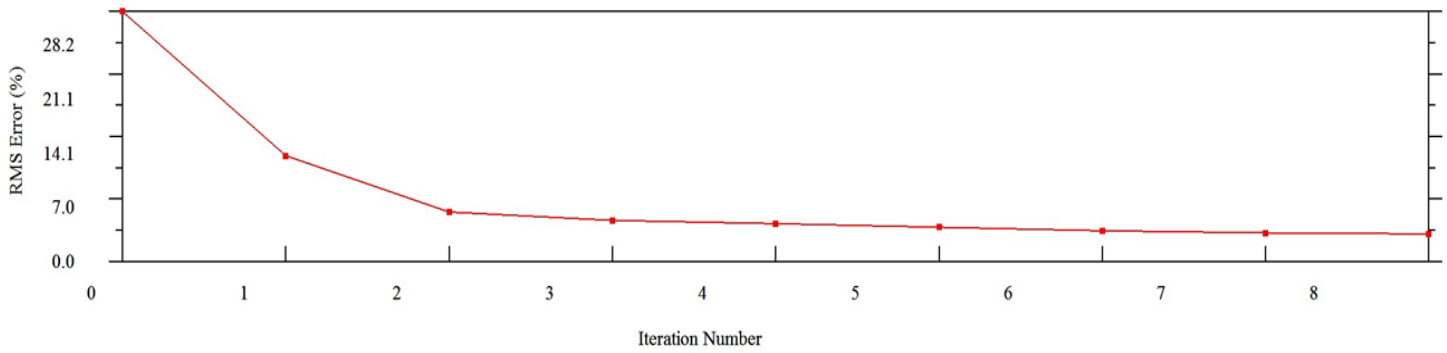

Slack's Cave line 5 Wenner survey

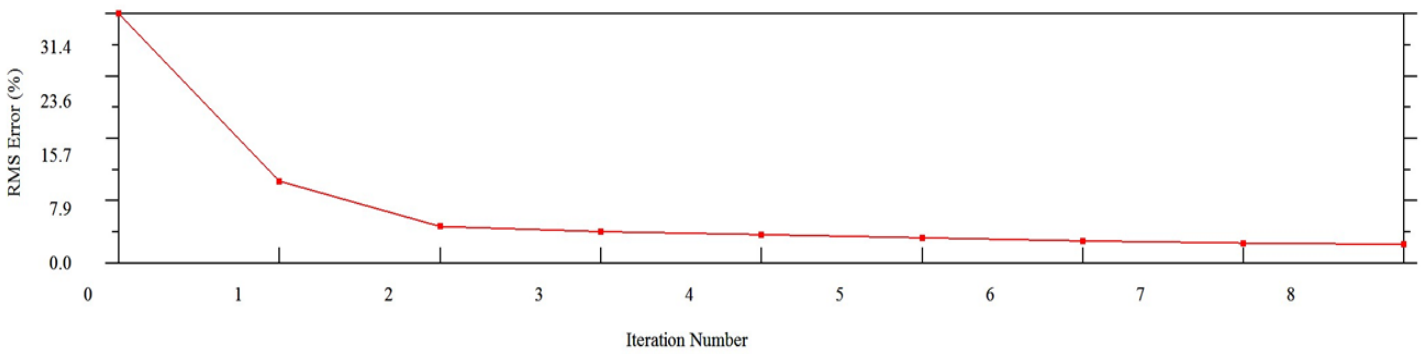

Kentucky Horse Park line 1 dipole-dipole survey

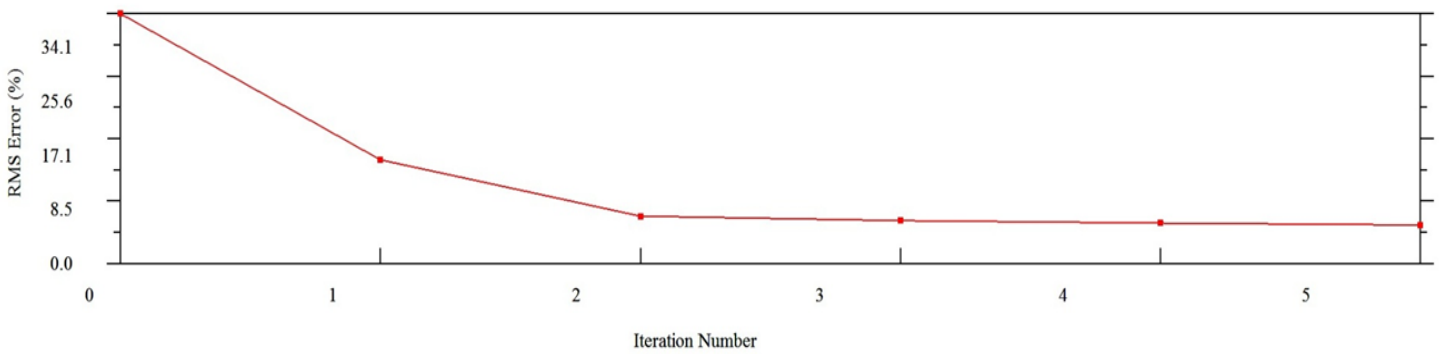

Kentucky Horse Park line 2 dipole-dipole survey

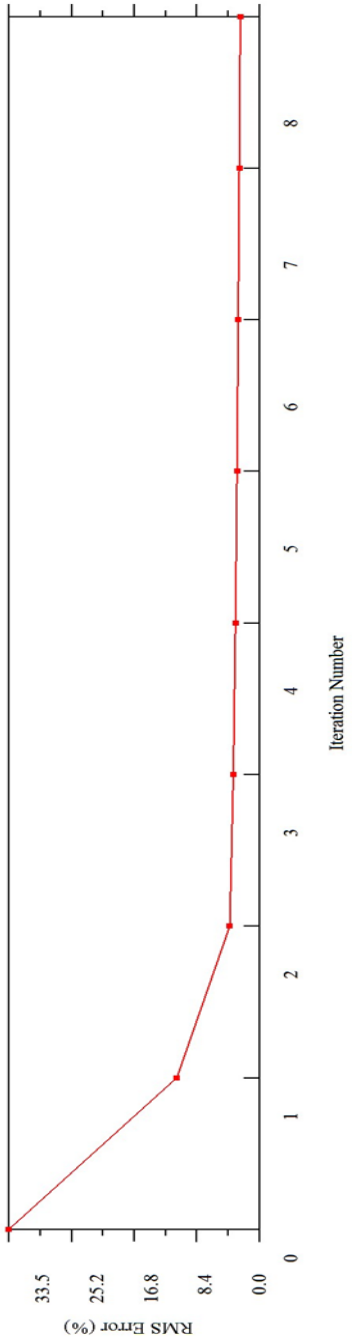

Kentucky Horse Park line 3 dipole-dipole survey

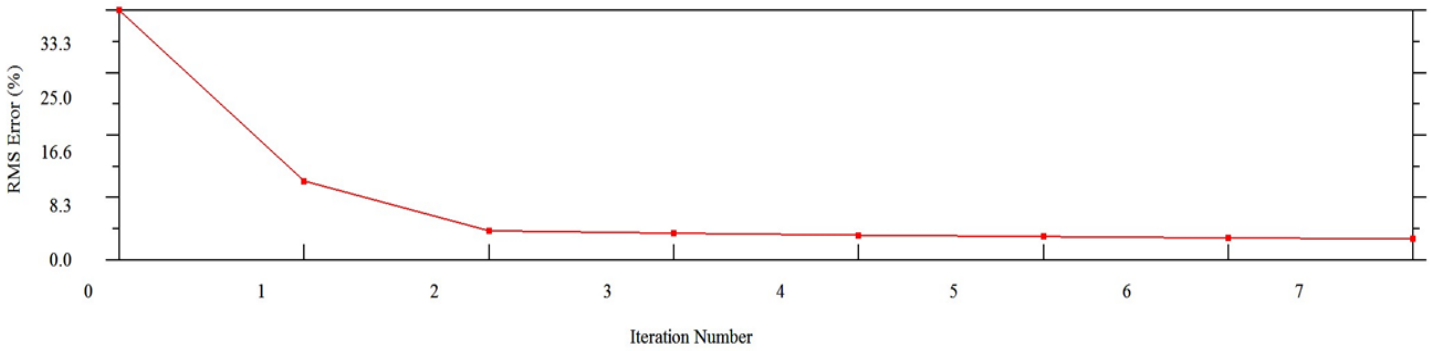

Kentucky Horse Park line 4 dipole-dipole survey

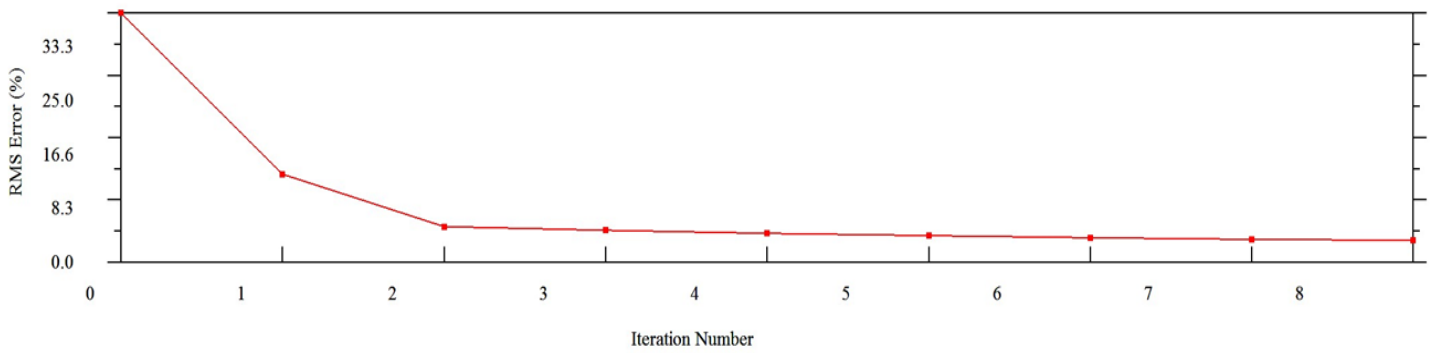

Kentucky Horse Park line 5 dipole-dipole survey

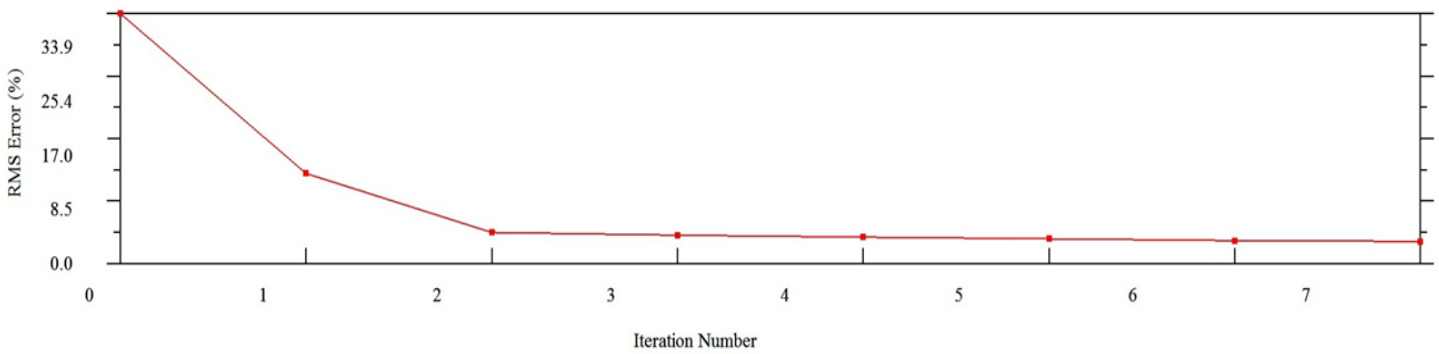

Appendix A

Section 3

Crossplots of measured vs. apparent resistivity data. No misfit data removed in any profile.

Slack's Cave line 1 dipole-dipole survey

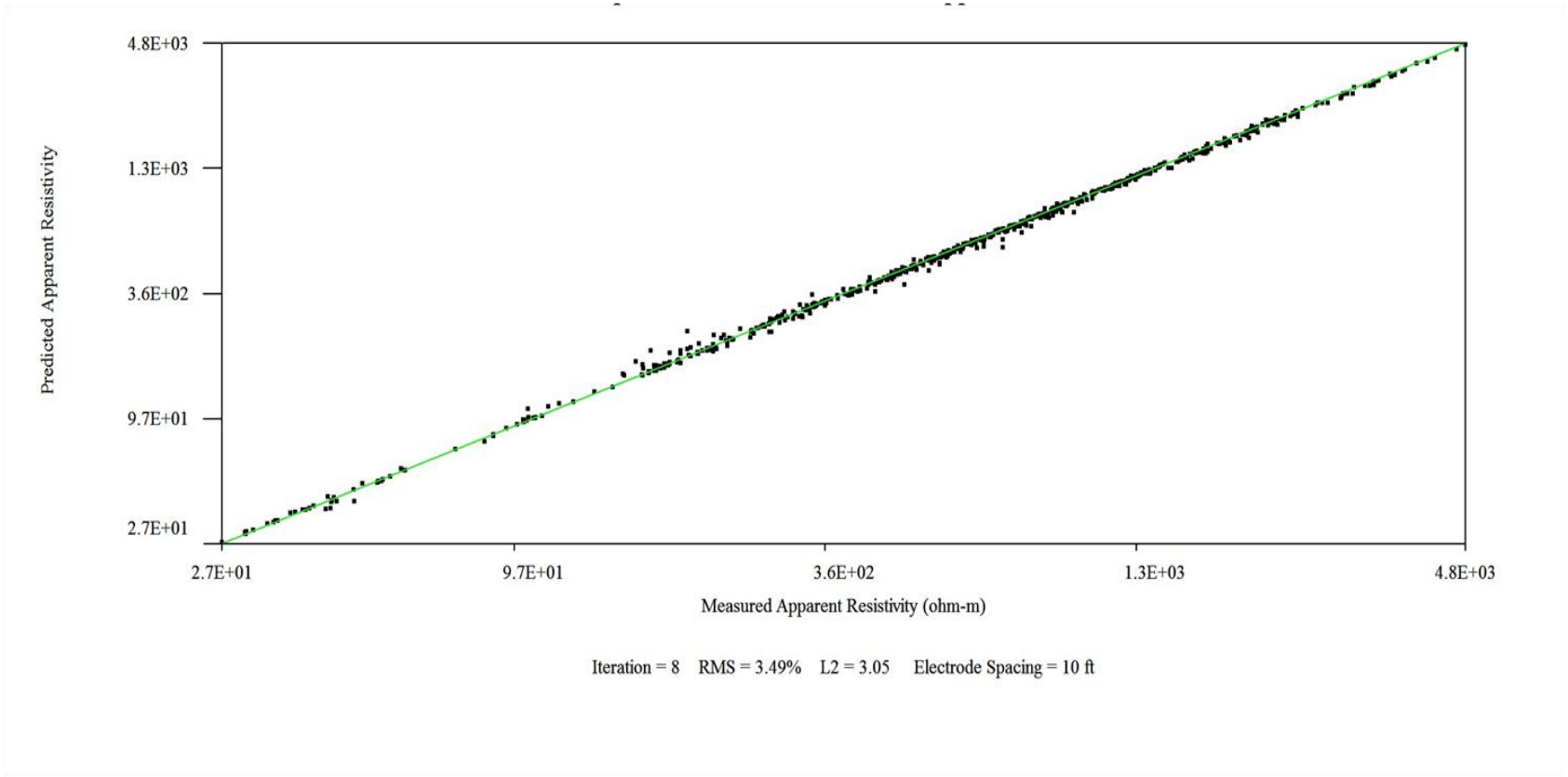

Slack's Cave line 1 Schlumberger survey

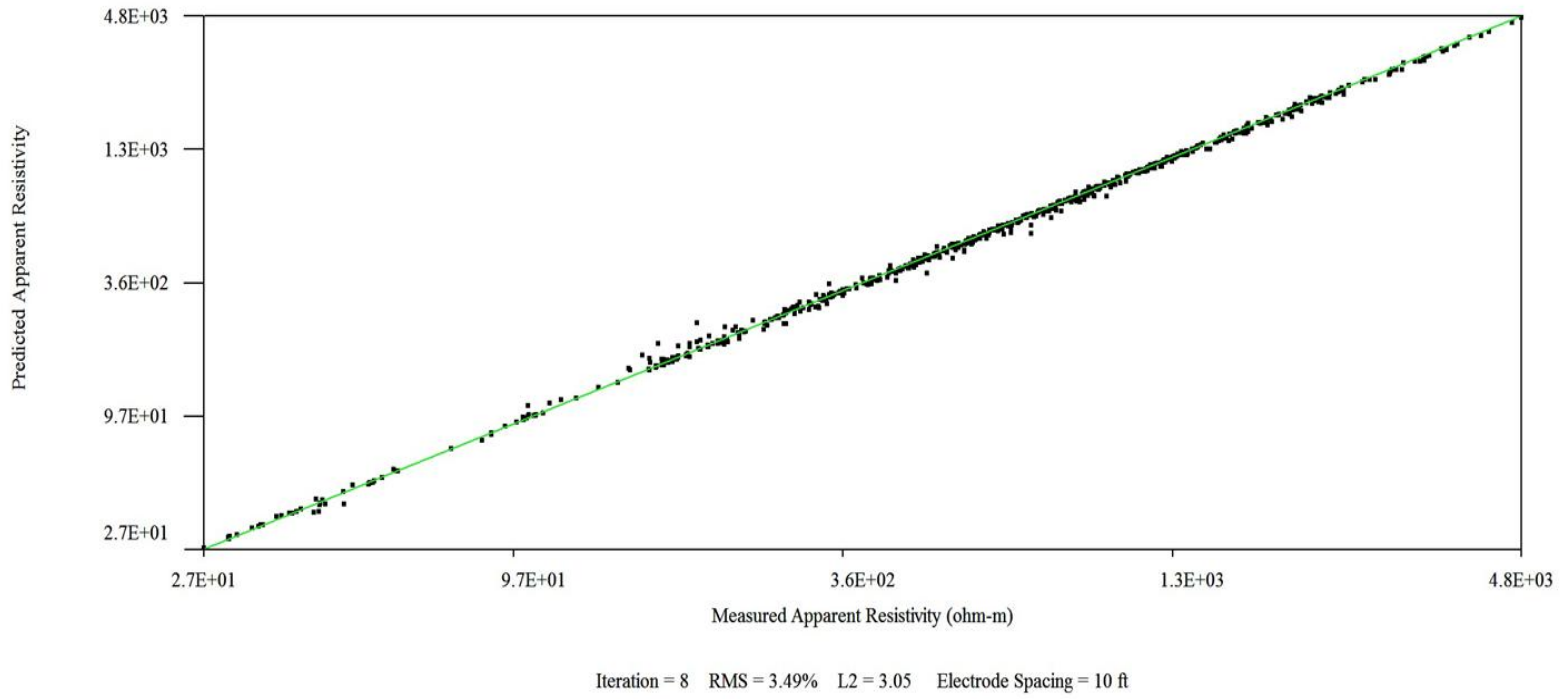

Slack's Cave line 1 Wenner survey

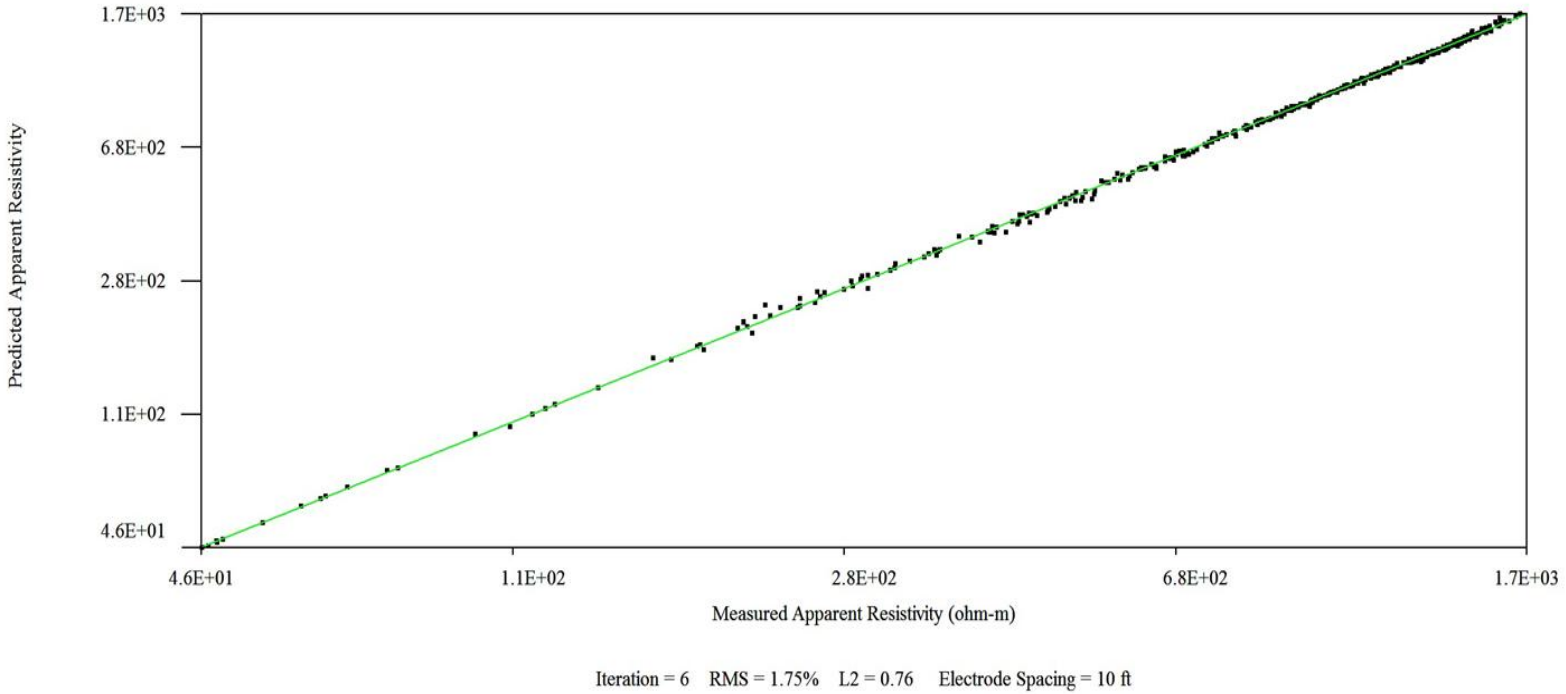

Slack's Cave line 2 dipole-dipole survey

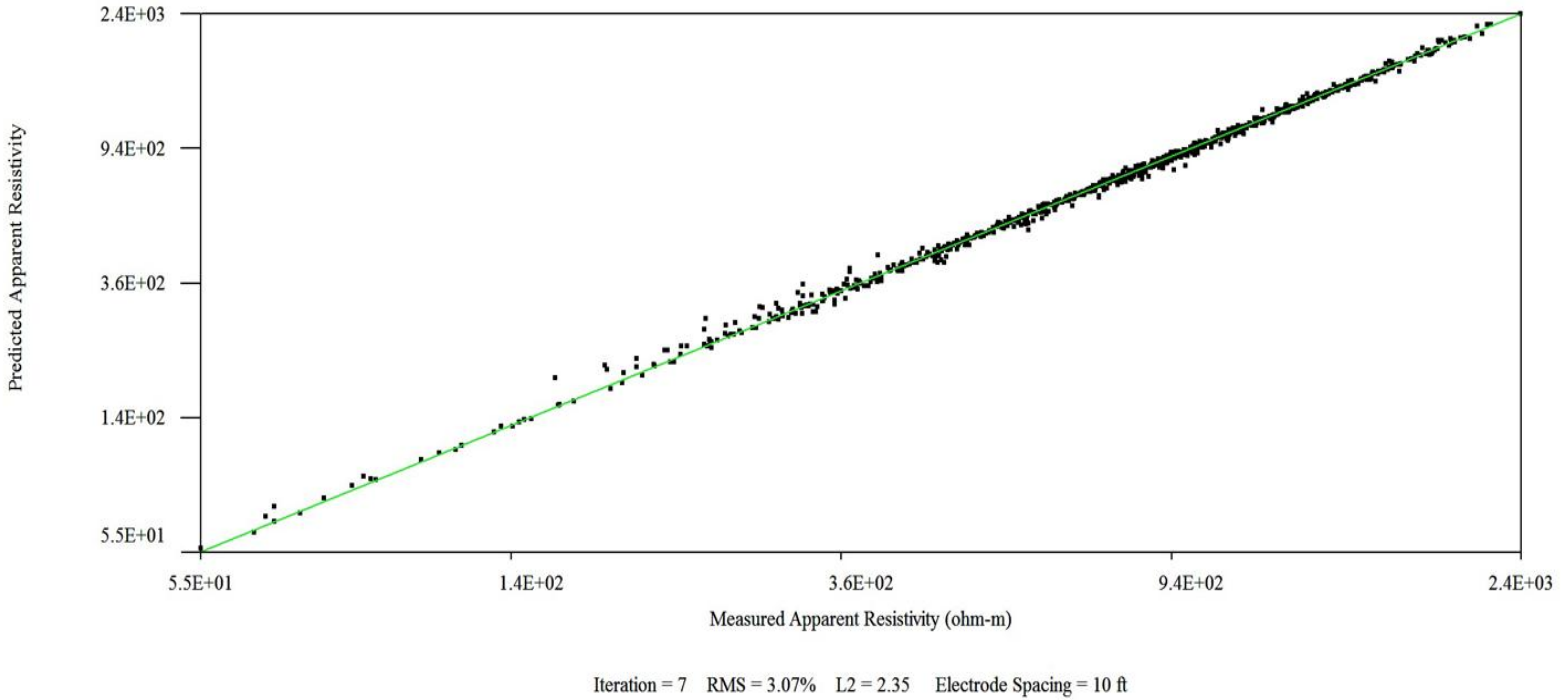

Slack's Cave line 3 dipole-dipole survey

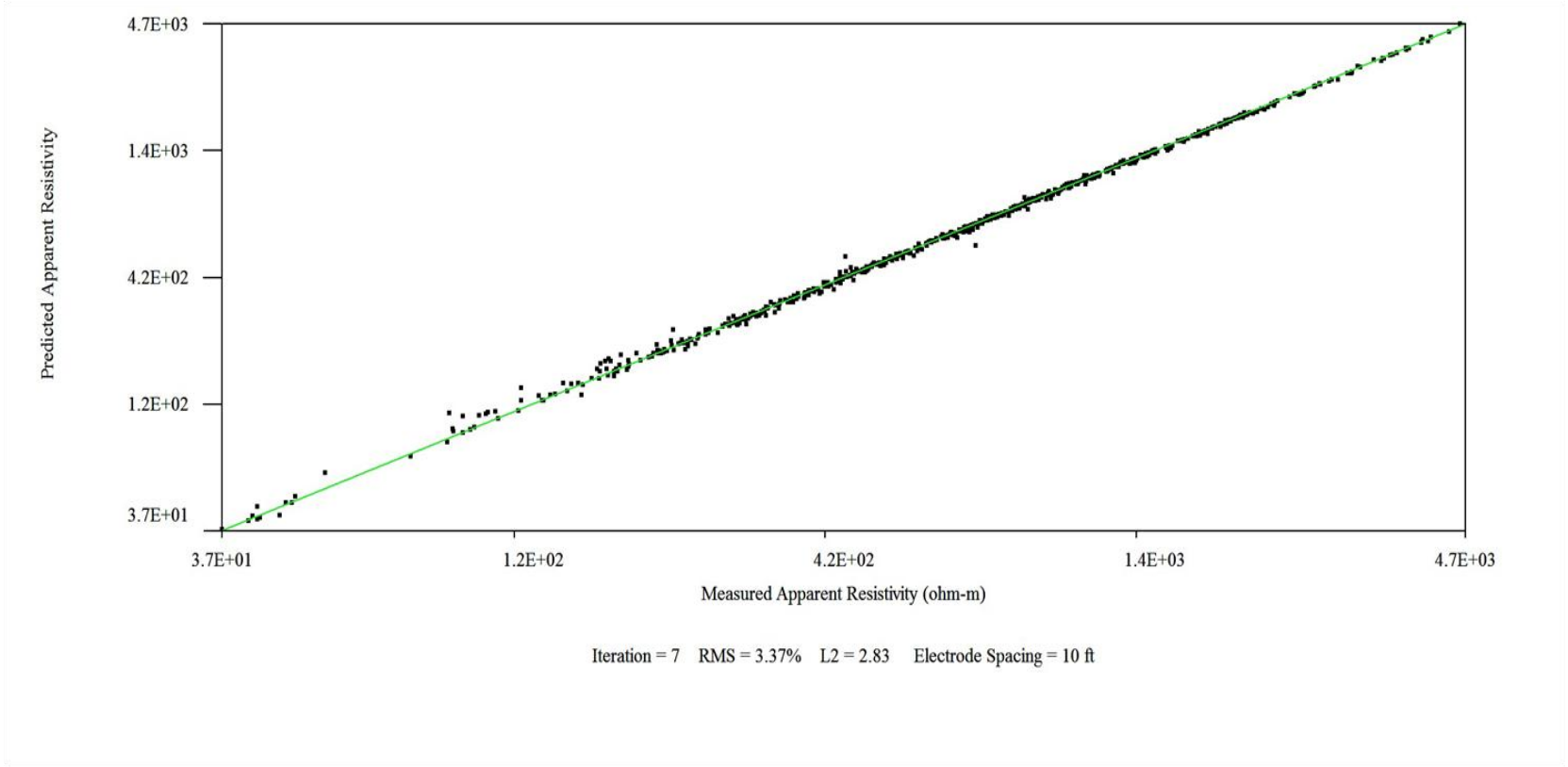

Slack's Cave line 4 dipole-dipole survey

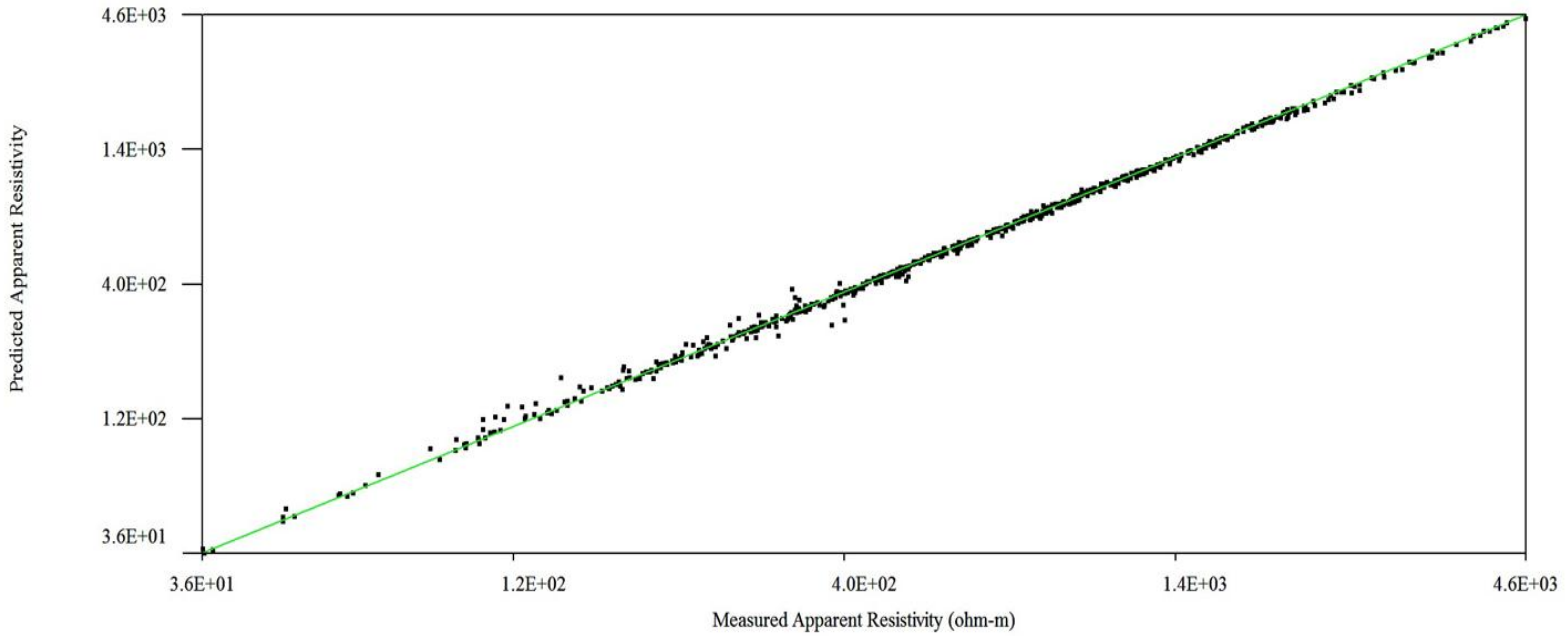

Slack's Cave line 5 dipole-dipole survey

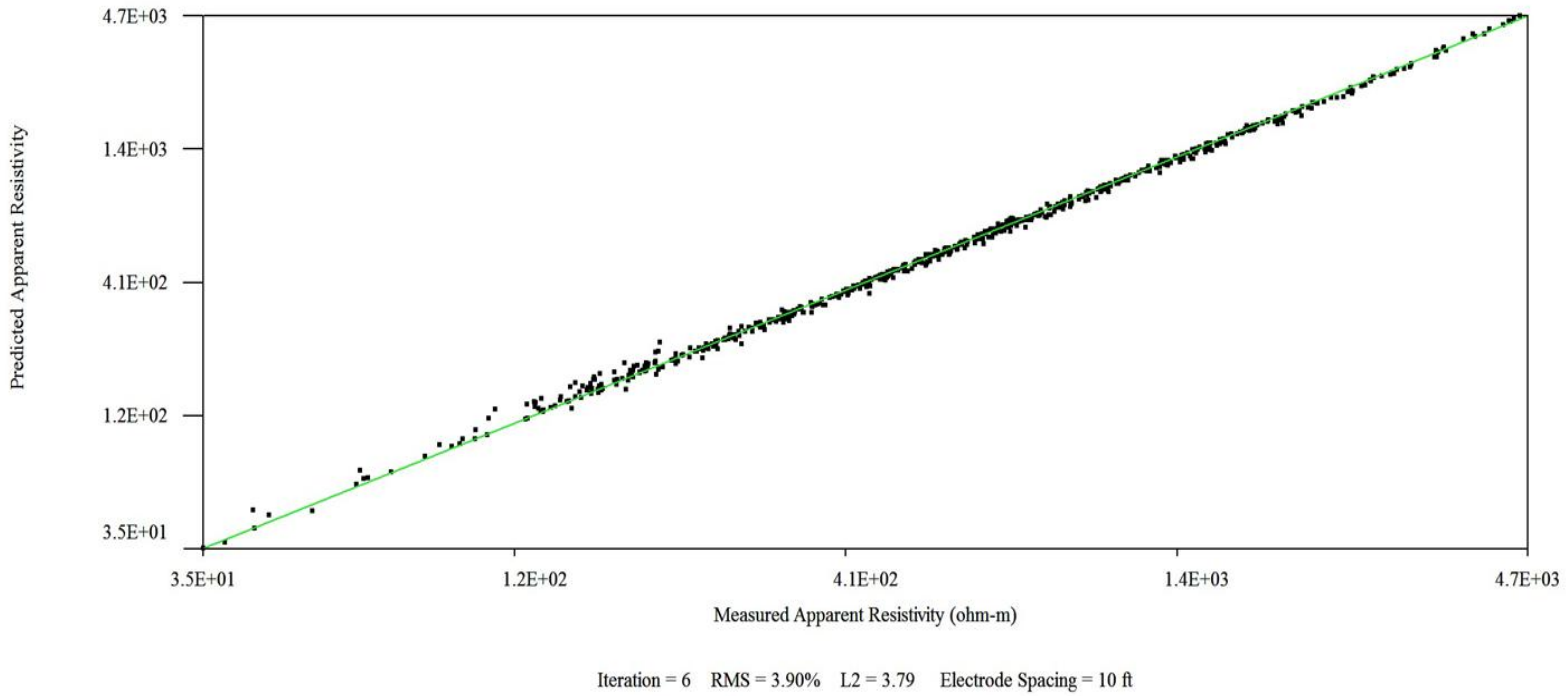

Slack's Cave line 5 Schlumberger survey

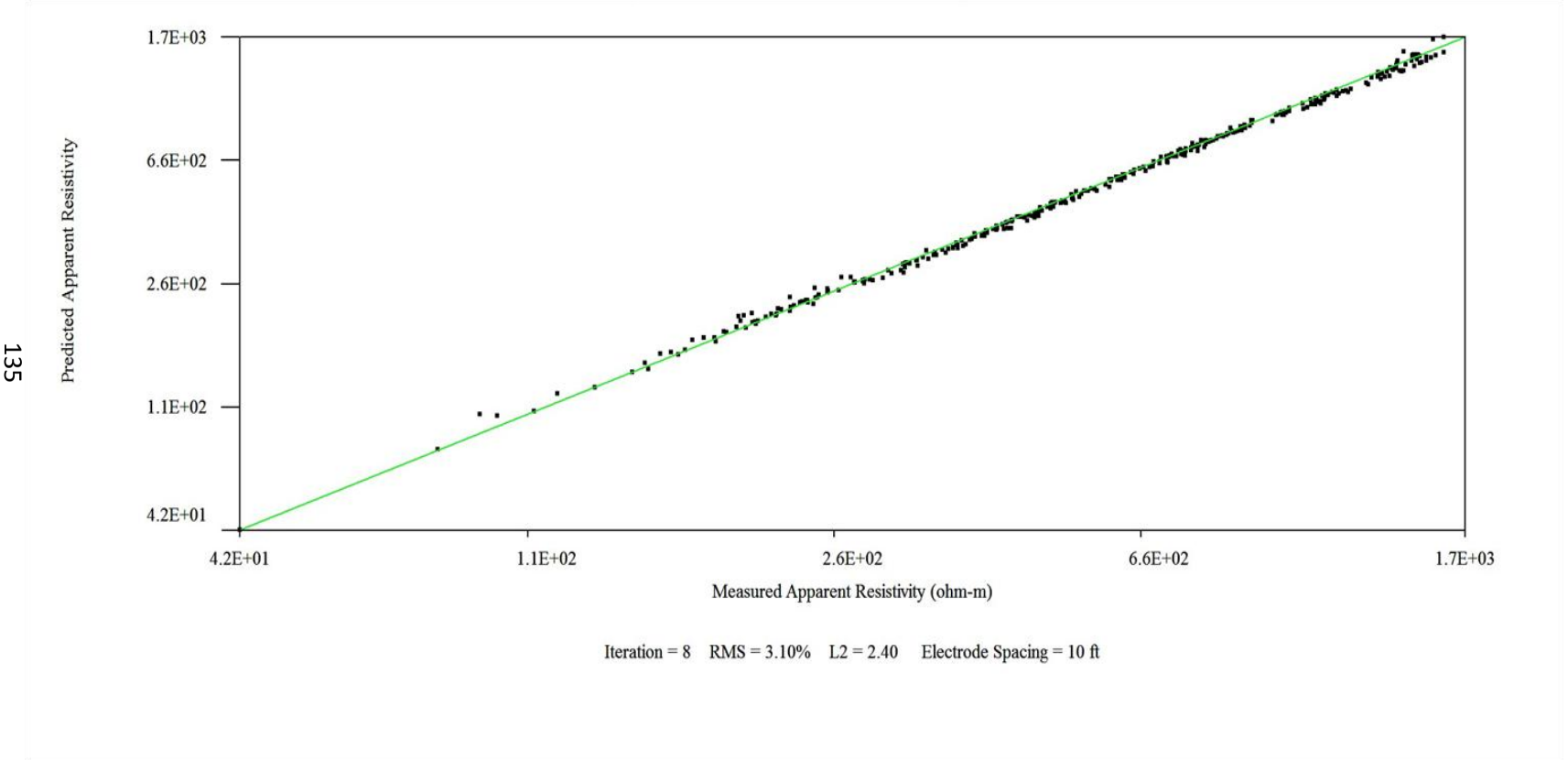

Slack's Cave line 5 Wenner survey

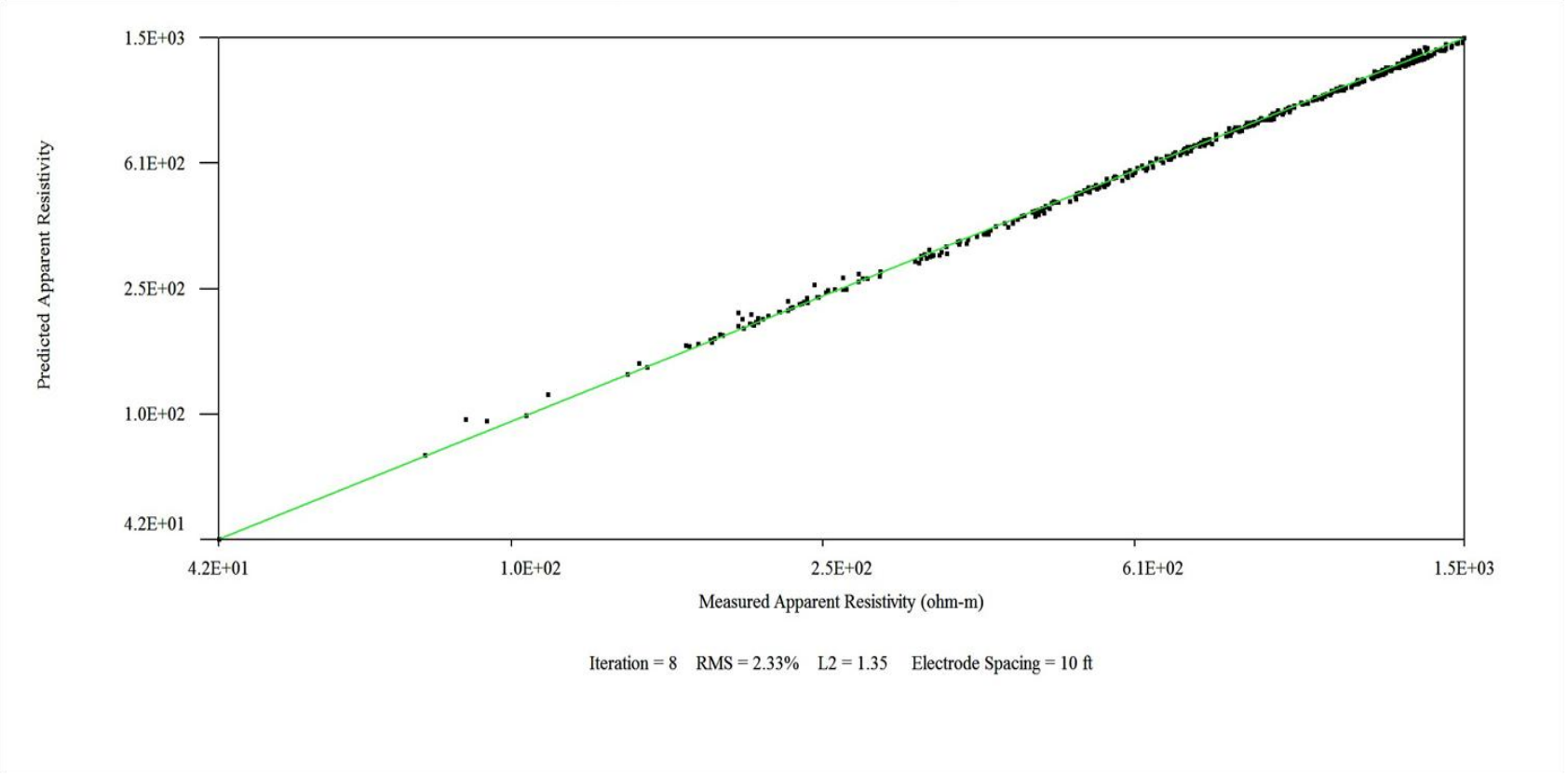

Kentucky Horse Park line 1 dipole-dipole survey

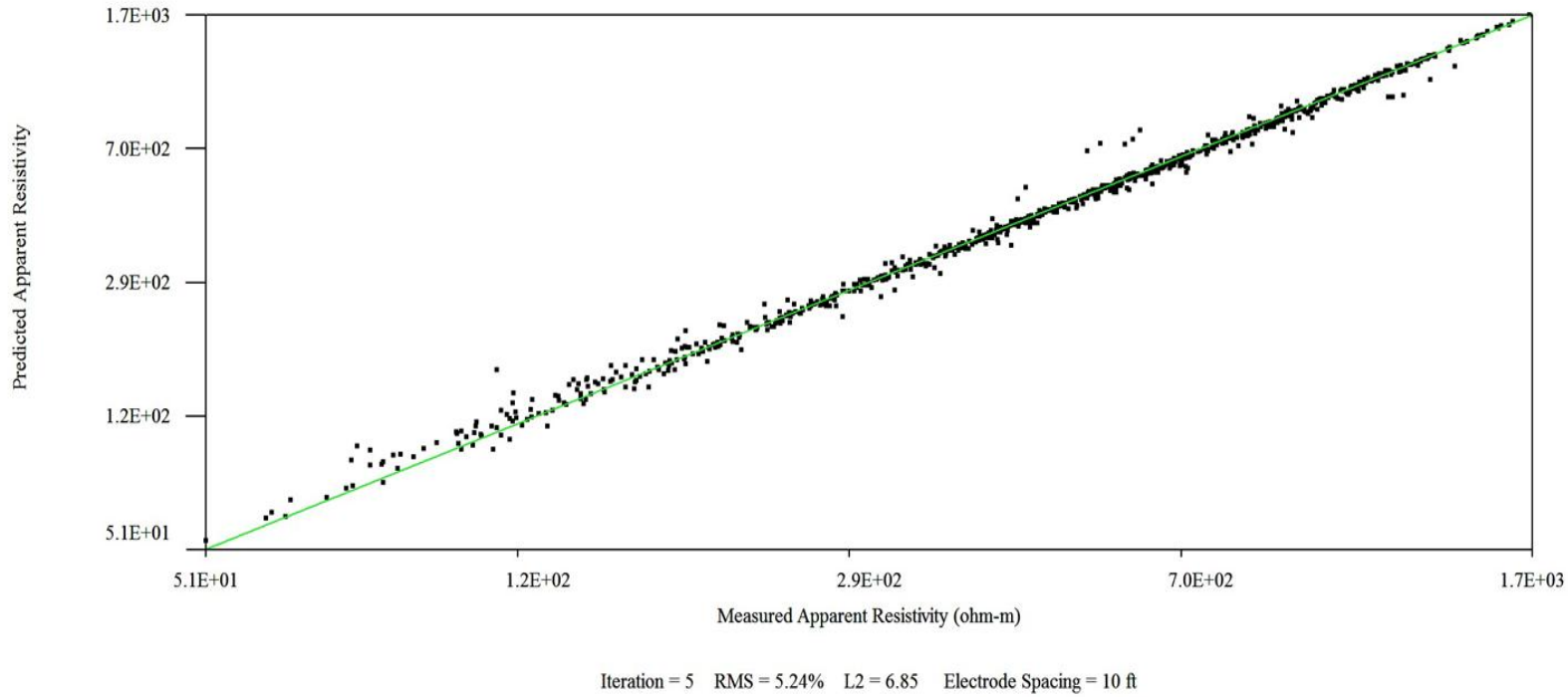

Kentucky Horse Park line 2 dipole-dipole survey

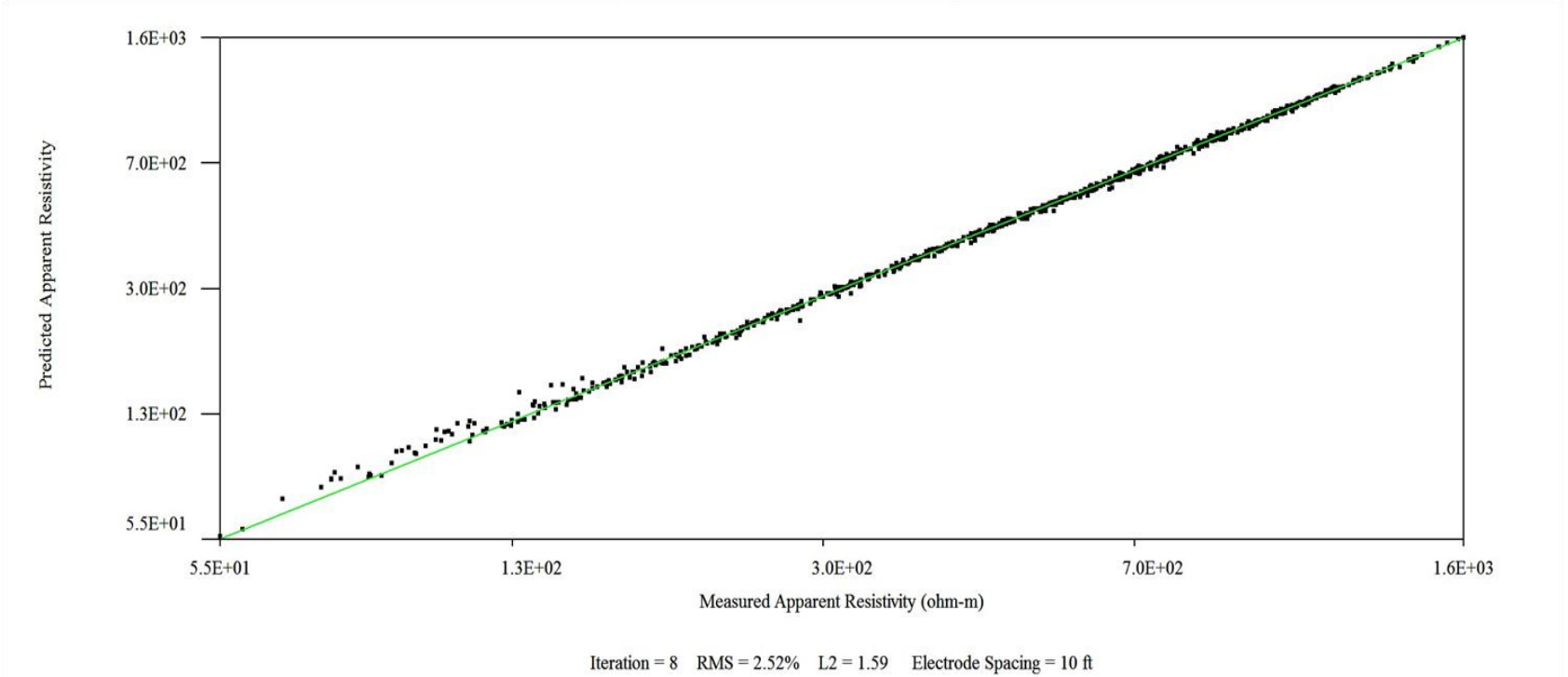

Kentucky Horse Park line 3 dipole-dipole survey

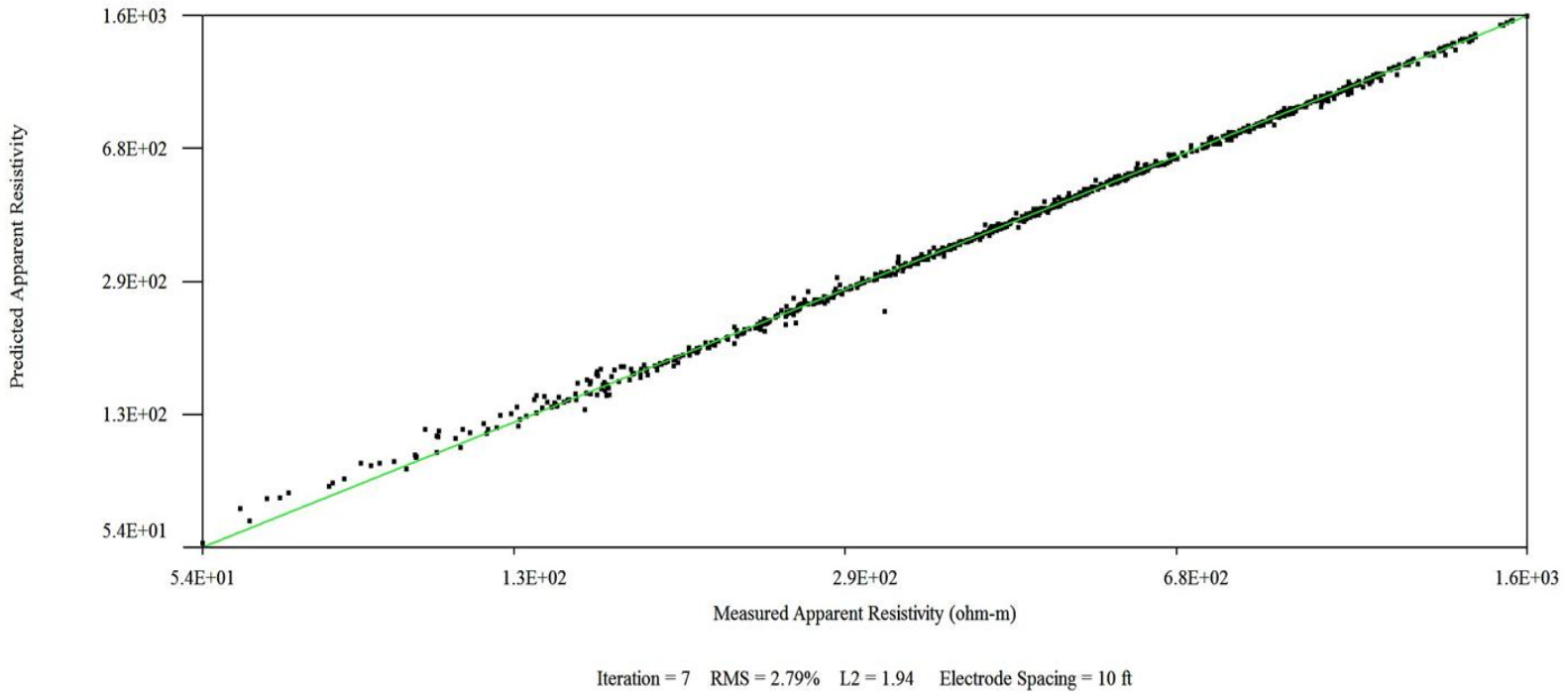

Kentucky Horse Park line 4 dipole-dipole survey

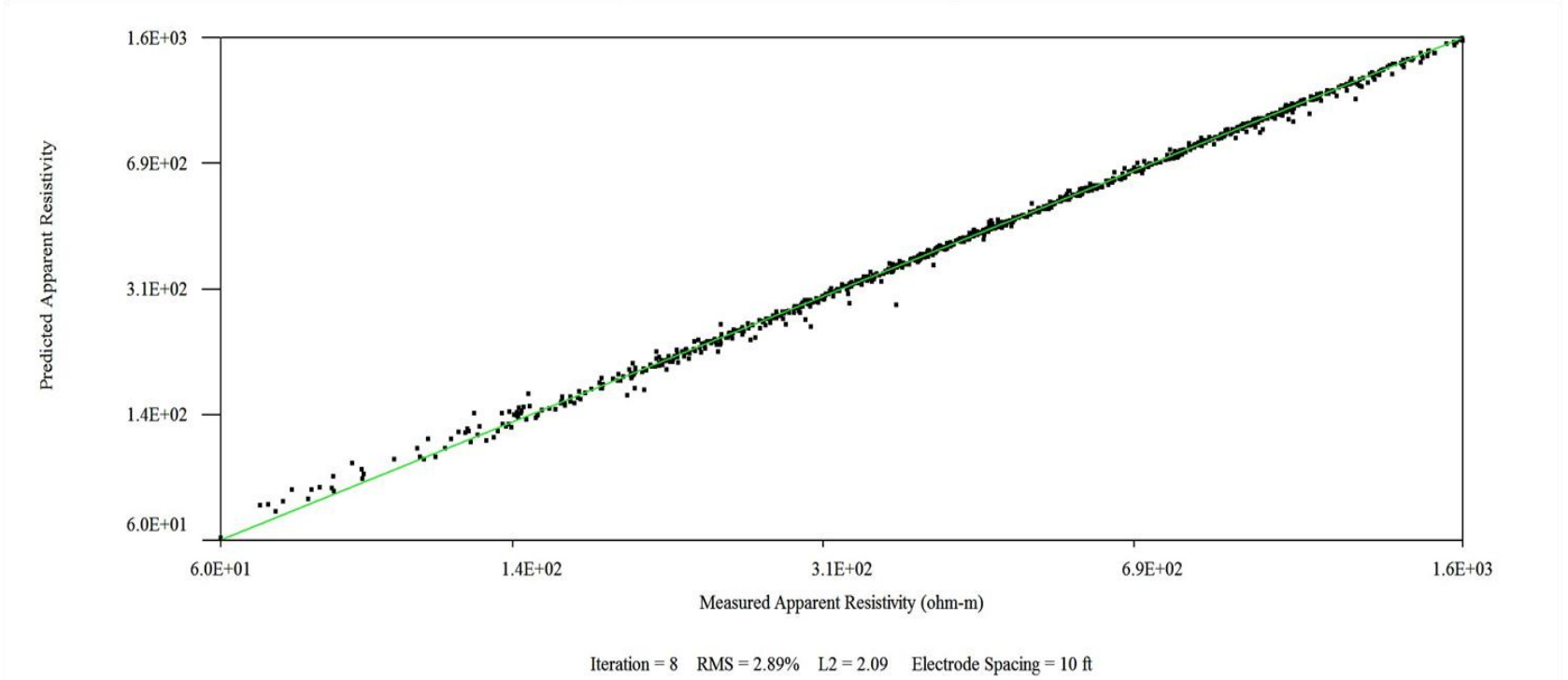

Kentucky Horse Park line 5 dipole-dipole survey

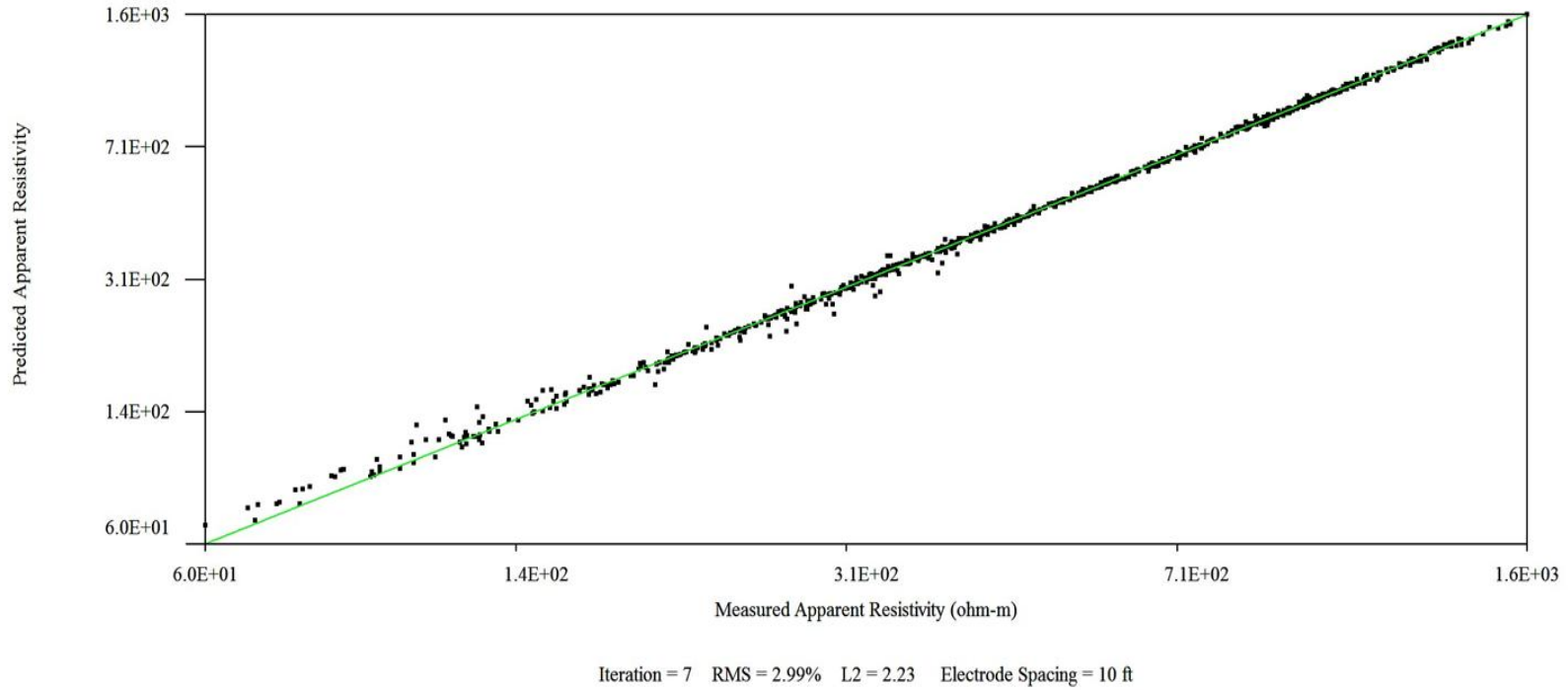

Iteration = 7 RMS = 2.99% L2 = 2.23 Electrode Spacing = 10 ft

APPENDIX B

Appendix B

Raw seismic refraction field files.

Slack's Cave line 1 P-Wave refraction shot 1

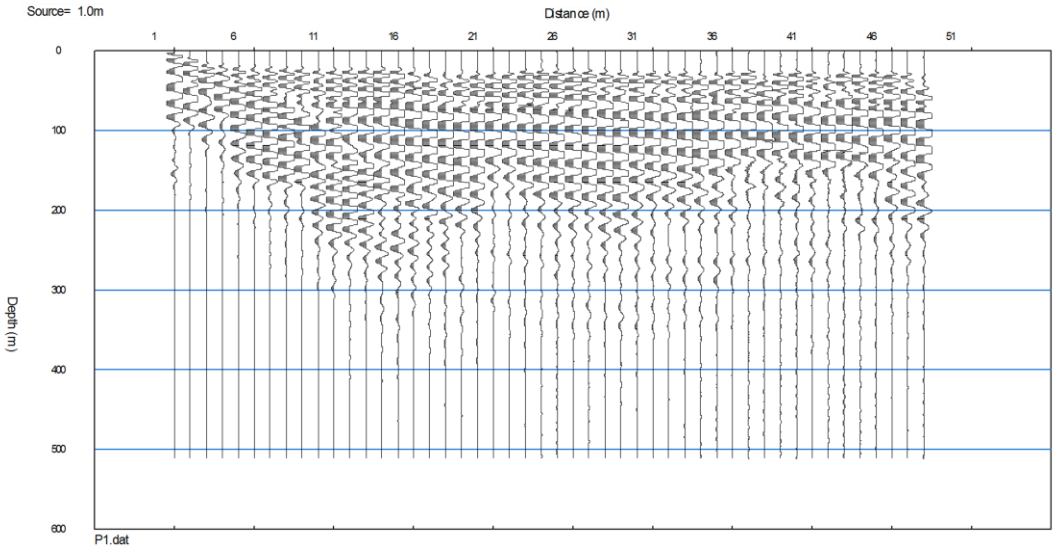

Slack's Cave line 1 P-Wave refraction shot 2

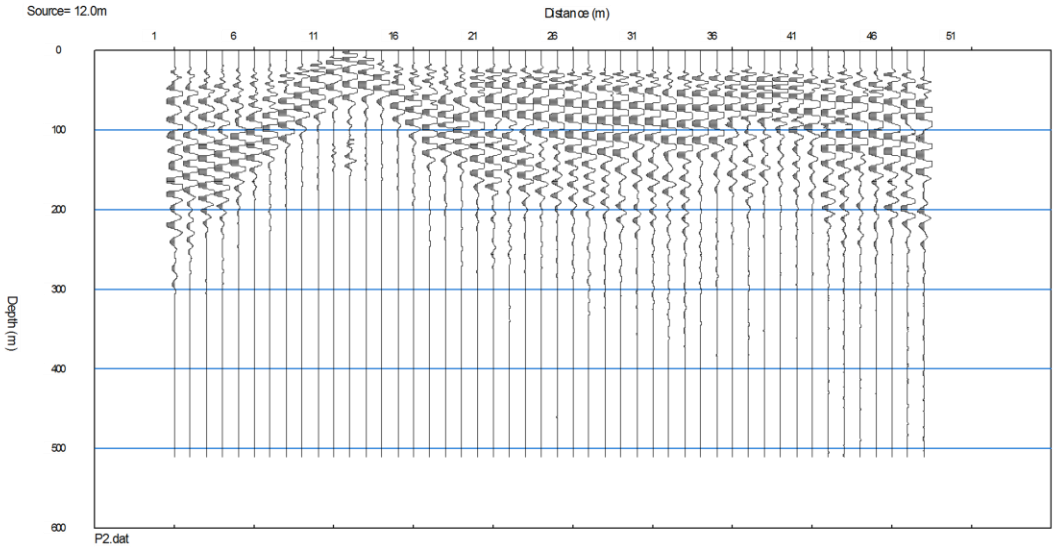

Slack's Cave line 1 P-Wave refraction shot 3

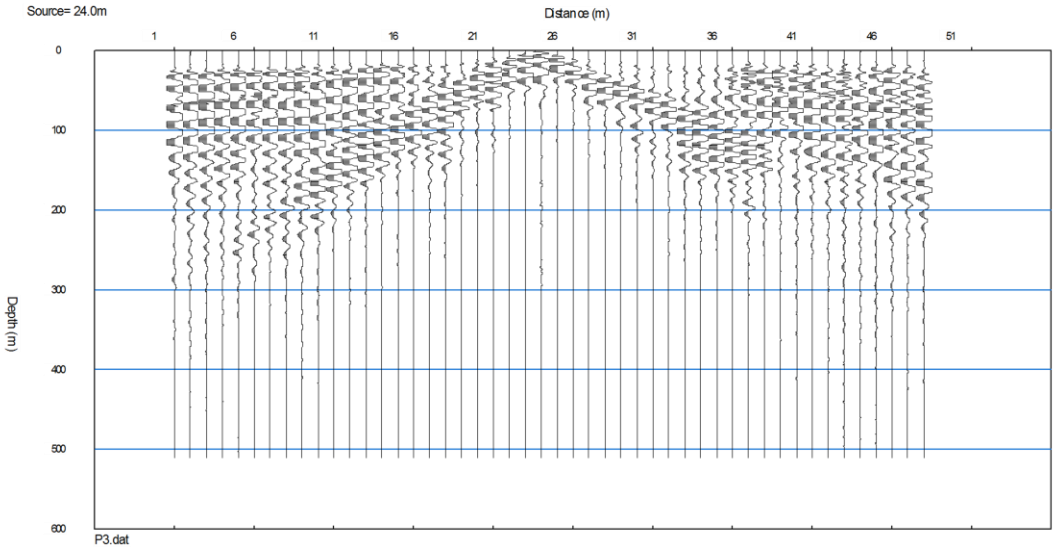

Slack's Cave line 1 P-Wave refraction shot 4

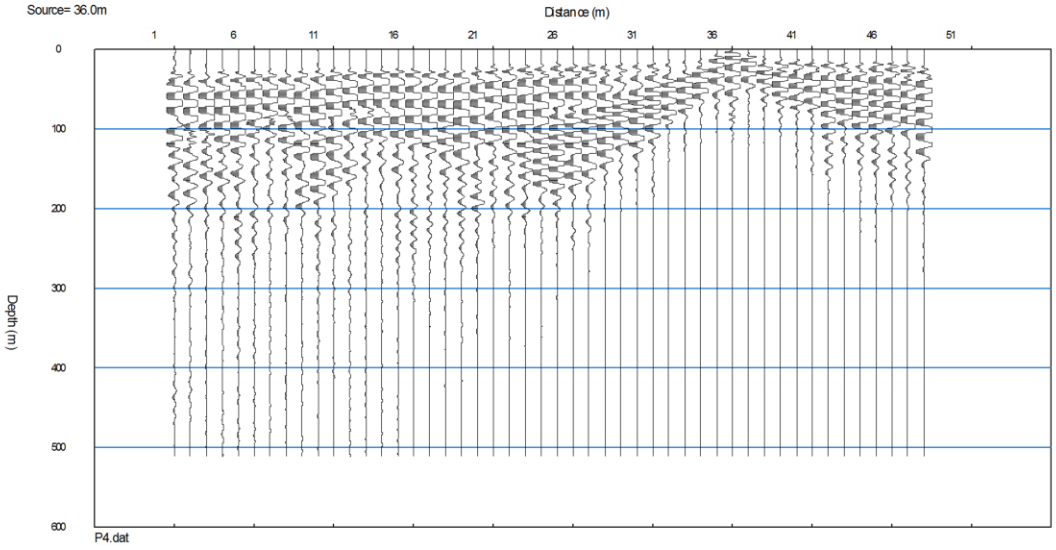

Slack's Cave line 1 P-Wave refraction shot 5

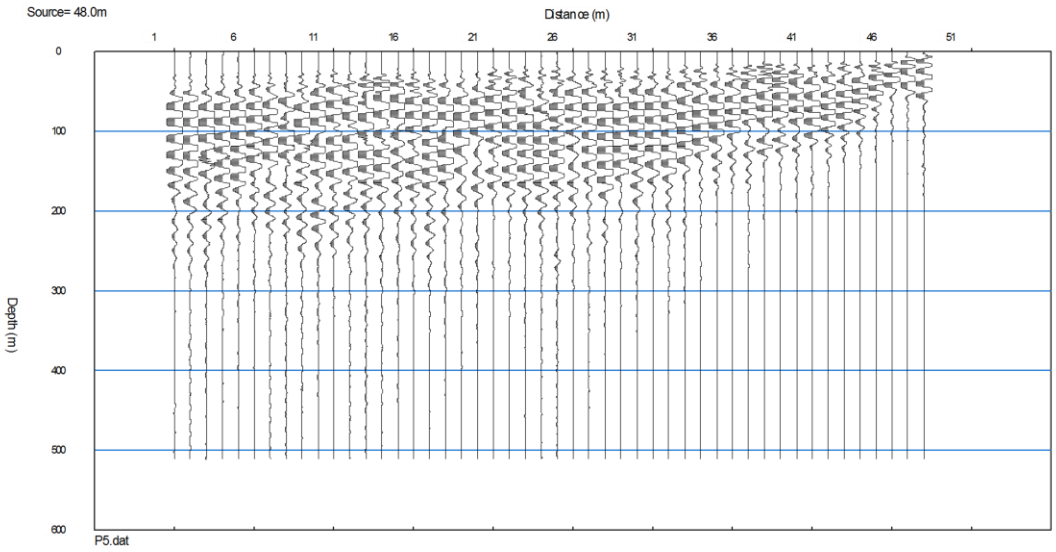

Slack's Cave line 1 P-Wave refraction shot 6

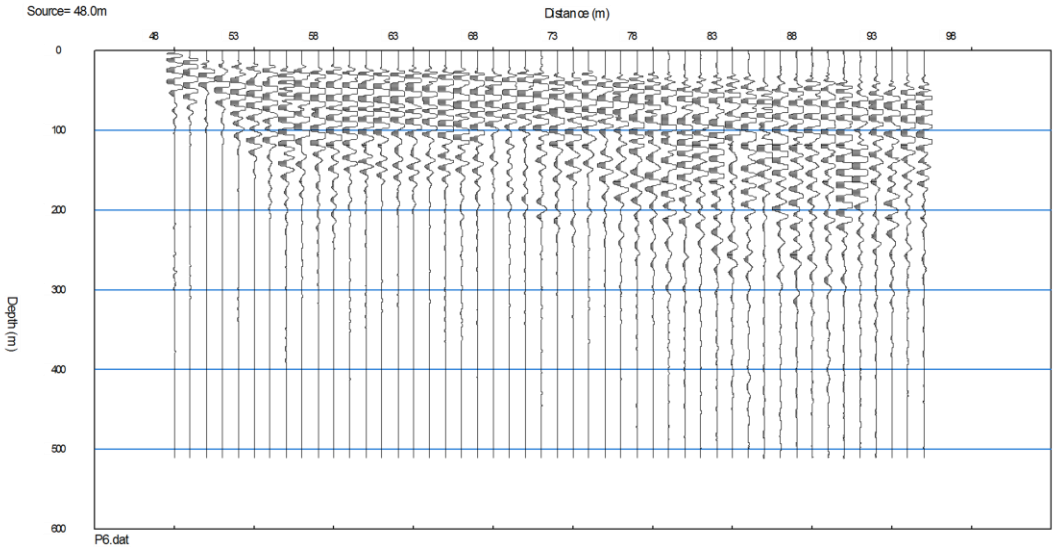

Slack's Cave line 1 P-Wave refraction shot 7

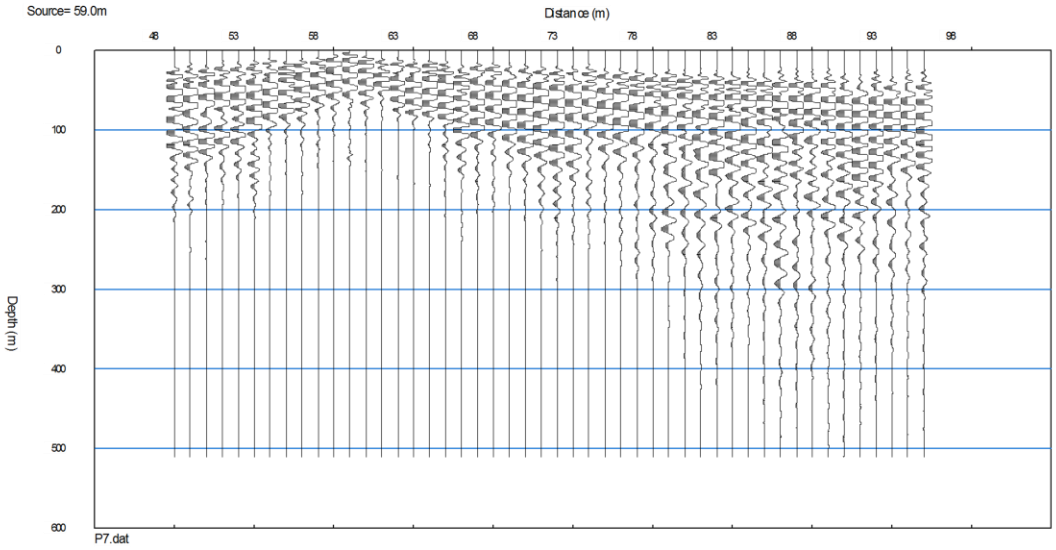

Slack's Cave line 1 P-Wave refraction shot 8

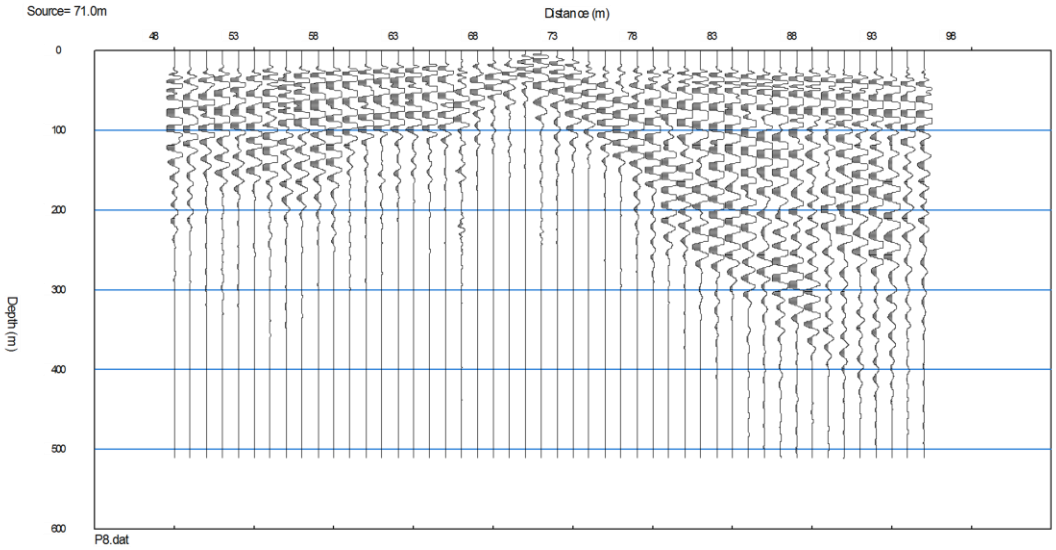

Slack's Cave line 1 P-Wave refraction shot 9

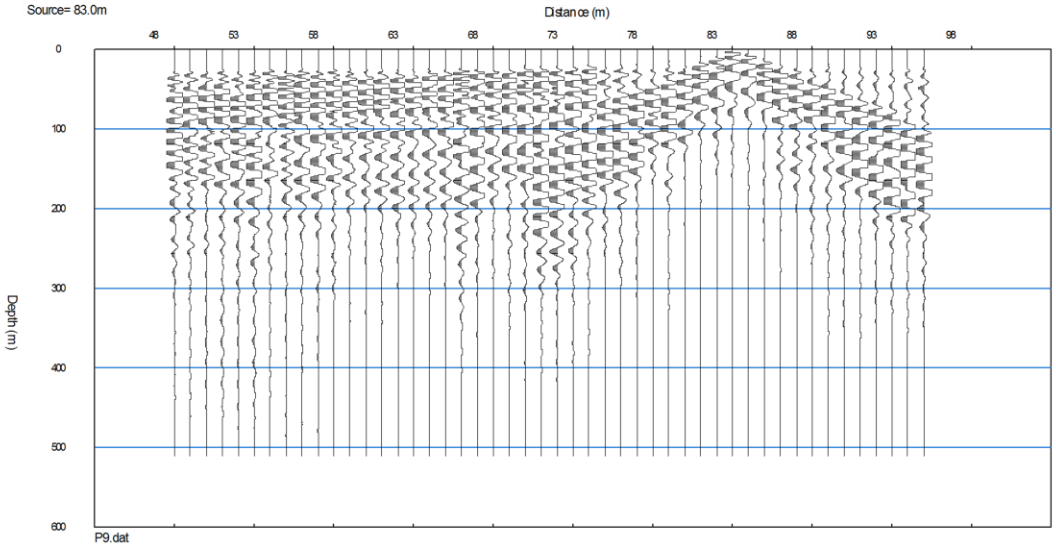

Slack's Cave line 1 P-Wave refraction shot 10

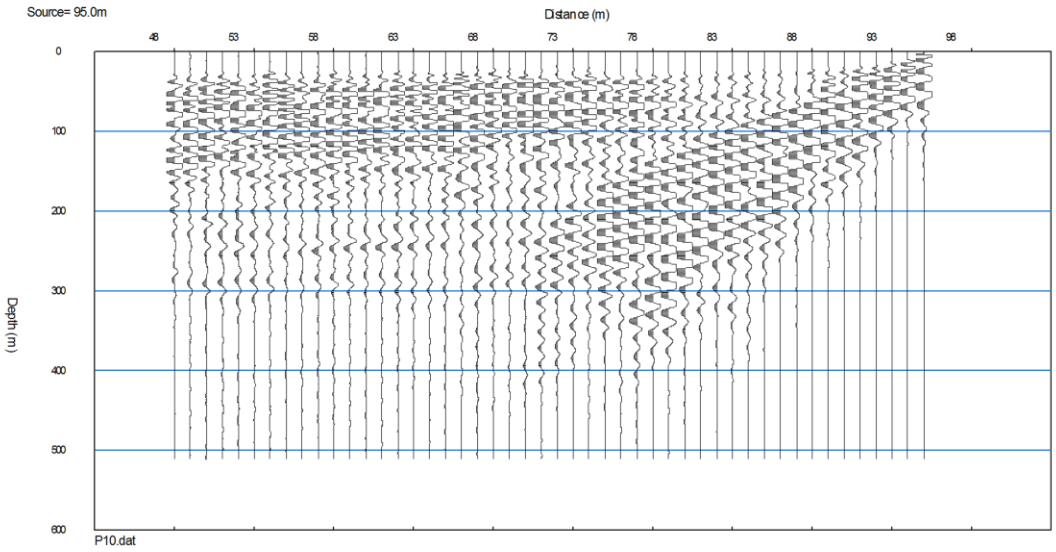

Slack's Cave line 2 P-Wave refraction shot 1

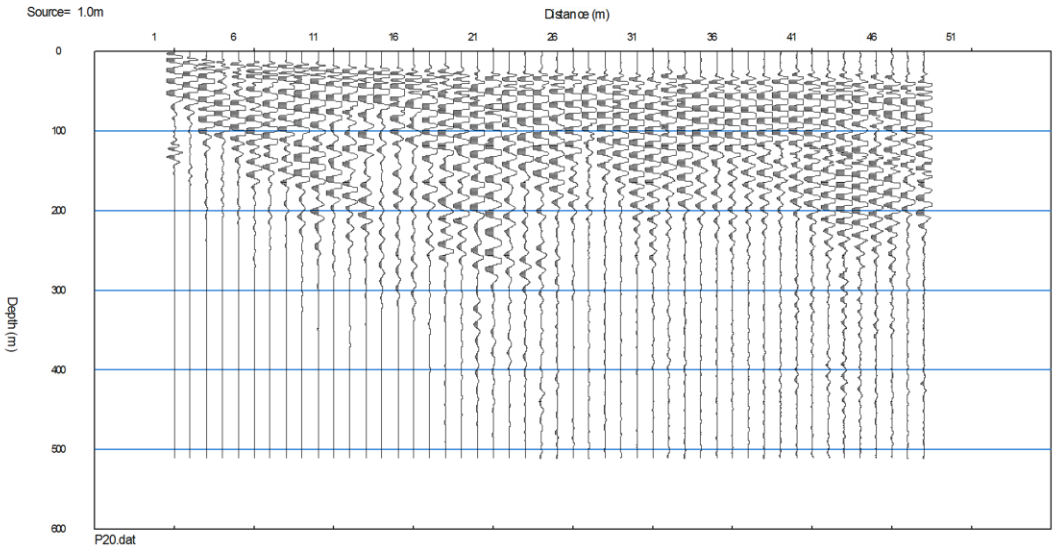

Slack's Cave line 2 P-Wave refraction shot 2

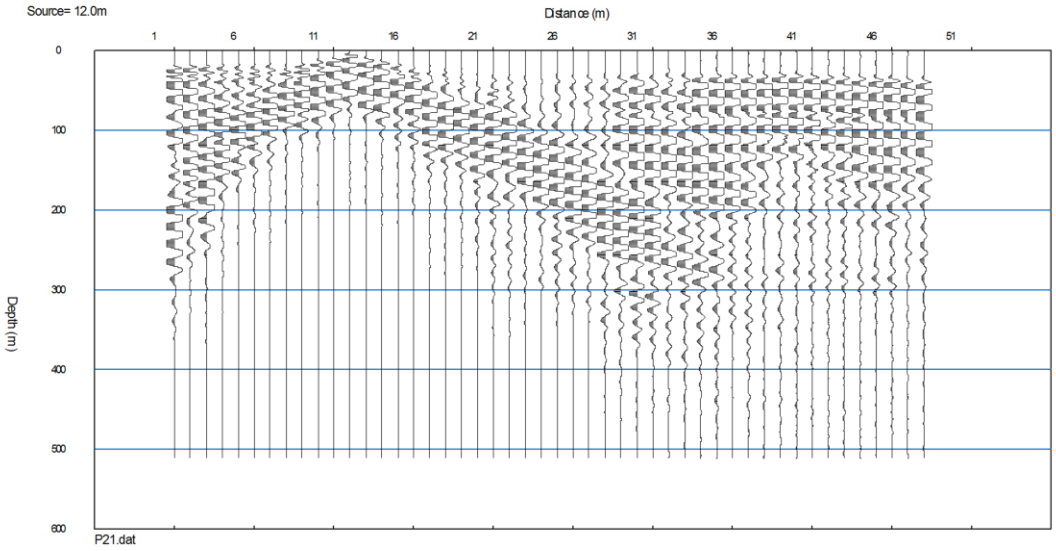

Slack's Cave line 2 P-Wave refraction shot 3

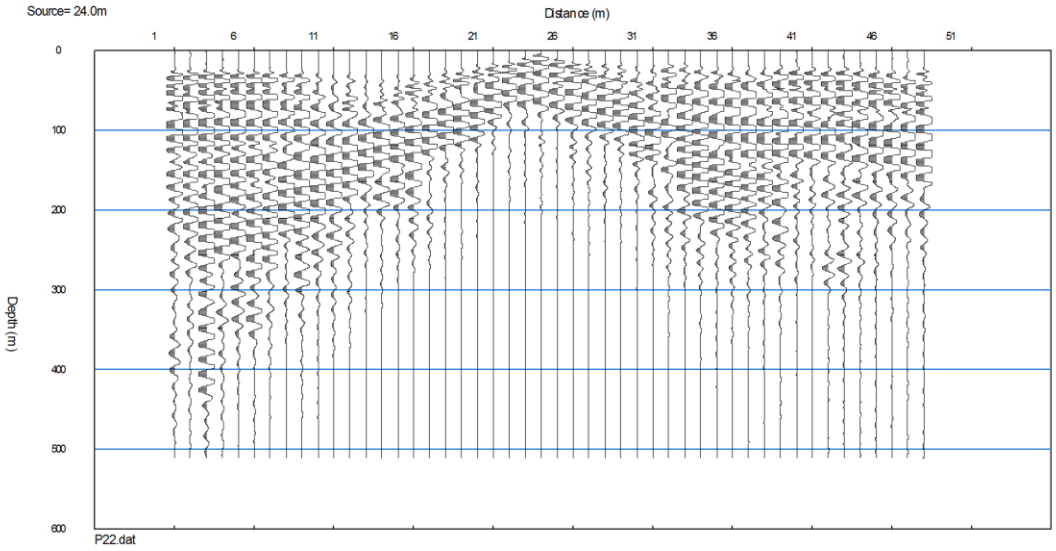

Slack's Cave line 2 P-Wave refraction shot 4

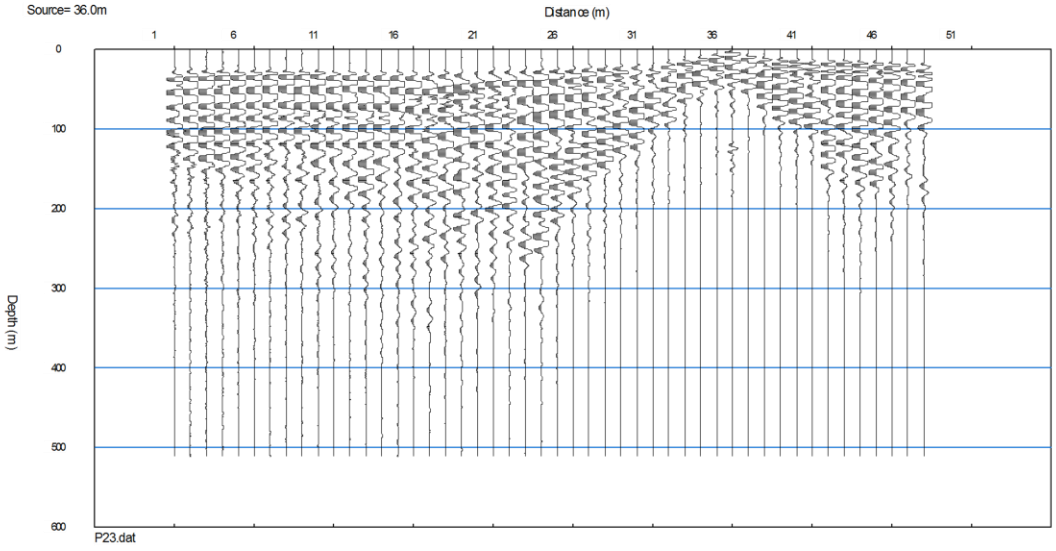

Slack's Cave line 2 P-Wave refraction shot 5

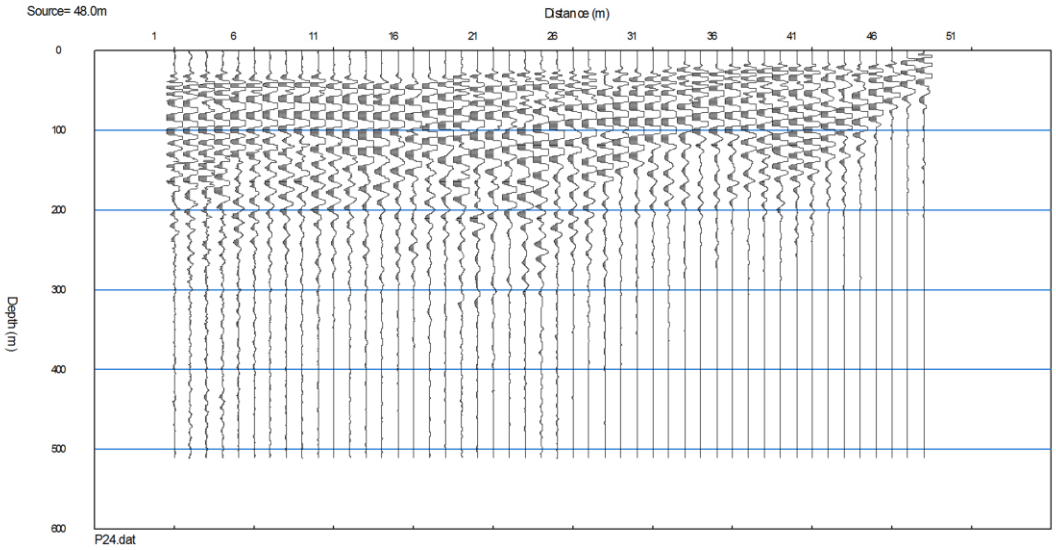

Slack's Cave line 1 S-Wave refraction shot 1

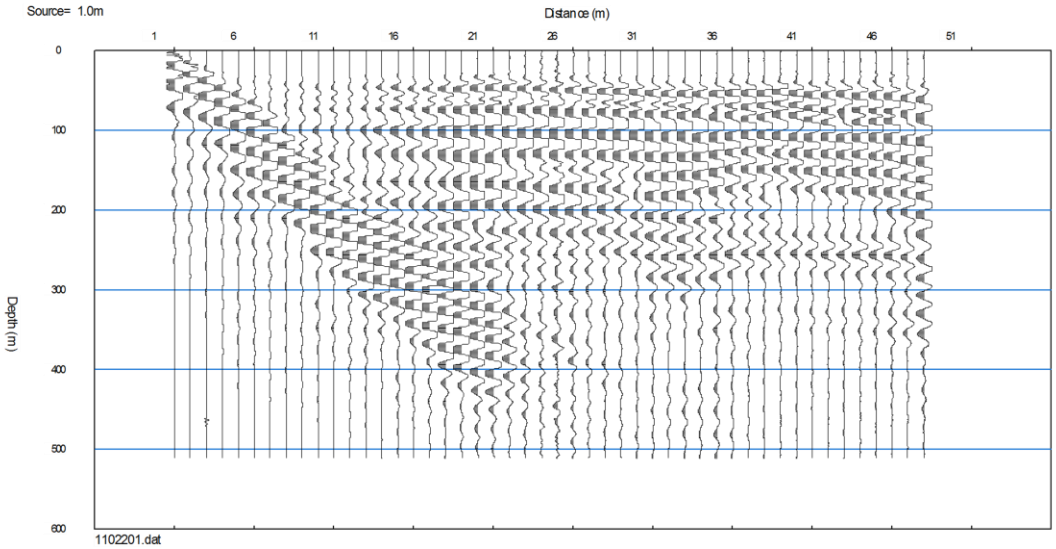

Slack's Cave line 1 S-Wave refraction shot 2

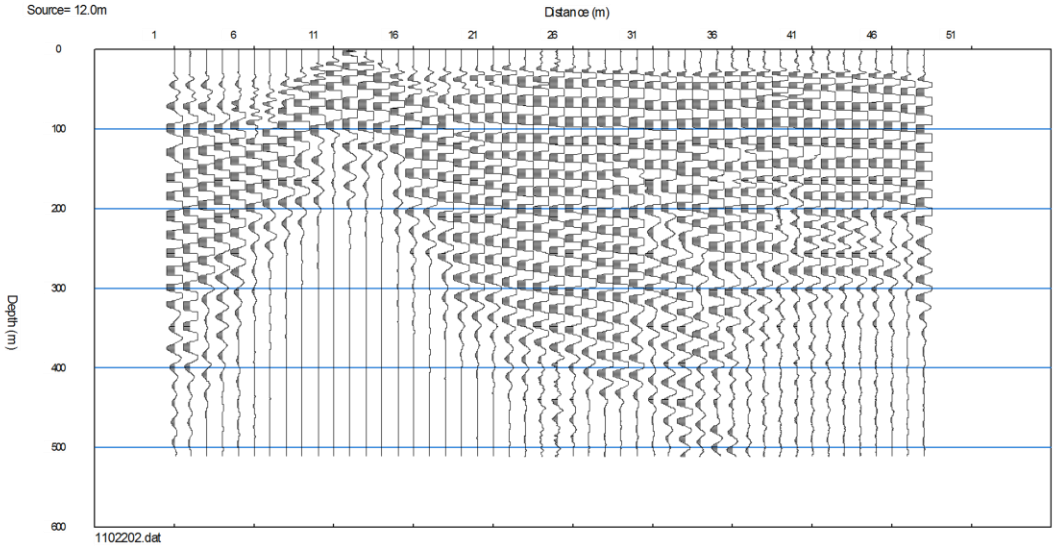

Slack's Cave line 1 S-Wave refraction shot 3

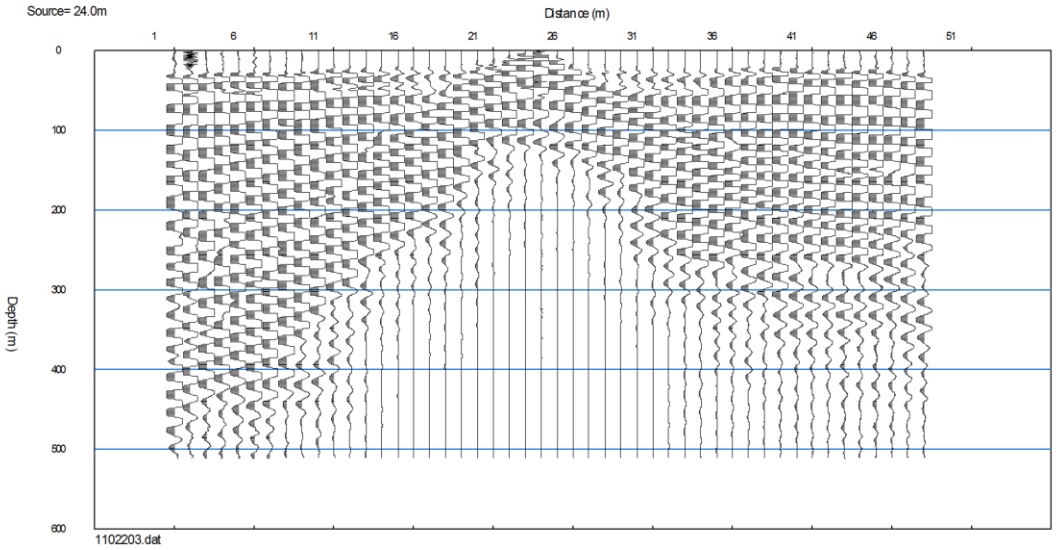

Slack's Cave line 1 S-Wave refraction shot 4

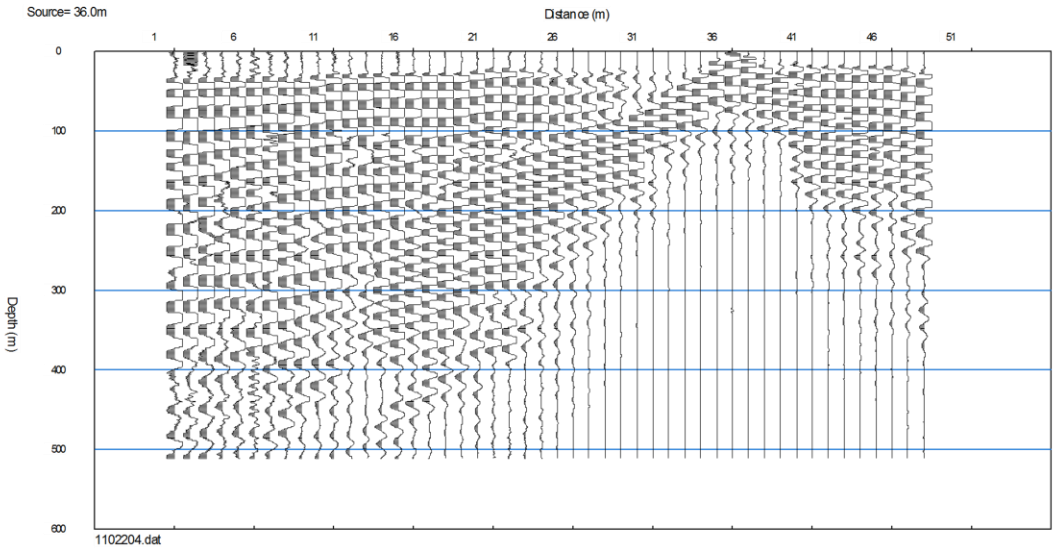

Slack's Cave line 1 S-Wave refraction shot 5

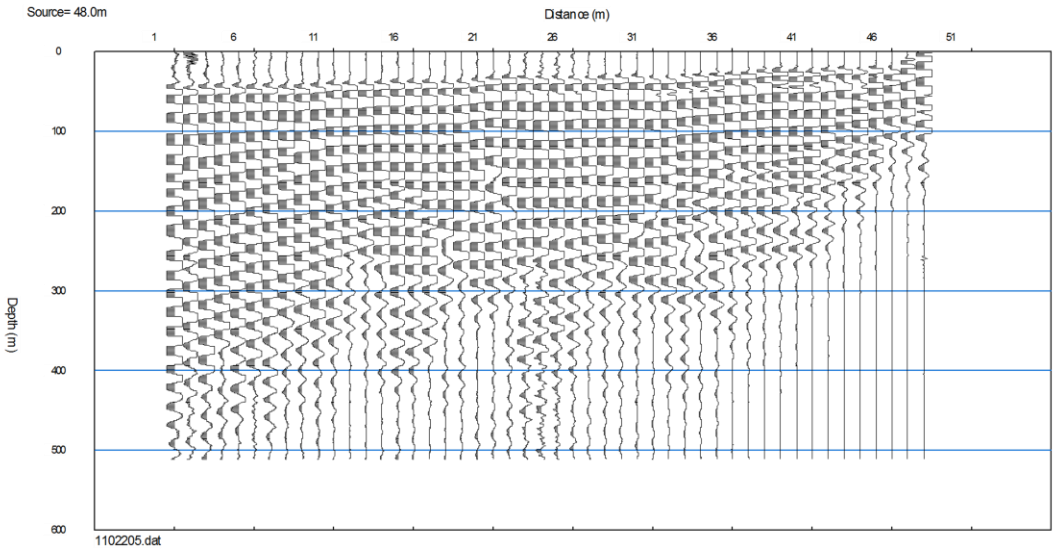

Slack's Cave line 1 S-Wave refraction shot 6

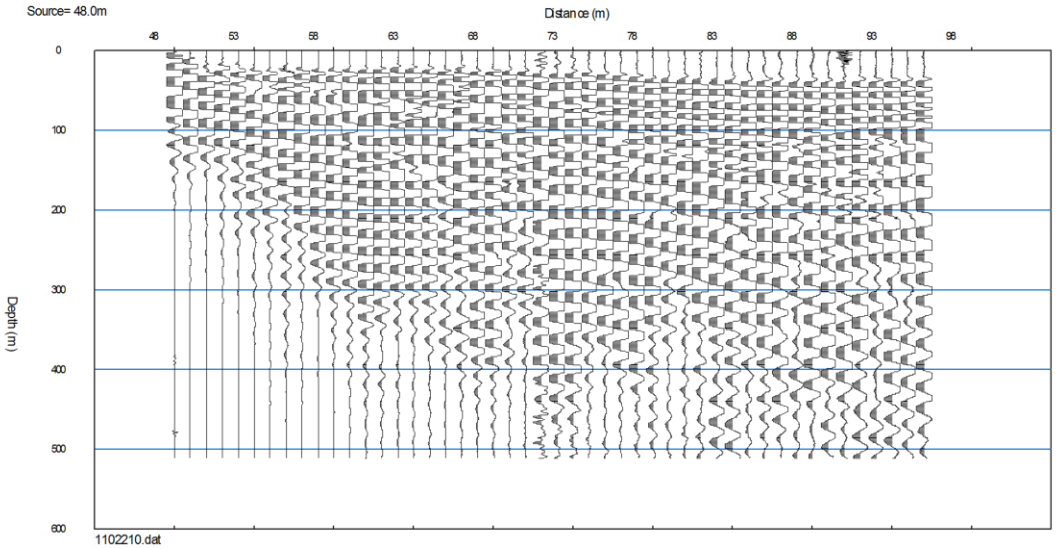

Slack's Cave line 1 S-Wave refraction shot 7

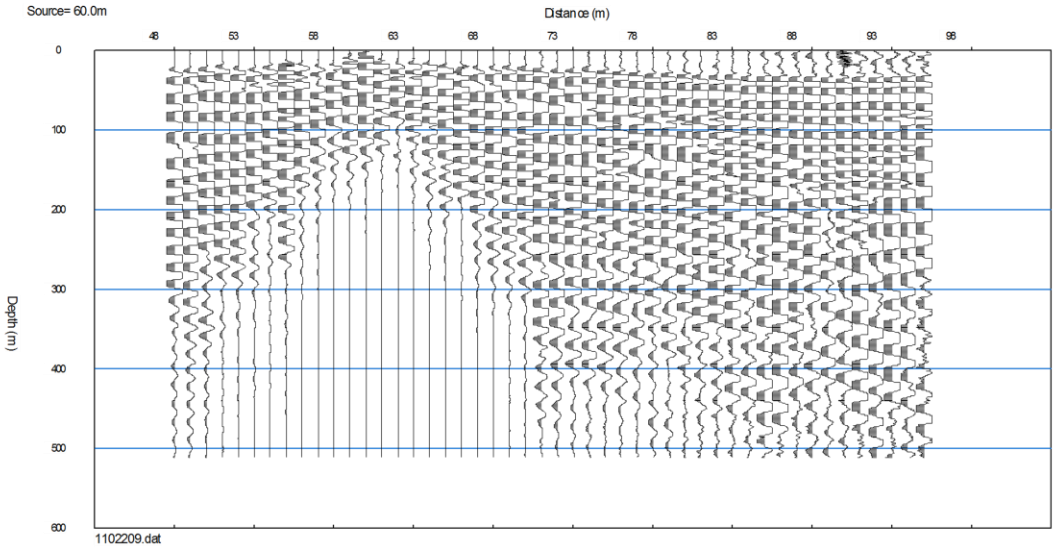

Slack's Cave line 1 S-Wave refraction shot 8

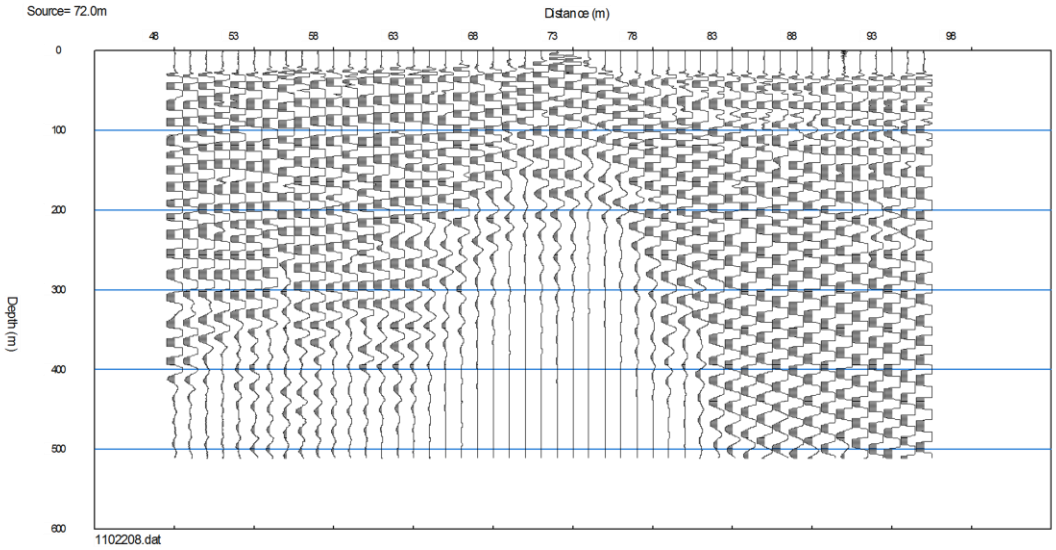

Slack's Cave line 1 S-Wave refraction shot 9

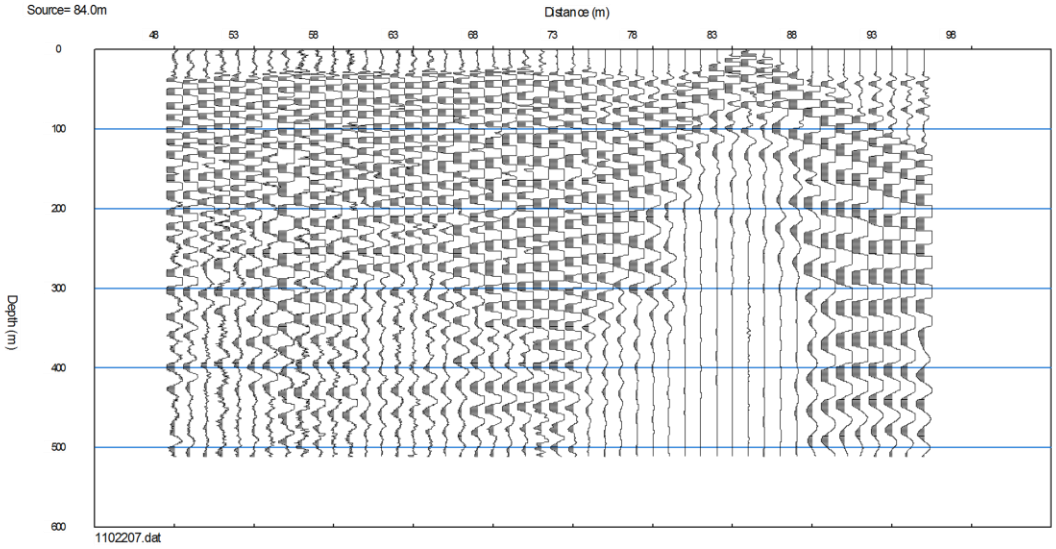

Slack's Cave line 1 S-Wave refraction shot 10

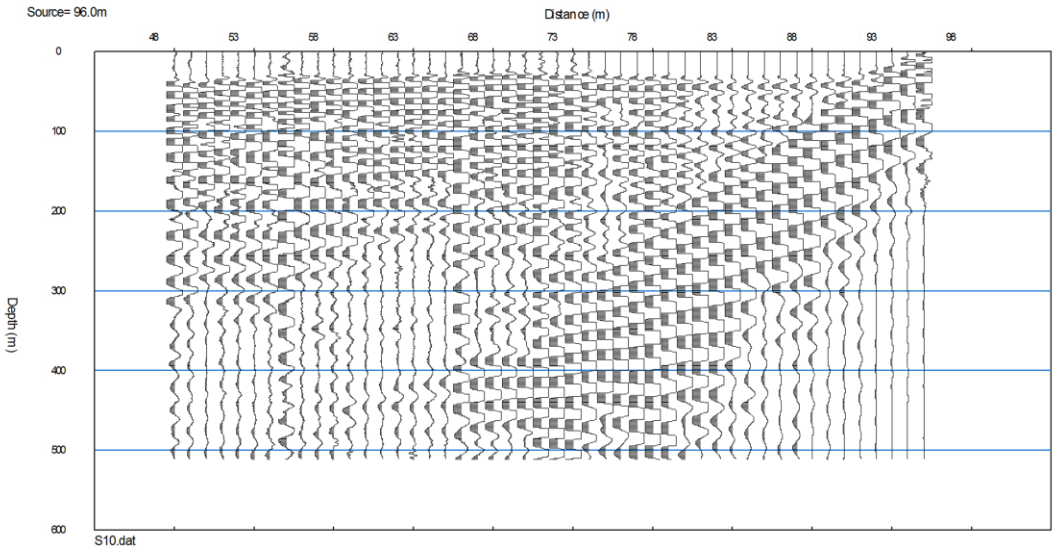

Slack's Cave line 2 S-Wave refraction shot 1

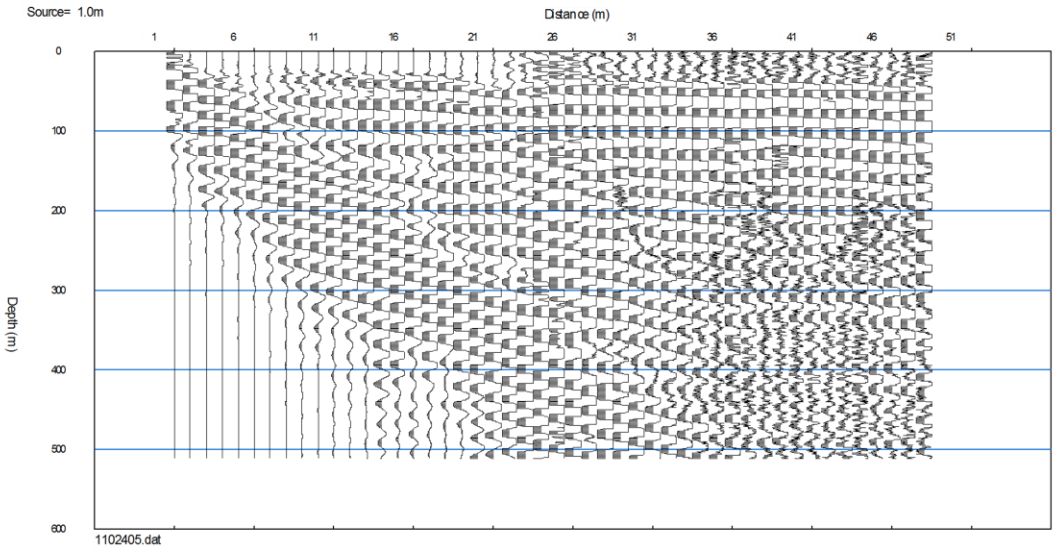

Slack's Cave line 2 S-Wave refraction shot 2

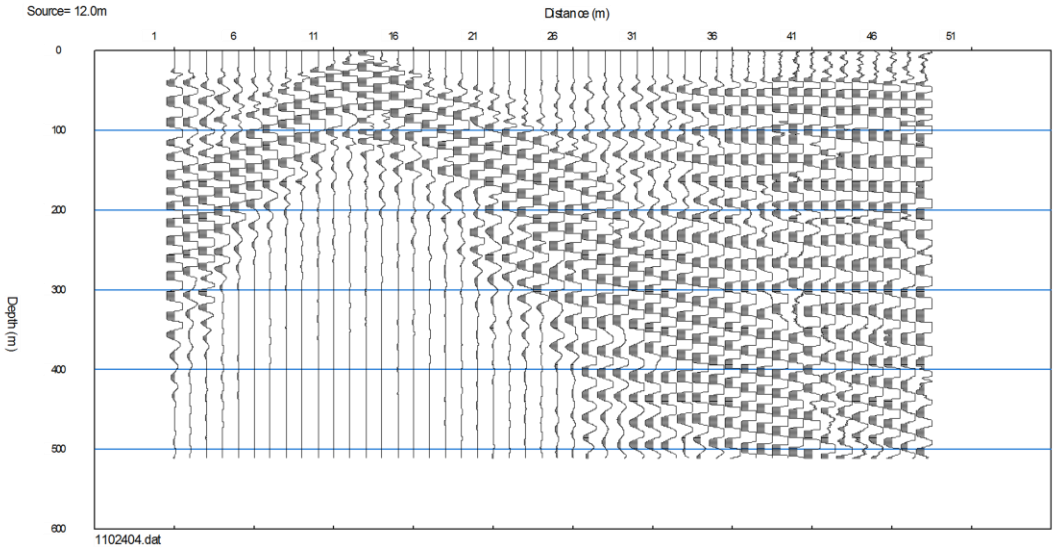

Slack's Cave line 2 S-Wave refraction shot 3

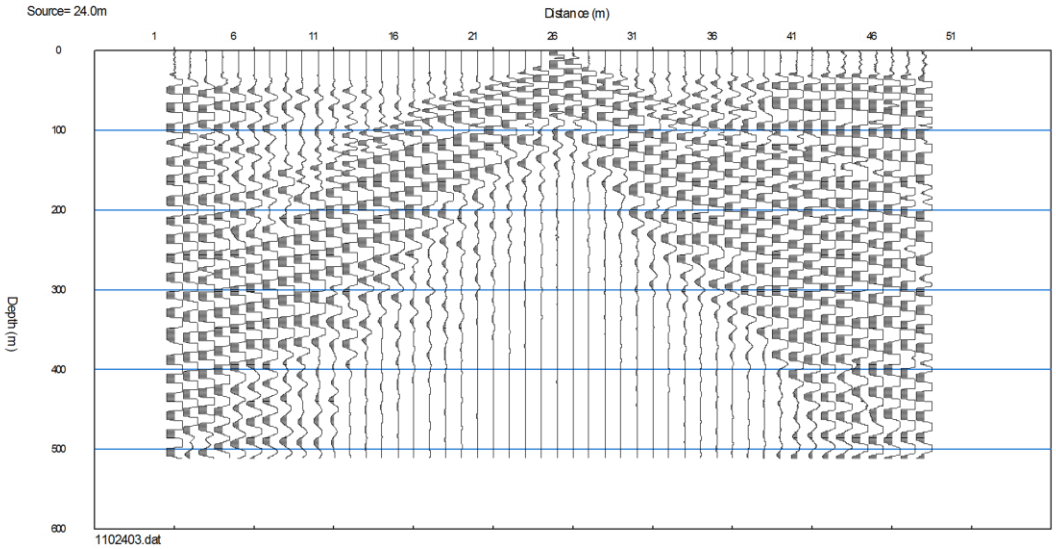

Slack's Cave line 2 S-Wave refraction shot 4

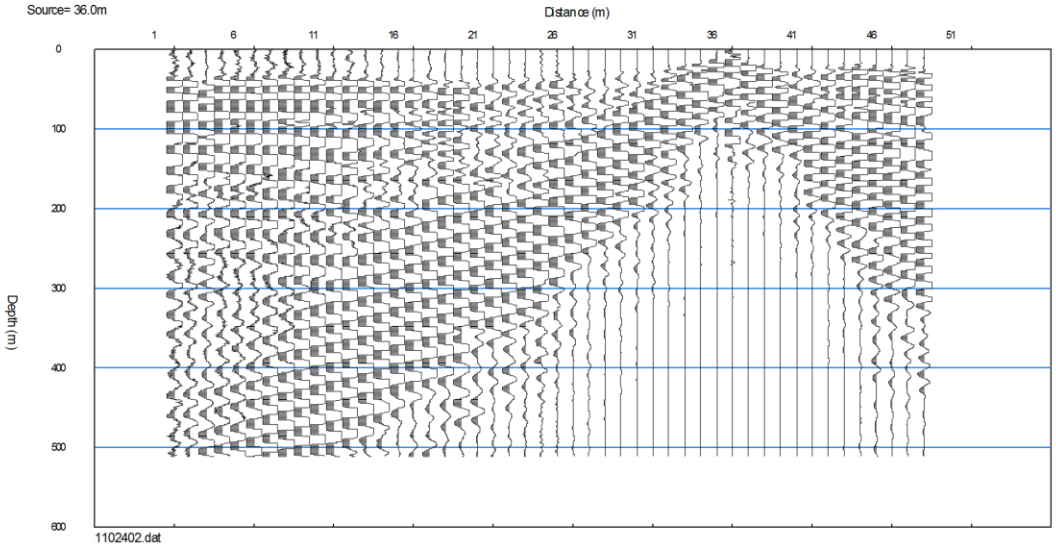

Slack's Cave line 2 S-Wave refraction shot 5

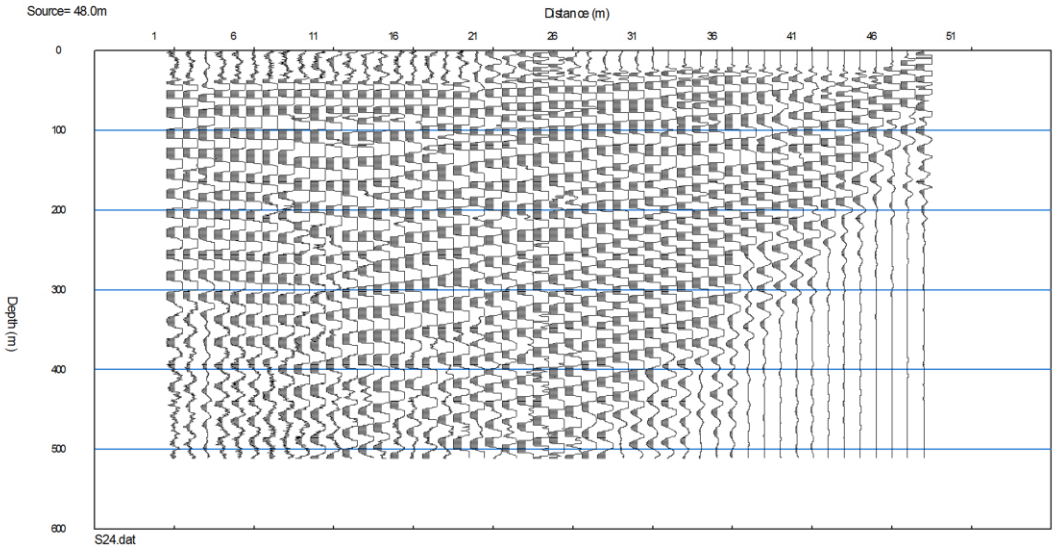

Kentucky Horse Park line 1 P-Wave refraction shot 1

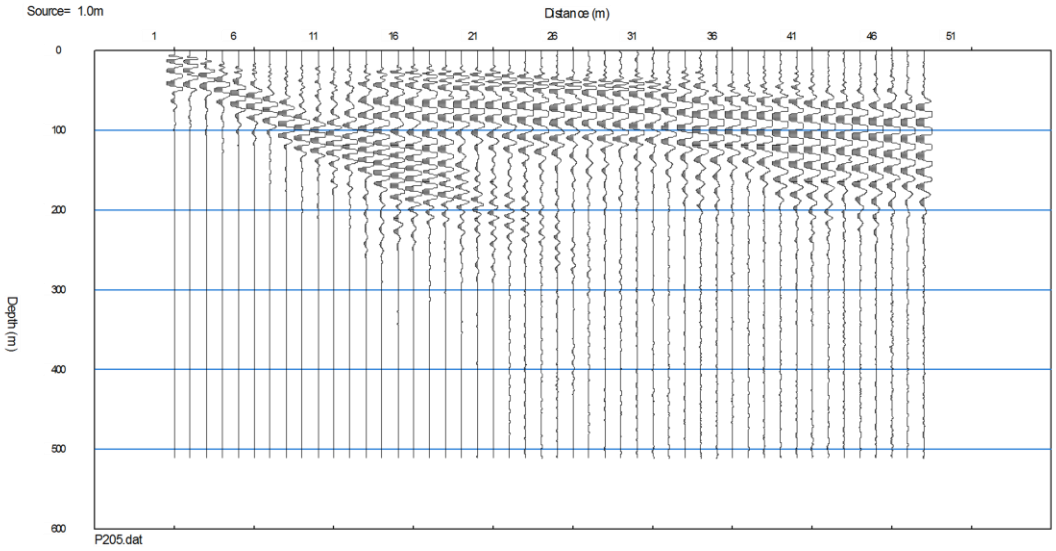

Kentucky Horse Park line 1 P-Wave refraction shot 2

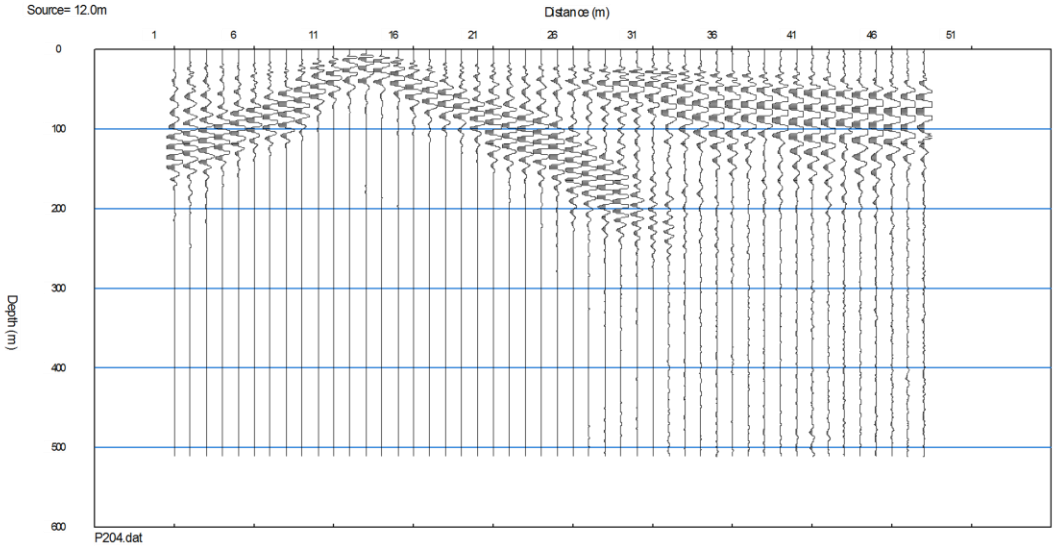

Kentucky Horse Park line 1 P-Wave refraction shot 3

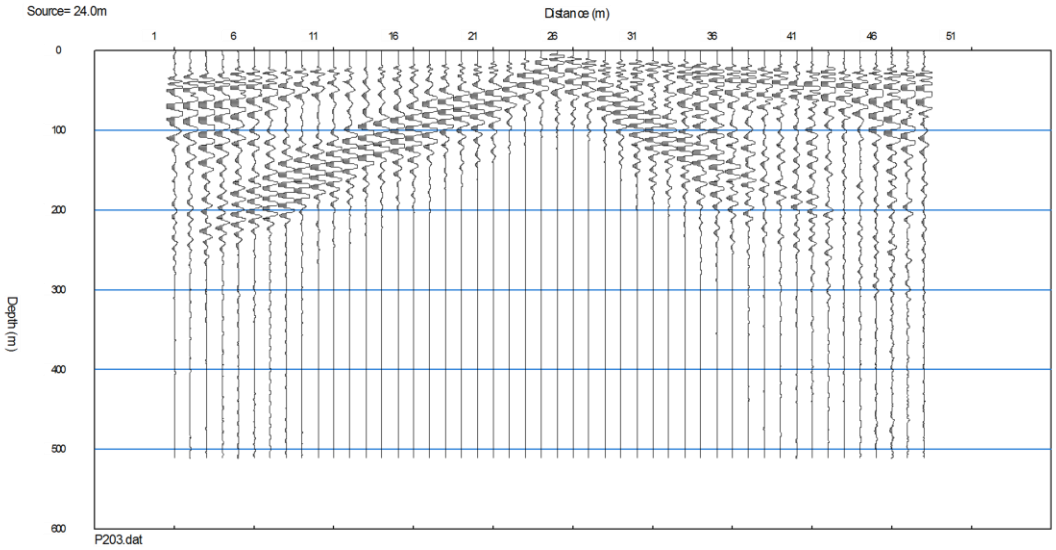

Kentucky Horse Park line 1 P-Wave refraction shot 4

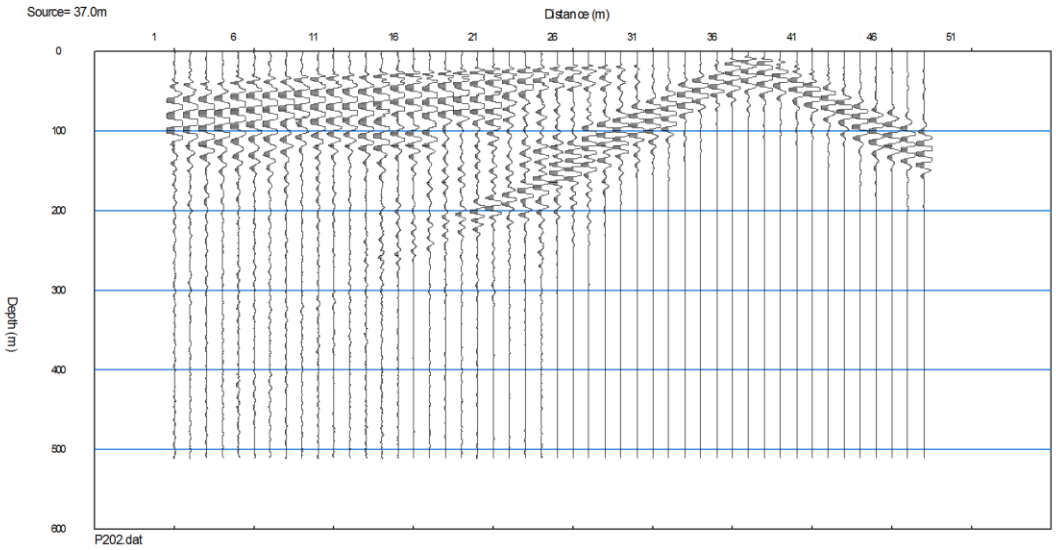

Kentucky Horse Park line 1 P-Wave refraction shot 5

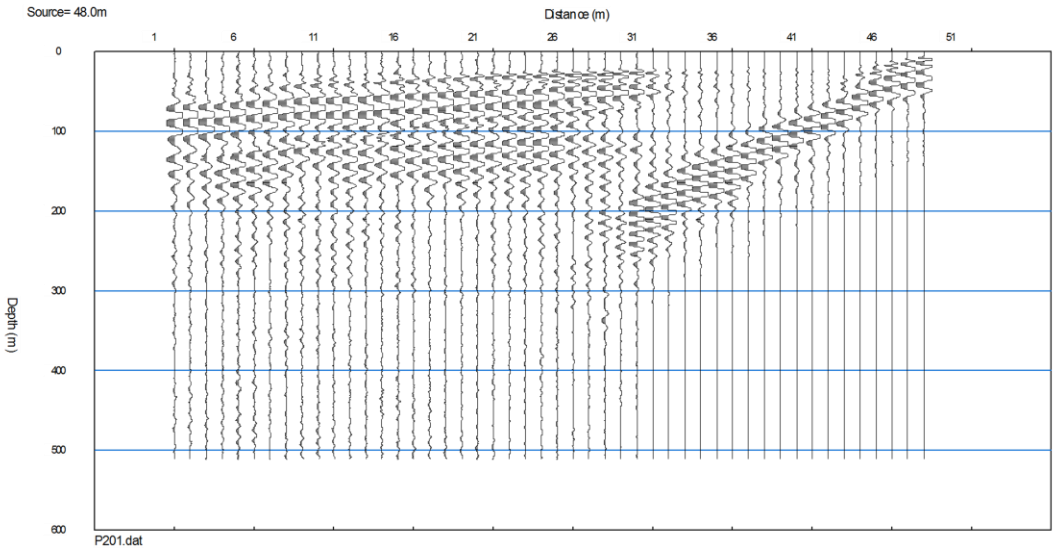

Kentucky Horse Park line 1 P-Wave refraction shot 6

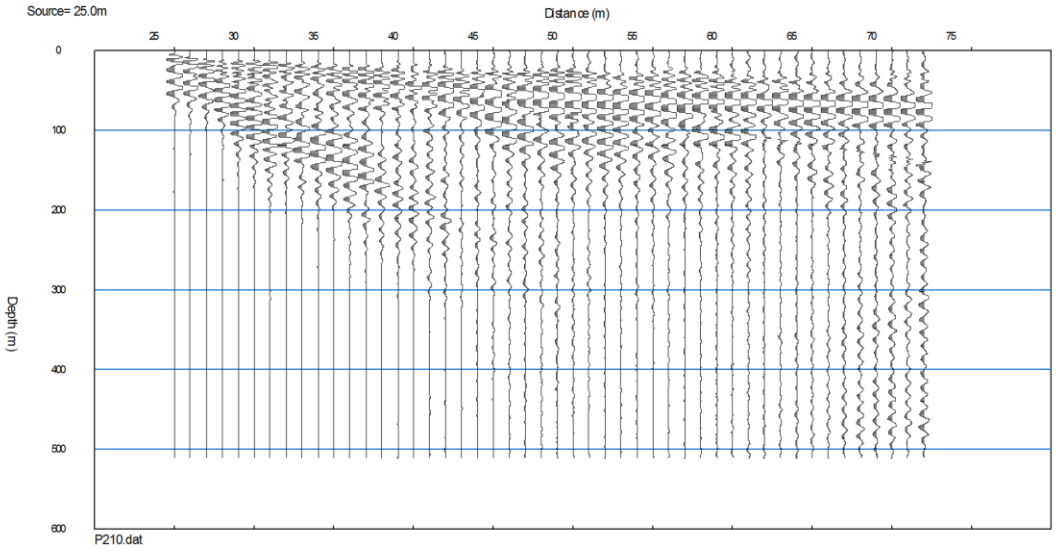

Kentucky Horse Park line 1 P-Wave refraction shot 7

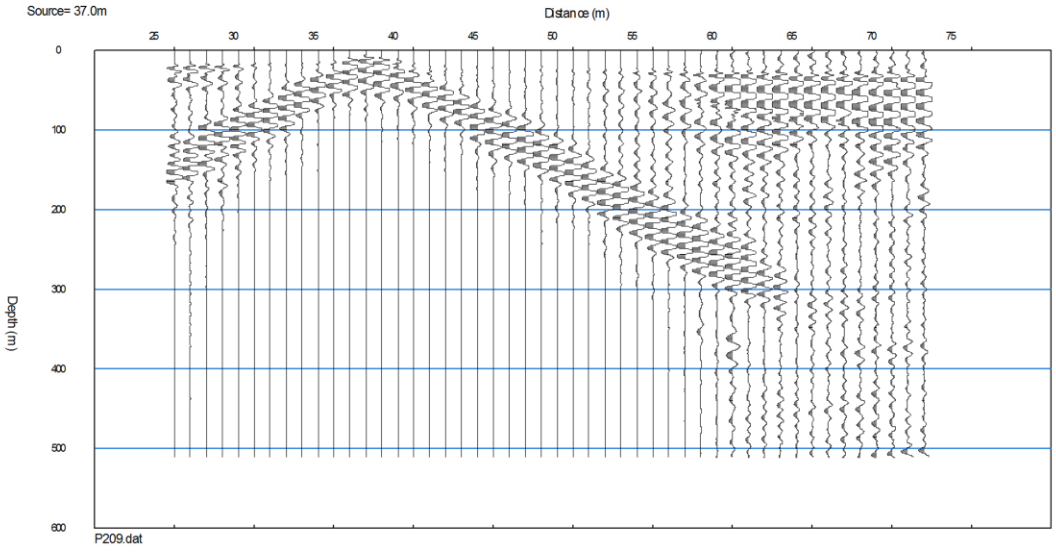

Kentucky Horse Park line 1 P-Wave refraction shot 8

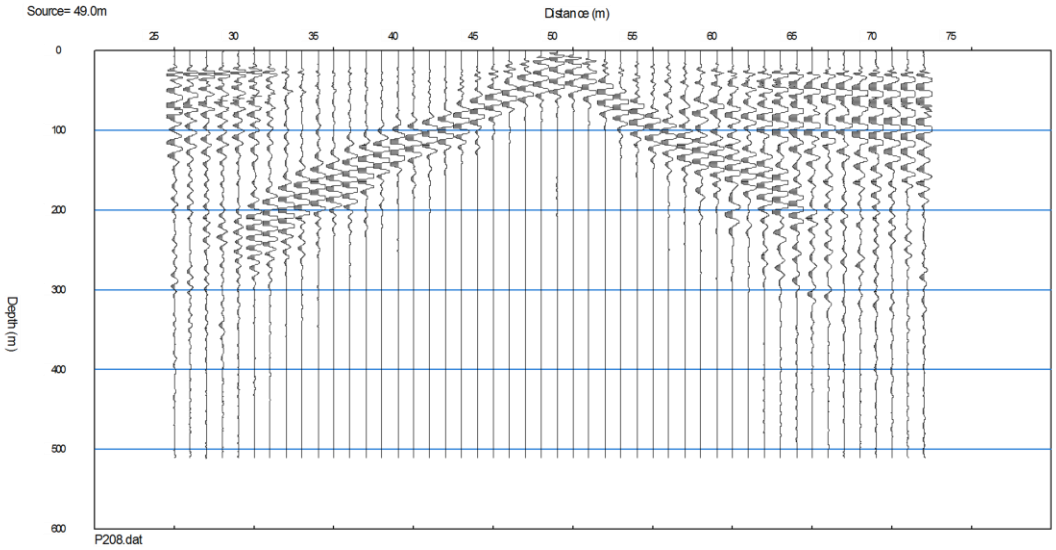

Kentucky Horse Park line 1 P-Wave refraction shot 9

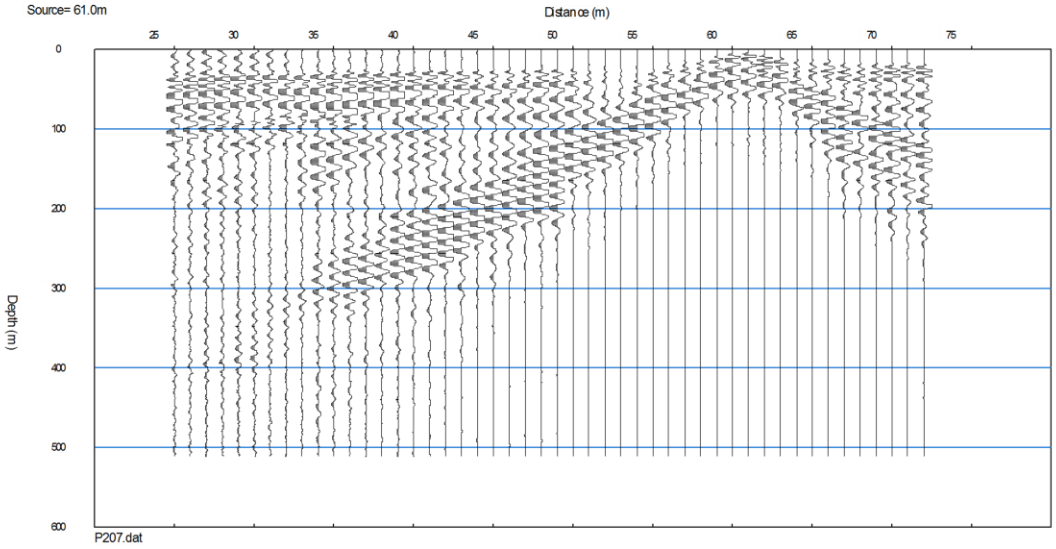

Kentucky Horse Park line 1 P-Wave refraction shot 10

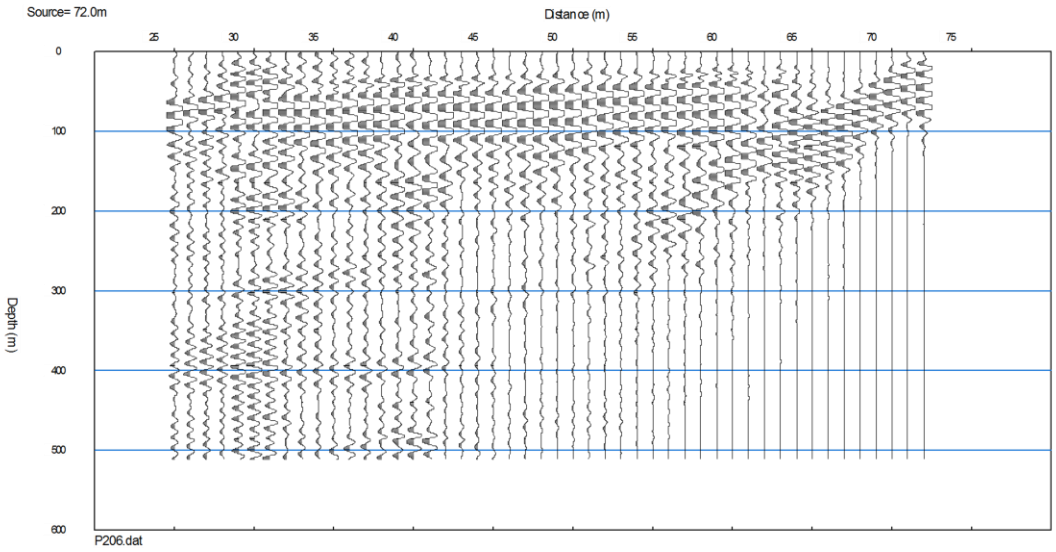

Kentucky Horse Park line 1 S-Wave refraction shot 1

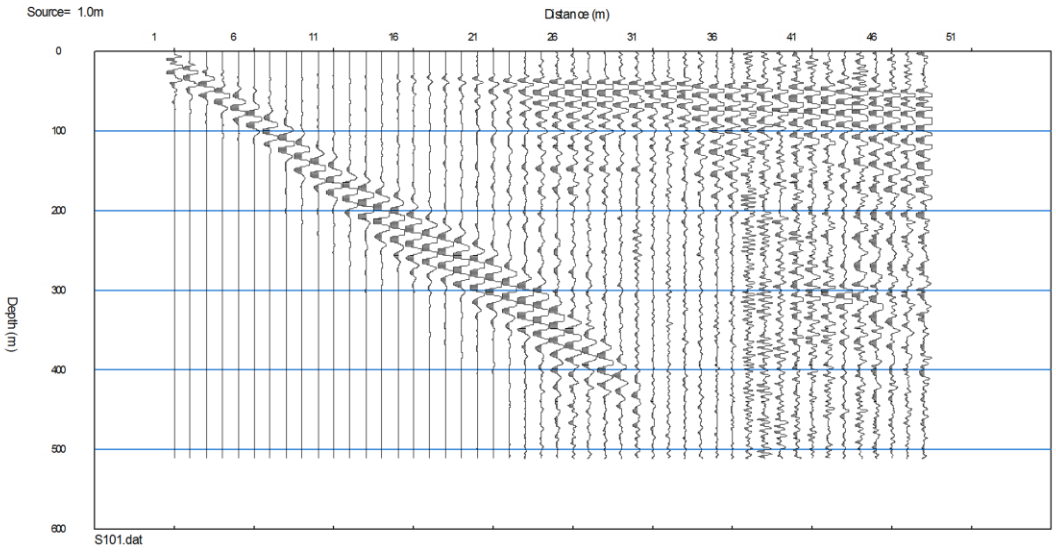

Kentucky Horse Park line 1 S-Wave refraction shot 2

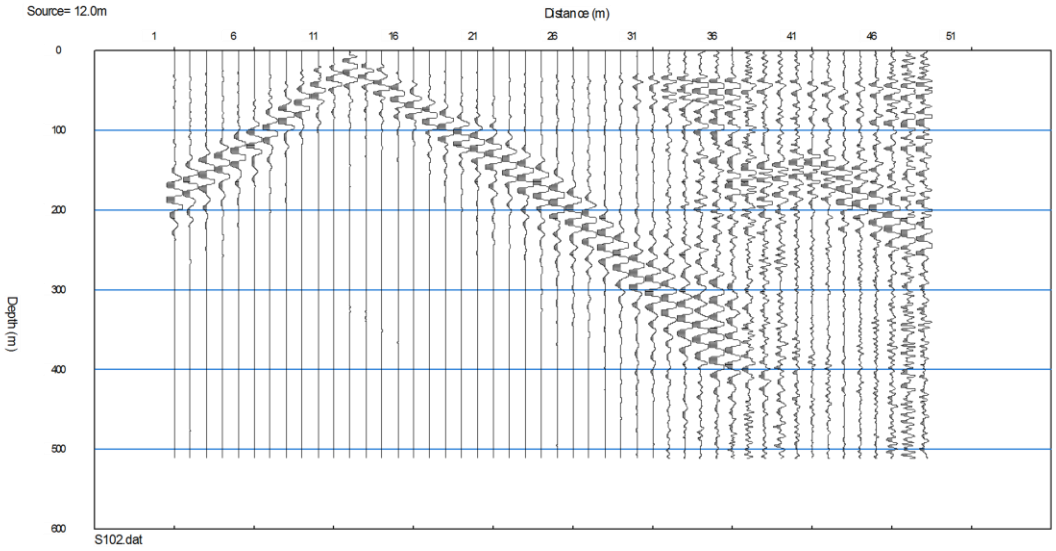

Kentucky Horse Park line 1 S-Wave refraction shot 3

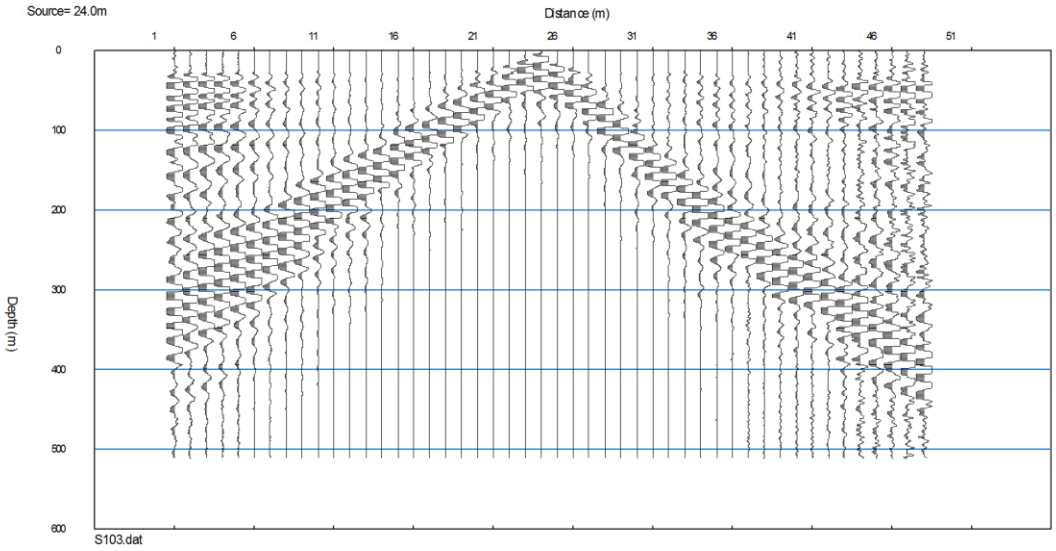

Kentucky Horse Park line 1 S-Wave refraction shot 4

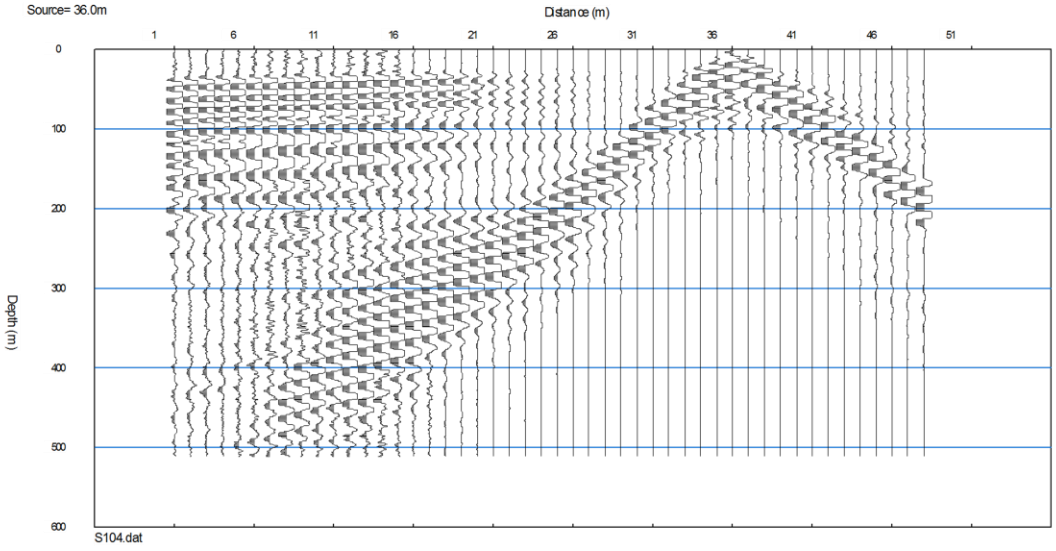

Kentucky Horse Park line 1 S-Wave refraction shot 5

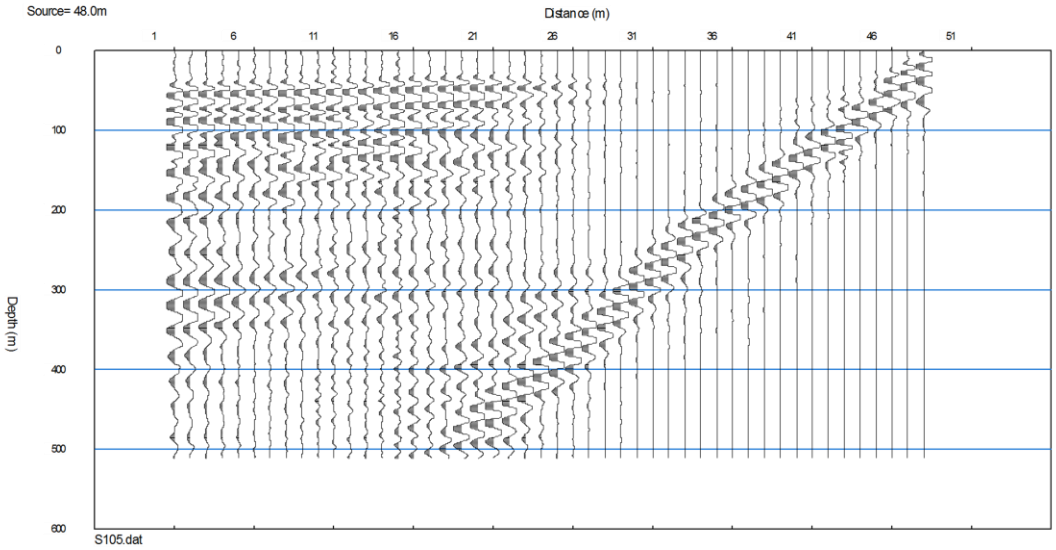

Kentucky Horse Park line 1 S-Wave refraction shot 6

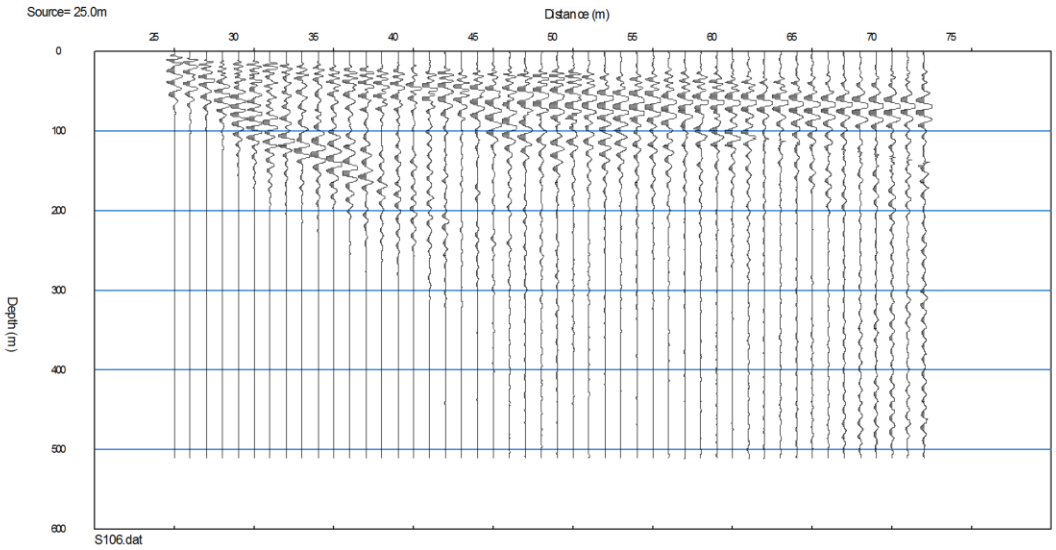

Kentucky Horse Park line 1 S-Wave refraction shot 7

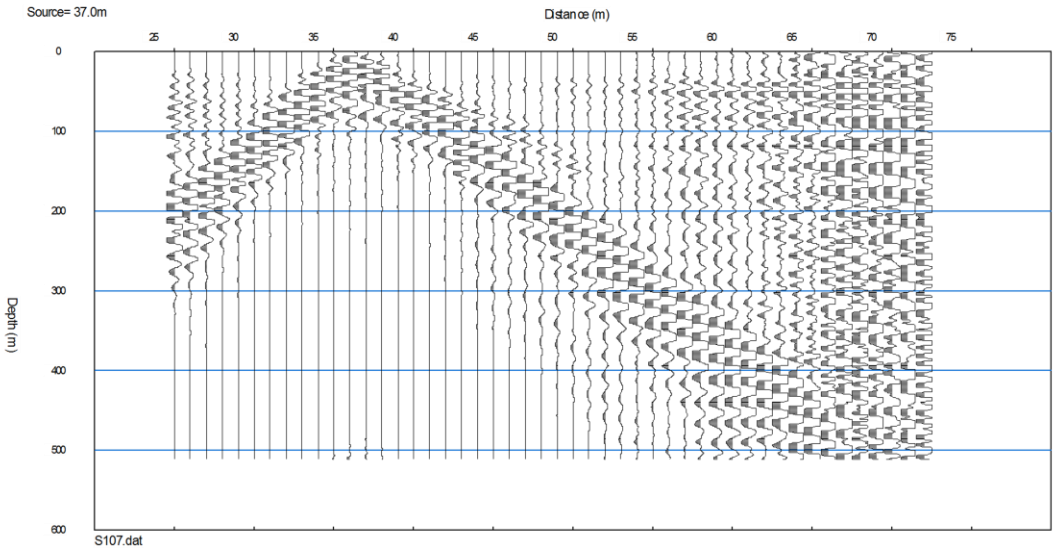

Kentucky Horse Park line 1 S-Wave refraction shot 8

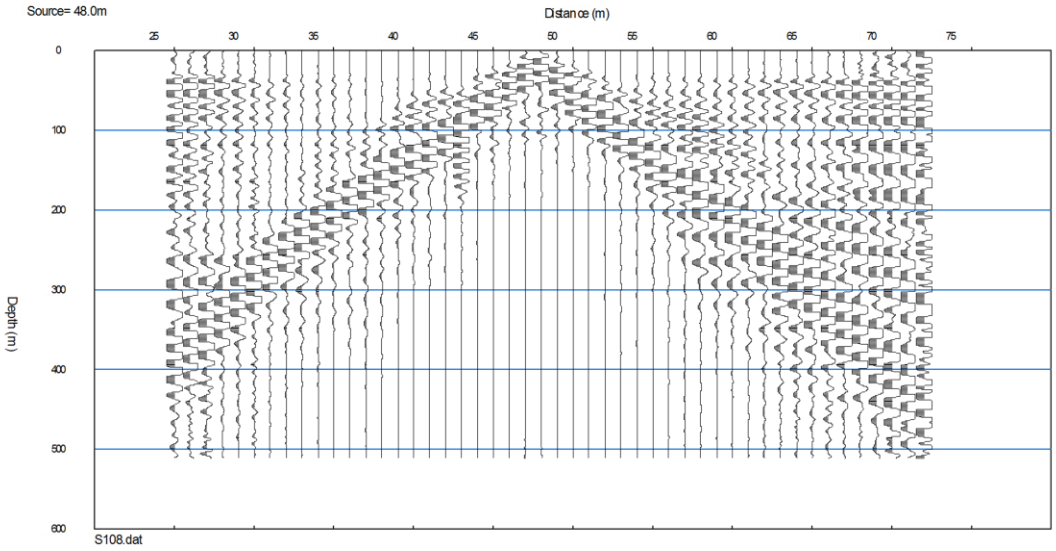

Kentucky Horse Park line 1 S-Wave refraction shot 9

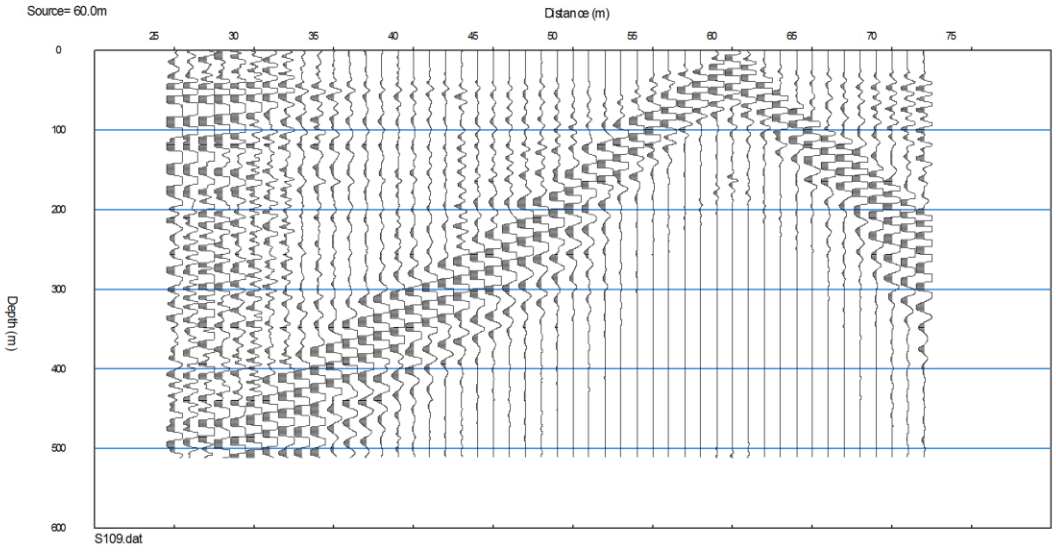

Kentucky Horse Park line 1 S-Wave refraction shot 10

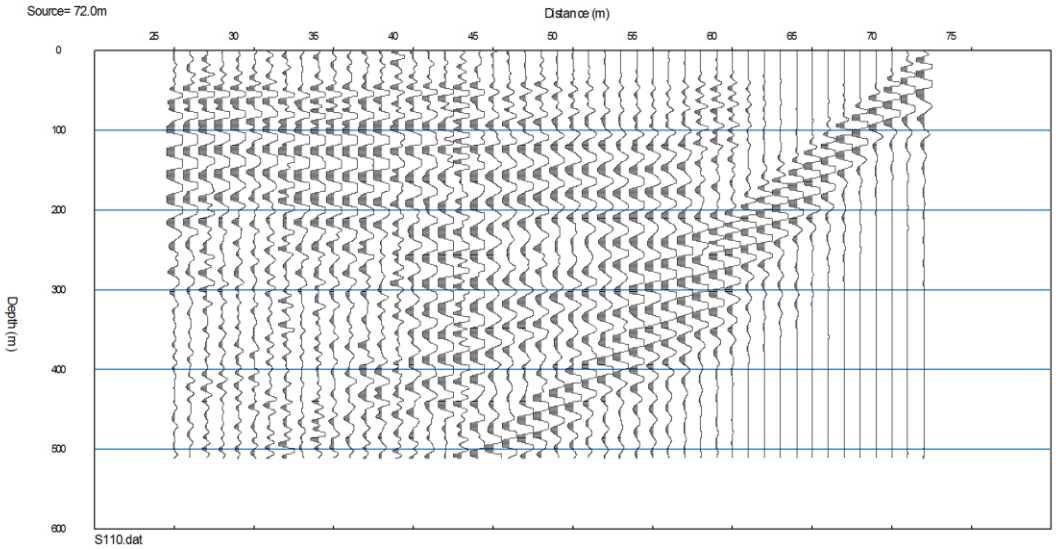

Berea Road line 3 P-Wave refraction shot 1

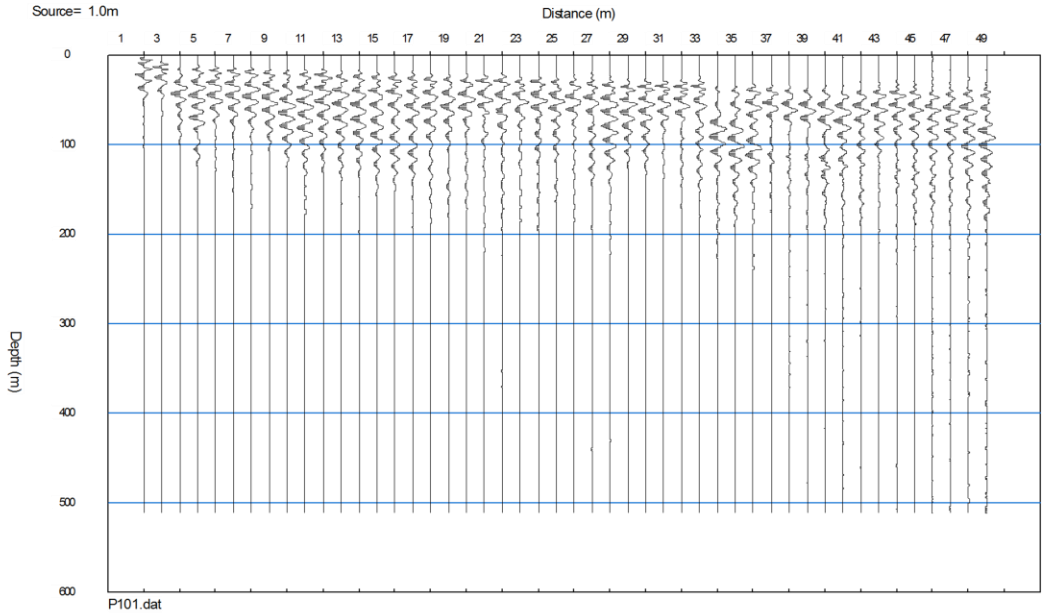

Berea Road line 3 P-Wave refraction shot 2

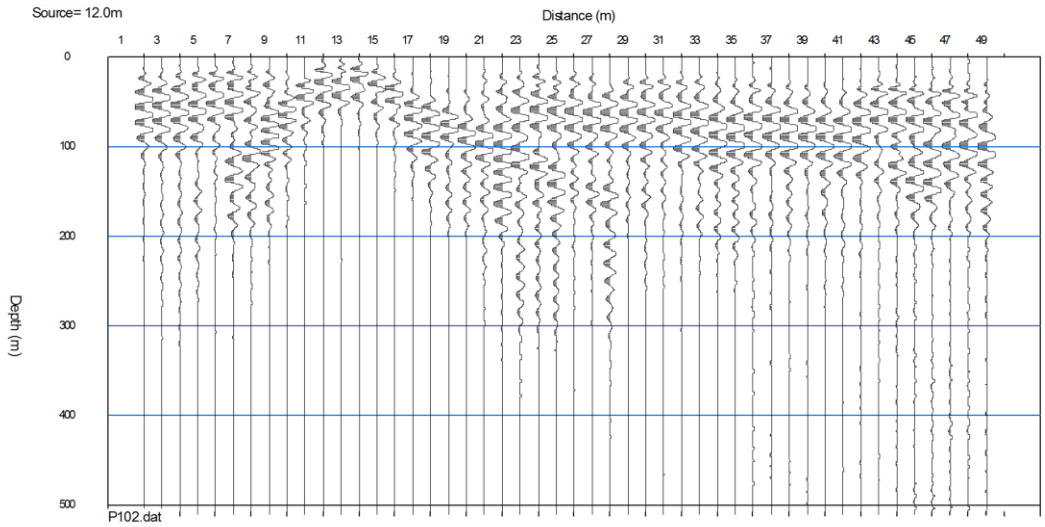

Berea Road line 3 P-Wave refraction shot 3

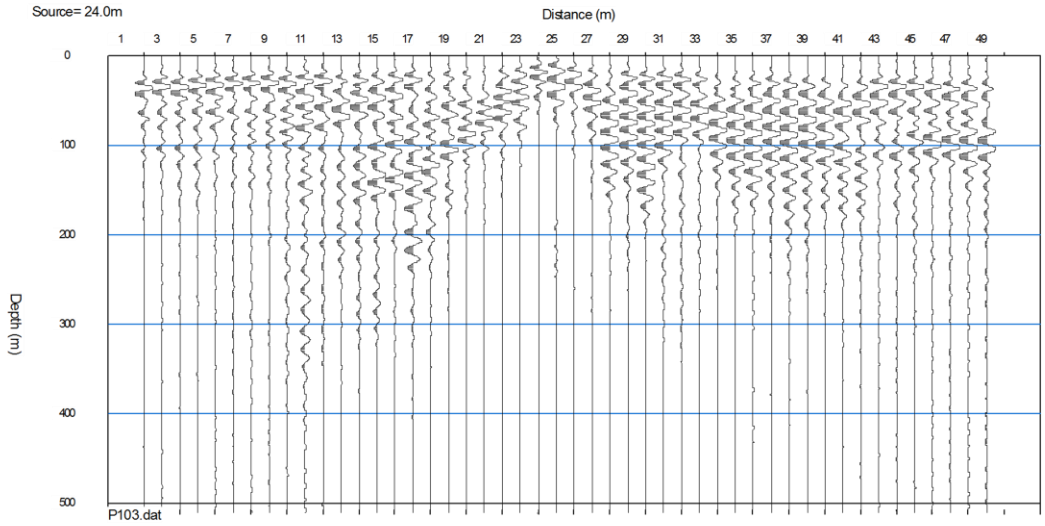

Berea Road line 3 P-Wave refraction shot 4

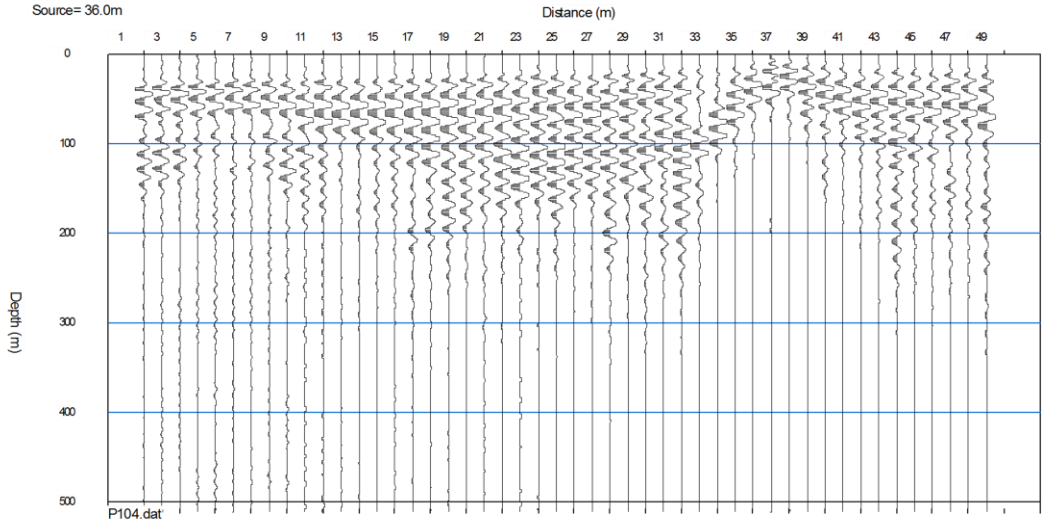

Berea Road line 3 P-Wave refraction shot 5

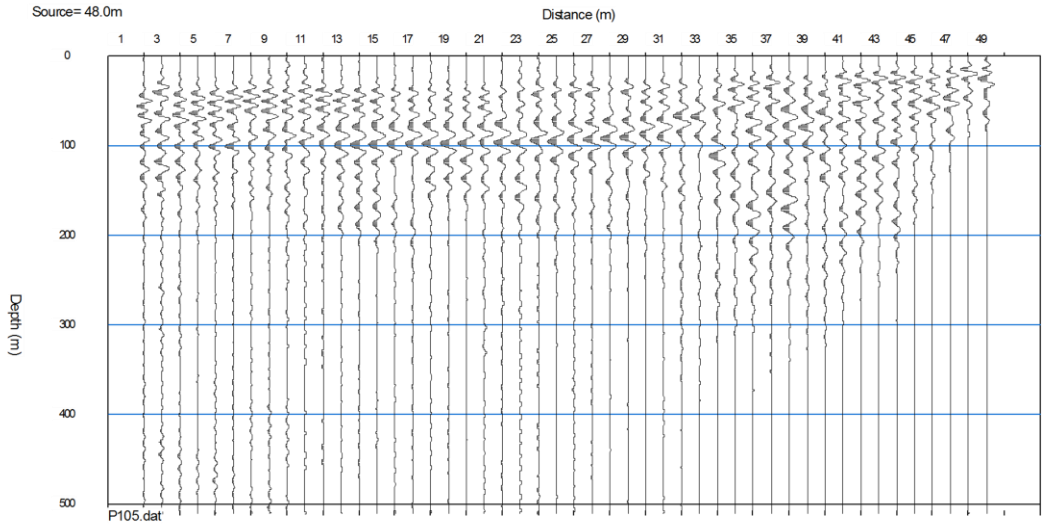

Berea Road line 3 P-Wave refraction shot 6

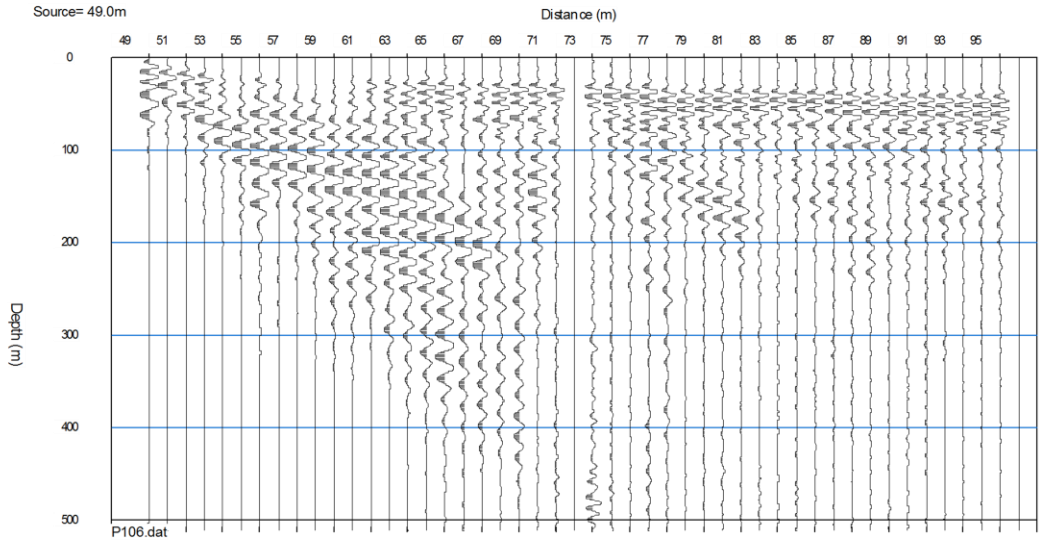

Berea Road line 3 P-Wave refraction shot 7

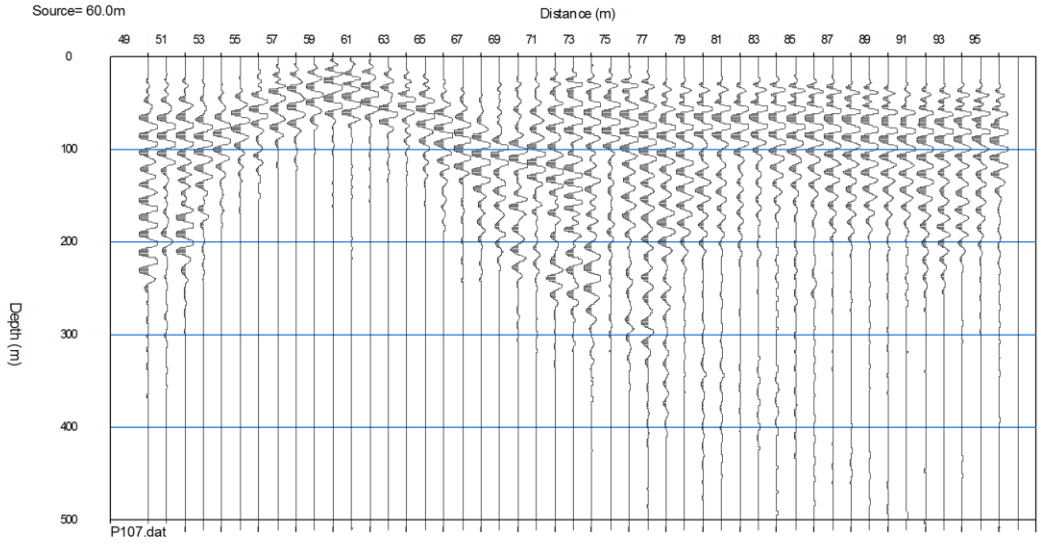

Berea Road line 3 P-Wave refraction shot 8

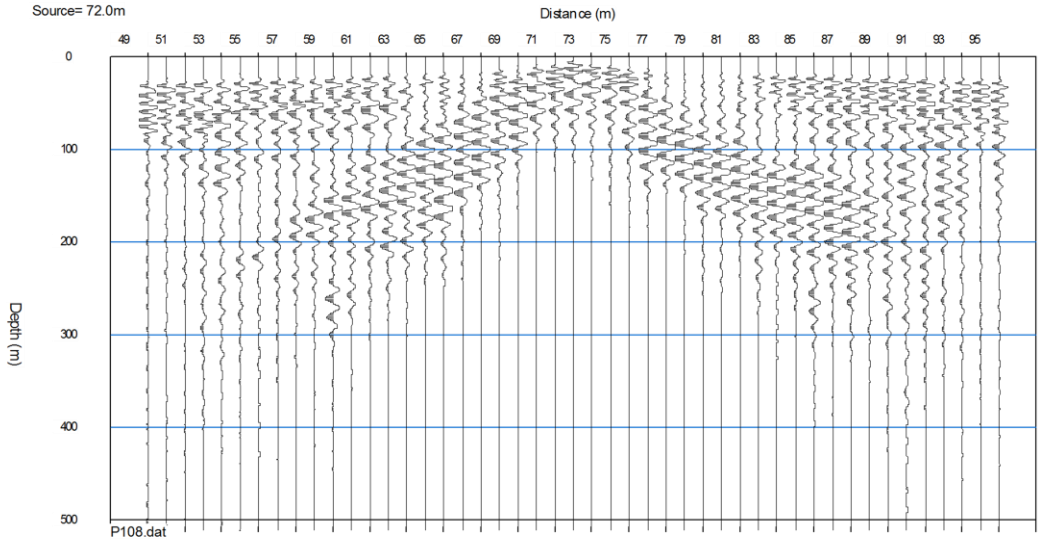

Berea Road line 3 P-Wave refraction shot 9

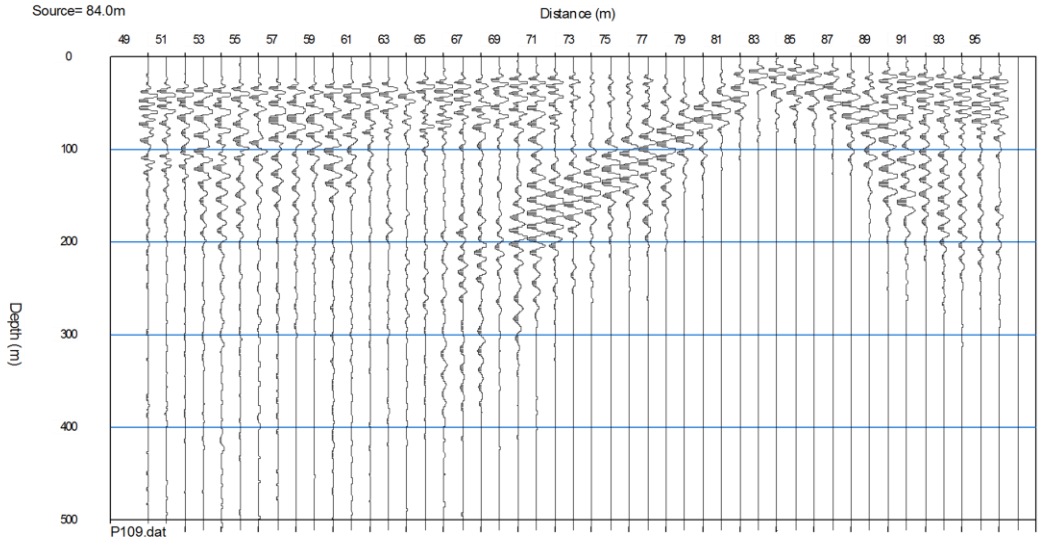

Berea Road line 3 P-Wave refraction shot 10

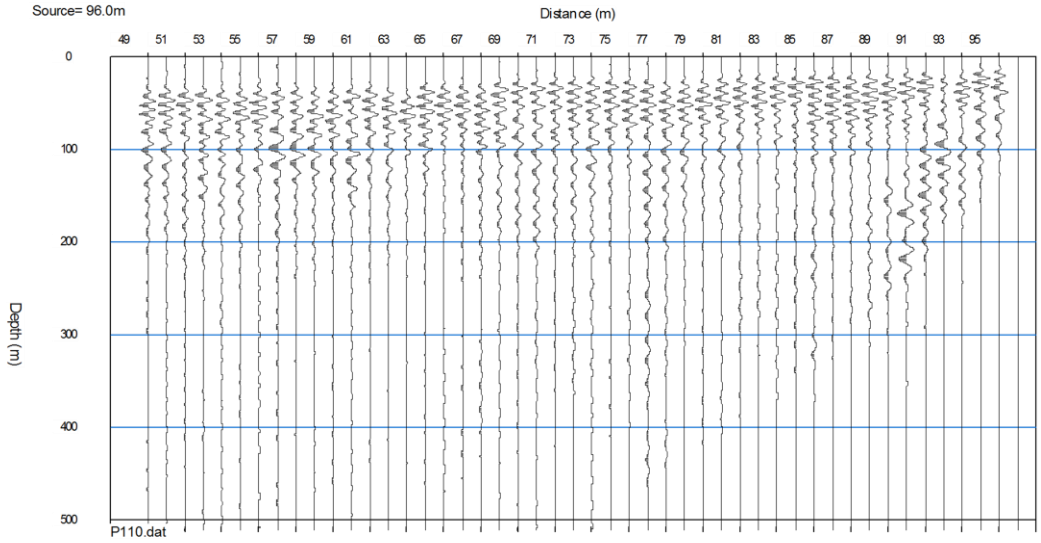

Berea Road line 3 P-Wave refraction shot 11

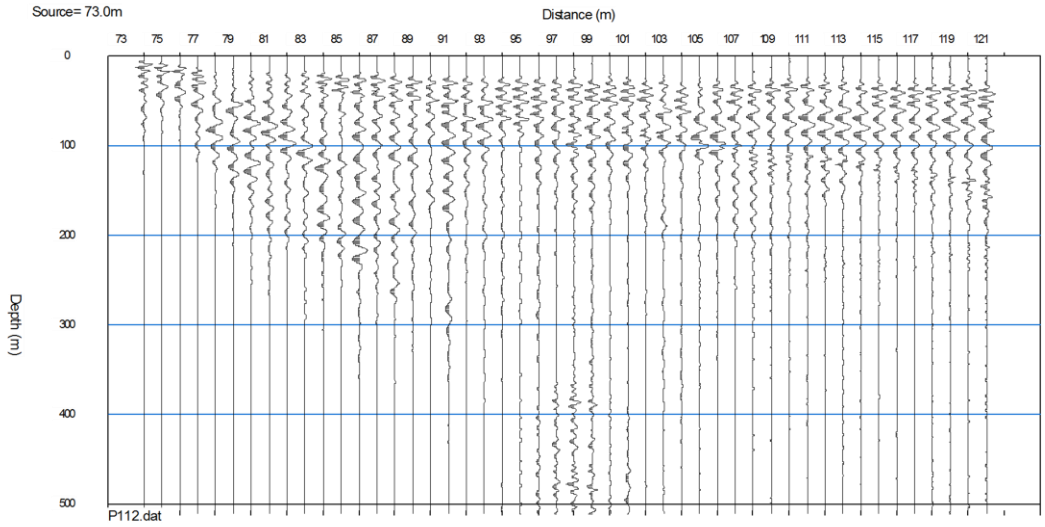

Berea Road line 3 P-Wave refraction shot 12

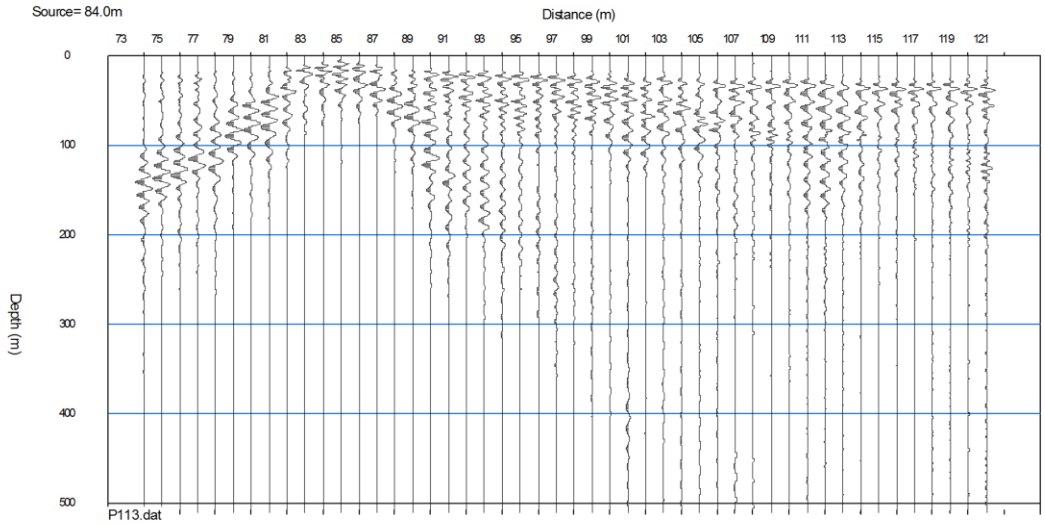

Berea Road line 3 P-Wave refraction shot 13

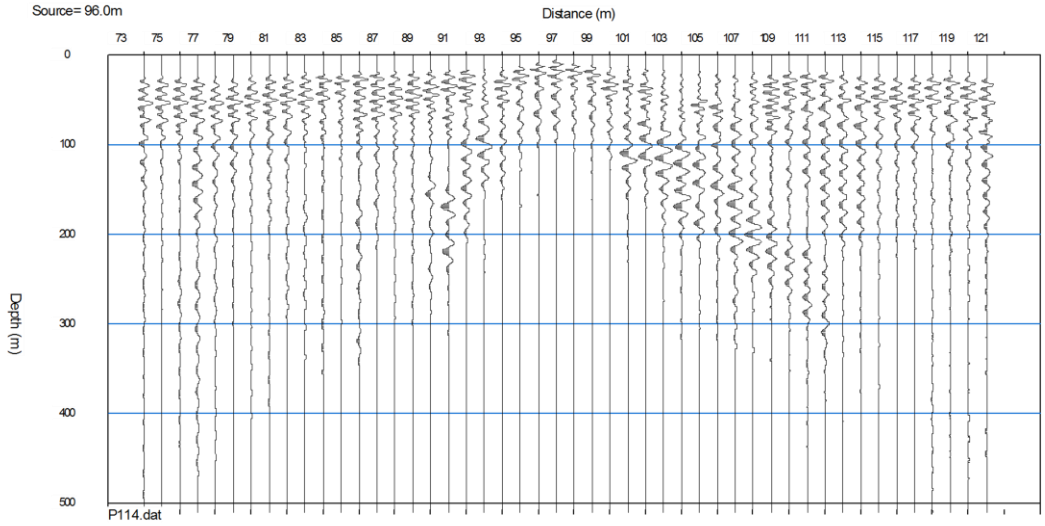

Berea Road line 3 P-Wave refraction shot 14

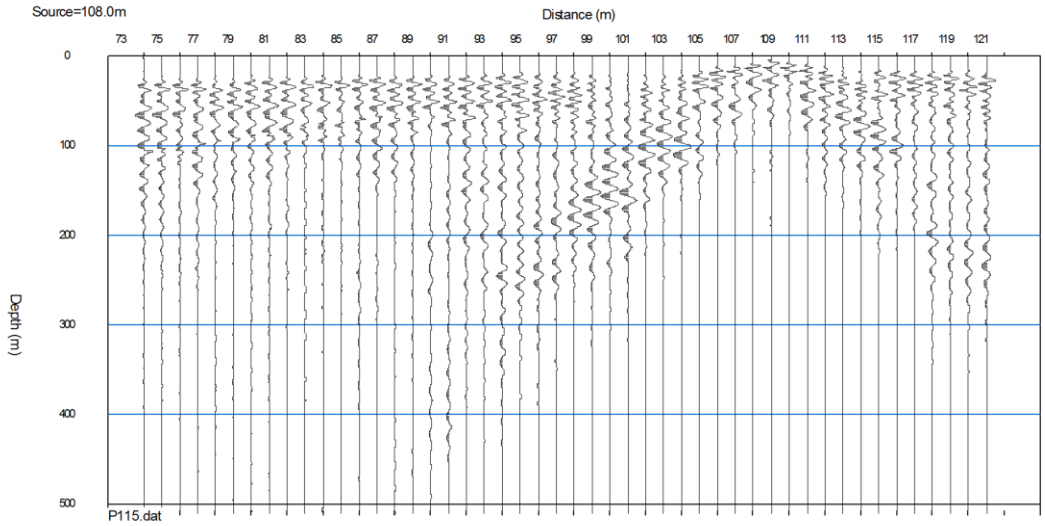

Berea Road line 3 P-Wave refraction shot 15

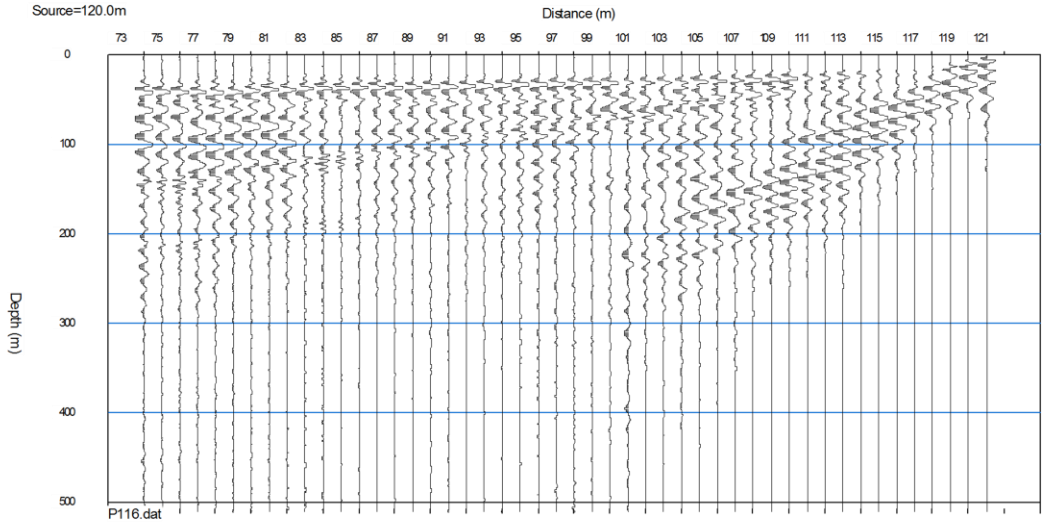

Berea Road line 4 P-Wave refraction shot 1

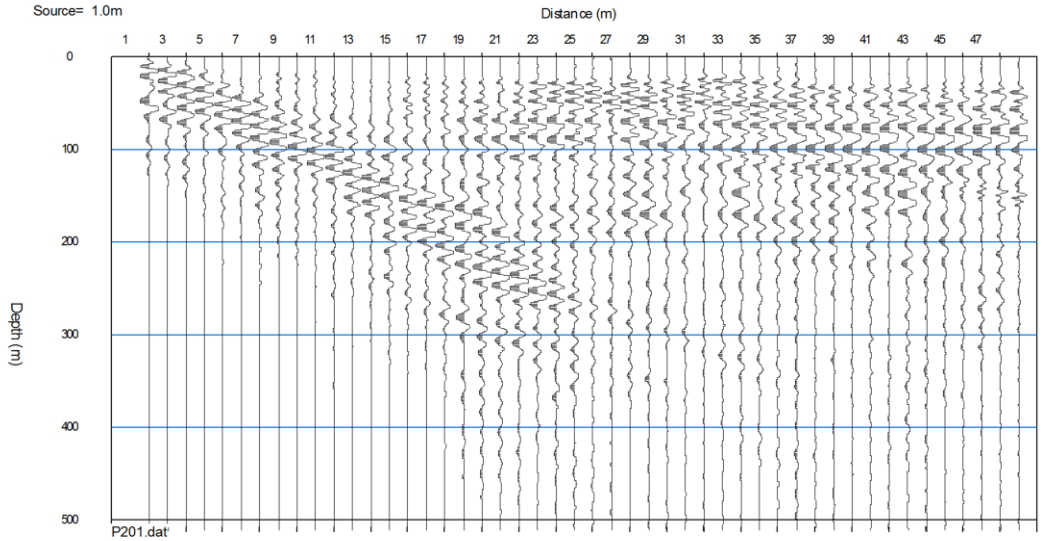

Berea Road line 4 P-Wave refraction shot 2

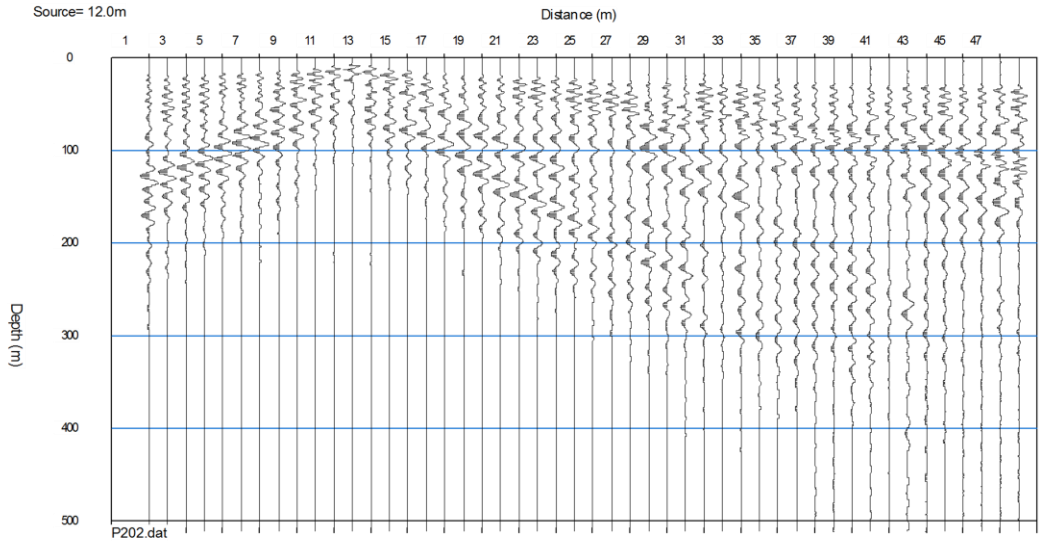

Berea Road line 4 P-Wave refraction shot 3

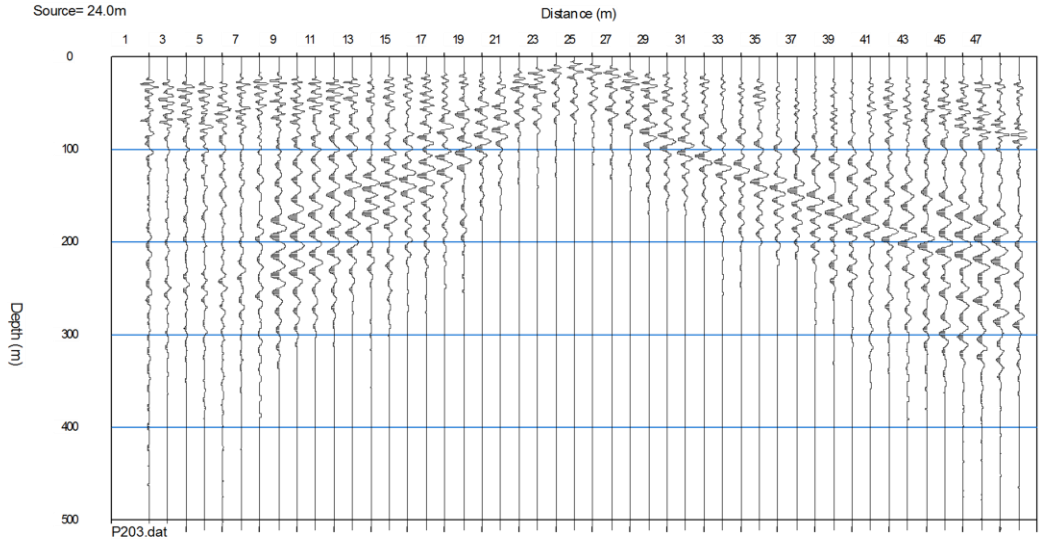

Berea Road line 4 P-Wave refraction shot 4

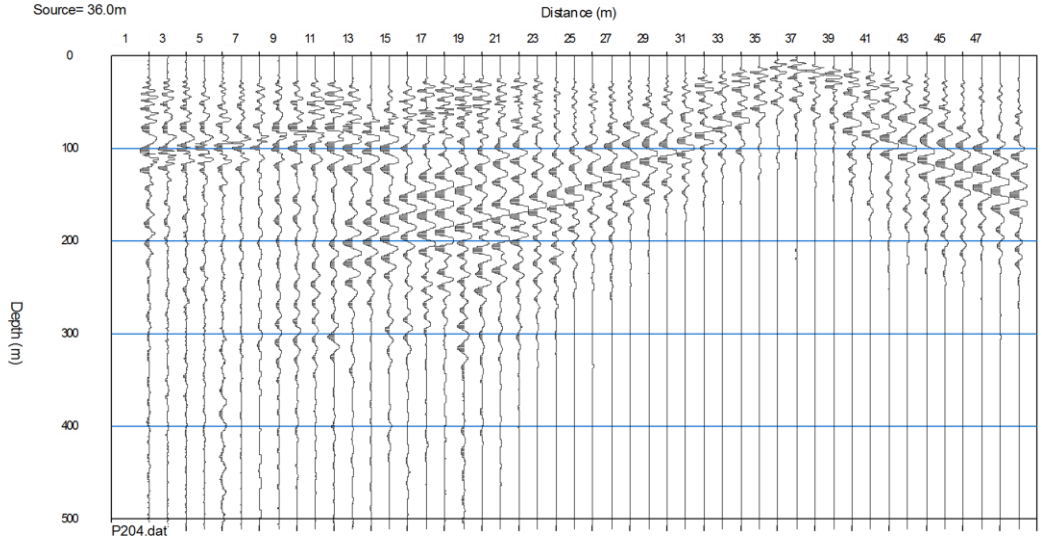

Berea Road line 4 P-Wave refraction shot 5

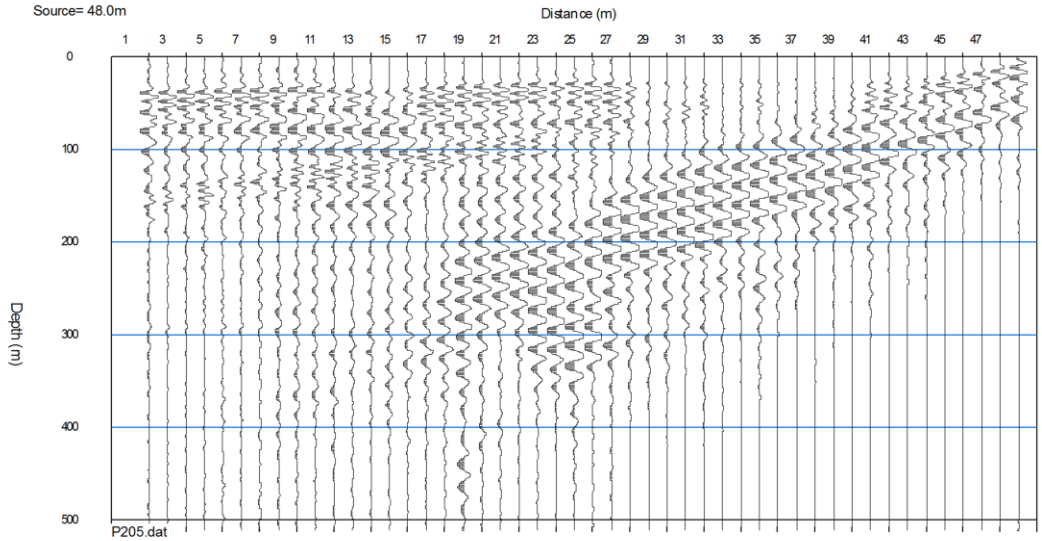

Berea Road line 4 P-Wave refraction shot 6

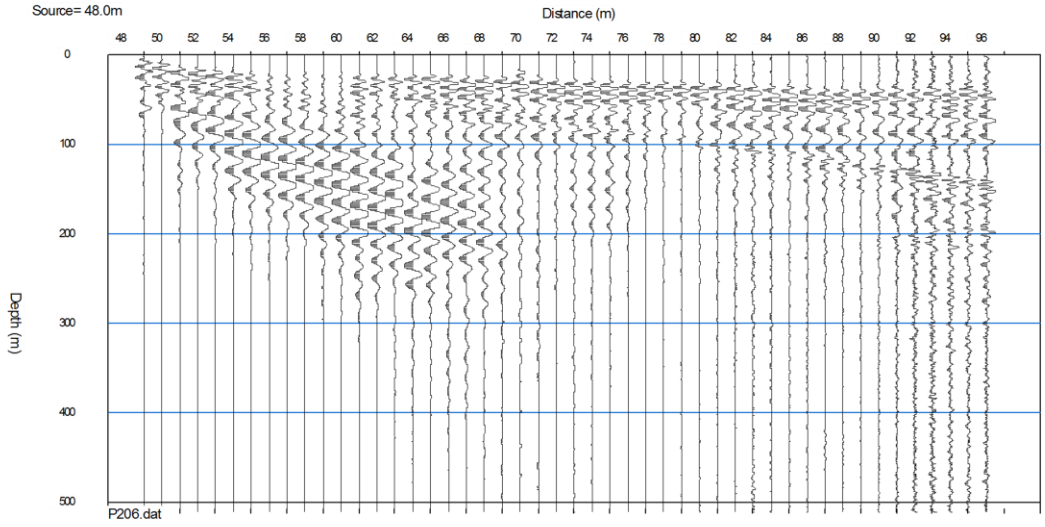

Berea Road line 4 P-Wave refraction shot 7

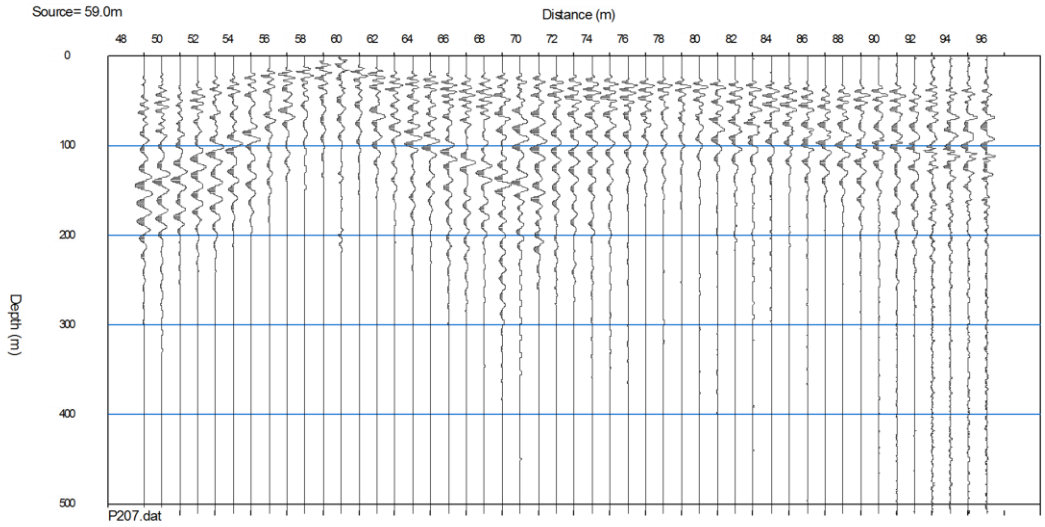

Berea Road line 4 P-Wave refraction shot 8

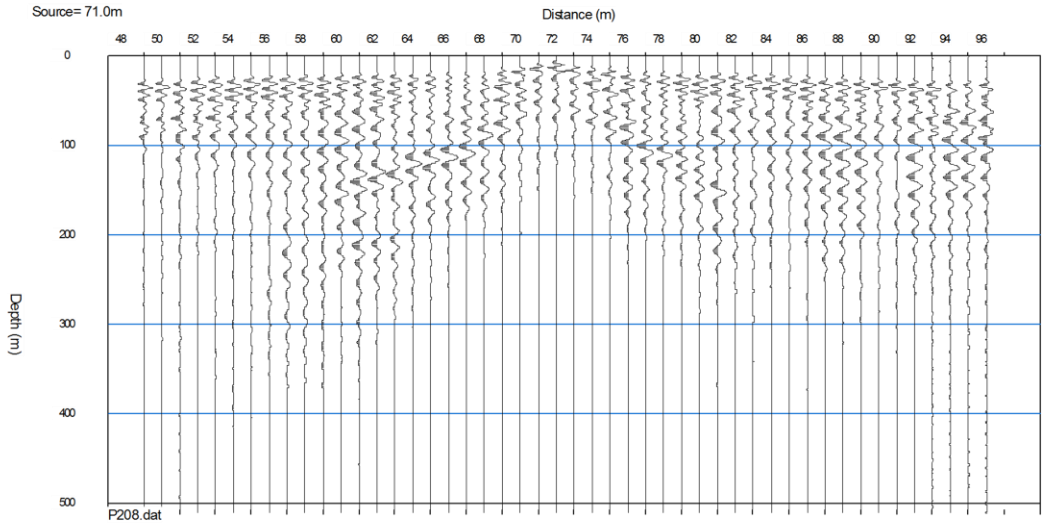

Berea Road line 4 P-Wave refraction shot 9

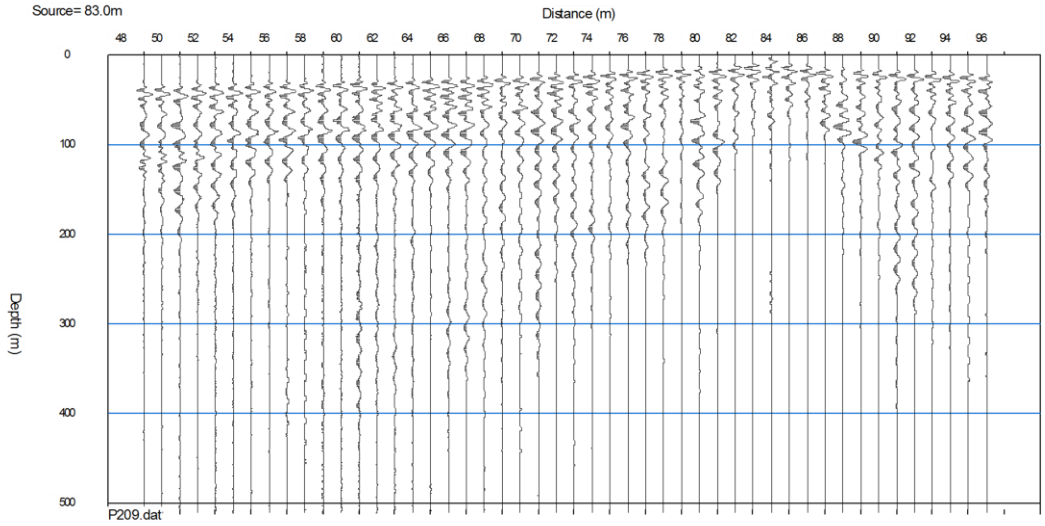

Berea Road line 4 P-Wave refraction shot 10

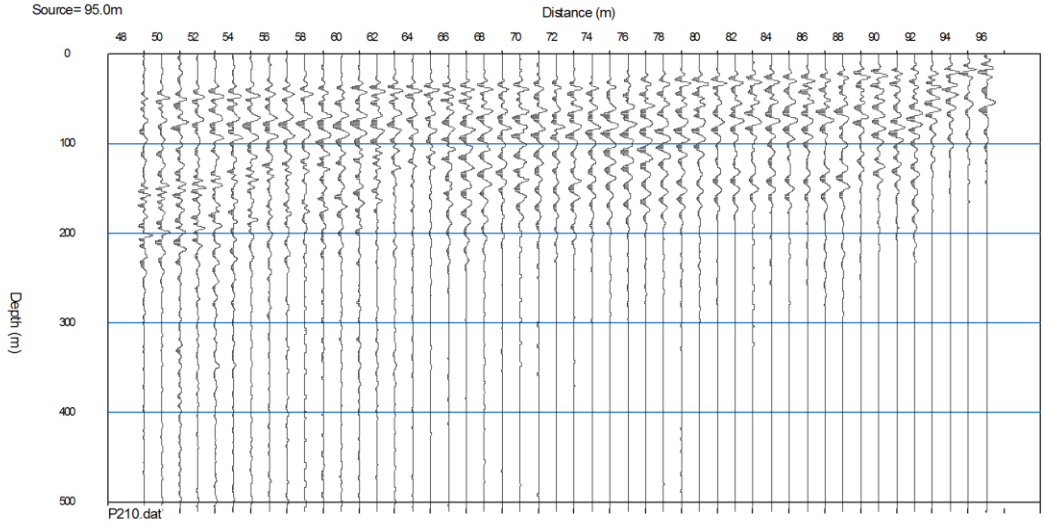

BIBLIOGRAPHY

Advanced Geosciences Inc. (AGI), 2006, Instruction manual for EarthImager 2D version 2.2.0 resistivity and IP inversion software: Austin, Tex, Advanced Geosciences Inc.,134 p.

Advanced Geosciences Inc. (AGI), 2007. Seminar on resistivity imaging: AGI Resistivity Imaging Seminar, Sept. 11−12, Austin, Tex., 135 p.

Anderson, N.L., 1998, Reflection seismic mapping of an abandoned coal mine, Belleville, Illinois: Journal of Environmental and Engineering Geophysics, v. 3, no. 2, p. 81−88.

Baker, G.S., and Society of Exploration Geophysicists, 1999, Processing near-surface seismic-reflection data: A primer: Society of Exploration Geophysicists, 77 p.

Baker, G.S., Steeples, D.W., Drake, M., 1998, Muting the noise cone in near-surface reflection data: An example from southeastern Kansas: Geophysics, v. 63, no. 4, p. 1332−1338.

Ballard, R.F., 1983: Detection of karst cavities by geophysical methods: Bulletin of the International Association of Engineering Geology, v. 26-27, p. 153−157.

Bekler, T., Ekinci, Y.L., Demirci, A., Erginal, A. E., Ertekin, C., 2011, Characterization of a landslide using seismic refraction, electrical resistivity and hydrometer methods, Adatepe-Canakkale, NW Turkey: Journal of Environmental and Engineering Geophysics, v. 16, no. 3, p. 115−126.

Black, D.F.B., Cressman, E.R., and MacQuown, W.C., Jr., 1965, The Lexington Limestone (Middle Ordovician) of central Kentucky: U.S. Geological Survey Bulletin 1224-C, 29 p.

Black, D.F.B., and Cuppels, N.P., 1973, Strodes Creek Member (Upper Ordovician)—A new map unit in the Lexington Limestone of north-central Kentucky: U.S. Geological Survey Bulletin 1372-C, 16 p.

Bonita, J.A. 1993, An electrical resistivity and fracture trace study in the Inner Bluegrass karst region of north-central Kentucky. *University of Kentucky, M. S. Thesis*, 155 p.

Blits, C.A., 2008, Integrated geophysical imaging of subsurface geologic conditions across a contaminant plume, McCracken county, Kentucky: Lexington, University of Kentucky, master's thesis, 300 p.

Burger, H. R., A. F. Sheehan, and Jones, C.H., 2006, Introduction to applied geophysics: Exploring the shallow subsurface: New York, W.W. Norton, 600 p.

Cardarelli, E., Cercato, M., et al. 2010, Electrical resistivity and seismic refraction tomography to detect buried cavities: Geophysical Prospecting, v. 58, no. 4, p. 685−695.

Cardarelli, E., Di Filippo, G., Cerrato, A., Di Filippo, G., 2006, Electrical resistivity tomography to detect buried cavities in Rome: A case study: Near Surface Geophysics, v. 4, no. 6, p. 387−392.

Cercato, M., Cardarelli, E., Di Filippo, G., 2010, Geophysical investigation for the rehabilitation of a flood control embankment: Near Surface Geophysics, v. 8, no. 4, p. 287−296.

Chalikakis, K., Plagnes, V., Guerin, R., Valois, R., Bosch, F., 2011, Contribution of geophysical methods to karst-system exploration: An overview: Hydrogeology Journal, v. 19, no. 6, p. 1169−1180.

Cook, J.C., 1965, Seismic mapping of underground cavities using reflection amplitudes: Geophysics, v. 30, no. 4, p. 527-538.

Cook, J.C., 1975, Radar transparencies of mine and tunnel rocks: Geophysics, v. 40, no. 5, p. 865−885.

Cressman, E.R., 1965. Geologic map of the Keene quadrangle, central Kentucky: U. S. Geological Survey Geologic Quadrangle Map GQ-440.

Cressman, E.R., 1967, Geologic map of the Georgetown quadrangle, Scott and Fayette Counties, Kentucky: U.S. Geological Survey Geologic Quadrangle Map GQ-605, scale 1:24,000.

Currens, J.C., 2001, Generalized block diagram of the Inner Bluegrass Karst: Kentucky Geological Survey, ser. 12, Map and Chart 15, 1 sheet. http://kgs.uky.edu/kgsweb/olops/pub/kgs/mc15_12.pdf

Dahlin, T., and Zhou, B., 2004, A numerical comparison of 2D resistivity imaging with 10 electrode arrays: Geophysical Prospecting, v. 52, no. 5, p. 379−398.

Dahlin, T., and Zhou, B., 2005, Reply to "Comment on: 'A numerical comparison of 2D resistivity imaging with 10 electrode arrays' by T. Dahlin and B. Zhou": Geophysical Prospecting, v. 53, no. 6, p. 855−857.

Daniels, J.J., 1988. Locating caves, tunnels and mines: The Leading Edge, v. 7, no. 3, p. 32−52.

Dinger, J.S., Zourarakis, D.P., Currens, J.C., 2007, Spectral enhancement and automated extraction of potential sinkhole features from NAIP imagery—Initial investigations: Journal of Environmental Informatics, v. 10, no. 1, p. 22−29.

Doolittle, J.A., and Collins, M.E., 1998, A comparison of EM induction and GPR methods in areas of karst: Geoderma, v. 85, no. 1, p. 83−102.

Driad, L.P., and Bodgan, P., 2002, Detection and characterization of underground cavities using high resolution seismic reflection (HRSR): Proceedings, 8th meeting, Environmental and Engineering Geophysics, Aveiro, Portugal, p. 31−34.

Dutta, N.P., 1970, Detection of solution channels in limestone with electrical resistivity method: Geophysical Prospecting, v. 18, no. 3, p. 405−414.

Elawadi, E., El-Qady, G., Nigm, A., Shaaban, F., Ushijima, K., 2006, Integrated geophysical survey for site investigation at a new dwelling area, Egypt: Journal of Environmental and Engineering Geophysics, v. 11, no. 4, p. 249−259.

Felton, G.K., and Currens, J.C., 1994, Peak flow-rate and recession-curve characteristics of a karst spring in the Inner Bluegrass, central Kentucky: Journal of Hydrology, v. 162, nos. 1-2, p. 99−118.

Feroci, M., Orlando, L., Balia, R., Bosman, C., Cardarelli, E., Deidda, G., 2000, Some considerations on shallow seismic reflection surveys: Journal of Applied Geophysics, v. 45, no. 2, p. 127−139.

Gochioco, L.M., 1990, Seismic surveys for coal exploration and mine planning: The Leading Edge, v. 9, no. 4, p. 25−28.

Graham, C.D.R., 1995, Electrical resistivity studies in the Inner Bluegrass karst region, Kentucky: Lexington, University of Kentucky, master's thesis, 101 p.

Grandjean, G., and Leparoux, D., 2004, The potential of seismic methods for detecting cavities and buried objects: Experimentation at a test site: Journal of Applied Geophysics, v. 56, no. 2, p. 93−106.
Greenfield, R., 1979, Review of geophysical approaches to the detection of Karst: Bulletin of the Association of Engineering Geologists, v. 16, p. 393−408.
Griffiths, D.H., and Barker, R.D., 1993: 2-dimensional resistivity imaging and modeling in areas of complex geology: Journal of Applied Geophysics, v. 29, nos. 3-4, p. 211−226.
Hiltunen, D., Hudyma, N., Quigley, T., and Samakur, C., 2007, Ground proving three seismic refraction tomography programs: Transportation Research Record: Journal of the Transportation Research Board, v. 2016, no. 1, p. 110−120.
Hiltunen, D.R. and Cramer, B.J., 2008, Application of seismic refraction tomography in karst terrane: Journal of Geotechnical and Geoenvironmental Engineering, v. 134, no. 7, p. 938−948.
Hiltunen, D.R., Hudyma, N., Quigley, T.P., and Samakur, C., 2006, Ground-truthing seismic refraction tomography for sinkhole detection in Florida: Conference Proceedings, Missouri University of Science and Technology, 11 p.
Hunter, J.A., Pullan, S.E., Burns, R.A., Gagne, R.M., Good, R.L., 1984, Shallow seismic reflection mapping of the overburden-bedrock interface with the engineering seismograph—Some simple techniques: Geophysics, v. 49, no. 8, p. 1381−1385.
Kentucky Geological Survey, Beneath the surface [geologic structures: http://www.uky.edu/KGS/geoky/beneath.htm
Knapp, R.W., and Steeples, D.W., 1986, High-resolution common-depth point profiling—Field acquisition parameter design—Reply: Geophysics, v. 51, no. 10, p. 2012−2012.
Knapp, R.W., and Steeples, D.W., 1986, High-resolution common-depth-point reflection profiling—Field acquisition parameter design: Geophysics, v. 51, no. 2, p. 283−294.
Knapp, R.W., and Steeples, D.W., 1986, High-resolution common-depth-point seismic-reflection profiling—Instrumentation: Geophysics, v. 51, no. 2, p. 276−282.
Kosecki, A., Piwakowski, B., and Driad-Lebeau, L., 2010, High resolution seismic investigation in salt mining context: Acta Geophysica, v. 58, no. 1, p. 15−33.
McCann, D.M., Jackson, P.D., and Culshaw, M.G., 1987, The use of geophysical surveying methods in the detection of natural cavities and mineshafts: Quarterly Journal of Engineering Geology, v. 20, no. 1, p. 59−73.
McGrath, R.J., Styles, P., Thomas, E., and Neale, S., 2002, Integrated high-resolution geophysical investigations as potential tools for water resource investigations in karst terrain: Environmental Geology, v. 42, no. 5, p. 552−557.
Militzer, H., Rosler, R., and Losch, W., 1979, Theoretical and experimental investigations for cavity research with geoelectrical resistivity methods: Geophysical Prospecting, v. 27, no. 3, p. 640−652.
Miller, R.D., Pullan, S.E., Waldner, J.S., and Haeni, F.P., 1986, Field comparison of shallow seismic sources: Geophysics, v. 51, no. 11, p. 2067−2092.

Miller, R.D., Pullan, S.E., Steeples, D.W., and Hunter, J.A., 1992, Field comparison of shallow seismic sources near Chino, California: Geophysics, v. 57, nol. 5, p. 693−709.

Miller, R.D., Pullan, S.E., Steeples, D.W., and Hunter, J.A., 1994, Field comparison of shallow P-wave seismic sources near Houston, Texas: Geophysics, v. 59, no. 11, p. 1713−1728.

Miller, R.D., and Steeples, D.W., 1991, Detecting voids in a 0.6 m coal seam, 7-m deep, using seismic-reflection: Geoexploration, v. 28, no. 2, p. 109−119.

Nosow, E. & McFarlan, A. 1960, Geology of the central Bluegrass area. Series X, Guidebook 12, Kentucky Geological Survey, 56 p.

Pawar, S.D., Murugavel, P., and Lal, D.M., 2009, Effect of relative humidity and sea level pre electrical conductivity of air over Indian Ocean: Journal of Geophysical Research−Atmospheres, v. 114, 8 p.

Paylor, R., and Currens, J.C., 2004, Royal Spring karst groundwater travel time investigation: Kentucky Geological Survey, prepared for Georgetown Municipal Water and Sewer Service, . 23 p.

Robinson, E.S., and Çoruh, C., 1988, Basic exploration geophysics: New York, Wiley, 562 p.

Sheehan, J.R., 2005, Application of seismic refraction tomography to karst cavities: : http://pubs.usgs.gov/sir/2005/5160/PDF/Part1_2.pdf

Sheehan, J.R., Doll, W.E., and Mandell, W.A., 2005, An evaluation of methods and available software for seismic refraction tomography analysis: Journal of Environmental and Engineering Geophysics, v. 10, no. 1, p. 21−34.

Sheets, R.A., 2002, Use of electrical resistivity to detect underground mine voids in Ohio: U.S. Geological Survey Water-Resources Investigations Report 02-4041, 12 p. http://oh.water.usgs.gov/reports/wrir/wrir02-4041.pdf

Sloan, S.D., Steeples, D.W., Tsoflias, G.P., 2009, Ultra-shallow imaging using 3D seismic-reflection methods: Near Surface Geophysics, v. 7, nos. 5-6, p. 307−314.

Sloan, S.D., Peterie, S.L., Ivanov, J., Miller, R.D., McKenna, J.R., 2010, Void detection using near-surface seismic methods; in R.D. Miller, J.H. Bradford, and K. Holliger, eds., Advances in Near-surface Seismology and Ground-penetrating Radar: Geophysical Developments No. 15, 201-218

Smith, D.L., 1986, Application of the pole-dipole resistivity technique to the detection of solution cavities beneath highways: Geophysics, v. 51, no. 3, p. 833−837.

Sparks, T.N., Dever, G.R., Jr., Anderson, W.H., 2002, Geologic map of the Lexington 30 x 60 Minute Quadrangle, Central Kentucky: Kentucky Geological Survey, ser. 12, Geologic map 2, 1 sheet.

Steeples, D.W., Green, A.G., McEvilly, T.V., Miller, R.D., Doll, and W.E., Rector, J.W., 1997, A workshop examination of shallow seismic reflection surveying: The Leading Edge, v. 16, no. 11, p. 1641−1647.

Steeples, D.W., and Miller, R.D., 1998, Avoiding pitfalls in shallow seismic reflection surveys: Geophysics, v. 63, no. 4, p. 1213−1224.

Sumanovac, F., and Weisser, M., 2001, Evaluation of resistivity and seismic methods for hydrogeological mapping in karst terrains: Journal of Applied Geophysics, v. 47, no. 1, p. 13−28.

Taylor, C.J., 1992, Ground-water occurrence and movement associated with sinkhole alignments in the Inner Bluegrass karst region of central Kentucky: Lexington, University of Kentucky, master's thesis, 113 p.

Thrailkill, J., 1985. Flow in a limestone aquifer as determined from water tracing and water levels in wells: Journal of Hydrology, v. 78, nos. 1-2, p. 123−136.

Thrailkill, J., and Spangler, L.E., 1982, Groundwater in the Inner Bluegrass karst region, Kentucky: University of Kentucky, KentuckyWater Resources Research Institute, 136 p.

Thrailkill, J., Sullivan, S.B., and Gouzie, D.R., 1991, Flow parameters in a shallow conduit-flow carbonate aquifer, Inner Bluegrass karst region, Kentucky, USA: Journal of Hydrology, v. 129, nos. 1-4, p. 87−108.

Tripathi, G.N., 2009, Use of surface geophysical techniques to locate a karst conduit in the Cane Run–Royal Spring Basin, Kentucky: Lexington, University of Kentucky, master's thesis, 115 p.

University of Kentucky, Physiographic diagram of Kentucky: http://www.uky.edu/KentuckyAtlas/kentucky-atlasp.html

Kuniansky, E.L., ed., 2005, U.S. Geological Survey Karst Interest Group proceedings, Rapid City, South Dakota, September 12-15, 2005: U.S. Geological Survey Scientific Investigations Report 2005-5160. http://pubs.usgs.gov/sir/2005/5160/index.html#PDF

Waltham, A.C., and Fookes, P.G., 2003, Engineering classification of karst ground conditions: Quarterly Journal of Engineering Geology and Hydrogeology, v. 36, p. 101−118.

Waltham, T., 2008, Sinkhole hazard case histories in karst terrains: Quarterly Journal of Engineering Geology and Hydrogeology, v. 41, p. 291−300.

Zhu, J.C., Currens, J.C., and Dinger, J.S., 2011, Challenges of using electrical resistivity method to locate karst conduits—A field case in the Inner Bluegrass Region, Kentucky: Journal of Applied Geophysics, v. 75, p. 523-530.

VITA

Jamin Charles Frommel was born in Cincinnati, Ohio on December 2, 1979. He graduated summa cum laude from Northern Kentucky University in May of 2010, receiving a Bachelor of Science degree in Geology. He held the position of Research Assistant in the Department of Earth and Environmental Sciences from August 2010 to May 2011, and again from January 2012 to May 2012. He held the position of Teaching Assistant in the Department of Earth and Environmental Sciences from August 2011 to December 2011.